BOOK OF ABSTRACTS NSSY 2026

Here we present the Abstract Book of the sixth international edition of Nanoscience Summer School Yachay (NSSY2026), held from the 17th of May until the 23rd of May 2026 at Puerto Ayora, Galapagos Islands, Ecuador.

The NSSY2026 had plenary sessions from the most eminent scientists, invited talks from leading researchers in the field, and contributed talks chosen from the best-submitted abstracts.

We will also feature a two-day poster session.

In this international edition of NSSY2026, there was the participation of 97 delegates, including speakers, keynote lecturers, professors, researchers, and students. The event included talks on the latest work in different topics of nanoscience and nanotechnology, covering theoretical and experimental works and their applications.



Dr. Gema González
Dean, School of Physical Sciences and Nanotechnology,
Yachay Tech University
NSSY2026 Conference Chair
Chair Editor in Chief, Acta Microscopica

Acta Microscopica Vol.35, Supp.1, 2026
Abstract Book NSSY 2026 - Galapagos 17th–23rd May 2026

NANOSCIENCE SUMMER SCHOOL 2026 @ YACHAY TECH

INTERNATIONAL SIXTH EDITION

May 17th to 23rd, 2026

SCHOOL OF PHYSICAL SCIENCES AND NANOTECHNOLOGY

Organizing Committee

Gema González *(chair)*
Yachay Tech University – Ecuador
Charlotte Berrezueta *(co-chair)*
Freie Universität Berlin – Germany
Vincent Meunier
Penn State University – USA
Norman Wray
Galapagos Hub – Ecuador
Melany Aguilar Ramirez
Yachay Tech University – Ecuador
Alexis Garzón
Yachay Tech University – Ecuador
Cristina Rubio
Penn State University – USA
María Fernanda Bósquez
Yachay Tech University – Ecuador
Andrés Vera Ochoa
Yachay Tech University – Ecuador
Pedro Zamora
Yachay Tech University – Ecuador

National Scientific Committee

Vincent Meunier *(chair)*
Penn State University – USA
Carlos Reinoso *(Coordinator)*
Yachay Tech – Ecuador
Juan Francisco Nicolalde
UIDE – Ecuador
Marbel Torres
ESPE – Ecuador
Marcos Guevara
ESPOCH – Ecuador
Patricio Espinoza-Montero
PUCE – Ecuador
Víctor Guarochico Moreira
ESPOL – Ecuador
Víctor Guerrero
EPN – Ecuador

Scientific Advisory Board

Eric Anglaret
Univ. Montpellier – France
Carla Bittencourt
University of Mons – Belgium
Gabriela Borin-Barin
EMPA Zurich – Switzerland
Sofie Cambré
Antwerp University – Belgium
Rodrigo Capaz
Universidade Federal do Rio de Janeiro – Brazil
Alan Dalton
University of Sussex – UK
Silvia Giordani
Dublin City University – Ireland
Gema González
Yachay Tech – Ecuador
Sarah Haigh
University of Manchester – UK
Thomas Heine
Technische Universität Dresden – Germany
Ernesto Joselevich
Weizmann Institute of Science – Israel
Ado Jorio
Universidad Minas Gerais – Brazil
Zoraya López
University of Talca – Chile
Shigeo Maruyama
Tokyo University – Japan
Vincent Meunier
Penn State University – USA
Stephanie Reich
Freie Universität Berlin – Germany
Mariana Rossi
Max Planck Institute – Germany
Humberto Terrones
Rensselaer Polytechnic Institute – USA

Community Outreach Advisory Board

Humberto Terrones *(chair)*
Rensselaer Polytechnic Institute – USA
Byron Tipán
Yachay Tech University – Ecuador

SCIENTIFIC PROGRAM NSSY 2026

	Sunday, May 17	Monday, May 18	Tuesday, May 19	Wednesday, May 20	Thursday, May 21	Friday, May 22	Saturday, May 23
8:00 AM		BREAKFAST 8:00 - 8:30					
8:30 AM		TUTORIAL Gabriela Borin-Barin 8:30 - 9:30	TUTORIAL Mariana Rossi 8:30 - 9:30	TUTORIAL Arkady Krasheninnikov 8:30 - 9:30	TUTORIAL Thomas Heine 8:30 - 9:30	TUTORIAL Silvia Giordani 8:30 - 9:30	
9:30 AM		INVITED SPEAKER Mark Hersam 9:30 - 10:00	INVITED SPEAKER Yu-Yang Zhang 9:30 - 10:00	INVITED SPEAKER Mauricio Tamayo 9:30 - 10:00	INVITED SPEAKER Eduardo Costa Girão 9:30 - 10:00	INVITED SPEAKER Yolanda Angulo 9:30 - 10:00	
10:00 AM		ORAL CONTRIBUTION Andrey Mereshchenko 10:00 - 10:20	ORAL CONTRIBUTION Zoran Miskovic 10:00 - 10:20	ORAL CONTRIBUTION Katherine Vaca-Escobar 10:00 - 10:20	ORAL CONTRIBUTION Eva Scholtzova 10:00 - 10:20	ORAL CONTRIBUTION Julio Chacon 10:00 - 10:20	
10.20 AM		YOUNG RESEARCH Charlotte Berrezueta 10:20 - 10:35	YOUNG RESEARCH Jorge Castro Angamarca 10:20 - 10:35	YOUNG RESEARCH Kevin Gerein 10:20 - 10:35	YOUNG RESEARCH Cristina Rubio 10:20 - 10:35	YOUNG RESEARCH Laura Ochoa Rodríguez 10:20 - 10:35	
		COFFEE BREAK **10:35 - 11:00**					
11:00 AM	ARRIVAL	INVITED SPEAKER Vincent Meunier 11:00 - 11:30	INVITED SPEAKER Begoña Espiña 11:00 - 11:30	INVITED SPEAKER Duncan Mowbray 11:00 - 11:30	INVITED SPEAKER Vladimíra Petráková 11:00 - 11:30	INVITED SPEAKER Humberto Terrones 11:00 - 11:30	
11:20 AM		INVITED SPEAKER Hong-Jun Gao 11:30 - 12:00	INVITED SPEAKER Carla Bittencourt 11:30 - 12:00	INVITED SPEAKER Akhlesh Lakhtakia 11:30 - 12:00	INVITED SPEAKER Ernesto Medina 11:30 - 12:00	INVITED SPEAKER Thibault Terencio 11:30 - 12:00	
12:00 PM		ORAL CONTRIBUTION Guido Schmitz 12:00 - 12:20	ORAL CONTRIBUTION Sarah Briceño 12:00 - 12:20	ORAL CONTRIBUTION Patricio Espinoza 12:00 - 12:20	YOUNG RESEARCH Domenica Bermeo Alvaro 12:00 - 12:15	CLOSING REMARKS 12:00 - 13:00	DEPARTURE
		YOUNG RESEARCH Paula Tris Marzo 12:20 - 12:35	INDUSTRY TECHNICAL TALK Julie Chen 12:20 - 12:35	YOUNG RESEARCH Byron Tipán 12:20 - 12:35	YOUNG RESEARCH Vanessa Hinojosa 12:15 - 12:30		
		YOUNG RESEARCH Elena Stroici 12:35 - 12:50	YOUNG RESEARCH Johanna Pilicita 12:35 - 12:50	YOUNG RESEARCH María Bósquez Cáceres 12:35 - 12:50			
1:00 PM		MINIWORKSHOPS	MINIWORKSHOPS	MINIWORKSHOPS	MINIWORKSHOPS	MINIWORKSHOPS	
2:00 PM			**COMMUNITY OUTREACH** 15:00 - 17:00		**CONFERENCE TOUR INTEGRATION** 14:00 - 17:00		
4:00 PM	REGISTRATION **16:00-17:00**	ROUND TABLE **Science, Sustainability & Galápagos** 16:00 - 18:00		**ROUND TABLE** **Embarking on a career in Nanoscience** 16:00 - 18:00			
6:00 PM							
7:00 PM	**WELCOME RECEPTION** 18:00 - 19:00	POSTER SESSION I 18:00 - 20:00		**POSTER SESSION II** 18:00 - 20:00	**CONFERENCE DINNER** 18:00 - 22:00		

Acta Microscopica Vol.35, Supp.1, 2026
Abstract Book NSSY 2026 - Galapagos 17th–23rd May 2026

Monday

Atomically Precise Graphene Nanoribbons: from Synthesis to Device Integration
Gabriela Borin Barin 1

Mixed-dimensional heterostructures for electronic and energy technologies
Mark C. Hersam 2

Tuning the properties of β-$NaYF_4$:Ln^{3+} nanomaterials: The role of lanthanide nature on structure, morphology, and functional properties
Andrey Mereshchenko 3

Optical and vibrational properties of amorphous graphene
Charlotte Berrezueta-Palacios 5

Flexoelectricity in Self-Assembled Graphene Nanowrinkles
Vincent Meunier 6

Ordered and tunable Majorana-zero-mode lattice in iron-based superconductors
Hong-Jun Gao 7

Breaking the Materials Barrier: Atom Probe Tomography as an emerging Tool in Chemical Analysis of Soft Matter and Complex Interfaces
Guido Schmitz 8

Molecular anodes based on self-assembled bilayers for (photo)electrocatalytic water oxidation
Paula Tris-Marzo 11

Hexacyano-trimethyl-cyclopropane as a Raman probe for quantifying charge transfer in molecule-2D-materials
Elena Stroici 13

Science, Sustainablility & Galápagos
Round Table: Claudia Alarcon, Begona Espiña, Patricio Espinoza, Julio Chacon, Washington Tapia .....

Tuesday

Machine learning for electronic structure and atomistic simulations
Mariana Rossi 16

Monte Carlo–Based Active Learning Framework for Monolayer Amorphous Materials
Yu-Yang Zhang 17

Anisotropic DC mobility of doped phosphorene due to charge carrier scattering on charged impurities calculated by the energy loss method
Miskovic Zoran 18

Incorporating Nuclear Quantum and Anharmonic Effects into Tip-Enhanced Raman Spectroscopy
Jorge Castro 20

Nanotechnology-based tools for water contaminants' monitoring
Begoña Espiña 22

Marine Microplastics in Tulear: The Silent Threat from Woven Bags and Ropes Evaluated by Infrared Spectroscopy
Carla Bittencourt 23

Magnetic Nanoparticles for Microplastics Remediation
Sarah Briceño 25

Sustainable Conversion of Rice Husk into Functional Silica for Advanced Nanostructured Materials
Pilicita-Carua Johanna 26

Orthogonal Size and Number Concentration Calibration for Improved Quantitative Biological Analyses
Julie Y. Chen 29

Wednesday

Engineering the structure and properties of 2D materials by defects and impurities
Arkady V. Krasheninnikov 31

Multiscale Diffusion in CNT Polymer Nanocomposites: Analytical Modelling, Monte Carlo Simulation and Physics-Informed Neural Networks
Tamayo-Vegas Sebastian 32

Simultaneous production of hydrogen peroxide and bioelectricity generation at the cathode using modified graphite electrodes
Katherine Vaca-Escobar 34

Highly Efficient Functionalization and Covalent Patterning of Graphene by Photoactivation
Kevin Gerein 37

Optical absorption: A primer
Duncan John Mowbray 39

Transmission-mode geometric-phase characteristics of sculptured thin films
Akhlesh Lakhtakia 40

Materials Design of BDD/$BiVO_4$–BDD/Bi_2CuO_4 Photoelectrode Systems for Visible-Light-Driven Microplastic Degradation and Hydrogen Production
Patricio J. Espinoza-Montero 42

Laser induced graphene from avocado seed
Byron Tipán 44

Carbonaceous materials derived from carboxymethylcellulose loaded with ZnO NPs for supercapacitors: correlation between structure and performance
María Fernanda Bósquez-Cáceres 46

Embarking on a career in nanoscience
Round Table .....

Thursday

Precision Chemistry
Thomas Heine 48

Graph theory tools for nanocarbon symmetry, structural generation, and beyond
Eduardo Costa Girão 49

Influence of topological defects on the adsorption properties of graphene for small molecules
Scholtzova Eva 51

Tuning 2D materials through substitutional doping: Vibrational Properties of V–WS_2
Cristina Rubio 53

Exploiting mirage in microscopy to monitor molecular interactions
Vladimíra Petráková 56

Orbital angular momentum textures and currents in helical molecules
Ernesto Medina 57

Towards Scalable Quantum Photonics: Diamond Meets AlGaN/AlN Platform
Domenica Bermeo Alvaro 58

Bridging Phonon Dispersion Mapping and Junction Nanoelectronics in InP-Based Nanowires Using GI-IXS And TERS
V. Hinojosa-Chasiquiza 60

Friday

Biomedical Applications of Carbon Nanomaterials
Silvia Giordani 64

Cyanobacteria–Nanoparticle Biohybrid Systems: Toward Enhanced Energy Production and Agricultural Applications
Yolanda Angulo 65

Mechanical Properties of Functionalized Chitosan Biofilms
Julio C. Chacón-Torres 67

Physicochemical Stability and Preliminary Biocompatibility of Geraniol-Loaded SNEDDS Nanoemulsions
Ochoa-Rodríguez Laura Raquel 69

2D Materials: Challenges and Opportunities in a Quantum World
Humberto Terrones 71

Going beyond the classical view of cat-ions
Thibault Terencio 72

Monday

Poster Session

Electrochemically activated carbon nanostructures as nano-enhancers for phase change materials in sustainable thermal management systems: experimental and simulation analysis
Andres Chico-Proano 74

Antibacterial Properties of Nanostructured Chitosan Biofilms
Jeniffer L. Andrango Quinga 76

Synthesis of Ag-impregnated hydrochars assisted by the concentrate derived from the spent liquor of hydrothermal carbonization
Daniela Armijos 78

Transition-Metal Complexes of Oxalate and Carbonate as EUV Photoresists
Norman Barreno 81

From Waste to Medicine: Cocoa Bean Shell-AgNP Hydrothermal Synthesis for Enhanced Chitosan/Gentamicin Films for Potential Drug Delivery
Ian Boada 83

Laser Printing of Single-Walled Carbon Nanotube Conductive Tracks on Silicon
Daniela Briceño C. 85

Hybrid Carbon Nanomaterials: Quantum Dot Encapsulation in Nanotube Cavities
Jose Campo 87

Magnetic - Chitosan Microspheres for Microplastics Recovery
Anderson Cañamar 89

Synthesis and characterization of hybrids based on VCL-PEGDA stimuli-

responsive gels and carbon quantum dots with potential luminescent properties
Simón Choez 92

Nanoparticles for Intranasal Delivery of Temozolomide With Potential Application in the Treatment of Glioblastoma Multiforme
Marlus Chorilli 94

Effect of graphene oxide on the germination and early growth of agronomically important plants
Sarahi Josefina Estrada Loredo 96

Conductive Bio-Based Polymer Composites with Percolated Graphite Networks
Daniela Fernández-Sánchez 98

Growth temperature influence on graphitic ribbons synthesis: Characterization and systematic cyclic voltammetry study
Flores-López Zacek David 100

Arsenic removal from aqueous solutions using biochar derived from green banana peel
Giseth Freire 102

Synthesis and characterization of composites based on vinyl polymers and nanoparticles with potential photocatalytic properties
David Garcés 104

Sustainable development of carbon nanostructures on recycled steel: annealing-induced surface optimization for CNT growth and enhanced surface conductivity
Domenica Garcia 107

Xerogel-based hybrid system loaded with quantum dots and nanotubes for controlled release of vitamins B6 and B12: Physicochemical characterization and release kinetics
Gómez Angel 109

Computational Study of External Quantum Efficiencies: A quantum photoinduced treatment of OPV
Daniel E. Gonzalez-Tamayo 111

Hard Carbon Derived from Banana Pseudostem (Musa paradisiaca): A Sustainable Approach for Energy Storage Materials
Joseph Granja-Vélez 113

Efficient N_2 activation in transition metal complexes: Computational approach
R. Guañuna 116

Development of hydroxyapatite-functionalized polyacrylonitrile polymeric membranes (PAN/HAp) and their application for fluoride removal in aqueous medium
Santiago Guerrero-Jaramillo 118

Density Functional Theory Calculations to model the Adsorption of Microplastics on $CoFe_2O_4$
Daheny Lopez 120

Wednesday

Poster Session

From excited states to a precise description of van der Waals interactions
Maisincho Brayan 122

Phytochemical profiling, antioxidant properties, and anticancer activity of Pourouma cecropiifolia Mart. from the Ecuadorian Amazon
Carlos Méndez-Durazno 124

Optical Coherence Tomography Enhancement via Tartrazine Optical Clearing in Biological Tissues
Genesis M. Mendoza-Celorio 126

Development and characterization of hydrogels containing solid lipid nanoparticles as carriers of α-bisabolol for sensitive skin inflammation
Meneses-Arguelles Rossie Inelle 128

Exploring the Use of Chitosan-Based Gels and LED Light in Sustainable Crop Development
Tahis Montalvo 131

Advances in Thermal Conductivity Enhancement of Bio-Based Phase Change Materials through Nano-Additives: A Comprehensive Review
Juan Francisco Nicolalde 133

Synthesis and layer-by-layer assembly of a silicon–organic hybrid diode
Sebastian Ojeda Maza 135

Ab initio study of the electronic properties and magnetic phases of thermoelectric oxide material $Ca_3Co_4O_9$
Alan I. Palma 138

Design of pathogen-responsive nanoencapsulated fungicides for soil-borne disease control
Michael A. Pantoja 139

KUST-1 as a platform for the controlled release of drugs: Synthesis, Characterization, and kinetic study
Cinthia Perugachi 141

Visible light driven degradation of bisphenol A using BiOI/BiOBr heterojunctions immobilized in poly(vinyl alcohol)
Pillajo Anahi 143

Comparative Study of Electrodeposition Techniques Applied to Gas Diffusion Layers (GDLs) for Electrical Conductivity Enhancement
D. Rodriguez 146

From biological carbon capture to nanostructured biosorbents: processing and characterization of bio-derived carbons
María J. Salazar Macías 149

Laser beam induced current based assessment of a recycled p-type silicon Solar Cell
K. Sulca 152

Nickel Sulfide Nanostructures and Nitrogen-Doped Multiwalled Carbon Nanotubes: Synthesis, Characterization, and Electrochemical Properties
Torres-Xolocotzin A. Paulina 154

Structure and Optical Properties of Heterometallic Luminescent Antenna Complexes $Eu_xLa_{1-x}TTA_3Phen$ for Latent Fingerprint Detection (LFPs)
Bryan Vargas 156

Magnetic sands: A sustainable nanotech approach to microplastic removal
Josue Vargas 158

Magneto-responsive electrospun PVA/chitosan nanofibers functionalized with magnetite nanoparticles for on-demand ciprofloxacin release
Velasco Henry 162

Phytochemical Characterization and Evaluation of the Pharmacological Properties of Ecuadorian Sugarcane (Saccharum officinarum L.) Extracts
Ariana Véliz 164

$BiFeO_3$/BiOBr Hybrid Photo-Piezocatalysts: Synthesis, Structural–Optical Characterization, and ROS-Mediated Rhodamine B Degradation
Andrés G. Vera-Ochoa 166

Optimization of Electrochemical Sensors by Using Conducting Polymers and Carbon Quantum Dots (CQDs)
Shamison Villarreal 168

Diatomites grounded Carbon Nanotubes and potential applications in Li-ion systems
Pedro Zamora 170

Influence of Carbonization Temperature on the Structure and Surface Chemistry of Hard Carbon Derived from Banana Pseudostem
Jenny E. Zamora Cepeda 172

Acta Microscopica Vol.35, Supp.1, 2026
Abstract Book NSSY 2026 - Galapagos 17th–23rd May 2026

Conference

Monday

Acta Microscopica Vol.35, Supp.1, 2026
Abstract Book NSSY 2026 - Galapagos 17th–23rd May 2026

Atomically Precise Graphene Nanoribbons: from Synthesis to Device Integration

Gabriela Borin Barin[1]

[1] *Swiss Federal Laboratories for Materials Science and Technology, Empa*
gabriela.borin-barin@empa.ch

Abstract

Graphene nanoribbons (GNRs) show exciting properties deriving from electron confinement and related band gap tunability [1]. The ability to tune GNRs' electronic and magnetic properties at the single-atom level makes them an ideal platform for a wide range of device applications, from classical transistors to spintronics. In this tutorial, I will provide an overview of the necessary steps to bring GNRs from ultra-high vacuum (UHV) to device integration, focusing on synthesis, characterization, device architectures, and transport measurements. After UHV bottom-up synthesis, GNRs are transferred using wet or semi-dry/dry transfer methods. Those processes allow the characterization of GNRs fingerprint modes via Raman spectroscopy and the characterization of their electronic properties on decoupled substrates such as quasi-free-standing graphene via scanning probe methods [2]. Finally, I will discuss progress in integrating GNRs into field-effect transistors with different gate and contact configurations, as well as the main challenges in achieving clean contacts and high performance with 1D low-dimensional systems [3].

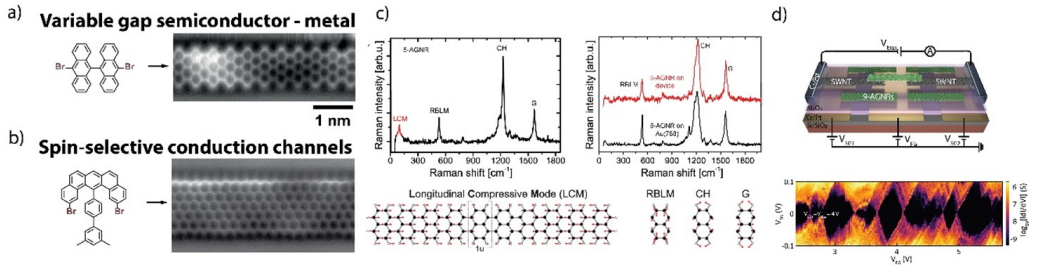

Figure 1: a) and b) precursor monomers for GNRs with different edge topology and correspondent noncontact atomic force microscopy images, c) Raman spectrum of 5-AGNRs with the assignment of the most prominent peaks on Au (111) and on the device substrate after transfer; atomic displacement profiles obtained from DFT calculations of 5-AGNRs, d) Schematic of the device, using CNT as electrodes, including the measurement circuit; stability diagram showing single-electron charging behavior.

References

[1] Cai, J. et al. *Nature* **2010**, *466*.

[2] Kinikar, A. et al. *ACS Applied Nanomaterials* **2025**, *8*.

[3] Hwang, J. et al. *ACS Nano* **2025**, *19*.

Acta Microscopica Vol.35, Supp.1, 2026
Abstract Book NSSY 2026 - Galapagos 17th–23rd May 2026

Mixed-dimensional heterostructures for electronic and energy technologies

Mark C. Hersam[1]

[1] *Northwestern University, 2220 Campus Drive, Evanston, IL 60208-3108, USA*
m-hersam@northwestern.edu

Abstract

Layered two-dimensional (2D) materials interact primarily via van der Waals bonding, which has created opportunities for heterostructures that are not constrained by epitaxial lattice matching requirements [1]. However, since any passivated, dangling bond-free surface interacts with another via non-covalent forces, van der Waals heterostructures are not limited to 2D materials alone. In particular, 2D materials can be integrated with a diverse range of other materials, including those of different dimensionality, to form mixed-dimensional van der Waals heterostructures. Furthermore, chemical functionalization provides additional opportunities for tailoring the properties of 2D materials and the degree of coupling across heterointerfaces. In this manner, a variety of optoelectronic and energy applications can be enhanced including photodetectors, optical emitters, supercapacitors, and batteries [2]. Furthermore, mixed-dimensional heterostructures enable unprecedented electronic device function to be realized (Figure 1) that exploit neuromorphic, opto-spintronic, and quantum phenomena [3]. In addition to technological implications for electronic and energy technologies, this talk will explore several fundamental issues including band alignment, doping, trap states, and charge/energy transfer across mixed-dimensional heterointerfaces.

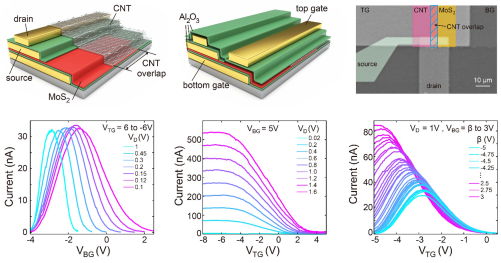

Figure 1: Mixed-dimensional heterojunctions based on 1D p-type semiconducting carbon nanotubes and 2D n-type semiconducting MoS2 enable fully gate-tunable Gaussian, sigmoid, or mixed-kernel characteristics for energy-efficient hardware accelerators for machine learning. Adapted from [3].

References

[1] Hadke, S. et al. *Chemical Reviews* **2025**, *125*, 835.

[2] Clegg, C. et al. *Nature Photonics* **2025**, *19*, 1178.

[3] Yan, X. et al. *Nature Electronics* **2023**, *6*, 862.

Acta Microscopica Vol.35, Supp.1, 2026
Abstract Book NSSY 2026 - Galapagos 17th–23rd May 2026

Tuning the properties of β-$NaYF_4$:Ln^{3+} nanomaterials: The role of lanthanide nature on structure, morphology, and functional properties

Andrey Mereshchenko[1], Anna A. Betina[2], Nikita A. Bogachev[2]

[1] *School of Physical Sciences and Nanotechnology, Yachay Tech University, Urcuquí 100119, Ecuador*
[1] *Institute of Chemistry, Saint Petersburg State University, St. Petersburg 198504, Russia*
amereshchenko@yachaytech.edu.ec

Abstract

Hybrid inorganic functionalized nanocomposites incorporating rare-earth elements are among the most extensively studied nanomaterials today. In medicine and biology, they show significant promise for bioimaging applications, including luminescence imaging, magnetic resonance imaging (MRI), and positron emission tomography (PET). This potential arises from their unique optical and chemical properties, such as low autofluorescence, a high signal-to-noise ratio, deep tissue penetration, reduced toxicity (including phototoxicity), high chemical stability, large Stock's shifts, and tunable luminescence properties achievable through synthesis. Furthermore, their synthetic procedures are relatively straightforward. These advantages are particularly inherent to nanomaterials based on NaYF4. Their low phonon energy, compared to oxide matrices and metal-organic complexes, results in a low efficiency of luminescence quenching by the transfer of electronic energy to the matrix's vibrational modes.

This work studies the effect of lanthanide ion nature on the size, morphology, and structure of NaYF4-doped nanoparticles for two series of β-$NaYF_4$:Ln^{3+} nanoparticles (Ln = La–Nd, Sm–Lu) doped with 20 at.% and 40 at.% Ln^{3+} [1]. The resulting materials consist of uniform hexagonal prism-shaped particles, with sizes ranging from 80 to 1100 nm depending on the specific lanthanide ion and its concentration (Figures 1 and 2). The mean crystal diameter exhibits a non-monotonic dependence on the lanthanide's atomic number, with the smallest size observed for Gd^{3+}-doped materials. Concurrently, X-ray diffraction (XRD) analysis confirms that the unit cell parameters decrease consistently from La to Lu. The study also explores the optical properties and cytotoxicity of several surfactant-coated NaMF4-based materials (M = Y, Gd, Lu), which exhibit both down-conversion (NaMF4: Eu/Tb/Nd) and up-conversion (NaMF4: Yb, Ho/Er) photoluminescence [2, 3]. The surfactant coating stabilizes the colloidal solutions. These nanoparticles are promising candidates for biological and medical applications, serving as dyes for fluorescence microscopy and fluorescence-guided surgery, as well as contrast agents for MRI.

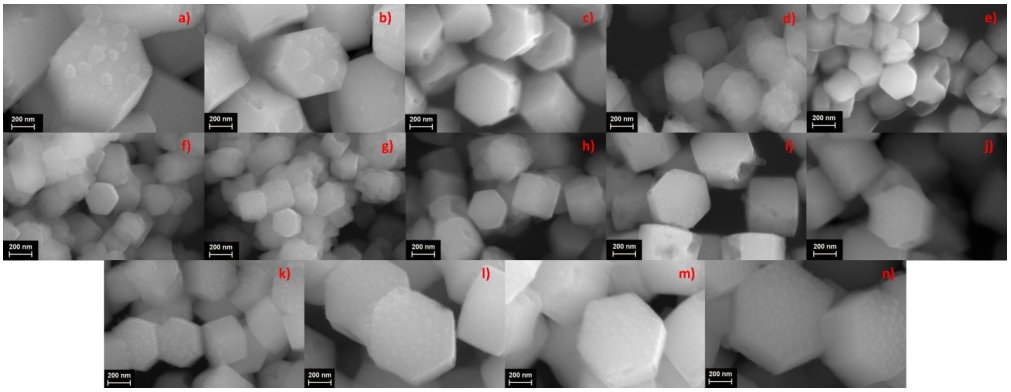

Figure 1: SEM images of the NaY0.8Ln0.2F4 samples, Ln = a) La b) Ce c) Pr d) Nd e) Sm f) Eu g) Gd h) Tb i) Dy j) Ho k) Er l) Tm m) Yb n) Lu

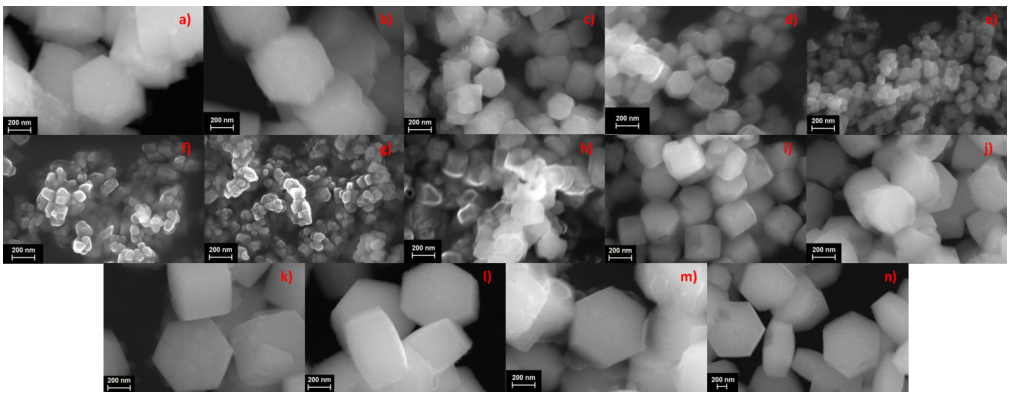

Figure 2: SEM images of the NaY0.6Ln0.4F4 samples, Ln = a) La b) Ce c) Pr d) Nd e) Sm f) Eu g) Gd h) Tb i) Dy j) Ho k) Er l) Tm m) Yb n) Lu

References

[1] Bogachev, N. A.; Betina, A. A.; Bulatova, T. S.; Nosov, V. G.; Kolesnik, S. S.; Tumkin, I. I.; Ryazantsev, M. N.; Skripkin, M. Y.; Mereshchenko, A. S. Lanthanide-Ion-Doping Effect on the Morphology and the Structure of $NaYF_4$:Ln^{3+} Nanoparticles. *Nanomaterials* **2022**, *12*, 2972.

[2] Betina, A. A.; Bulatova, T. S.; Nosov, V. G.; Kolesnikov, I. E.; Bogachev, N. A.; Skripkin, M. Y.; Mereshchenko, A. S. Morphology and Luminescent Properties of Nanocrystalline $NaGdF_4$ Luminophores Doped with Neodymium(III) Ions. *Russian Journal of General Chemistry* **2023**, *93*, 1300–1306. DOI: 10.1134/S1070363223080157.

[3] Dovzhenko, A. A.; Betina, A. A.; Bulatova, A. A.; Bogachev, N. A.; Nikiforov, V. G.; Voloshina, A. D.; Zairov, R. R.; Mustafina, A. R.; Mereshchenko, A. S.; Akhmadeev, B. S. Dual Contrasting Ability of $NaGd_{0.7}Eu_{0.3}F_4$ Nanocrystals Tuned by Their Hydrophilic Coating Mode. *Mendeleev Communications* **2024**, *34*, 637–639. DOI: 10.1016/j.mencom.2024.09.004.

Optical and vibrational properties of amorphous graphene

Charlotte Berrezueta-Palacios[1], Katayoun Gharagozloo-Hubmann[1], Sabrina Juergensen[1], Tibor Lehnert[2], Ute Kaiser[2], Mateus Silva Rego[3], Paloma Vieira Silva[3], Eduardo Costa Girão[3], Vincent Meunier[4], Stephanie Reich[1], Georgy Gordeev[1,5]

[1] *Department of Physics, Freie Universität Berlin, Germany*
[2] *Ulm University, Central Facility of Electron Microscopy, Germany*
[3] *Departamento de Física, Universidade Federal do Piauí, Brazil*
[4] *Department of Engineering Science and Mechanics,Pennsylvania State University, USA*
[5] *University of Luxembourg, Luxembourg*
charlotte.berrezueta@fu-berlin.de

Abstract

We show that topology-induced localization of π-electronic states governs both the broadband optical absorption and the resonant Raman response of monolayer amorphous graphene. This material is a structurally distinct form of graphene in which the absence of translational symmetry fundamentally modifies electronic and vibrational excitations. It forms a continuous sp^2 network of non-hexagonal ring motifs, yet the link between atomic topology, electronic localization, and optical response remains largely unexplored.

To understand the optical response of amorphous graphene, we combine atomic-resolution transmission electron microscopy, tight-binding simulations, optical absorption measurements, and resonant Raman spectroscopy. Atomic-resolution imaging enables the reconstruction of the two-dimensional lattice, providing a structural model for mapping the electronic states. Tight-binding calculations reveal strongly localized π states at low energies that progressively extend over larger regions of the network with increasing energy, reflecting the topology-dependent electronic structure of the amorphous lattice. This evolution is directly reflected in the optical response, where we observe broadband absorption up to 20% across the visible range for a single atomic layer. Consistently, resonant Raman spectroscopy reveals a strong excitation-energy-dependent enhancement of the G mode, reaching up to about fiftyfold toward lower excitation energies, closely following the evolution of the optical absorption and indicating that the Raman response is governed by the same localization-driven electronic structure.

These results establish a direct link between atomic topology and light–matter interaction, showing that disorder can be used as a design parameter to tune optical and vibrational properties in atomically thin materials.

Flexoelectricity in Self-Assembled Graphene Nanowrinkles

Vincent Meunier[1]

[1] *Department of Engineering Science and Mechanics, Pennsylvania State University (USA)*
vincent.meunier@psu.edu

Abstract

Flexoelectricity, the polarization induced by strain gradients, manifests with remarkable intensity in two-dimensional materials due to their extraordinary mechanical flexibility and structural sensitivity. This phenomenon reaches peak expression in highly curved nanostructures, where extreme charge redistribution creates measurable electrostatic effects.

Our presentation will begin with an introduction to flexoelectricity's fundamental principles in 2D materials [1]. We will then explore its microscopic origins in graphene nanowrinkles (NW) through density functional theory (DFT), demonstrating how intense curvature at top of the NWs generates significant local Gaussian curvature values, producing observable macroscopic effects.

Our experimental observations focus on self-assembled graphene NWs formed on flat MoS_2 substrates. The mismatch in elastic properties between these materials creates strain gradients, which we mapped using sub-micro Raman spectroscopy. Conductive atomic force microscopy (c-AFM) measurements revealed consistent, reproducible flexoelectric currents under appropriate bias potential across extensive networks of dense NWs.

Our research establishes graphene NWs as an ideal system for investigating strong flexoelectric effects. The findings highlight significant potential applications in strain-engineered nanoscale electronic and electromechanical devices, opening new avenues for harnessing this phenomenon in future technologies. This work bridges theoretical predictions with experimental validation, advancing our understanding of how nanoscale structural deformations in 2D materials can be leveraged for novel electronic properties and functionalities [2].

References

[1] Kalinin, S.; Meunier, V. *Phys. Rev. B* **2008**, *77*, 033403.

[2] Sathvik Ajay Iyengar et al., manuscript in preparation, 2025.

Ordered and tunable Majorana-zero-mode lattice in iron-based superconductors

Hong-Jun Gao, G. Li[1,2], D.F. Wang[1,2], S.Y. Zhu[1,2], M. Li[1,2], H. Chen[1,2], P. Fan[1,2], H. Guo[1,2], L. Cao[1,2], Y.Y. Zhang[2,1], L.Y. Kong[1,2], W.Y. Liu[1,2], J. Schneeloch[3], R.D. Zhong[3], G.D. Gu[3], L. Fu[4], H. Ding[1,2], Z.Q. Wang[5]

[1] *Institute of Physics, Chinese Academy of Sciences, CAS, Beijing 100190, PR China*
[2] *School of Physical Sciences, University of Chinese Academy of Sciences, Beijing 100190, PR China*
[3] *Brookhaven National Laboratory, Upton, New York 11973, USA*
[4] *Department of Physics, Massachusetts Institute of Technology, Cambridge, Massachusetts 02139, USA*
[5] *Department of Physics, Boston College, Chestnut Hill, MA 02467, USA*
hjgao@iphy.ac.cn

Abstract

Majorana zero-modes (MZMs) are spatially-localized zero-energy fractional quasi-particles with non-Abelian braiding statistics. They are believed to hold great promise for topological quantum computing. By using low-temperature and strong-magnetic-field scanning tunneling microscopy/spectroscopy, a breakthrough of Majorana zero mode has been firstly achieved in a single material platform of high-T_c iron-based superconductor, $FeTe_{0.55}Se_{0.45}$. The mechanism of two distinct classes of vortices presented in this system was revealed, which directly tied with the presence or absence of zero-bias peak. We further found the Majorana conductance plateau in the vortices, approaching the quantized value of $2e^2/h$. Moreover, we confirmed the existence of MZMs in the vortex cores of $CaKFe_4As_4$ and LiFeAs. Based on these works mentioned above, we have successfully achieved the large-scale, highly-ordered and tunable MZM lattice in strained LiFeAs. Notably, more than 90% of the vortices are topological and possess isolated MZMs at the vortex center, forming ordered MZM lattice with the density and the geometry tunable by external magnetic field. With decreasing the spacing of neighboring vortices, the MZMs start to couple with each other. More recently, we demonstrated that MZMs can be pinned by one-dimensional wrinkles. By controlling these wrinkles, the spatial position of the MZMs can be effectively manipulated. Our results show a great potential of MZMs in the application of topological quantum computations in the future.

References

[1] Wang, D. F. et al. *Science* **2018**, *362*, 333.
[2] Zhu, S. Y. et al. *Science* **2020**, *367*, 189.
[3] Li, M. et al. *Nature* **2022**, *606*, 890.

Breaking the Materials Barrier: Atom Probe Tomography as an emerging Tool in Chemical Analysis of Soft Matter and Complex Interfaces

Guido Schmitz[1], Sebastian Eich[1], Kuan Meng[1], Sakshi Sinha[1], Jianshu Zheng[1]

[1] *Institute of Materials Science, University of Stuttgart, Germany*
guido.schmitz@imw.uni-stuttgart.de

Abstract

Atom probe tomography is a method of microscopic analysis that is well-established in the study of hard materials. It is based on the controlled field desorption of atoms or small molecular fragments from nanometric specimens and stands out by combining single-atom sensitivity with a 3D volume reconstruction. A particular stronghold of the method is the accurate measurement of chemical segregation at grain boundaries and interfaces in complex nanostructured matter.

By supplying moderate high voltage to needle-shaped samples of typically 30 nm apex radius, extreme electrical field strengths are achieved. The fields are so strong that they severely deform the electron distribution of covalent bonds in solid materials. With increasing field strength, single atoms start evaporating from the sample surface in a thermally activated process. They are recorded by a two-dimensional detector setup of single-atom sensitivity. Triggering the atomic evaporation by ultra-short laser pulses enables a time-of-flight spectroscopy that identifies the desorbed species. From the recorded hitting positions of millions of atoms, the analyzed volume is reconstructed to sub-nanometer accuracy.

Our current efforts progress advanced volume reconstruction schemes, the simulation by first-principles methods of the evaporation process and a full statistical understanding of chemical fluctuations in the data sets, which form the base for a direct measurement of Gibbs mixing energy of alloys. Most recently, we desire to break the materials limitations towards the analysis of soft matter and polymeric materials with this method.

In order to investigate the structure of complex fluids, micro-droplets of liquids are quench-frozen in tiny metallic beakers cut into tungsten tips and then, after freezing, shaped with focused ion beams to cone-shaped nano-needles. These have to be transferred into the atom probe measurement chamber without melting. Meanwhile, with this method, nanometric needles have been produced from aqueous solutions, alkanes and organic solvents as well as complex molecular liquids such as liquid crystals. The talk shortly presents the recent progress in volume reconstruction methods based on advanced evaluation of event density maps on the detector aperture using mathematical principles of differential geometry. It also illustrates how a sophisticated statistical analysis of fluctuations can link the atom probe data directly to the thermodynamic properties of the studied materials [1].

The major part, however, will be devoted to the field desorption of complex liquids presenting typical time-of-flight mass spectra and their dependence on field or laser intensity. In comparison to measurements of metals and other simple-structured hard materials, the mass spectra of polymeric materials become remarkably complex, since the lower field strength in the evaporation provokes larger molecular fragments in the mass spectra. So, even a rather simple liquid like water, becomes quite interesting, although it contains only hydrogen and oxygen atoms. Water field-evaporates in form of many different molecular clusters organized by hydrogen bonds, while the size distribution of the clusters may be used as a measure for the cluster´s thermodynamic stability. Required details of the evaporation process can be only understood by comparison to DFT calculations (see the example of alkanes in [2]).

At the high end of complexity, we investigated frozen liquid crystals. Atom probe data demonstrate that under suitable conditions the amorphous or smectic state of the liquid can indeed be frozen in the samples and so interfaces in the apparent liquid state can be analyzed. On the other hand, controlled annealing of the droplets slightly below the critical temperature can provoke crystallization before quenching. In consequence, periodic lattice plane stacking of the liquid crystal molecules can be observed and measured in the reconstructed volume of the atom probe tomography [3] (see Fig. 1).

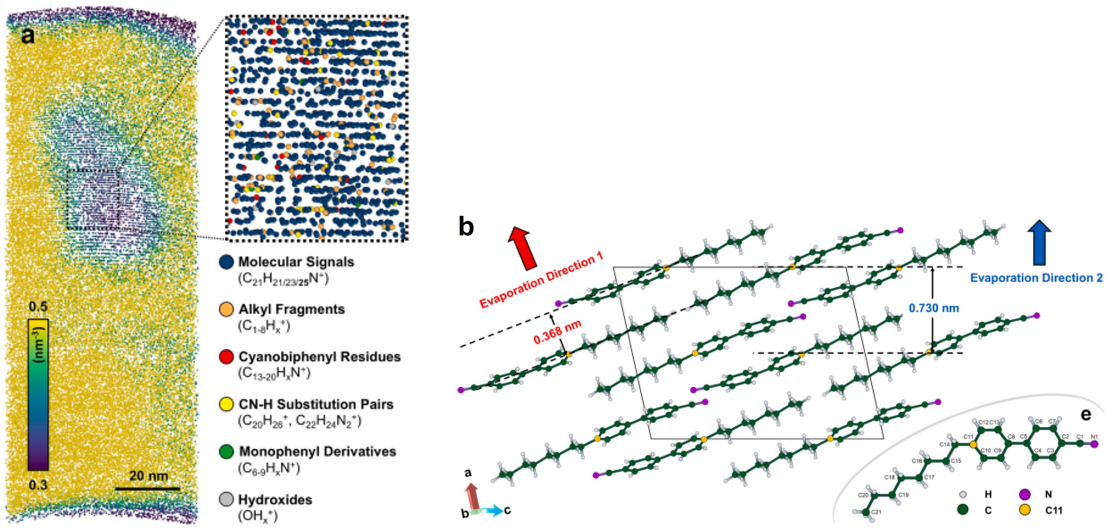

Figure 1: Atom probe tomography of a partly crystallized 8CB liquid crystal (4'-octyl-4-cyanobiphenyl). a) spatial reconstruction showing the arrangement of major molecular fragments. b) identified lattice stacking in the crystalline nucleus. Inset at bottom right shows the structure of a single molecule. [3]

References

[1] Zheng, J.; Duran, R.; Diwan, P.; Schmitz, G.; Eich, S. M. Direct measurement of the Gibbs free energy of mixing via atom probe tomography. *Acta Materialia* **2026**, *308*, 121950. DOI: 10.1016/j.actamat.2026.121950.

[2] Dietrich, C. A.; Schwarz, T. M.; Meng, K.; Stender, P.; Schmitz, G.; Kästner, J. Postdesorption fragmentation of tetradecane in Atom-Probe tomography simulated by DFT. *The Journal of Physical Chemistry A* **2025**, *129*, 3963–3968. DOI: 10.1021/acs.jpca.5c01332.

[3] Meng, K.; Wang, K.; Eich, S.; Nacke, P.; Bruckner, J. R.; Stender, P.; Giesselmann, F.; Schmitz, G. Revealing nanoscale molecular organization in Liquid Crystals via cryogenic Atom Probe Tomography. *Journal of Molecular Liquids* **2026**, *448*, 129358. DOI: 10.1016/j.molliq.2026.129358.

Molecular anodes based on self-assembled bilayers for (photo)electrocatalytic water oxidation

Paula Tris-Marzo[1], Daniele Veclani[2], Alessandro Venturini[2], Marta Martínez-Belmonte[1], Marcos Gil-Sepulcre[3], Antoni Llobet[1]

[1] *Institute of Chemical Research of Catalonia (ICIQ), University Rovira i Virgili (URV), Tarragona, Spain*
[2] *Institute for Organic Synthesis and Photoreactivity (ISOF), Bologna, Italy*
[3] *Department of Chemistry, Autonomous University of Barcelona (UAB), Barcelona, Spain*
ptris@iciq.es

Abstract

The design of robust and efficient molecular water oxidation catalysts (WOCs) for integration with conductive oxide electrodes remains a significant challenge for artificial photosynthesis. Herein, we report the development of self-assembled bilayer (SAB) systems[1] incorporating a Ru-based oligomeric WOC,[2] $[Ru^{II}(tda)\mu\text{-}b12]_{12}(b12)$ (tda^{2-} is [2,2':6',2"-terpyridine]-6,6"-dicarboxylate and b_{12} is 3,3'-didodecyl-4,4'-bipyridine), with long alkyl chains facilitating robust anchoring on fluorine-doped tin oxide (FTO) and nano-antimony-doped tin oxide (nATO) electrodes. The nATO-based molecular anodes exhibit two orders of magnitude higher catalyst loading compared to FTO, owing to the porous architecture and enhanced alkyl–alkyl interactions.

Electrochemical studies reveal efficient water oxidation at pH 7 with faradaic efficiencies exceeding 92% and turnover numbers above 33,800. The assemblies demonstrate exceptional stability attributed to the dynamic rebound mechanism of the Ru–tb12 oligomer and the hydrophobic protection of the alkyl–silanotrisolate layer. Furthermore, electron relay effects mediated by $[Ru(bpy)_3]^{2+}$ and the Ru centers enhance catalytic performance and minimize deactivation.[3]

In addition, we have extended this approach to photoelectrochemical systems by applying the SAB strategy to $BiVO_4/WO_3$-based photoanodes. These results underscore the potential of SABs for creating durable and efficient molecular (photo)anodes for solar fuel applications.

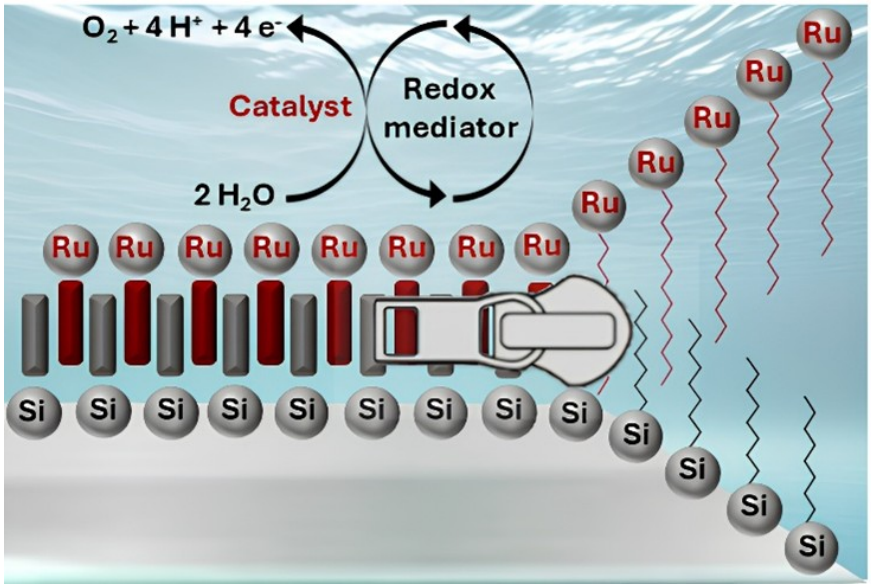

Figure 1: Scheme representing the supramolecular anchoring of a Ru^{II} molecular water oxidation catalyst via multiple alkyl chains on a silanolate-functionalized oxide conductor, yielding a robust and efficient water oxidation electrocatalyst.

References

[1] Wang, L.; Polyansky, D. E.; Concepcion, J. J. Self-Assembled bilayers as an anchoring strategy: catalysts, chromophores, and Chromophore-Catalyst assemblies. *Journal of the American Chemical Society* **2019**, *141*, 8020–8024. DOI: 10.1021/jacs.9b01044.

[2] Hoque, M. A. et al. Water oxidation electrocatalysis using ruthenium coordination oligomers adsorbed on multiwalled carbon nanotubes. *Nature Chemistry* **2020**, *12*, 1060–1066. DOI: 10.1038/s41557-020-0548-7.

[3] Tris-Marzo, P.; Veclani, D.; Venturini, A.; Martínez-Belmonte, M.; Gil-Sepulcre, M.; Llobet, A. Molecular anodes for electrocatalytic water oxidation based on Self-Assembled bilayers driven by electron transfer mediators. *Journal of the American Chemical Society* **2025**, *147*, 12686–12695. DOI: 10.1021/jacs.5c00489.

Acta Microscopica Vol.35, Supp.1, 2026
Abstract Book NSSY 2026 - Galapagos 17th–23rd May 2026

Hexacyano-trimethyl-cyclopropane as a Raman probe for quantifying charge transfer in molecule-2D-materials

Elena Stroici[1], Charlotte Berezueta-Palacios[1], Sviatoslav Kovalchuck[1], Jan Soyka[2], Siegfried Eigler[2], Kirill Bolotin[1], Stephanie Reich[1]

[1] *Freie Universitat Berlin, Institute of Physics*
[2] *Freie Universitat Berlin, Institute of Chemistry and Biochemistry*
stroie99@zedat.fu-berlin.de

Abstract

Charge-transfer mechanisms lie at the core of many modern devices, including solar batteries, phototransistors, fuel cells, and a variety of sensors. Understanding these processes is essential for the development of next-generation technologies. Recently discovered two-dimensional (2D) materials have emerged as exceptional platforms for probing charge-transfer behavior, as they exhibit rich spectroscopic signatures, and enable in situ measurements with high sensitivity [1]. Up to now the charge transfer was able to be tracked only form the 2D material side. For many charge transferring agents, the spectroscopic signature remains missing.

Hexacyano-trimethyl-cyclopropane (CN6-CP) is a custom made molecular acceptor that exhibits a high electron affinity (-5.94 eV) due to its unique [3]-radialene framework and the presence of six strongly electron withdrawing cyano-groups making it an ideal benchmark for studying charge transfer in hybrid systems. Graphene is an excellent candidate for testing these molecules, as the effects of charge transfer on graphene and its vibrational properties have been extensively studied, resulting in a well-established understanding of its doped behavior [2].

Here we show that it is possible to track the charge transfer mechanism of graphene to CN6-CP by monitoring *in situ* their Raman signatures.

Molecular deposition on graphene was carried out in the cryostat at 4 K and 10^{-5} mbar via resistive heating. The cryostat with its connections (liquid helium, power supply and vacuum pump) are shown in Figure 1 (d). Both the chip containing the graphene flake and a second chip with a gold coil were mounted on a chip carrier, as illustrated in Figure 1 (b). The chip with the gold coil (lower left corner) is wire-bonded to the chip carrier with silver wires and, together with a power supply Agilent 34401a, forms an electric circuit, Figure 1 (c). A small amount of CN6-CP, bright orange powder as shown in Figure 1 (a), was placed on the gold coil. The application of voltage to the coil generates resistive heating that causes the molecules to evaporate and deposit in the surroundings, including the graphene flake. The voltage was incrementally increased from zero to 28 V allowing for gradual and controlled evaporation of the molecules. After each voltage application, a Raman spectrum was recorded.

When evaporated on graphene, a concomitant reduction of the molecule and doping of graphene will occur. In the formed heterostucture, both Raman signatures

of the charge transfer agent (CP_{NM}, CP_{NM}) and graphene (G, 2D) are present, as displayed in Figure 2 (b). Upon accepting the electron, CN6-CP forms a radical anion, Figure 2 (a), that displays a distinct Raman shift of the CP vibration from 1763 to 1852 cm^{-1}, providing a clear marker of its reduction. The amount of charge transfer is monitored by the increasing intensity of the CP_{RA} peak throughout the doping evolution. Complementary, G and 2D modes of graphene blue-shift by 13 cm^{-1} and 9 cm^{-1}, respectively, compared to the pristine graphene (lower spectrum) shown in Figure 2 (c). The integrated intensity of the radical anion peak reaches its maximum around the same voltage as the saturation of G peak of graphene, indicating a quantitative correlation between the two. Employing Frohlicher et al. [3] G-shift vs charge transfer correlation plot, the corresponding charge transfer density of 0.75×10^{13} cm^{-2} was determined. This correlation establishes the CN6-CP radical anion Raman signature as a reliable tool for quantifying charge transfer. Such an approach could be particularly advantageous for 2D systems lacking clear spectroscopic markers, with the relevant information instead provided by the doping agent.

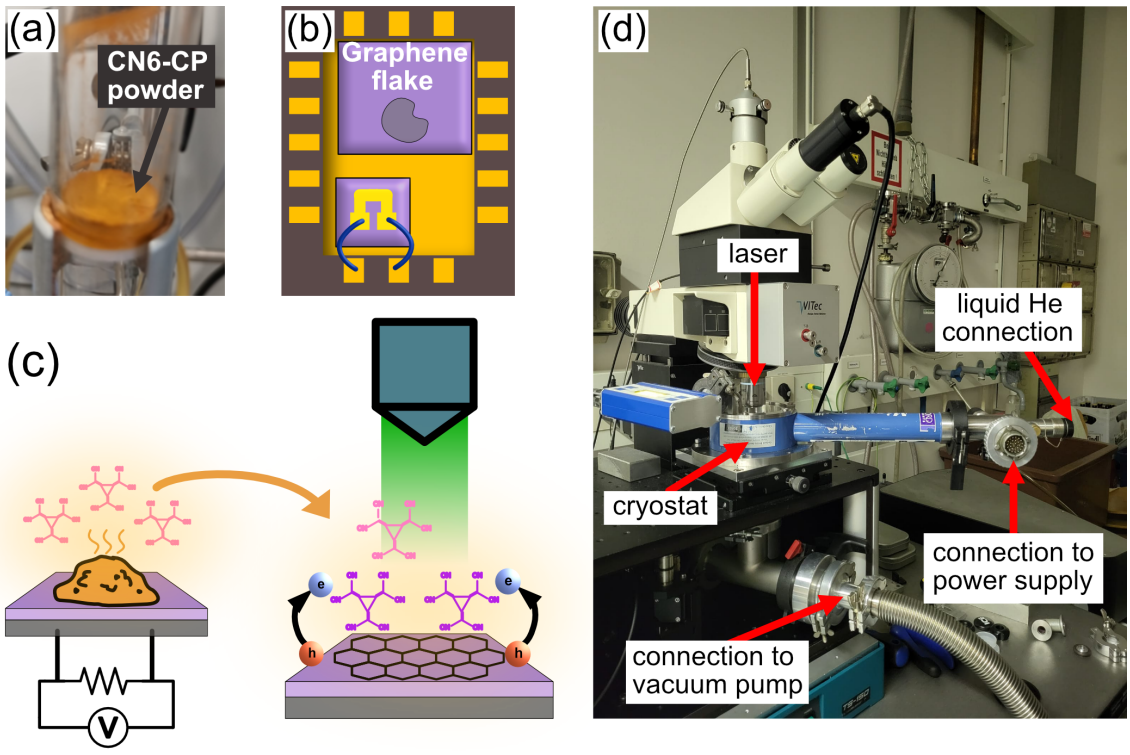

Figure 1: Experimental procedure (a) freshly synthesized CN6-CP molecules in powder form (b) chip carrier with golden coil (lower left) and chip with graphene flake (upper right) (c) left - evaporation of molecules using resistive heating, right - Raman measurement of graphene/CN6-CP heterostructure (d) experimental set-up

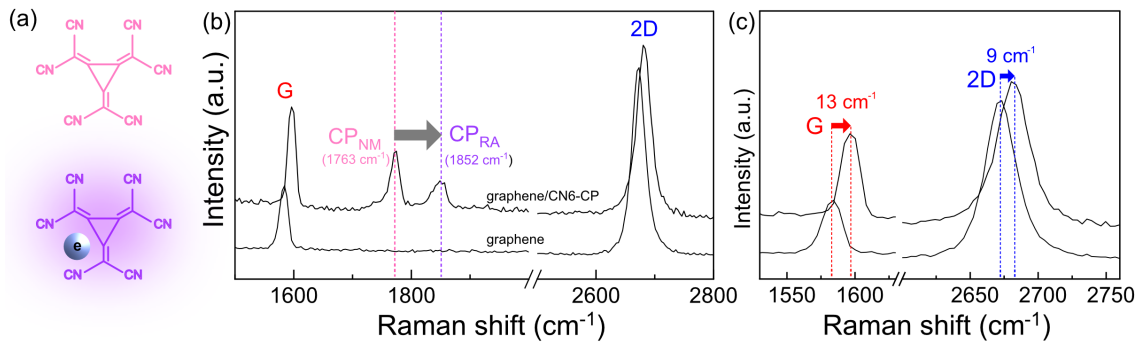

Figure 2: (a) neutral CN6-CP molecule (pink) and reduced CN6-CP molecule (purple) (b) Raman spectrum of graphene/CN6-CP heterostructure. The CP Raman mode shifts from 1763 cm^{-1} in neutral molecule (CP_{NM}) to 1852 cm^{-1} in radical anion (CP_{RA}) (c) maximum blue shift of G and 2D modes of graphene upon doping with CN6-CP

References

[1] Novoselov, K. S.; Mishchenko, A.; Carvalho, A.; Neto, A. H. C. 2D materials and van der Waals heterostructures. *Science* **2016**, *353*, aac9439. DOI: 10.1126/science.aac9439.

[2] Lee, H.; Paeng, K.; Kim, I. S. A review of doping modulation in graphene. *Synthetic Metals* **2018**, *244*, 36–47. DOI: 10.1016/j.synthmet.2018.07.001.

[3] Froehlicher, G.; Berciaud, S. Raman spectroscopy of electrochemically gated graphene transistors: Geometrical capacitance, electron-phonon, electron-electron, and electron-defect scattering. *Phys. Rev. B* **2015**, *91*, 205413. DOI: 10.1103/PhysRevB.91.205413.

Tuesday

Machine learning for electronic structure and atomistic simulations

Mariana Rossi[1]

[1] *MPI for the Structure and Dynamics of Matter, Hamburg, Germany*
[2] *Yusuf Hamied Department of Chemistry, Cambridge, UK*
mariana.rossi@mpsd.mpg.de

Abstract

In this tutorial, I will cover the basics of the most common machine-learning methods used to perform regression on datasets: neural networks and Gaussian process regression. I will then explain how these concepts can be extended to high-dimensional atomistic systems, including local and non-local atomic representations, and finalise with a showcase application in which we use these methods to simulate polarization-dependent Raman spectra of single crystals.

Monte Carlo–Based Active Learning Framework for Monolayer Amorphous Materials

Yu-Yang Zhang[1]

[1] *University of Chinese Academy of Sciences*
zhangyuyang@ucas.ac.cn

Abstract

Amorphous materials exhibit various characteristics that are not featured by crystals and can sometimes be tuned by their degree of disorder (DOD). Here, we report an kinetic-Monte-Carlo (kMC)-assisted active-learning framework for efficient potential energy surface exploration of Monolayer amorphous materials. Utilizing this method, we collect monolayer amorphous configurations with various DOD and train accurate machine learning potentials (MLP). Then, we report results on the mechanical properties of monolayer amorphous carbon (MAC) and monolayer amorphous boron nitride (maBN) with different DOD. An intuitive order parameter, namely the areal fraction Fx occupied by crystallites within the continuous random network, is proposed to describe the DOD. We find that Fx captures the essence of the DOD: Samples with the same Fx but different sizes and distributions of crystallites have virtually identical radial distributions functions as well as bond-length and bond-angle distributions. Furthermore, by simulating the fracture process with molecular dynamics, we found that the mechanical responses of MAC and maBN before fracture are solely determined by Fx and are insensitive to the sizes and specific arrangements of the crystallites. The behavior of cracks in the two materials is analyzed and found to mainly propagate in meandering paths in the CRN region and to be influenced by crystallites in distinct ways that toughen the material. The present results reveal the relation between structure and mechanical properties in amorphous monolayers and may provide a universal toughening strategy for 2D materials.

References

[1] Zhang, Y.-T. et al. *Nano Letters* **2022**, *22*, 8018.

[2] Zhang, Y.-T. et al. *Applied Physics Letters* **2022**, *120*, 222201.

[3] Zhang, X. et al. *Physical Review B* **2024**, *109*, 174106.

Acta Microscopica Vol.35, Supp.1, 2026
Abstract Book NSSY 2026 - Galapagos 17th–23rd May 2026

Anisotropic DC mobility of doped phosphorene due to charge carrier scattering on charged impurities calculated by the energy loss method

Miskovic Zoran[1]

[1] *University of Waterloo, Applied Mathematics Department, Waterloo, Ontario, Canada*
zmiskovi@uwaterloo.ca

Abstract

We study the mobility of charge carriers in an anisotropic two-dimensional (2D) material, represented by doped phosphorene (monolayer black phosphorus), which is controlled by elastic scattering of charge carriers on charged impurities (CIs) in the presence of a weak, constant electric field applied across phosphorene. The anisotropy of phosphorene is caused by large differences in the effective masses for conduction and valence electron bands along the principal directions of the phosphorene atomic lattice, known as the armchair and the zig-zag directions. While a similar problem is routinely tackled in isotropic 2D materials by utilizing a straightforward solution of the linearized Boltzmann transport equation (LBTE) in the approximation of the momentum relaxation time (MRT), the situation becomes much more complicated in anisotropic 2D materials, where the MRT becomes dependent on the direction of the applied electric field [1]. In this case, the LBTE becomes an integral equation for the MRT that depends on the electron quasi-momentum vector, whose solution is computationally very demanding.

As an alternative approach to solving the above problem, we generalized the so-called energy loss method (ELM) and found it to be significantly more computationally efficient, while giving essentially the same results for the DC mobility of doped phosphorene as solutions of the LBTE. The ELM in the case of carrier scattering on CIs is based on the Galilean transformation between the laboratory frame where the impurities are at rest while charge carriers in phosphorene are drifting with constant velocity $\mathbf{v}_d$ (see Figure 1), and a frame where the impurities move in the opposite direction with velocity $-\mathbf{v}_d$ while phosphorene is at rest [2]. Invoking equivalence of the Joule power released in phosphorene and the energy loss rate for the system of moving impurities, and assuming that the drift speed is low, makes it possible to circumvent the concept of relaxation time and express the DC mobility tensor of phosphorene as an integral involving the energy loss function (ELF) for charge carriers in phosphorene that is approximated to the leading order in frequency [2]. The ELF of phosphorene is obtained by combining the Green's function of the Poisson equation for surrounding dielectrics with the polarization function of doped phosphorene, which is obtained from the well-known Lindhard function of an isotropic 2D electron gas by suitably re-scaling the electron quasi-

momentum vector components by means of the anisotropic electron effective masses of phosphorene.

Taking advantage of the computational tractability of the ELM, we investigated some more complex aspects of the problem, such as the effects of spatial correlation among the CIs, inclusion of interband electronic transitions in the polarization function of phosphorene, and the use of the Maldague formula to evaluate the effects of finite temperature on the mobility. Besides showing comparisons of our results for the mobility using the ELM with those obtained by other groups using the LBTE method, we also present some aspects of modeling of anisotropy effects in phosphorene devices [3].

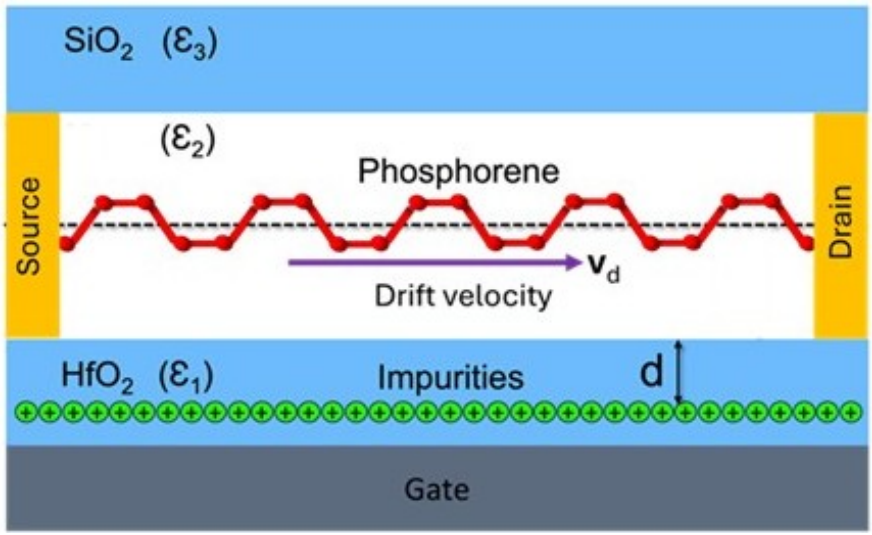

Figure 1: Schematic diagram of the problem.

References

[1] Rudenko, A.; Katsnelson, M. *2D Mater.* **2024**, *11*, 042002.

[2] Moshayedi, M.; Miskovic, Z. *Phys. Rev. B* **2023**, *108*, 245404.

[3] Chalechale, A. et al. *Phys. Rev. Appl.* **2025**, *23*, 064031.

Incorporating Nuclear Quantum and Anharmonic Effects into Tip-Enhanced Raman Spectroscopy

Jorge Castro[1], Krystof Brezina[1], Mariana Rossi[1]

[1] *Max Planck Institute for the Structure and Dynamics of Matter*
jorge.castro@mpsd.mpg.de

Abstract

Vibrational spectroscopy provides fundamental insight into molecular structure and dynamics. Nuclear quantum effects (NQEs) can be critical in vibrational spectroscopy, where they modulate the position, shape, and intensity of spectral features. Recently, we demonstrated that the partially adiabatic elevated-temperature centroid molecular dynamics (PA-T$_e$-CMD)[1] approach accurately reproduces vibrational spectra across molecular and condensed-phase systems, including at low temperatures where NQEs are most pronounced. This method allows the study quantum infrared and Raman scattering vibrational signals in a variety of spectroscopy techniques. Tip-Enhanced Raman Spectroscopy (TERS)[2] is a powerful technique for imaging single-molecule vibrational motion and surface defects, as it enables sub-nanometer spatial resolution. Building on recent first-principles finite-field formulations of TERS[3], we combine this framework with PA-T$_e$-CMD to explore the role of nuclear quantum motion and anharmonicity in near-field spectroscopic observables. As a first application, we study hydrogen-bonded chains of 2,5-diamino-1,4-benzoquinonediimine (DABQDI) and discuss how NQEs may influence vibrational features in simulated TERS images.

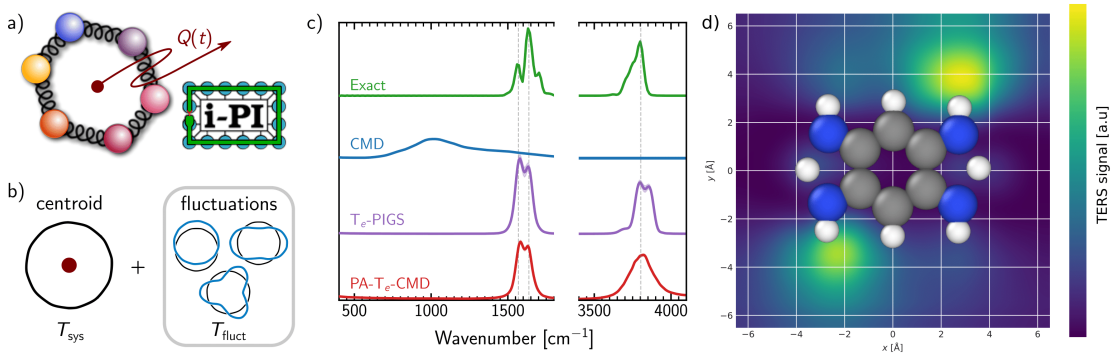

Figure 1: (a) Nuclear quantum effects (NQEs) are captured within the path-integral molecular dynamics (PIMD) formalism, where each atom is represented by a ring polymer of P replicas connected by harmonic springs. Vibrational spectra are computed from the dynamics of the ring-polymer centroids (b) In centroid molecular dynamics (CMD), the centroids evolve at the system temperature Tsys under mean-field forces from the internal modes. When the fluctuation temperature Tfluct=Tsys, CMD can yield distorted spectra. In the elevated-temperature approach, Tfluct>Tsys, which suppresses these artifacts. (c) Infrared spectra of a water molecule at 50 K obtained from different imaginary-time path-integral methods. The exact spectrum is shown for reference, with vertical dashed lines as visual guides. (d) Simulated Tip-Enhanced Raman Spectroscopy (TERS) map of a hydrogen-bonded 2,5-diamino-1,4-benzoquinonediimine (DABQDI) molecule, illustrating the sub-nanometer spatial resolution achievable in near-field vibrational spectroscopy. In ongoing work, the PA-T_e-CMD framework will be employed to incorporate nuclear quantum and anharmonic effects into such TERS simulations.

References

[1] Castro, J.; Trenins, G.; Kapil, V.; Rossi, M. arXiv preprint. *arXiv* **2025**, https://arxiv.org/abs/2508.16246.

[2] Lee, J.; Crampton, K. T.; Tallarida, N.; Apkarian, V. A. Title not provided. *Nature* **2019**, *568*, 78–82.

[3] Brezina, K.; Litman, Y.; Rossi, M. arXiv preprint. *arXiv* **2025**, https://arxiv.org/abs/2509.13075.

Nanotechnology-based tools for water contaminants' monitoring

Begoña Espiña[1]

[1] *International Iberian Nanotechnology Laboratory*
begona.espina@inl.int

Abstract

Owing to their unique qualities and the almost infinite tailoring possibilities, engineered nanomaterials (ENMs) have been exponentially explored for many applications. Some of the most promising uses are in sensor development. In this talk, I will describe our recently developed detection system for biotoxins from Harmful Algal Blooms (HABs), based on specifically tailored nanomaterials and composites. Seafood aquaculture is heavily impacted by toxic harmful algal blooms (HABs) yearly. Significant efforts have been made to develop early warning systems for HABs, enabling the prediction of seafood contamination and facilitating early intervention. Here, I describe the development of a portable, semi-automated system using covalent organic frameworks and gold nanostars (COF/GNS) for surface-enhanced Raman scattering (SERS) detection of paralytic shellfish toxins (PST). The composites are accumulated in a microfluidic cartridge, and the read-out is performed using a portable Raman system with a 785 nm laser line. Finally, automated measurements and analyses are performed using ML/AI algorithms to estimate the toxin concentration in the sample. However, ENMs are also potentially hazardous contaminants if released into the environment, and one of the major bottlenecks in studying their potential environmental impact is the lack of fit-for-purpose analytical techniques. During this talk, I will also describe our recently developed nanomaterial-based sensors for the selective detection of silver nanoparticles and carbon-based nanomaterials.

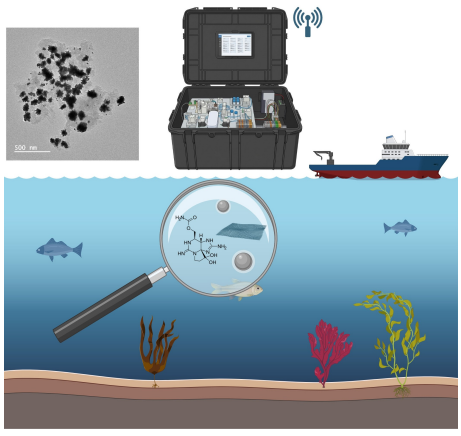

Figure 1: **Scheme: Nanotech-based in situ monitoring systems for water contaminants monitoring.**

Marine Microplastics in Tulear: The Silent Threat from Woven Bags and Ropes Evaluated by Infrared Spectroscopy

Carla Bittencourt[1], Lovasoa Rina Raharinaivo[1], Jean Roquin Rabehavana[1], Vatosoa Raheriarilala[1], Jérôme Delroisse[1], Gildas Todinanahary[1], Maherizo Tiandrainy Gédice Fernand[1], Thierry Lavitra[1], Igor Eckhaut[1]

[1] *University of Mons – Research Institute for Biosciences, Biology of Marine Organisms and Biomimetics Unit, Belgium*
carla.bittencourt@umons.ac.be

Abstract

Over the past few decades, plastic pollution has emerged as a major environmental concern, particularly affecting marine ecosystems. While macroplastics have long been recognized, microplastics (MPs) have become a critical issue since the 1970s. These tiny particles are durable and widespread in aquatic environments, originating mainly from industrial microbeads (primary MPs) and the degradation of larger plastics (secondary MPs). They are not confined to oceans; MPs travel long distances via wind and water, contaminating various ecosystems. Annually, an estimated 4.8 to 12.7 million metric tons of plastic waste reach the oceans, highlighting the severity of the problem (Jambeck et al., 2015). Fishing and aquaculture activities contribute to MP pollution by degrading plastic gear, such as nets, floats, and ropes, generating significant plastic waste despite their economic importance. Domestic activities, including the breakdown of single-use plastics and synthetic fabrics, also play a role. A study in Southwestern Madagascar revealed that about 40% of anthropogenic marine debris (AMD) collected from beaches and mangroves was linked to small-scale fisheries (SSF) and community-based aquaculture (CBA). This debris mainly comprises macroplastics from fishing gear and repurposed materials, which can fragment into smaller particles through processes such as UV radiation, ultimately entering the marine environment. Currently, no definitive study has confirmed whether plastic particles in Southwestern Madagascar's marine environments come from marine or land sources. Most existing research relies on estimates to determine MP sources. Identifying foams, filaments, films, and pellets is generally easier than identifying fragments. For example, filaments are often linked to fishing gear degradation, foams to flotation devices, films to packaging, and pellets to primary MPs. Fragments, however, result from the breakdown of larger plastics, making their sources harder to identify. Understanding these sources is vital to connect local human activities with MP pollution. This study examines MP contamination in sediments and waters of Southwestern Madagascar to identify the main MP shapes and their links to local practices. We first focused on macroplastics with clear sources, building an FT-IR library of these materials. Then, we assessed MP abundance and traits in beaches, mangroves, and seawater, which are likely sites of MP accumulation. Using FT-IR fingerprinting, we

analyzed MPs in relation to our IR library of macroplastic debris linked to local human activities, including SSF and CBA, to determine their origins under human influence. Results reveal notable differences in MP concentrations across various environments, with the highest levels found in seafloor sediments, which tend to accumulate MPs due to hydrodynamic forces and particle density. The study identified only secondary MPs, with filaments being the most common shape, followed by fragments, films, and foams. Variations in size and color underscore the complex degradation and transport processes in marine environments. To trace the sources of these MPs, an infrared library of macroplastic debris linked to local activities—such as small-scale fishing and community aquaculture—was used. Findings indicate that breaking down larger plastic items, especially woven polypropylene bags and ropes, significantly contributes to MP pollution. This study highlights the need for improved plastic waste management and sustainable solutions for fishing and aquaculture materials to mitigate marine pollution.

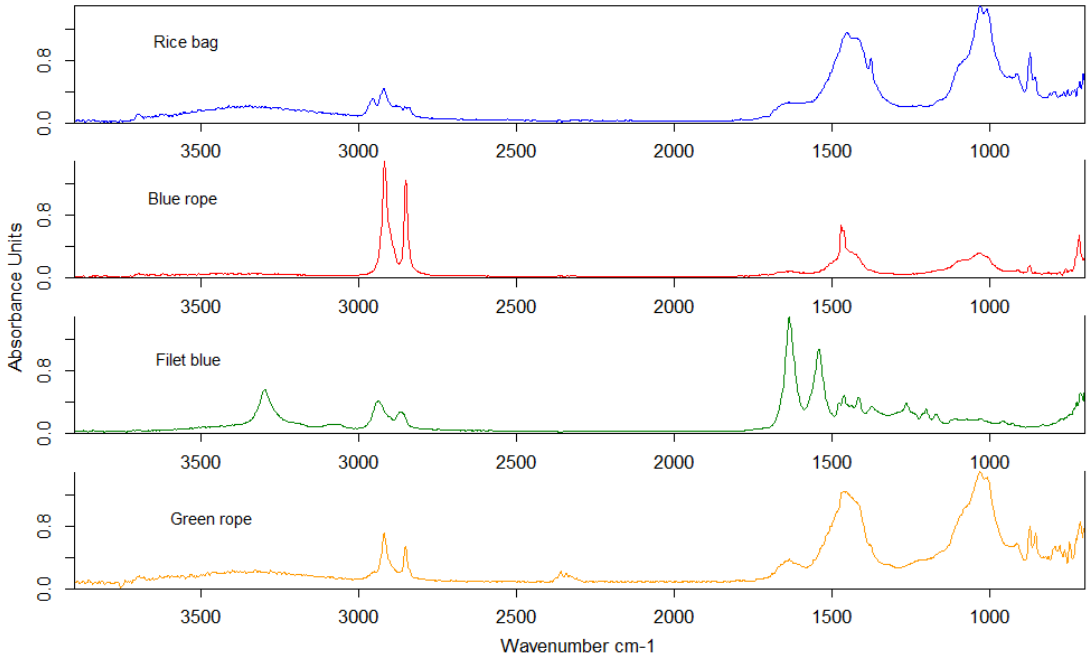

Figure 1: Typical IR spectra recorded to build up the used library used to identify the studied microplastics

References

[1] Raharinaivo, L. R.; Todinanahary, G. B. G.; Delroisse, J.; Raquez, J.-M.; Bittencourt, C.; Maherizo, T. G. F.; Lavitra, T.; Eeckhaut, I. Quantification of Anthropogenic Debris from Small Scale Fisheries and Community-Based Aquaculture in Marine and Coastal Ecosystems of Southwestern Madagascar. *Marine Pollution Bulletin* **2025**, *213*, 117631.

Magnetic Nanoparticles for Microplastics Remediation

Sarah Briceño[1]

[1] *School of Physical Sciences and Nanotechnology, Yachay Tech University, Urcuquí 100119, Ecuador*
sarahbriara@gmail.com

Abstract

Microplastics have become a major environmental concern due to their resistance to degradation, wide distribution, and potential uptake by organisms. In this work, we highlight the application of magnetically controlled, nanoparticles with different functional groups for microplastics removal. By leveraging hydrophobic interactions, surface modifications, and tailored additives, these magnetic nanoparticles provide a sustainable, eco-friendly approach to mitigating microplastic pollution and offer improved magnetic separation performance achieving removal efficiencies often exceeding 90% in minutes, and maintaining the efficiency after several cycles. The synergistic integration of magnetic separability with tailor-made surface functionalities underpins the effectiveness of these magnetic nanoparticles, setting the stage for their future commercialization and widespread adoption in water remediation technologies.

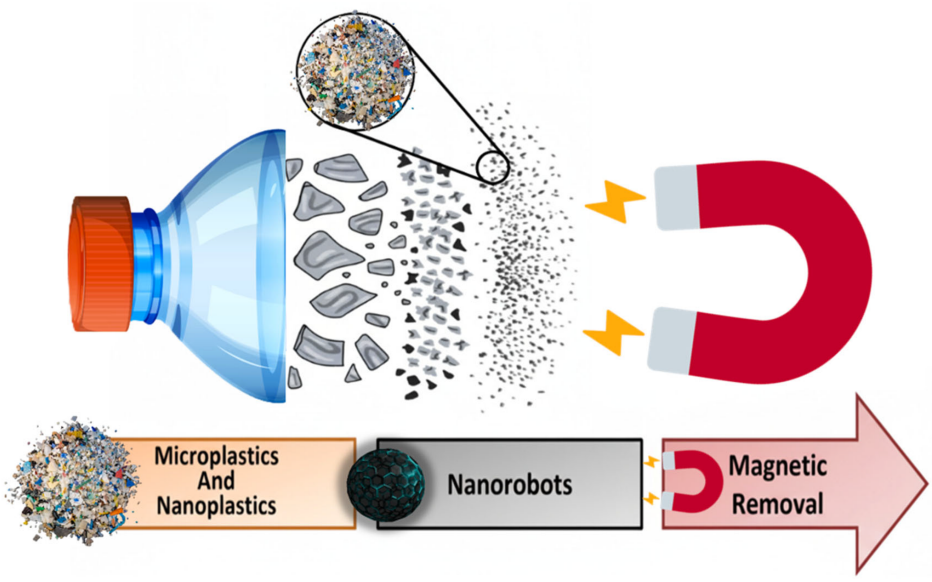

Figure 1: Magnetic Nanoparticles for Microplastics Remediation

References

[1] Briceño, S.; Arevalo-Fester, J. E.; Fierro-Sanchez, I. A. Sustainable magnetic nanorobots for microplastics remediation. *Microplastics* **2025**, *4*, 97. DOI: 10.3390/microplastics4040097.

Sustainable Conversion of Rice Husk into Functional Silica for Advanced Nanostructured Materials

Pilicita-Carua Johanna[1], Darquea-Córdova Francisco[2], Jerves Alex X.[3,4], Albuja Sánchez Jorge[5,6], Córdova G. Federico[2], Ortiz Abril Daniela[2], Chacón-Torres Julio C.[1]

[1] *Yachay Tech University, School of Physical Science and Nanotechnology, Urcuquí, Ecuador*
[2] *Universidad Católica de Cuenca, Unidad Académica de Ingeniería, Industria y Construcción, Cuenca, Ecuador*
[3] *Universidad Católica de Cuenca, Unidad Académica de Informática, Ciencias de la Computación, e Innovación Tecnológica, Cuenca, Ecuador*
[4] *Institute of Scientific Pioneering Research of Ecuador (INSPIRE), Quito, Ecuador*
[5] *Pontifical Catholic University of Ecuador, Faculty of Engineering, Laboratory of Materials Resistance, Soil Mechanics, Pavements and Geotechnics, Quito, Ecuador*
[6] *Pontifical Catholic University of Ecuador, International Faculty of Innovation PUCE-Icam, Quito, Ecuador*
jpilicita@yachaytech.edu.ec

Abstract

The increasing demand for sustainable materials has promoted the use of renewable resources as substitutes for conventional materials. In this context, agro-industrial residues have gained attention for their potential to generate functional materials with high added value [1]. Among these, rice husks (RH) is characterized by its high availability and silica content, an ideal precursor for obtaining reactive mineral additives [2]. This work presents the controlled thermal conversion of RH for obtaining amorphous silica with high pozzolanic activity. This property enhances the ability of cementitious compound materials to react with calcium hydroxide in the presence of water improving the mechanical performance of mortars reducing the environmental footprint associated with traditional building materials.

Rice husk was thermally treated in air (O_2) at temperatures between 200°C and 900°C in a constant heating rate of $10\frac{^\circ C}{min}$ for one hour. The thermal degradation process and structural evolution of the material were analyzed using complementary characterization techniques. Thermogravimetric analysis (TGA) was used to identify the main stages of decomposition, while infrared spectroscopy (FTIR) demonstrated the elimination of organic functional groups and the appearance of $Si-O-Si$ bands characteristic of amorphous silica. X-ray diffraction (XRD) confirmed that the material obtained at 400°C showed a broad pattern centered around 22° (2θ) indicating the presence of an amorphous silica phase with high pozzolanic reactivity. X-ray photoelectron spectroscopy (XPS) confirmed a substantial reduction from the organic surface carbon of the RH and an increased presence of silica in samples treated at temperatures above 400°C. To corroborate the improved mechanical performance in mortars, these were prepared substituting 4% and 8% of cement with rice husk ash (RHA), following the ASTM C109 standard for compressive strength testing at 7 and 28 days.

The results revealed that the removal of organic matter was completed at around 400°C, leading to high-purity amorphous silica with excellent pozzolanic character-

istics. At this temperature, the transformation of the organic matrix into a reactive amorphous phase was evidenced, while at higher temperatures crystallization was promoted, reducing the chemical reactivity. In mechanical tests, mortar with 4% RHA achieved strengths of 11.9 MPa at 7 days and 23.6 MPa at 28 days, while the 8% mortar achieved 13.1 MPa at 7 days and 22.4 MPa at 28 days; all these values were 0.8%, 6,8%, 11.0%, and 1.5% higher than those of the control mortar, respectively. The increase in strength is attributed to the reaction between amorphous silica and $Ca(OH)_2$ released during hydration, that promotes the formation of additional hydrated calcium silicate $C-S-H$ responsible for the structural reinforcement of the material [3]. These findings confirm that pozzolanic RHA improves early strength in mortars maintaining a long-term stability.

Overall, the controlled thermal treatment of rice husks in air atmosphere produces functional amorphous silica having advanced pozzolanic behavior, which is suitable for the production of sustainable materials. The identification of 400°C as the optimal activation temperature establishes an effective strategy for transforming agricultural waste into reactive siliceous materials, reducing dependence on non-renewable mineral resources and the CO_2 emissions associated with their production. This approach connects advanced materials research with circular economy principles, providing an efficient and environmentally responsible alternative for the valorization of agricultural residues in materials engineering.

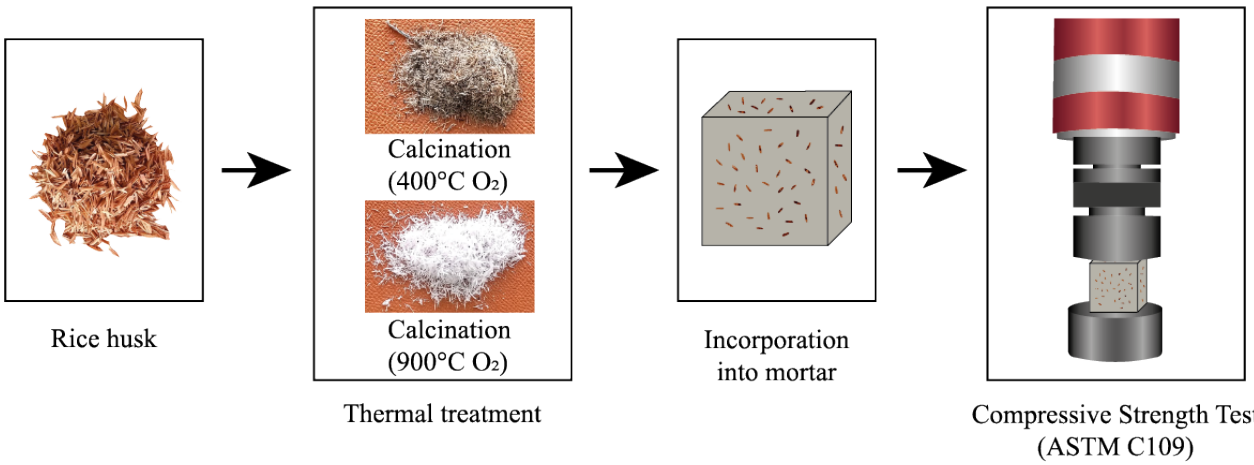

Figure 1: Schematic representation of the experimental procedure. Rice husk was exposed to controlled thermal treatment using temperatures between 200°C and 900°C at O_2 atmosphere to obtain rice husk ash with different physicochemical characteristics. The material was then incorporated as a supplementary component into mortar mixtures. Finally, compressive strength tests were implement according to ASTM C109 to evaluate the mechanical performance of the mortar specimens.

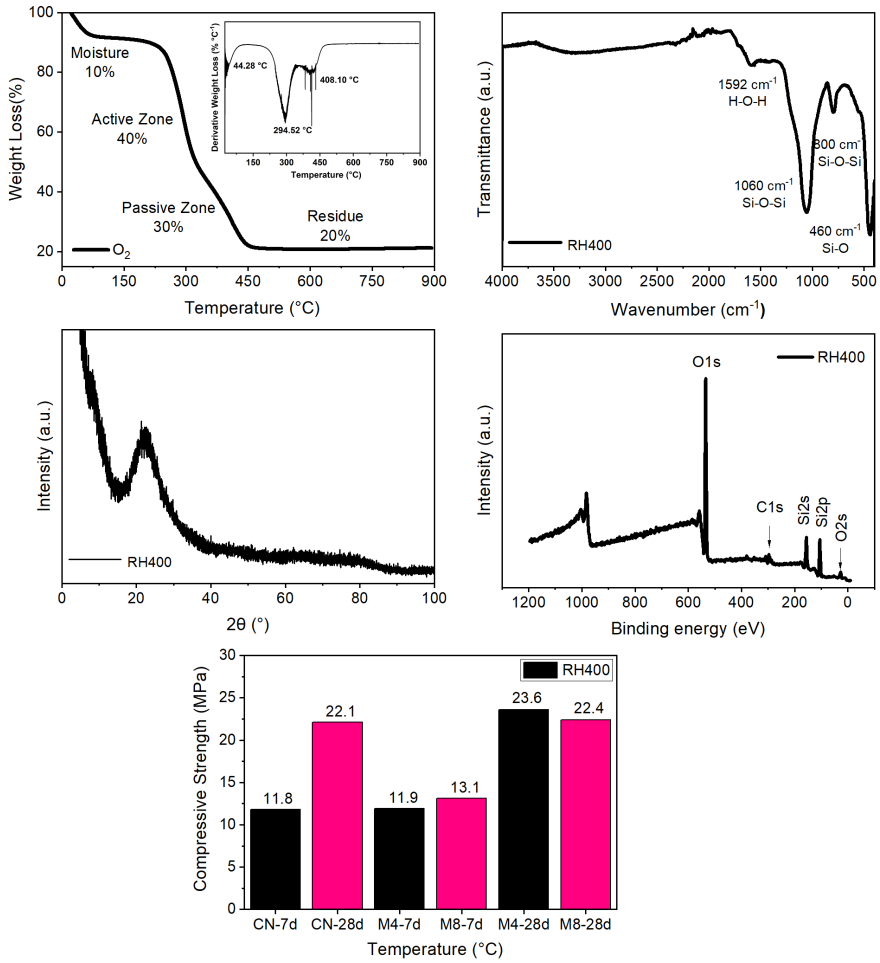

Figure 2: Characterization of rice husk ash treated at 400°C (RH400): (a) Thermogravimetric analysis (TGA) identifying moisture, active, and passive zones as well as residual content; (b) Fourier-transform infrared spectroscopy (FTIR) spectra showing the main functional groups; (c) X-ray diffraction (XRD) pattern corresponding to the structural characteristics of the material; (d) X-ray photoelectron spectroscopy (XPS) survey spectrum used to determine the elemental composition; and (e) Compressive strength test performed according to ASTM C109 for mortar specimens prepared with RH400.

References

[1] Conterosito, E.; Paul, G.; Toson, V.; Gianotti, V.; Milanesio, M.; Gastaldi, D.; Boccaleri, E. Single-step eco-efficient mild chemical process for the total valorisation of rice husk: a focus on the inorganics as a cement additive. *RSC Advances* **2024**, *14*, 36314–36326.

[2] Nair, D. G.; Fraaij, A.; Klaassen, A.; Kentgens, A. A structural investigation relating to the pozzolanic activity of rice husk ashes. *Cement and Concrete Research* **2008**, *38*, 861–869.

[3] Jamil, M.; Kaish, A. B. M. A.; Raman, S. N.; Zain, M. F. M. Pozzolanic contribution of rice husk ash in cementitious system. *Construction and Building Materials* **2013**, *47*, 588–593.

Orthogonal Size and Number Concentration Calibration for Improved Quantitative Biological Analyses

Julie Y. Chen[1], Jeff Bodycomb[1]

[1] *HORIBA*
julie.chen-EX@horiba.com

Abstract

Accurate particle quantification requires robust instrument calibration. However, current calibration practices introduce significant and often underrecognized uncertainty. This limitation directly impacts the characterization of advanced drug formulations, including vaccines, extracellular vesicles, lipid nanoparticles (LNPs), and other nanoscale drug delivery systems, for which particle concentration is a Critical Quality Attribute (CQA). Nanoparticle tracking analysis (NTA) instruments are commonly calibrated using latex particle standards, with number concentrations derived from nominal solids fractions (e.g., 1% w/v). This value is not reported as carefully as, for example, particle size. This implies a rather large uncertainty in the calibration standard which is propagated into NTA measurements. In this study, size and number concentration standards are analyzed using orthogonal techniques and subsequently incorporated for NTA calibration. The use of orthogonal techniques will significantly reduce concentration measurement uncertainties. In this study, particle size and number concentration standards were independently characterized using orthogonal analytical techniques and subsequently applied to NTA calibration. By reducing calibration-derived uncertainty, this approach improves quantification of biological nanoparticles, whose inherent heterogeneity already contributes substantial measurement variability, enabling clearer distinction between true sample effects and analytical artifacts. 150 nm NIST traceable polystyrene latex size standard (Thermo Fisher Catalog Number 3150A) and 30 nm, 50 nm, and 100 nm diameter Ultra UniformTM Gold Nanospheres Number Standards (nanoComposix) were obtained for this study. These standards were analyzed in triplicates using the ViewSizer 3000 simultaneous multi-laser NTA from HORIBA. Multiple lasers with individually adjusted laser power settings and camera gains were carefully selected for each sample. Gold nanoparticle NTA size results were verified using JEOL 1010 Transmission Electron Microscopy (TEM); concentration (number standards only) were verified using Agilent 7800 single particle Inductively Coupled Plasma Mass Spectroscopy (sp-ICP-MS). To facilitate comparison with other orthogonal techniques, the average of the median diameters reported from each NTA measurement is used. Diameter distributions will be reported separately. NTA size and concentration from four standards were obtained and plotted as a direct comparison to TEM and sp-ICP-MS reporting. Percent Coefficient of Variation (CoV %) was used to assess differences and the results of

each technique were compared. NTA results after calibration by latex standards were similar to NTA concentration measurement of gold nanoparticles. Orthogonal techniques serve as independent confirmation to evaluate and qualify NTA's ability to accurately size and count number standards as small as 30 nm in diameter, thereby improving accuracy in characterizing (bio)pharmaceuticals particulates.

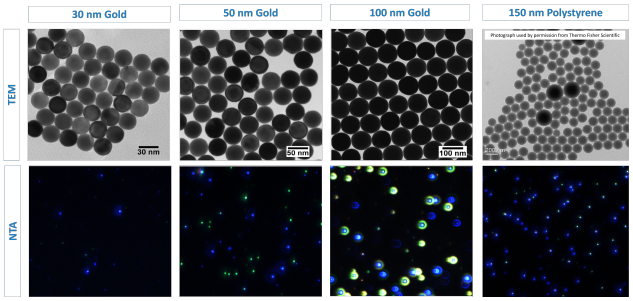

Figure 1: TEM images are compared as orthogonal technique to multispectral NTA.



Figure 2: 150 nm NIST traceable polystyrene latex size standard (Thermo Fisher Catalog Number 3150A) and 30 nm, 50 nm, and 100 nm diameter Ultra UniformTM Gold Nanospheres Number Standards (nanoComposix).

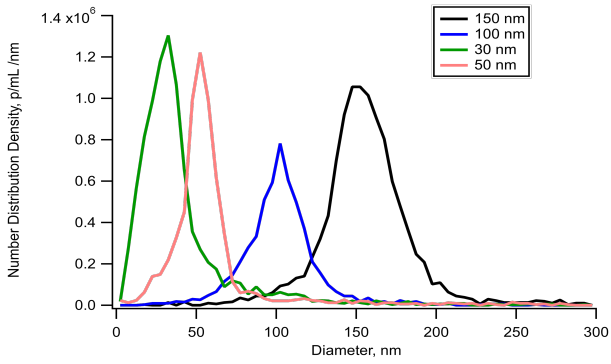

Figure 3: Particle Size Distribution plotted against concentration (particles/mL).

Wednesday

Engineering the structure and properties of 2D materials by defects and impurities

Arkady V. Krasheninnikov[1]

[1] *Institute of Ion Beam Physics and Materials Research, Helmholtz-Zentrum Dresden-Rossendorf, 01328 Dresden, Germany*
a.krasheninnikov@hzdr.de

Abstract

Following isolation of graphene, many other 2D systems, e.g., single sheets of transition metal dichalcogenides (TMDs) or h-BN have been manufactured. All these materials contain defects and impurities, which may govern their electronic, optical, mechanical and catalytic properties. Moreover, defects can intentionally be introduced using beams of energetic particles – ions and electrons, for example for single photon emission required for quantum computing/communication. Formation of defects may also give rise to phase transformations in these materials and/or tune their properties. All of these calls upon the studies on defects and mechanisms of their formation under irradiation. In my talk, I will first discuss the basics of defects in solids with a particular focus on 2D materials, then present the results of our recent theoretical studies [1] of point and line defects (such as mirror twin boundaries) in 2D TMDs obtained in close collaboration with several experimental groups. I will also touch upon the production of defects in 2D materials upon irradiation from both experimental and theoretical perspectives.

References

[1] The list of publications can be found at https://krasheninnikov.de/publist.html.

Multiscale Diffusion in CNT Polymer Nanocomposites: Analytical Modelling, Monte Carlo Simulation and Physics-Informed Neural Networks

Tamayo-Vegas Sebastian[1], Lafdi Khalid[1]

[1] *UNIVERSIDAD INTERNACIONAL DEL ECUADOR*
matamayove@uide.edu.ec

Abstract

Diffusion in polymer nanocomposites reinforced with carbon nanotubes (CNTs) arises from a multiscale relationship between particle geometry, agglomeration, porosity formation, and polymer degradation. Classical analytical models approximate simplified cases, whereas numerical simulations become expensive when microstructural variability increases. Physics Informed Neural Networks (PINNs) enable the integration of physical laws and data into a unified framework for predicting diffusion be haviour. This work combines analytical diffusion theory, CNT geometry–dependent effective diffusivity, Monte Carlo simulation, and PINNs to examine acid penetration into CNT polymer composites. CNT sphericity and hollow-cylinder geometry are incorporated into a physical diffusion coefficient model. Monte Carlo simulations provide anisotropic diffusivity values across variable CNT fractions. A PINN is then used to approximate Fick's second law, learning the diffusion field while matching both analytical behavior and Monte Carlo trends. The results show strong sensitivity of effective diffusivity to CNT geometry and aggregation. The PINN replicates analytical solutions, enforces the PDE, and produces smooth, physically consistent diffusion fields. The unified methodology provides an efficient tool for understanding mass transport in CNT-based composites and establishes a foundation for future multiscale material modelling.

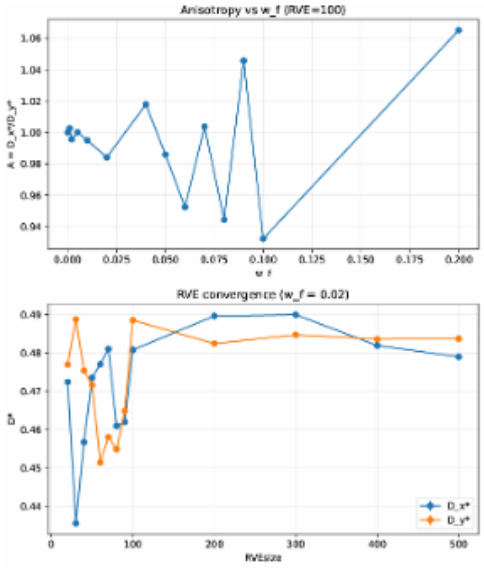

Figure 1: Profile Diffusion at time t(d) Analytical vs Physical Induced Neural Network.

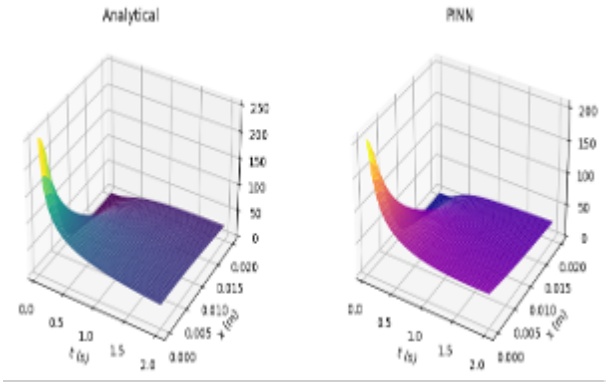

Figure 2: Comparison of analytical diffusion solution and PINN-predicted concentration field as a function of space and time.

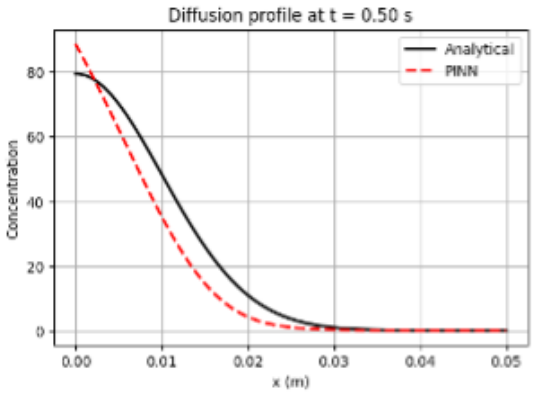

Figure 3: Concentration profiles at t=0.5" s" comparing analytical and PINN solutions.

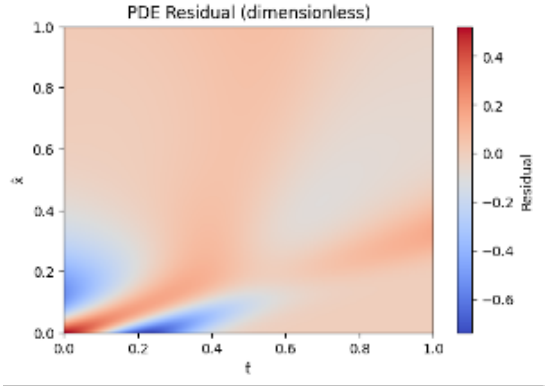

Figure 4: Spatial distribution of the PDE residual for the trained PINN.

References

[1] Crank, *The Mathematics of Diffusion*, 2nd ed.; Oxford University Press: Oxford, U.K., 1975.

[2] Iijima, S. Helical microtubules of graphitic carbon. *Nature* **1991**, *354*, 56–58.

[3] Lagaris, I. E.; Likas, A.; Fotiadis, D. I. Artificial neural networks for solving ordinary and partial differential equations. *IEEE Transactions on Neural Networks* **1998**, *9*, 987–1000.

Simultaneous production of hydrogen peroxide and bioelectricity generation at the cathode using modified graphite electrodes

Katherine Vaca-Escobar[1], Karla L. Montenegro-Rosero[2,3], Andrés V. Yar-Hernández[2], Cesar Huiliñir[4], Alexis Debut[5], Patricio J. Espinoza-Montero[1], Ricardo Salazar-González[2,6]

[1] *Escuela de Ciencias Químicas, Pontificia Universidad Católica del Ecuador, Quito 170525, Ecuador*
[2] *Analysis, Treatment, Electrochemistry, Recovery and Reuse of Water Research Group, WATER2, School of Chemistry, Faculty of Chemistry and Pharmacy, Pontifical Catholic University of Chile, Santiago, Chile*
[3] *Departamento de Ingeniería Química y Bioprocesos, Universidad de Santiago de Chile, Chile*
[4] *Green Technologies Research Group, Facultad de Ingeniería y Ciencias Aplicadas, Universidad de los Andes, Santiago de Chile, Chile*
[5] *Centro de Nanociencia y Nanotecnología, Universidad de Las Fuerzas Armadas (ESPE), Sangolquí 171103, Ecuador*
[6] *Centro de Derecho y Gestión de Aguas, Pontificia Universidad Católica de Chile, Chile*
kathyvaca22@gmail.com

Abstract

This work reports a novel bioelectrochemical strategy that integrates enhanced hydrogen peroxide (H_2O_2) electrosynthesis with wastewater denitrification and bioelectricity generation through surface-engineered graphite cathodes [1–3]. The cathodes are modified by electrospinning nylon-6 nanofibers containing goethite (α-FeO(OH)) nanoparticles onto graphite plates, followed by calcination to obtain conductive carbon nanofiber layers doped with iron oxides. This modification increases the electroactive surface area by approximately 50% and significantly improves oxygen reduction reaction (ORR) kinetics, favoring the two-electron ORR pathway and enabling efficient in situ H_2O_2 production under acidic conditions [2, 3].

Structural characterization by SEM-EDX confirms uniform adhesion of the nanofiber coating and homogeneous dispersion of iron oxide particles on the graphite surface, with clear detection of C, O, and Fe [1]. Electrochemical characterization using the ferri/ferrocyanide redox couple shows that nylon- and nanoparticle-modified electrodes preserve reversible redox behavior while exhibiting higher peak currents and smaller peak separations than bare graphite, indicating enhanced electron-transfer kinetics. In O_2-saturated Na_2SO_4 at pH 2, modified electrodes display higher capacitive currents and positive shifts in the half-wave potentials for both two- and four-electron ORR pathways, demonstrating improved catalytic activity. Increasing the goethite loading (NP1, 1 g L^{-1}) further enhances capacitance and shifts $E_{1/2}$ to more positive values, consistent with a higher density of catalytically active iron sites promoting selective H_2O_2 formation [3].

H_2O_2 electrosynthesis is optimized in single-compartment electrochemical cells by varying aeration rate and current density [2]. At an aeration rate of 6.0 L min^{-1} per liter of reactor, maximum H_2O_2 concentrations of 0.26, 0.44, and 0.68 mM are achieved for bare graphite, nylon-modified, and NP1 cathodes, respectively. Higher

aeration rates reduce performance due to shorter gas–liquid contact times. At a current density of 0.25 mA cm^{-2}, H_2O_2 concentrations after 120 min reach 0.48 ± 0.06 mM for graphite, 0.66 ± 0.05 mM for nylon-modified, and 0.83 ± 0.09 mM for NP1 electrodes. Corresponding H_2O_2 generation rates increase from 40 μmol h^{-1} (graphite) to 95 μmol h^{-1} (nylon) and 192.5 μmol h^{-1} (NP1), representing up to a 14-fold improvement over previously reported graphite-based bioelectrochemical cathodes.

The optimized cathode architecture is subsequently integrated into H-type bioelectrochemical systems (BES), including microbial fuel cells (MFCs) and microbial electrolysis cells (MECs). The anodic chamber is inoculated with pre-adapted denitrifying activated sludge and fed with synthetic wastewater containing 100 mg N-NO_3- L^{-1} and approximately 250 mg L^{-1} COD. In MFC operation, heterotrophic anodic denitrification is coupled with cathodic ORR to H_2O_2. After biofilm maturation, the MFC reaches maximum cell voltages of about 265 mV, corresponding to power and current densities of 4.39 ± 0.07 mW m^{-2} and 16.56 ± 0.16 mA m^{-2}. Although energy recovery is moderate, nitrate removal is highly efficient, achieving complete nitrate removal within 8 h, outperforming both a heterotrophic denitrification control and the MEC, which reach approximately 75% removal in the same period. After 24 h, both MFC and MEC systems accomplish complete nitrate removal and about 95% COD abatement, indicating strong synergy between bioelectrogenesis and denitrification [2].

Because the relatively low COD load limits cathodic H_2O_2 accumulation in MFC mode, the system is switched to MEC operation by applying an external current of 0.004 A (0.25 mA cm^{-2}). In abiotic electrochemical controls, the NP1 cathode produces up to 1.83 mM H_2O_2 after 8 h. In the MEC, initial cycles show lower H_2O_2 accumulation; however, as the anodic biofilm matures, H_2O_2 production increases markedly, reaching 2.74 mM (93.16 ± 2.8 mg L^{-1}) after 8 h from the third cycle onward. This corresponds to a volumetric production rate of 0.14 kg m^{-3} d^{-1}, with Faradaic efficiencies exceeding 98% [1, 2]. Notably, the achieved H_2O_2 concentrations exceed by 2–18 times those typically required for COD removal, disinfection, and degradation of emerging contaminants [3].

Overall, this study demonstrates that iron-oxide-doped, nylon-derived carbon nanofibers effectively convert low-cost graphite into a highly selective $2e^-$-ORR cathode. The resulting bioelectrochemical platform enables simultaneous H_2O_2 production, bioelectricity generation, and efficient denitrification, offering a promising approach for decentralized and sustainable wastewater treatment, although long-term stability and scale-up require further investigation [2, 3].

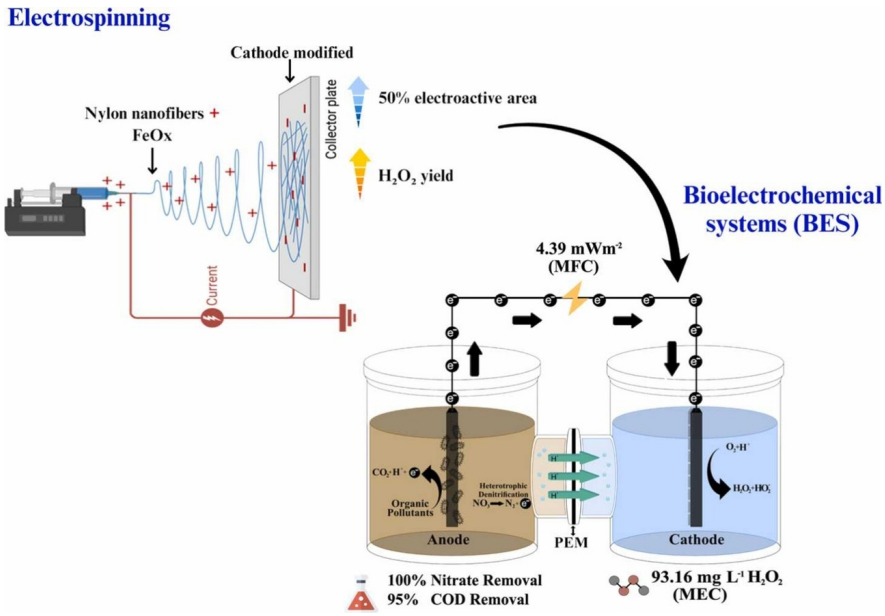

Figure 1: Bioelectrochemical system using nylon nanofibers with iron oxide nanoparticles produced via electrospinning

References

[1] Chen, J.-Y.; Li, N.; Zhao, L. Three-dimensional electrode microbial fuel cell for hydrogen peroxide synthesis coupled to wastewater treatment. *Journal of Power Sources* **2014**, *254*, 316–322. DOI: 10.1016/j.jpowsour.2013.12.114.

[2] Chung, T. H.; Meshref, M. N.; Hai, F. I.; Al-Mamun, A.; Dhar, B. R. Microbial electrochemical systems for hydrogen peroxide synthesis: Critical review of process optimization, prospective environmental applications, and challenges. *Bioresource Technology* **2020**, *313*, 123727. DOI: 10.1016/j.biortech.2020.123727.

[3] Zhao, Q.; An, J.; Wang, X.; Li, N. In-situ hydrogen peroxide synthesis with environmental applications in bioelectrochemical systems: A state-of-the-art review. *International Journal of Hydrogen Energy* **2020**, *46*, 3204–3219. DOI: 10.1016/j.ijhydene.2020.05.227.

Acta Microscopica Vol.35, Supp.1, 2026
Abstract Book NSSY 2026 - Galapagos 17th–23rd May 2026

Highly Efficient Functionalization and Covalent Patterning of Graphene by Photoactivation

Kevin Gerein[1], Michael Moritz[2,3], Christian Papp[3], Frank Hauke[1], Andreas Hirsch[1]

[1] *Chair of Organic Chemistry II & Center of Advanced Materials and Processes (ZMP), Friedrich Alexander University of Erlangen Nürnberg*
[2] *Chair of Physical Chemistry II, Friedrich Alexander University of Erlangen Nürnberg*
[3] *Institute of Chemistry and Biochemistry; Physical and Theoretical Chemistry, Freie Universität Berlin*
kevin.gerein@fau.de

Abstract

Since its first isolation, graphene has remained at the forefront of materials research owing to its remarkable electronic, mechanical, and optical properties.[1] These unique characteristics hold the potential to revolutionize material applications similar to how polymers did in the past. However, its practical implementation is hindered by poor processability, arising from insolubility, and by the absence of an intrinsic bandgap, which limits its use in electronic devices such as transistors. To overcome these limitations, structural modification strategies have been explored, with chemical functionalization emerging as particularly promising. Covalent grafting of functional groups onto graphene can enhance its dispersibility and induce a tunable bandgap, thereby tailoring its properties for specific applications.[2] Yet, the high chemical inertness of graphene renders covalent modification challenging. Although various reactions on the carbon lattice have been reported, functionalization yields are typically low, and efficient modification often requires harsh conditions, such as plasma treatment, electrochemical activation, or the use of strong reducing agents, which demand specialized equipment and expertise.[3] Consequently, accessible and efficient routes for the covalent modification of substrate-supported graphene remain scarce. Here, we present facile and scalable approaches for the light-induced covalent functionalization of graphene employing non-toxic and readily available iodonium salts as active reagents. Upon photoexcitation of graphene, the planar carbon lattice reacts efficiently with these reagents, affording high functionalization yields under mild reaction conditions. Furthermore, spatially controlled modification with micrometer-scale resolution is achieved, enabling the integration of pristine and functionalized regions within a single sample. This method offers a versatile and accessible platform for tailoring graphene's properties towards future applications.

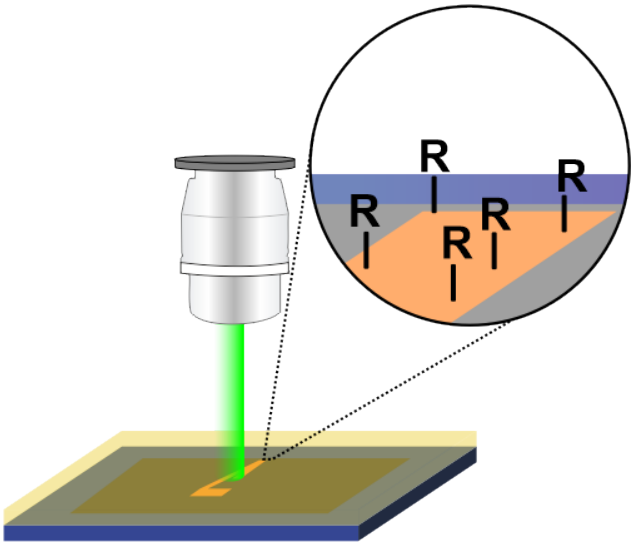

Figure 1: Schematic representation of the laser writing procedure for the spatially resolved covalent functionalization of graphene

References

[1] Novoselov, K. S.; Fal'ko, V. I.; Colombo, L.; Gellert, P. R.; Schwab, M. G.; Kim, K. *Nature* **2012**, *490*, 192–200.

[2] Chua, C. K.; Pumera, M. *Chem. Soc. Rev.* **2013**, *42*, 3222–3233.

[3] Elias, D. C.; Nair, R. R.; Mohiuddin, T. M.; Morozov, S. V.; Blake, P.; Halsall, M. P.; Ferrari, A. C.; Boukhvalov, D. W.; Katsnelson, M. I.; Geim, A. K.; Novoselov, K. S. *Science* **2009**, *323*, 610–613.

Acta Microscopica Vol.35, Supp.1, 2026
Abstract Book NSSY 2026 - Galapagos 17th–23rd May 2026

Optical absorption: A primer

Duncan John Mowbray[1], Vito Despoja[2]

[1] *School of Physical Sciences and Nanotechnology, Yachay Tech University (UITEY), Urcuqui 100119, Ecuador*
[2] *Institute of Physics, 10000 Zagreb, Croatia*
dmowbray@yachaytech.edu.ec

Abstract

The interaction of matter with light, i.e., optical absorption, is of fundamental, experimental, and technological importance, with implications for the characterization of nanomaterials and their design for photovoltaic applications. However, the variety of theoretical methodologies now available for calculating optical absorbance at various levels of theory and computational efficiency, complicate the process of optical absorption simulation. In this work we provide a detailed first principles analysis and comparison of methodologies for calculating optical absorbance using exact theoretical methods, numerical methods based on time propagation, linear response, the Bethe-Salpeter equation, and non-equilibrium Green's function (NEGF) methods. We pay special attention to differences in efficiency and included/neglected contributions to the optical absorbance for each method, as applied to either a two-level system or the full matrix elements obtained from density functional theory (DFT). In this way we provide a roadmap for modelling the optical absorbance of nanomaterials via a set of benchmarks comparing the various levels of theory, their ranges of validity, relative efficiencies, and overall applicability. This work should prove of fundamental interest for both the measurement and modelling of optical absorbance of nanomaterials.

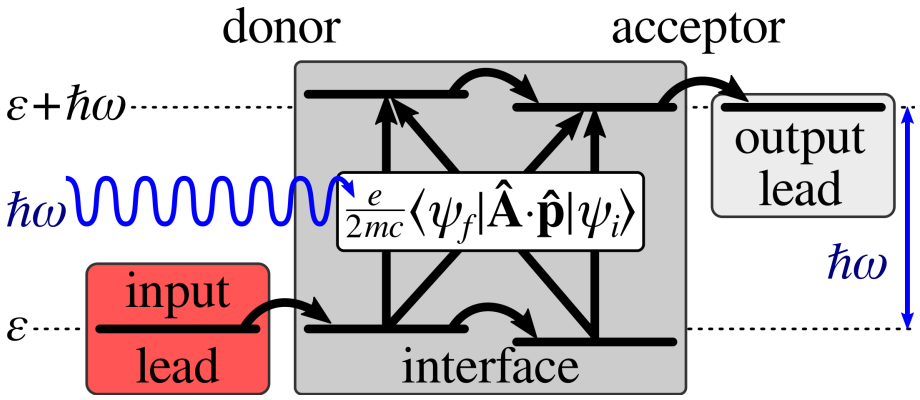

Figure 1: Schematic of the optical absorption process showing the incident photon of energy $\hbar\omega$ (blue arrow) and the excitation from an occupied level of energy ε to an unoccupied level of energy $\varepsilon + \hbar\omega$ via the matrix element $\langle\psi_f|\hat{A}\cdot\hat{p}|\psi_i\rangle$ (black arrows and white box) within the interface between the donor and acceptor (grey box).

Acta Microscopica Vol.35, Supp.1, 2026
Abstract Book NSSY 2026 - Galapagos 17th–23rd May 2026

Transmission-mode geometric-phase characteristics of sculptured thin films

Abdul Rehman[1], **Akhlesh Lakhtakia**[1]

[1] *The Pennsylvania State University. Department of Engineering Science and Mechanics*
akhlesh@psu.edu

Abstract

The concept of geometric phase arose in optics to compare two plane waves by distinguishing their locations on the Poincaré sphere. This concept is useful to compare the plane wave transmitted through a thin film to the incident plane wave. Theoretical calculations indicate that transmission-mode geometric phase (TMGP) is sensitive to the nanoscale architecture of the thin film [1] and there is preliminary experimental evidence too [2].

Therefore, we undertook to comprehensively study the effect of nanoscale architecture on the TMGP characteristics of sculptured thin films (STFs). An STF is an assembly of identical shaped nanowires grown on a planar substrate using physical vapor deposition [3].

We fabricated two types of STFs: non-chevronic periodic columnar-thin-film bilayers (NC-PCTFBs) and structurally right-handed chiral sculptured thin films (CSTFs). STFs of both morphologies were deposited of ZnSe in a custom-built thermal evaporation system. A NC-PCTFB consists of alternating layers of obliquely deposited nanocolumns with different tilt angles. The nanocolumns of the first CTF in the unit cell are tilted at an angle χ_1 with respect to a fixed axis in the substrate plane, whereas the nanocolumns of the second CTF in the unit cell are tilted at $180^\circ - \chi_2$ relative to the same axis, the angles χ_1 and χ_2 being less than 90°. The CSTFs were fabricated using the serial-bideposition technique, in which deposition was carried out at a vapor incidence angle χ_v, which is the angle between the collimated vapor flux and the substrate plane, for a specified time, followed by a clockwise rotation of the substrate holder by 180° about the substrate normal, a second deposition for the same duration, and a subsequent clockwise rotation by 183°; this sequence was repeated to fabricate an assembly of nanohelixes with a fixed pitch. Both STFs were sufficiently thick to exhibit pronounced Bragg phenomenon within the 500–900 nm spectral regime.

Field-emission scanning electron microscopy (FE-SEM) was used to examine the morphology of both STFs, and their SEM images are presented in Fig. 1.

Optical characterization was performed using a custom-built, automated, motorized polarization-resolved system, which can perform both spectroscopy and polarimetry. Spectroscopy was used to measure linear transmittances of NC-PCTFBs and circular transmittances for CSTFs, which allowed the determination of the Bragg regimes. The incident light of a chosen polarization state was incident on a

thin-film sample at an azimuthal angle θ_{inc} varying from 0° to 70° and polar angle ψ varying from 0° to 180°, with the wavelength varying within the 500–900 nm range. Polarimetry was carried out using the rotating quarter-wave plate method, with intensities measured for four incident plane-wave polarization states: s-polarized, p-polarized, right-circularly polarized, and left-circularly polarized. The Stokes parameters were then calculated to determine the asymmetric and the symmetric geometric phases of the transmitted plane wave relative to the incident plane wave for both types of STFs. Measurements were conducted over the same angular and wavelength ranges as for spectroscopy.

Analyzing the spectral and directional data, we confirmed that nanoscale architecture directly affects the symmetric and the asymmetric TMGP characteristics. In particular, the Bragg phenomenon has identifiable TMGP characteristics that depend on the polarization state of the incident plane wave. We expect these findings will guide the designs of optical devices containing STFs.

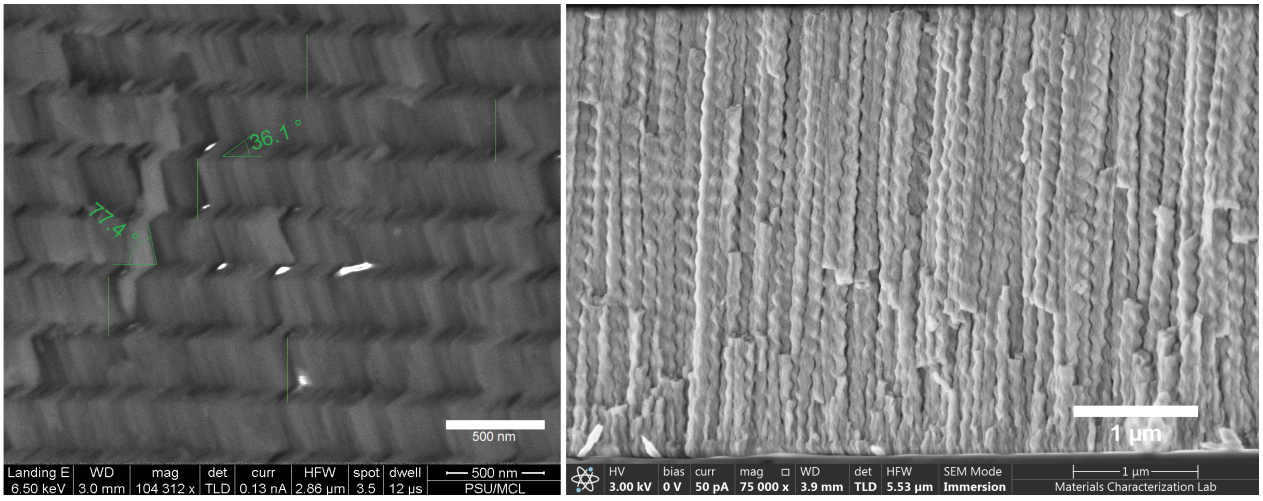

Figure 1: FE-SEM images of (left) a NC-PCTFB and (right) a structurally right-handed CSTF.

References

[1] Das, A.; et al. *J. Opt. Soc. Am. A* **2023**, *40*, 2418.

[2] Lakhtakia, A. *Phys. Rev. A* **2024**, *109*, 043517.

[3] Lakhtakia, A.; Messier, R., *Sculptured Thin Films: Nanoengineered Morphology and Optics*; SPIE Press: Bellingham, WA, USA, 2005.

Acta Microscopica Vol.35, Supp.1, 2026
Abstract Book NSSY 2026 - Galapagos 17th–23rd May 2026

Materials Design of BDD/$BiVO_4$–BDD/Bi_2CuO_4 Photoelectrode Systems for Visible-Light-Driven Microplastic Degradation and Hydrogen Production.

Patricio J. Espinoza-Montero[1], Leonardo E. Navarrete-Cevallos[1]

[1] *Escuela de Ciencias Química, Pontificia Universidad Católica del Ecuador, Quito, 170525*
pespinoza646@puce.edu.ec

Abstract

Microplastics (MPs), defined as plastic particles smaller than 5 mm, have become ubiquitous contaminants in aquatic environments, including groundwater and drinking water, and have been detected in biota, including humans. Their small size and chemical composition render them particularly hazardous, as they can act as vectors for viruses and bacteria, facilitate the transport of organic and inorganic pollutants, and enter the food chain through ingestion by smaller organisms. Owing to their persistence and resistance to natural degradation, the removal of MPs from water systems remains a significant environmental challenge.

Conventional approaches for MPs removal, such as adsorption, coagulation-flocculation, flotation, filtration, and magnetic separation, primarily focus on phase separation rather than complete degradation of the particles [1]. Consequently, there is a growing interest in advanced oxidation and photoelectrochemical (PEC) strategies capable of achieving mineralization of MPs.

In this study, we report the PEC degradation of high-density polyethylene (HDPE) microplastics using a boron-doped diamond/bismuth vanadate (BDD/$BiVO_4$, denoted as B/BVO) photoanode. Additionally, a dual-function system is proposed, coupling MPs degradation with hydrogen production using a boron-doped diamond/bismuth copper oxide (BDD/Bi_2CuO_4, denoted as B/BCO) photocathode.

The B/BVO photoanode was fabricated via a drop-casting method followed by thermal treatment. A precursor solution containing $Bi(NO_3)_3{\cdot}5H_2O$, NH_4VO_3, and citric acid was deposited onto the BDD substrate and dried at 100 °C for 10 min. The electrode was subsequently annealed at 450°C (heating rate of 3°C min^{-1}) for 2 h. This deposition-annealing cycle was repeated multiple times to obtain the desired film thickness and optimize the photoelectrode performance [2].

The B/BCO photocathode was prepared using a precursor solution of $Bi(NO_3)_3{\cdot}5H_2O$ and $Cu(NO_3)_2{\cdot}9H_2O$ dissolved in ethylene glycol, followed by annealing at 500°C for 2 h. Linear sweep voltammetry (LSV) measurements under chopped illumination confirmed the semiconductor behavior of both electrodes. The B/BVO photoanode exhibited typical n-type characteristics, with increased photocurrent under anodic bias, whereas the B/BCO photocathode displayed p-type behavior, with enhanced

response under cathodic potentials. In both systems, a significant shift in the onset potential was observed under illumination (Fig. 1a, d).

The photoelectrochemical performance showed photocurrent densities of approximately 30 μA cm^{-2} for B/BVO and -40 μA cm^{-2} for B/BCO (Fig. 1b, e), indicating efficient charge carrier generation and separation. Electrochemical impedance spectroscopy (EIS) analysis further revealed that BDD/$BiVO_4$ under visible LED irradiation exhibited the smallest semicircle diameter, corresponding to reduced charge transfer resistance at the electrode-electrolyte interface (Fig. 1c). The degradation of microplastics was investigated in the presence of three different surfactants. Chemical oxygen demand (COD) analysis demonstrated that surfactants play a critical role in enhancing degradation efficiency. In particular, sodium lauryl sulfate significantly improved MP degradation in the PEC system, achieving COD values of up to 80 mg O_2 L^{-1} after 8 h of treatment, representing an improvement of approximately 20 mg O_2 L^{-1} compared to the bare electrode (Fig. 1f). These findings highlight the potential of BDD-based photoelectrochemical systems as an effective and sustainable approach for the degradation of persistent microplastic pollutants, while simultaneously enabling hydrogen production as a value-added process.

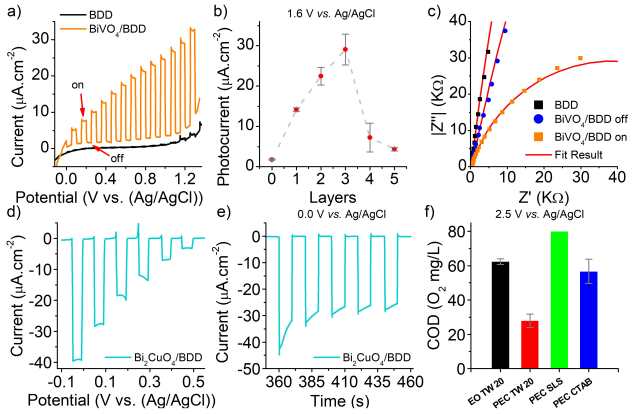

Figure 1: Results of lineal sweep voltammetry under chopped light of a) $BiVO_4$/BDD and d) BDD/Bi_2CuO_4. b) Transient photocurrent vs. layers plot and c) EIS of BDD/$BiVO_4$. e) Transient photocurrent of BDD/Bi_2CuO_4 photocathode. f) Chemical oxygen demand of HDPE MPs degradation.

References

[1] Chen, Z.; Liu, X.; Wei, W.; Chen, H.; Ni, B.-J. Removal of microplastics and nanoplastics from urban waters: Separation and degradation. *Water Research* **2022**, *221*, 118820. DOI: 10.1016/j.watres.2022.118820.

[2] Tan, M.; Fu, Y.; Zhang, K.; Liu, Y.; Zhang, C.; Hao, D.; Wang, Q.; Du, H. Visible-light-responsive BiVO4/NH2-MIL-125(Ti) Z-scheme heterojunctions with enhanced photoelectrocatalytic degradation of phenol. *Journal of Alloys and Compounds* **2022**, *936*, 168345. DOI: 10.1016/j.jallcom.2022.168345.

Acta Microscopica Vol.35, Supp.1, 2026
Abstract Book NSSY 2026 - Galapagos 17th–23rd May 2026

Laser induced graphene from avocado seed

Byron Tipán[1,2], Gema González[1], Carlos Reinoso[1], Fernando Pantoja[2]

[1] *Yachay Tech University, School of Physical Sciences and Nanotechnology, 100119 Urcuquí, Ecuador*
[2] *Departamento de Materiales, Facultad de Ingeniería Mecánica, Escuela Politécnica Nacional, Ladrón de Guevara, E11-253 Quito, Ecuador*
btipan@yachaytech.edu.ec

Abstract

Laser-induced graphene (LIG) has emerged as a versatile and sustainable approach to fabricating porous, conductive graphitic structures from carbon-rich precursors. In this study, Fuerte avocado seed waste (Persea americana Mill.) was investigated as an unconventional biomass precursor for the green synthesis of LIG using CO_2 laser irradiation. [1] The avocado seed powder was processed into compact pellets and irradiated under systematically optimized synthesis parameters, including laser power, scan speed, irradiation area, number of laser passes, and processing atmosphere. Optimizing these variables is essential because laser energy strongly influences the thermal reorganization and graphitization processes within the precursor during irradiation. [2] In addition, the chemical composition and particle size of the precursor were found to play a crucial role in promoting graphitic conversion. Unlike many reported approaches, the optimized synthesis conditions enabled the successful formation of LIG without flame-retardant additives. Five samples were fabricated and irradiated over a rectangular area of 10×5 mm^2 to control a total irradiation area of 50 mm^2. Raman spectroscopy revealed a high degree of graphitization with a low defect density, reflected by an I_D/I_G ratio of 0.16 ± 0.07. Scanning electron microscopy confirmed the characteristic porous morphology of LIG, while electrical measurements showed a sheet resistance of $25.31 \pm 1.09\ \Omega\, sq^{-1}$. [3] These findings demonstrate that avocado seed biomass is a viable, low-cost, and sustainable precursor for fabricating LIG without flame retardants, highlighting the importance of optimizing synthesis parameters to tailor the structural and electrical properties of sustainable graphene-based materials.

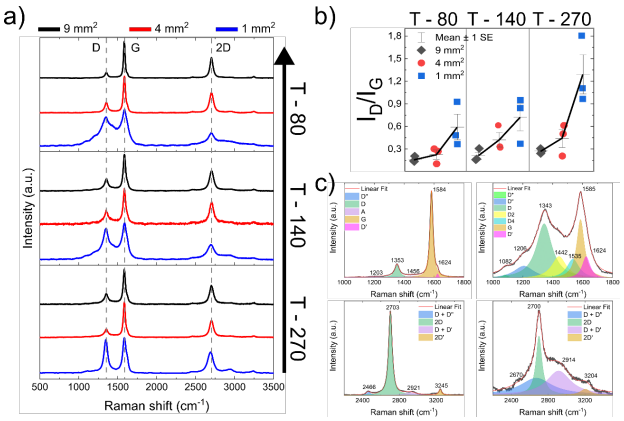

Figure 1: Influence of irradiation area and particle size on LIG structure. (a) Raman spectra of samples synthesized using T-80, T-140, and T-270 powders at irradiation areas of 9, 4, and 1 mm^2. (b) Evolution of Raman intensity ratio I*DIG*. (c) Fitting the Raman spectrum corresponding to samples with an irradiation area of 9 mm^2 and 1 mm^2.

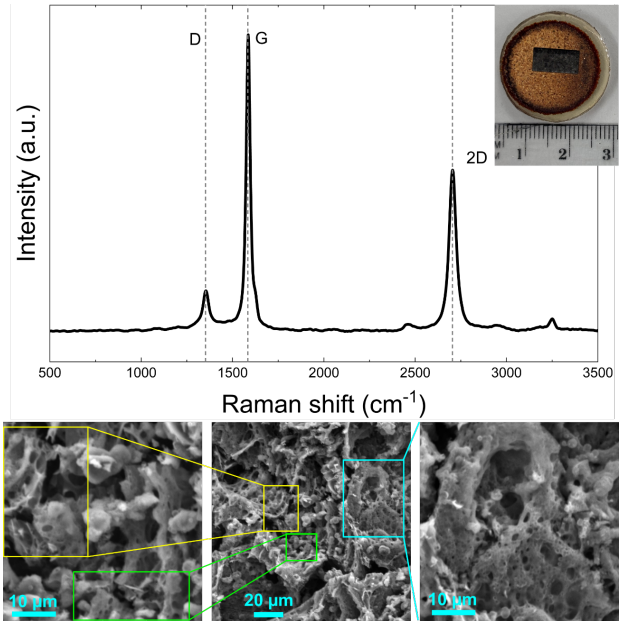

Figure 2: LIG was synthesized with a laser power of 11 %, at 50 mm $^{-1}$ with a defocus distance of 9 mm. (a) Ramana spectrum of a representative sample of the LIG synthesis. (b) SEM images (1000×) of the irradiated regions showing surface morphology.

References

[1] Ye, R.; James, D. K.; Tour, J. M. Laser-Induced Graphene: From Discovery to Translation. *Advanced Materials* **2018**, *31*. DOI: 10.1002/adma.201803621.

[2] Ghanam, A.; Mennani, M.; Kasbaji, M.; Benhamou, A. A.; Achaby, M. E.; Kassab, Z.; Ghamouss, F. Lignin-derived laser-induced graphene: toward a green and scalable route for energy and environmental applications. *Green Chemistry* **2026**, *28*, 2643–2668. DOI: 10.1039/d5gc05595d.

[3] Claro, P. I. C.; Pinheiro, T.; Silvestre, S. L.; Marques, A. C.; Coelho, J.; Marconcini, J. M.; Fortunato, E.; Mattoso, L. H. C.; Martins, R. Sustainable carbon sources for green laser-induced graphene: A perspective on fundamental principles, applications, and challenges. *Applied Physics Reviews* **2022**, *9*. DOI: 10.1063/5.0100785.

Acta Microscopica Vol.35, Supp.1, 2026
Abstract Book NSSY 2026 - Galapagos 17th–23rd May 2026

Carbonaceous materials derived from carboxymethylcellulose loaded with ZnO NPs for supercapacitors: correlation between structure and performance

María Fernanda Bósquez-Cáceres[1,2], Lorena Álvarez Contreras[3], Luis Corredor[2], Gerardo Acosta[1], Juan Pablo Tafur[4], Vivian Morera Córdova[2]

[1] *School of Physical Sciences and Nanotechnology, Yachay Tech University, Urcuquí, 100119, Ecuador*
[2] *Grupo de Investigación de Química Médica, School of Chemical Sciences and Engineering, Yachay Tech University, Urcuquí 100119, Ecuador*
[3] *Centro de Investigación en Materiales Avanzados S.C. (CIMAV), Miguel de Cervantes No. 120, Complejo Industrial Chihuahua, Chihuahua 31136, Mexico*
[4] *G-Aqua Research Group, Universidad Politécnica de Madrid, E.T.S. de Ingeniería y Diseño Industrial, Ronda de Valencia 3, 28012 Madrid, Spain*
maria.bosquez@yachaytech.edu.ec

Abstract

Electrochemical energy storage devices are fundamental components in the transition to more sustainable energy systems. Growing energy demand has driven the search for more efficient, economical, and environmentally friendly storage systems. This has led to the need to develop devices based on electrodes with high charge storage capacity due to their potential for applications that require high power density, fast charge-discharge times, and long service life [1]. In this context, hybrid materials that combine inorganic and carbonaceous compounds represent a promising alternative due to the synergistic effects between both phases [2].

This work proposes the development of ZnO/C hybrid composites to be tested as electrode materials in energy storage devices. The materials were synthesized using a simple and economical method based on the carbonization of carboxymethylcellulose (CMC) films doped with zinc chloride in a 2:1 mass ratio. The atmospheres (air and argon) and temperatures of 400 °C, 500 °C, and 600 °C were varied during carbonization. Characterization was performed using TGA, XRD, Raman, FTIR, UV-Vis, N_2 adsorption-desorption, XPS, SEM, and TEM. Electrochemical characterizations were performed using cyclic voltammetry, electrochemical impedance spectroscopy, and galvanostatic charge/discharge tests to evaluate their potential as electrode materials. A custom-built symmetric supercapacitor prototype was fabricated, enabling reproducible device-level testing (Figure 1).

The results show that combining the pseudocapacitance of ZnO with the electrical conductivity and porosity of the carbon matrix results in materials with improved electrochemical properties for the desired application. Regarding TEM micrographs, in the sample treated Ar_600, they reveal well-defined, mostly quasi-spherical particles with sizes ranging from 24 to 63 nm (Figure 2a). This hierarchical architecture explains the greater accessibility, providing a larger specific

surface area. In contrast, the sample calcined in air (Air_600) exhibits significantly larger particles, with sizes up to 132 nm, and a more amorphous and agglomerated morphology (Figure 2b). The materials exhibited combined pseudocapacitive and electric double layer capacitance (EDLC) behavior. This demonstrated the synergy between ZnO (redox active sites) and carbon (conductivity and surface area). An improvement in specific capacitance and cyclic stability was achieved, obtaining a maximum capacitance of 47.8 F/g at 0.25 A/g, demonstrating its applicability as electrodes for supercapacitors (Figure 3). Overall, the results indicate that higher carbonization temperatures improve the crystallinity of ZnO and enhance the graphitization of the carbon matrix, with the Ar_600 composite exhibiting superior electrochemical performance.

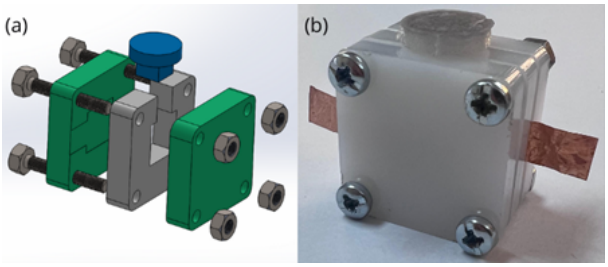

Figure 1: (a) 3D Design and Prototype of Supercapacitor Holder, (b) Assembled prototype.

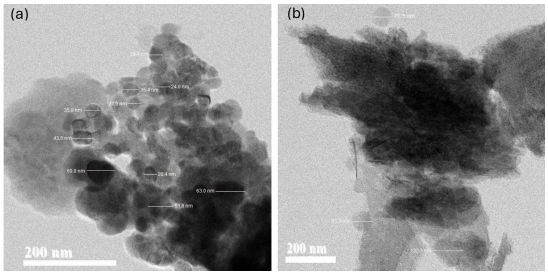

Figure 2: Transmission electron micrographs of ZnO/C composites synthesized at 600 °C under (a) argon and (b) air.

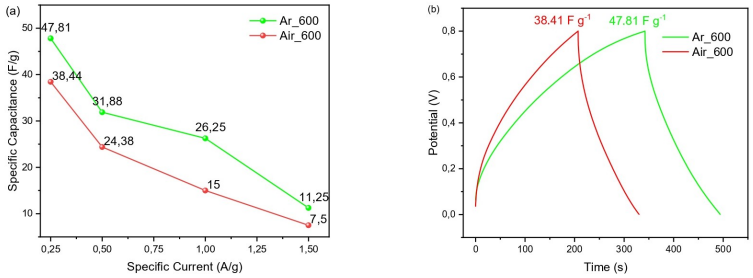

Figure 3: (a) Specific capacitance versus specific current of Ar_600 and Air_600 prototypes. (b) GCD curves taken at 0.25 A/g of the symmetrical supercapacitor prototype with samples synthesized in air and argon at 600 °C.

References

[1] Raha, S.; Ahmaruzzaman, M. Recent advances in nanostructured materials for energy storage. *Nanoscale Advances* **2022**, *4*, 1868–1925. DOI: 10.1039/D1NA00789A.

[2] Ates, M.; Chebil, A.; Yoruk, O.; Dridi, C.; Turkyilmaz, M. Conducting polymer nanocomposites for electrochemical applications. *Ionics* **2021**, *28*, 27–52. DOI: 10.1007/s11581-021-04120-7.

Thursday

Precision Chemistry

Thomas Heine[1]

[1] *TU Dresden*
thomas.heine@tu-dresden.de

Abstract

Precision chemistry is the basis for emerging materials with unprecedented physical phenomena. Precision materials combine local atomic precision with long-range order. Precision synthesis can link well-defined molecular building blocks to form long-range crystalline structures. This approach offers to combine the plethora of molecular functionality with the intrinsic properties of all mathematically possible lattices. Specially designed precision materials offer a variety of physical and chemical properties, such as topological features of the band structure (Dirac points, topologically flat bands, topological insulators), rich exciton physics, tunable electronic and optoelectronic properties, magnetic order, and highly selective catalytic and photocatalytic properties. I will illustrate the raise of precision materials on a range of examples. They will include carbon nanoribbons, where there the edge decoration determines if they are topologically trivial or not [1]. In twisted transition metal dichalcogenide bilayers we show the emergence of superlattices that determine the band structure near the fermi level [2]. In the emerging class of two-dimensional organic crystals [3] we demonstrate metallic behaviour, [4] highly tunable photocatalytic properties [5] and metal-free magnetism [6]. Finally, I will show how the activity of isolated Cu(I) sites in metal-organic frameworks can be boosted to become selective for the separation of helium isotopes [7].

References

[1] Arnold, F. M.; Liu, T.-J.; Kuc, A.; Heine, T. Structure-Imposed electronic topology in Cove-Edged graphene nanoribbons. *Physical Review Letters* **2022**, *129*, 216401. DOI: 10.1103/physrevlett.129.216401.

[2] Arnold, F. M.; Ghasemifard, A.; Kuc, A.; Heine, T. Implementing electronic signatures of graphene and hexagonal boron nitride in twisted bilayer molybdenum disulfide. *Materials Today* **2024**, *73*, 96–104. DOI: 10.1016/j.mattod.2024.01.012.

[3] Wang, Z.; Wang, M.; Heine, T.; Feng, X. Electronic and quantum properties of organic two-dimensional crystals. *Nature Reviews Materials* **2024**, *10*, 147–166. DOI: 10.1038/s41578-024-00740-8.

[4] Zhang, T. et al. Two-dimensional polyaniline crystal with metallic out-of-plane conductivity. *Nature* **2025**, *638*, 411–417. DOI: 10.1038/s41586-024-08387-9.

[5] Yu, H.; Jing, Y.; Heine, T. Physics and Chemistry of Two-Dimensional Triangulene-Based lattices. *Accounts of Chemical Research* **2024**, *58*, 61–72. DOI: 10.1021/acs.accounts.4c00557.

[6] Yu, H.; Heine, T. Prediction of metal-free Stoner and Mott-Hubbard magnetism in triangulene-based two-dimensional polymers. *Science Advances* **2024**, *10*, eadq7954. DOI: 10.1126/sciadv.adq7954.

[7] Heine, T.; Wulf, T.; Das, S.; Dongmo, E. Strong Cu(I)–He interaction at open metal sites enables isotope-selective helium adsorption. *Research Square* **2025**. DOI: 10.21203/rs.3.rs-7214188/v1.

Acta Microscopica Vol.35, Supp.1, 2026
Abstract Book NSSY 2026 - Galapagos 17th–23rd May 2026

Graph theory tools for nanocarbon symmetry, structural generation, and beyond

Eduardo Costa Girão[1], Lilac Macmillan[1], Vincent Meunier[1]

[1] *Universidade Federal do Piauí, Pennsylvania State University*
edu@ufpi.edu.br

Abstract

In this talk, I will present a mathematical framework we developed to describe the topology of sp^2 2D carbon allotropes: lattices where each carbon atom is linked to exactly three neighbors in the network. Such systems have been proposed and studied since mid 1990s, when extended distribution of defects over graphene were considered to hypothesize a lattice exclusively made of pentagons and heptagons. The underlying idea is to insert so many defects over the honeycomb lattice in a way that it makes more sense to talk about a completely new system (or allotrope) instead of referring to it as a defective graphene sheet. On one hand, countless non-graphitic 2D nanocarbons have been theoretically proposed over the last three decades. On the other hand, the relatively recent synthesis of 2D biphenylene has further boosted this field [1], so that, today, creating a detailed, duplicate-free list is a hard task. If a researcher comes up with a new proposal, there is no simple way to check if that system has been studied before. In this regard, systematic naming schemes have been proposed in a trial to facilitate their tracking [2].

In this context, well-defined mathematical methods to identify these lattices are welcomed. Graph theory is a natural framework to describe and classify these lattices through their topologies. A graph is simply a set of vertices connected by edges, analogous to an atomic structure that is composed of atoms linked to each other by chemical bonds. However, basic tools (like adjacency matrices) fail to give a precise identification structure-by-structure, since systems with a completely different set of rings can feature the same connectivity. In this work, we propose describing 2D nanocarbon allotropes by means of an entity we call the *embedding tensor* [3]. Instead of enumerating just the atoms (or vertices), we also enumerate bonds (or edges) and rings (or faces). Then, a cuboid data structure with binary entries indicates when a given face, edge, and vertex set of elements meet each other in the structure (1) or not (0). The non-zero elements of this tensor define objects called *flags*, that hold neighboring relations to each other, and define another graph: a *flag graph*. Such a graph carries the whole symmetry information of the lattice, allowing us to determine whether two structures correspond to the same topology or not, and to identify the system's symmetry group. An interesting point here is that these symmetry searches are done in the space of integer numbers, instead of working with explicit coordinates that demand real-valued tolerances.

The embedding tensor, and the resulting flag graph, can also be used as a tool to systematize and optimize the search for new such lattices by an add-dimer algorithm

[2, 3]. The basic idea is to create the generation of 2D sp^2 carbon systems with $N+1$ rings per primitive unit cell from the set of structures with N rings per primitive cell. This is done by adding dimers in the N-face parent structures. A dimmer is added by including atoms in the middle of two edges from a given face of a parent structure. These two atoms are linked by a new edge (bond) that cuts that face in two (creating an $N+1$-face lattice). This process is significantly empowered by the tensor approach, as it allows for an easy inclusion of the new dimer in the flag graph, and for a fast comparison of a new candidate system against the previous growing database. Symmetry is also trivially inserted in the algorithm to avoid testing many duplicates. While this algorithm systematically gives a complete list of all possible lattices for small ($N < 10$) systems, larger systems can be further generated with more specialized procedures.

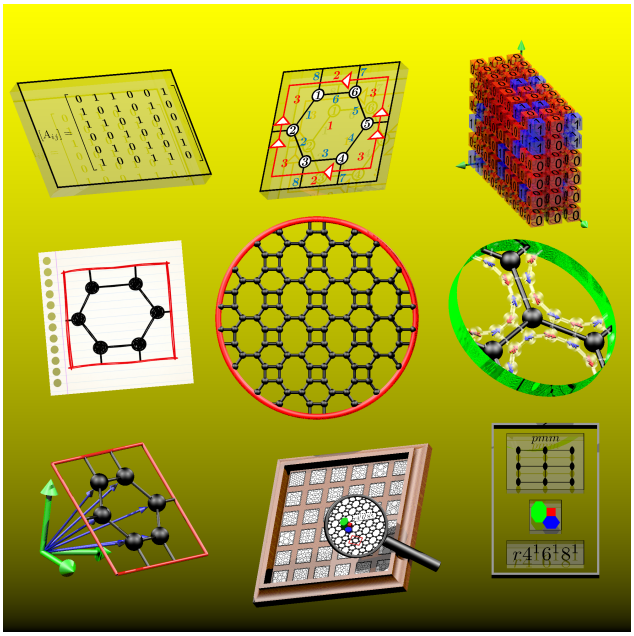

Figure 1: Expanding from the simple adjacency matrix to the embedding tensor/flag graph approach, we develop tools for tasks like symmetry identification and structure/coordinates generation.

References

[1] *Science*. **2021**, *372*, 852.

[2] *Carbon*. **2023**, *203*, 611.

[3] *Computational Materials*. **2026**, *12*, 65.

Influence of topological defects on the adsorption properties of graphene for small molecules

Scholtzova Eva[1], Moreno-Rodriguez Daniel[2], Nishihara Hirotomo[3]

[1] *Institute of Inorganic Chemistry, Slovak Academy of Science, Dúbravská cesta 9, 84536 Bratislava, Slovakia*
[2] *Dipartimento di Ingegneria Meccanica e Aerospaziale, Sapienza Università di Roma, 00184 Roma, Italy*
[3] *Institute of Multidisciplinary Research for Advanced Materials, Tohoku University, Sendai, 980-8577, Japan*
eva.scholtzova@savba.sk

Abstract

Graphene, as a 2D material, is formed by a one-atom-thick planar sheet of arranged sp^2 hybridised carbon atoms packed in a honeycomb-like lattice. The synthesis of these materials, like graphene, necessarily produces defects, e.g., point defects like vacancies, dislocations and functionalised groups. These defects impact the topology and distort the elementary lattice, affecting the physicochemical properties. Some defects, like adjacent pairs of pentagonal and heptagonal rings, may arise by rotating a single pair of carbon atoms 90° (Stone–Wales (SW) defect)[1]. Besides, the carbon vacancies in the graphene structure can cause the migration of adjacent atoms forming five and eight-membered rings, for example. The presence of these defect sites can diminish or enhance the adsorption ability and catalytic properties of these carbon materials.

The present study aims to elucidate how the presence of the defects mentioned above, found in graphene mesosponge material (GMS)[2], can affect the interactions and adsorption behaviour of CO_2 and NH_3 molecules, as well as the electronic structure of GMS material through computational modelling[3].

The Density Functional Theory (DFT) method was applied to examine the three structural models: pristine graphene (G) and two models of modified graphene: model with SW defects (5,7-membered rings) – MG7 and model with 5, 8-membered rings – MG8 (Fig. 1) to study adsorption of CO_2 and NH_3 molecules in different orientations to the surface of respective models. Since the weak interactions act in the structures, the D3 scheme for corrections of dispersion interactions was also applied. For example, a detailed electronic structure analysis of all the proposed models was done by calculating partial charges and bond orders. The interactions acting in the structure were analysed in detail. Adsorption energies as a measure of the structural stability of hybrid systems, adsorbed molecule - graphene/modified graphene, were calculated as the difference between the sum of the total energies of products and the sum of the total energies of reactants.

Topological defects in graphene, such as SW rearrangements and non-hexagonal ring formations, reshaped its electronic landscape and unlocked new adsorption pathways. The findings demonstrated that defect-induced distortions and localised electron density variations created active sites that intensified molecular interactions. Specifically, the model with 5- and 8-membered ring defects (MG8) exhibited

the strongest interactions for both CO_2 and NH_3. The MG8 obtained the lowest adsorption energy -15.85 kJ mol^{-1} for the CO_2 and -14.78 kJ mol^{-1} for the NH_3 molecule, compared with the rest of the models (MG8 > MG7 > G). Further, the mutual parallel orientation of the CO_2 molecule is favoured in comparison with the perpendicular arrangement.

The interplay between defect geometry and molecular orientation predetermined the adsorption strength. Defective graphene models with 5, 7- and/or 5, 8- membered rings showed enhanced adsorption energies compared to pristine graphene. These results underscore the potential of focused tailoring of graphene's defects for enhanced gas storage, sensing, and catalysis applications. They open new avenues for designing more efficient graphene-based materials with customisable adsorption properties.

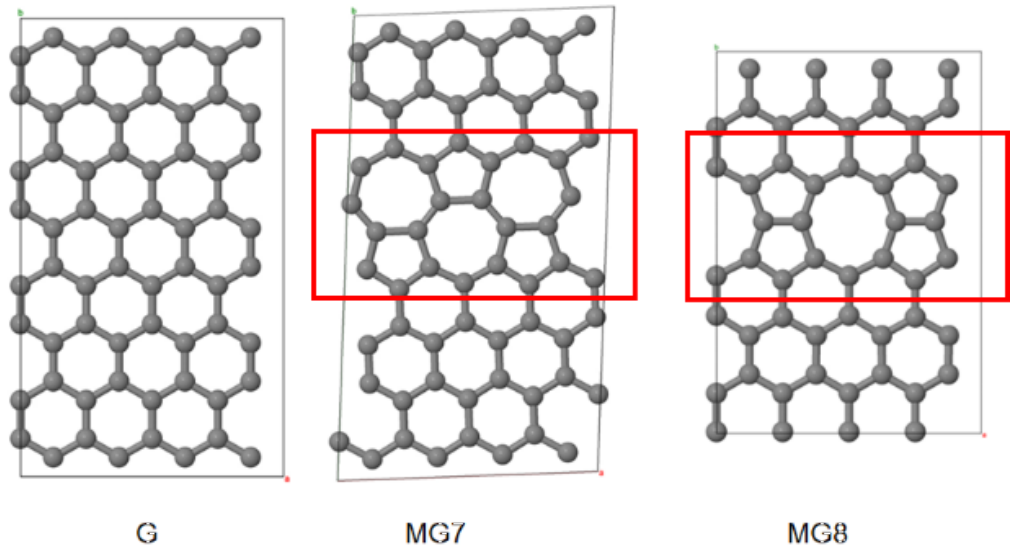

Figure 1: Structural models of pristine graphene (G), modified graphene with the 5,7-membered rings (MG7) and with the 5,8-membered rings (MG8) as defects.

References

[1] Tian, W. et al. *Micromachines* **2017**, *8*, 163.

[2] Yu, W. et al. *Adv. Sci.* **2023**, *10*, 2300268.

[3] Moreno-Rodríguez, D. et al. *Mater. Chem. Front.* **2025**, accepted.

Acta Microscopica Vol.35, Supp.1, 2026
Abstract Book NSSY 2026 - Galapagos 17th–23rd May 2026

Tuning 2D materials through substitutional doping: Vibrational Properties of V-WS_2

Cristina Rubio[1], Elizabeth Houser[1], Nikalabh Dihingia[1], Zhuohang Yu[1], Danielle Reifsnyder Hickey[1], Mauricio Terrones[1], Vincent Meunier[1]

[1] *The Pennsylvania State University*
csr5469@psu.edu

Abstract

This talk will focus on the density functional theory study of highly-doped V–WS_2. 2D materials have been studied for decades [1] due to their strong potential for energy storage and applications in electrocatalysis, electrochemistry, and optoelectronics. Transition metal dichalcogenides (TMDs) offer tunable properties for energy applications through nanoengineering strategies, including doping, strain, and heterostructure formation [2]. Within this family, Tungsten dichalcogenides (particularly WS_2) are of particular interest because their structural phase stability and vibrational response can be strongly modified by defects and dopants. In the present work, we combine experimental microscopy and Raman spectroscopy with Density Functional Theory (DFT) calculations, focusing on the VS_2–WS_2 alloy, in which a 2H-WS_2 host lattice stabilizes the metastable 2H-VS_2 at high V content. Raman spectroscopy serves as a non-destructive, symmetry-selective, and sensitive technique for phase, defects, and composition [3]. Experimentally, increasing V concentration activates 2H-VS_2-related peaks at 212, 365, 386, and 451 cm^{-1} and produces pronounced redshifts relative to pristine WS2, with measurable changes in phonon frequencies. The triangle, armchair, and zigzag dimers are the predominant defect clusters present in the structure. Finally, the phonon analysis suggests that V doping can introduce more localized vibrations, indicating that dopant ordering controls the Raman-active response. Different cluster geometries (single, triangle, armchair/zigzag dimers) redistribute the localized-state signals across distinct frequency ranges, providing geometry-dependent vibrational fingerprints. Together, this framework provides experimentally testable vibrational fingerprints for tracking 2H-VS_2 stabilization inside V-WS_2 to support the design of phase-tuned TMD alloys for energy applications [4].

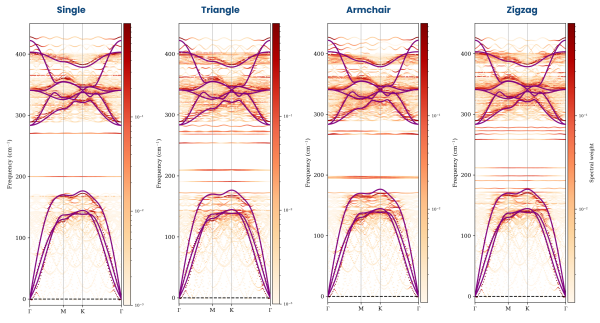

Figure 1: Unfolded phonon band structures for different V defect configurations in WS_2: Single, Triangle, Armchair, and Zigzag. The color intensity represents the spectral weight, while the purple lines show the reference phonon branches. Although the different dopant arrangements preserve similar overall features, they induce subtle differences in broadening, spectral-weight redistribution, and vibrational mode localization.

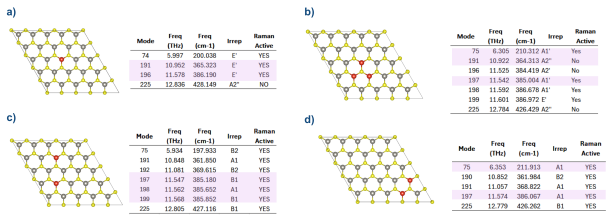

Figure 2: Defect geometries and symmetry assignment of representative vibrational modes in V-doped WS_2: (a) single substitution, (b) triangular cluster, (c) armchair dimer, and (d) zigzag dimer. The tables summarize the mode index, frequency (in THz and cm^{-1}), irreducible representation, and Raman activity for each case. Pink shading marks modes with frequencies in close agreement with experimentally reported Raman peaks

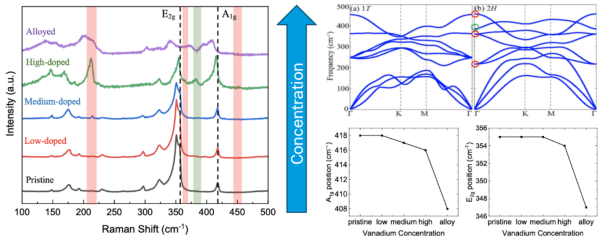

Figure 3: Experimental Raman spectra of pristine, low-doped, medium-doped, high-doped, and alloyed V-WS_2, shown together with the calculated phonon frequencies of 1T- and 2H-VS_2. With increasing vanadium concentration, the E_{2g} and A_{1g} modes progressively soften, and in the alloyed sample their positions approach the characteristic Raman-active modes reported for 2H-VS_2. The comparison supports the presence of 2H-VS_2-like local environments embedded in V-WS_2, consistent with the Raman modes reported by Zhuang *et al.* [2].

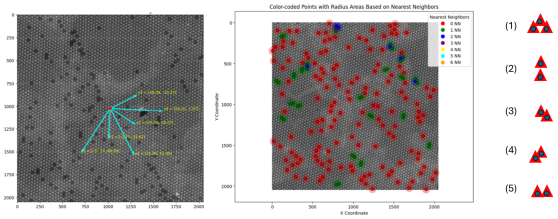

Figure 4: Experimental identification of dopant arrangements in the anisotropic direction. The left panel illustrates the nearest-neighbor construction used to define local coordination around each detected dopant site. The middle panel shows the spatial distribution of dopants, with markers color-coded by the number of nearest neighbors. The right panel summarizes the main types of local configurations observed experimentally, labeled as (1)–(5). The counts extracted from the image show that isolated defects (0 nearest neighbors) dominate, followed by a smaller population of dimers and higher-order local groupings.

References

[1] Bastos, C. M. O.; Besse, R.; Da Silva, J. L. F.; Sipahi, G. M. Ab initio investigation of structural stability and exfoliation energies in transition metal dichalcogenides based on Ti-, V-, and Mo-group elements. *Physical Review Materials* **2019**, *3*. DOI: 10.1103/physrevmaterials.3.044002.

[2] Lin, Z.; Carvalho, B. R.; Kahn, E.; Lv, R.; Rao, R.; Terrones, H.; Pimenta, M. A.; Terrones, M. Defect engineering of two-dimensional transition metal dichalcogenides. *2D Materials* **2016**, *3*, 022002. DOI: 10.1088/2053-1583/3/2/022002.

[3] Togo, A.; Tanaka, I. First principles phonon calculations in materials science. *Scripta Materialia* **2015**, *108*, 1–5. DOI: 10.1016/j.scriptamat.2015.07.021.

[4] Sheremetyeva, N.; Zhang, N.; Sanchez, D. E.; Yu, Z.; Lamparski, M.; Terrones, M.; Meunier, V. Raman Signature of stripe domains in monolayer WXMO1–XS2 alloys. *ACS Applied Materials & Interfaces* **2025**, *17*, 5430–5438. DOI: 10.1021/acsami.4c15937.

Acta Microscopica Vol.35, Supp.1, 2026
Abstract Book NSSY 2026 - Galapagos 17th–23rd May 2026

Exploiting mirage in microscopy to monitor molecular interactions

Niklas Hansen[1,3], Jakub Čopák[2,4], David Roesel[1], Ilko Bald[1,6], Petr Cígler[2], **Vladimíra Petráková**[1,5]

[1] *J. Heyrovský Institute of Physical Chemistry, Czech Academy of Sciences, Dolejškova 3, 182 23 Prague, Czechia*
[2] *Institute of Organic Chemistry and Biochemistry, Czech Academy of Sciences, Flemingovo nam 542/2, 160 00 Prague, Czechia*
[3] *Department of Physical Chemistry, Faculty of Chemical Engineering, University of Chemistry and Technology, Technická 5, 166 28 Prague 6, Czechia*
[4] *Department of Physical and Macromolecular Chemistry, Faculty of Science, Charles University, Hlavova 2030/8, 128 40 Prague 2, Czechia*
[5] *Faculty of Biomedical Engineering, Czech Technical University, Nam. Sítná 3105, 27201 Kladno, Czechia*
[6] *Institut fuer Chemie, Universitat Potsdam, Karl-Liebknecht-Strasse 24-25, 14476 Potsdam, Germany*
vladimira.petrakova@jh-inst.cas.cz

Abstract

Various photonic phenomena rely on precise positioning of photon sources in close configurations with nanometer precision. DNA nanotechnology offers a solution for this, taking advantage of the programmable nature of DNA spatial configuration. Moreover, it offers an opportunity to assemble additional light-modulating elements, like plasmonic nanoparticles, opening new exciting avenues to improve our fundamental understanding of plasmonic interactions. Here, we present a highly adaptable and easy-to-use platform that harnesses DNA nanotechnology to precisely position nanodiamonds containing fluorescent nitrogen-vacancy (NV) centers and plasmonic nanoparticles to investigate the modulations in the position of light emitted by an NV center using superresolution microscopy. NV centers are particularly well-suited for this investigation due to their broad absorption and emission spectra, large Stokes shift, and resistance to photobleaching. To demonstrate the capabilities of our platform, we conducted several case studies in which we varied the distance between nanodiamond and gold nanoparticles, the number of assembled nanoparticles, and the controlled orientation of assembly of asymmetric nanostructures such as gold nanorods. By doing so, we were able to engineer the position of the plasmon resonance that suits preferred applications and needs. We evaluate the plasmonic enhancement mechanism of coupled NV centers and the shifts in their projected position based on the assembly design. Additionally, by demonstrating controlled positioning of diamond nanoparticles containing NV centers, we open routes to use DNA-mediated assembly to improve magnetometry and other applications in the field of quantum optics where NV centers in diamond play a prominent role.

Orbital angular momentum textures and currents in helical molecules

Danny Cordova[1], Bertrand Berche[2], **Ernesto Medina**[1]

[1] *Physics Department, College and Science and Engineering, USFQ, Quito Ecuador*
[2] *Laboratoire de Physique et Chimie Th´eoriques, CNRS - Universit´e de Lorraine, France*
emedina@usfq.edu.ec

Abstract

Recently, models with out-of-equilibrium orbital angular momentum in low-dimensional systems have attracted considerable attention because they do not rely on magnetic or spin-orbit coupling. Building on previous models that exhibit intrinsic inversion asymmetry, we introduce a minimal model based on multiple-orbital Hamiltonians in which orbital angular momentum textures and currents arise intrinsically from the helical/chiral structure. Such textures and currents arise from a non-equilibrium that biases their materialization in the Edelstein scenario. We then compare the pure spin-Edelstein transport with the orbital to spin-coupled transport to argue that the latter is a stronger candidate for non-equilibrium spin injection into the contacts.

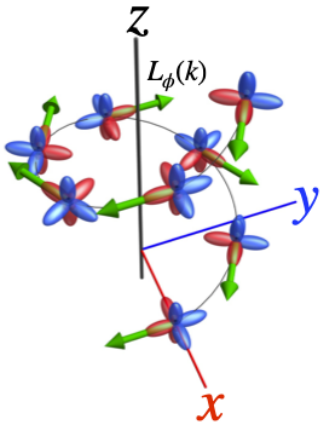

Figure 1: Orbital angular momentum texture for the simplified model where only t_{zr} couplings are present. The only texture present is due to the tangential component. There is no spin-orbit coupling contemplated, only coherences produced by the overlaps enabled by the chiral structure without inversion symmetry.

References

[1] Manchon, G.; Ghosh, S.; Barreteau, C.; Manchon, A. *Phys. Rev. B* **2020**, *101*, 174423.

[2] Yoda, T.; Yokoyama, T.; Murakami, S. *Sci. Rep.* **2015**, *5*, 12024.

[3] Fransson, J. *Phys. Rev. B* **2020**, *102*, 235416.

Acta Microscopica Vol.35, Supp.1, 2026
Abstract Book NSSY 2026 - Galapagos 17th–23rd May 2026

Towards Scalable Quantum Photonics: Diamond Meets AlGaN/AlN Platform

Domenica Bermeo Alvaro[1], Pascal Frehle[2], Grigory Kornilov[2], Ron Rosenberg[2], Marco E. Stucki[1,2], Tim Kolbe[1], Sylvia Hagedorn[1], Markus. Weyers[1], Tommaso Pregnolato[1,2], Tim Schröder[2,1]

[1] *Ferdinand-Braun-Institut (FBH), Gustav-Kirchhoff-Str. 4, 12489 Berlin, Germany*
[2] *Department of Physics, Humboldt-Universität zu Berlin, Newtonstr. 15, 12489 Berlin Germany*
domenica.bermeo@fbh-berlin.de

Abstract

Spin-photon interfaces are crucial for the development of large quantum networks which rely on the generation and distribution of entanglement between their nodes [1]. A highly efficient spin-photon interface can be achieved when diamond color centers are embedded in photonic crystal cavities, which enhance the light-matter interaction in the system and boost the emission rate of photons generated by the coherent zero-phonon-line transition [2]. The diamond substrate allows for the nanofabrication of such devices, as it has been demonstrated by our group before with the fabrication of the so known Sawfish cavity. Still, achieving a monolithic platform that takes advantage of those photonic crystal cavities and that is able to manipulate the emitted photons on a large scale remains a challenge. To overcome these limitations, we propose the hetero-integration of diamond nanostructures into AlGaN-based photonic integrated circuits (PICs). AlGaN/AlN PICs offer a wide transparency window, strong nonlinear and electro-optic properties, and wafer-scale compatibility features that can be exploited to realize low-loss, reconfigurable photonic circuits. For the realization of the hetero-integrated samples, we design a low-loss coupling section between diamond and AlGaN waveguides using finite-element numerical simulations, optimize the fabrication process of AlGaN-based photonic integrated circuits, and hetero-integrate diamond nanostructures via pick-and-place and transfer-printing approaches. Figure 1a shows a schematic of the hetero-integration approach. Finally, we optically characterize the integrated nanostructures. Initial simulations and experimental realizations of the hetero-integrated structures demonstrated the feasibility of the approach with a maximum achieved 57% coupling efficiency [3]. However, for complex quantum applications and therefore complex devices this is not enough. One critical parameter that limits the coupling efficiency is the waveguide sidewall angles which currently is of 75°. In our simulations we have optimize the design for several side wall angles and predict coupling efficiencies of up to 97% for sidewall angles of 90°. To validate our simulated design, diamond waveguides and sawfish cavities, both as individual devices and arranged in chiplets, were fabricated using electron-beam lithography and dry etching, followed by a quasi-isotropic etch to suspend the structures for

transfer. Interrupted AlGaN racetrack resonators were fabricated to enable the placement of diamond waveguides, together with optimization of the fabrication recipe to reduce sidewall angles and enhance coupling efficiency. Optimization of the AlGaN dry etching process improved waveguide sidewall angles from 75° to 82°, and with an additional wet etching step, near-vertical sidewalls were achieved. This optimization will allow us to test higher coupling efficiency designs. Initial placement was performed using a tungsten tip; however, a more scalable integration method based on PDMS transfer-printing stamps was developed by fabricating custom silicon molds for individual PDMS stamps. Figure 1b shows a fabricated diamond chiplet integrated onto the 82° AlGaN platform, demonstrating the feasibility of our hetero-integration approach. Further placement experiments and optical characterization of the coupling sections are ongoing. Still supported by our simulations, we expect high coupling efficiencies. This low-loss hetero-integration strategy represents an important step toward scalable photonic circuits for large-scale quantum networks.

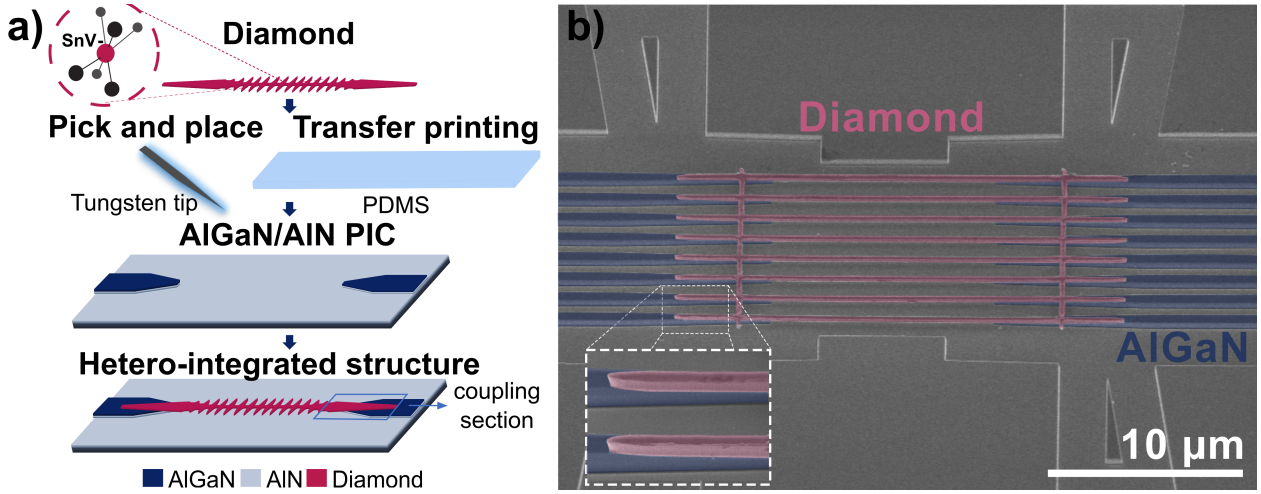

Figure 1: a) Scheme of the hetero-integration process b) SEM image of a diamond waveguide chiplet integrated in an AlGaN/AlN platform.

References

[1] Johannes, B. et al. Quantum networks with deterministic spin–photon interfaces. *Advanced Quantum Technologies* **2019**, *2*, 5–6.

[2] Bopp, J. M. et al. 'Sawfish' photonic crystal cavity for near-unity emitter-to-fiber interfacing in quantum network applications. *Adv. Opt. Mater.* **2023**, *12*, 2301286.

[3] Gündoğdu, S. et al. Hetero-integrated diamond-on-AlGaN/AlN waveguides for optical color center interfacing. **2025**, (accepted for publication in npj Nanophotonics).

Acta Microscopica Vol.35, Supp.1, 2026
Abstract Book NSSY 2026 - Galapagos 17th–23rd May 2026

Bridging Phonon Dispersion Mapping and Junction Nanoelectronics in InP¬ Based Nanowires Using GI-IXS And TERS

V. Hinojosa-Chasiquiza[1], D. A. Chaney[2], S. Bienz[3], I. Mediavilla[1], K. Adham[4], Y. Zhao[4], A. H. Romero[5], M. Borgström[3,6], A. Bosak[2], R. Zenobi[3], N. Kumar[3], J. L. Pura[1], J. Serrano[1,7,8]

[1] *Gds-Optronlab, Dpto. Física de la Materia Condensada, Universidad de Valladolid, Paseo de Belén 19, 47011 Valladolid, Spain*
[2] *European Synchrotron Radiation Facility, BP 220, F-38043 Grenoble, France*
[3] *Department of Chemistry and Applied Biosciences, ETH Zürich, Zurich, Switzerland*
[4] *NanoLund and Division of Solid-State Physics, Lund University, Lund, Sweden*
[5] *Department of Physics and Astronomy, West Virginia University, Morgantown, West Virginia, USA*
[6] *Wallenberg Initiative Materials Science for Sustainability, Division of Solid-State Physics, Lund University, Lund, Sweden*
[7] *Institute of Microelectronics of Barcelona (IMB-CNM, CSIC), Campus UAB, 08193 Bellaterra, Barcelona, Spain*
[8] *Meeting Life LLC, 1210 Washington Ave. Ste. 213, Miami Beach, Florida 33139, USA*
vanessagiselle.hinojosa@uva.es

Abstract

Nanostructured III–V semiconductor nanowires (NWs) have emerged as a promising platform for next-generation photovoltaic devices, particularly for tandem solar cells designed to surpass the Shockley–Queisser efficiency limit of single-junction silicon [1]. Their quasi-one-dimensional geometry enables efficient strain relaxation, bandgap engineering through axial and radial heterostructuring, and the integration of multiple subcells with complementary absorption spectra on silicon-compatible substrates [2]. However, achieving high-efficiency NW tandem photovoltaics critically depends on understanding and controlling lattice dynamics, which govern carrier scattering and thermalization, and the electronic quality of axial junctions, which determine recombination, series resistance, and tunneling efficiency [3]. Experimentally resolving these effects remains challenging, as the relevant physics spans both reciprocal space (phonon dispersion and lifetimes) and real space (morphology and local carrier density) at length scales well below the optical diffraction limit.

Here, we present a multiscale characterization framework that combines grazing-incidence inelastic x-ray scattering (GI-IXS), *ab initio* lattice-dynamical modelling, and tip-enhanced Raman spectroscopy (TERS) to probe vibrational and electronic properties in InP-based NW systems relevant to photovoltaic applications. While the two case studies address different crystal phases and heterostructure configurations, together they demonstrate how advanced characterization tools can be deployed synergistically to resolve nanoscale structure–property relationships that directly impact device performance.

In the first case study, we employ GI-IXS to experimentally resolve phonon dispersion relations in the wurtzite (WZ) phase of InP NWs, a crystal structure stabilized only at the nanoscale. A grazing-incidence geometry combined with high-resolution monochromation (Figure 1a) enables selective sensitivity to NW vibrational excitations while minimizing substrate contributions. *Ab initio* phonon dispersion relations calculated using density-functional perturbation theory (Figure 1b) provide a quantitative framework for interpreting the experimental data. Representative GI-IXS spectra acquired at selected momentum transfers along the Γ–M direction (Figure 1c–d) resolve multiple low-energy vibrational modes. By combining these spectra across reciprocal space, we extract the experimental phonon dispersion of WZ InP nanowires (Figure 1e). The measured dispersion shows excellent agreement with theoretical predictions, providing the first experimental validation of lattice-dynamical models for this nano-stable phase and demonstrating that GI-IXS enables momentum-resolved phonon spectroscopy in nanostructured materials with high energy and momentum resolution.

In the second case study, we focus on nanoelectronic junctions in zincblende (ZB) InP/InGaP axial heterostructure NWs engineered for tandem photovoltaic devices. Hyperspectral TERS is employed to probe p/p^{++} and p^{++}/n^{++} tunnel junctions with nanometer-scale spatial resolution. TERS exploits localized plasmonic field enhancement at the apex of a metallic AFM tip (Figure 2a). A representative near-field Raman spectrum (Figure 2a, inset) highlights characteristic vibrational modes and a phonon–plasmon coupled mode (L_1). Spatially resolved TERS mapping across the two axial interfaces (Figure 2b) reveals that junctions nominally designed as abrupt are in fact compositionally and electronically graded over finite lengths. Importantly, the phonon–plasmon coupled L_1 mode acts as an internal nanoscale probe of free-carrier concentration, enabling direct differentiation between electronic transition widths and chemically defined interfaces traced by alloy-sensitive transverse optical modes. These measurements demonstrate that electronic junction profiles extend differently from chemical transitions, providing direct nanoscale evidence of junction grading inaccessible to far-field optical or purely topographic techniques.

To assess the electronic implications of the experimentally measured junction profiles, band-edge simulations and Wentzel–Kramers–Brillouin tunneling probability calculations are performed using transition widths extracted from TERS. Rather than aiming to predict absolute device currents, these calculations quantify the dependence of tunneling probability on the interfacial transition length. The results reveal a systematic decrease in tunneling probability with increasing junction grading, consistent with the formation of an extended transition compared to an ideal abrupt junction. This trend highlights the strong sensitivity of carrier transport to nanoscale junction morphology. It underscores the importance of quantitatively resolving buried interface profiles when evaluating tunnel-junction quality in NW tandem photovoltaic architectures.

In conclusion, GI-IXS enables direct access to phonon dispersion relations in nano-stable crystal phases such as WZ InP, and TERS provides non-destructive, nanoscale mapping of electronic and chemical transitions at junctions in ZB InP/InGaP. Together, these complementary approaches bridge reciprocal-space lattice dynamics and real-space nanoelectronics, establishing a powerful experimental toolbox for advanced materials processing and characterization, and for the rational design of next-generation nanowire-based tandem photovoltaics beyond the efficiency limits of conventional silicon solar cells.

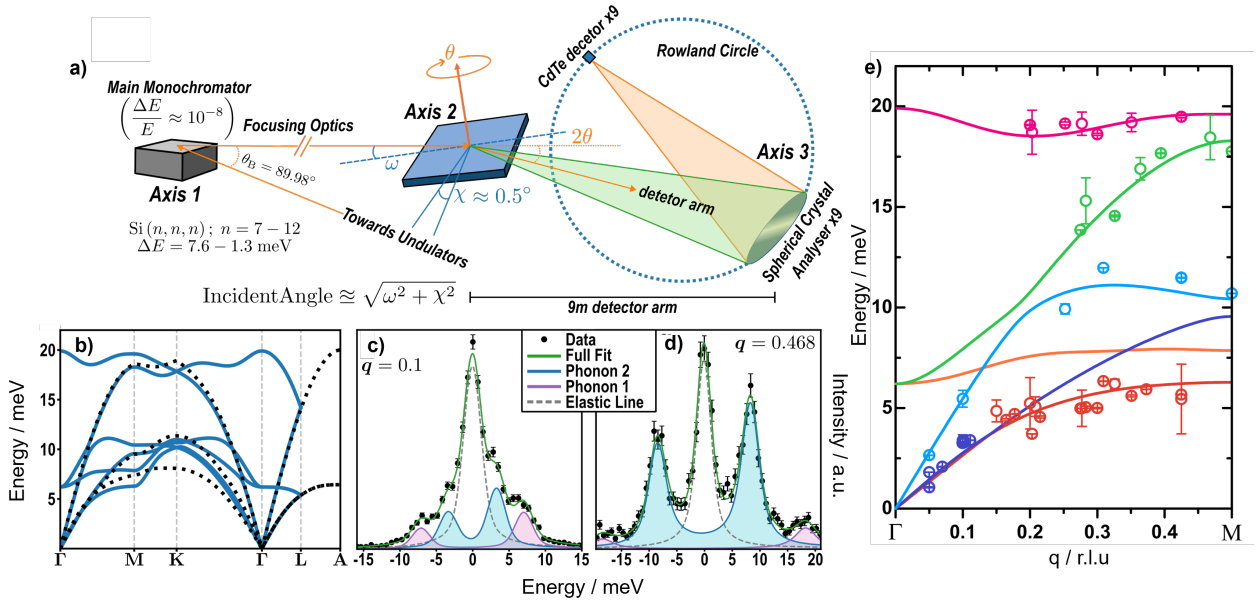

Figure 1: Grazing-incidence inelastic x-ray scattering of wurtzite InP nanowires. a) Schematic of the GI-IXS experimental geometry and high-resolution monochromator setup, illustrating the grazing-incidence illumination and momentum-resolved detection used to selectively probe nanowire vibrational excitations. b) *Ab initio* phonon dispersion relations of the wurtzite phase of InP calculated using density-functional perturbation theory along high-symmetry directions of the wurtzite Brillouin zone. c-d) Representative GI-IXS spectra acquired at selected momentum transfers along the Γ–M direction, showing multiple resolved low-energy vibrational modes of the nanowires. e) Experimentally extracted phonon dispersion of wurtzite InP nanowires along the Γ–M direction. *Ab initio* calculated dispersion is shown as coloured lines, while experimentally extracted phonon energies are shown as open coloured circles. Error bars represent the half width at half maximum (HWHM) of the fitted phonon linewidths.

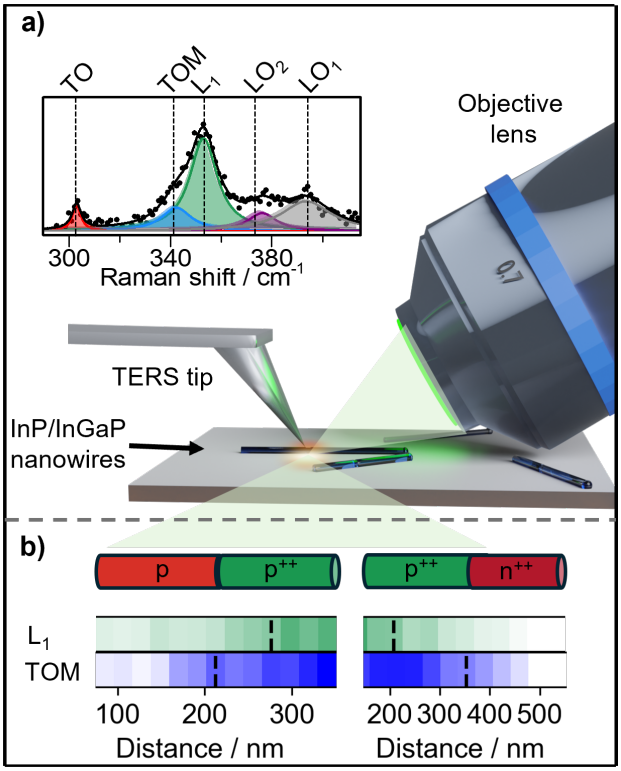

Figure 2: Nanoscale TERS characterization of buried axial junctions in the tunnel diode of zincblende InP/InGaP nanowire heterostructures. a) Schematic of the tip-enhanced Raman spectroscopy (TERS) setup used for nanoscale vibrational mapping. Inset: representative TERS spectrum acquired in the InGaP segment, with vibrational modes highlighted, including the phonon–plasmon coupled L_1 mode and composition-sensitive modes. b) Spatially resolved TERS intensity maps across the two axial junctions of the nanowire: p/p^{++} (left) and p^{++}/n^{++} (right). Colour maps show the integrated intensity of the L_1 mode (electronic transition) and the TOM mode (chemical transition), revealing distinct electronic and compositional transition widths at each interface. The data demonstrate that electronic junction profiles extend differently from chemically defined interfaces, providing direct nanoscale evidence of junction grading.

References

[1] Anttu, N. Shockley–Queisser detailed balance efficiency limit for nanowire solar cells. *ACS Photonics* **2015**, *2*, 446–453. DOI: 10.1021/ph5004835.

[2] Borgström, M. T.; Wallentin, J.; Heurlin, M.; Fält, S.; Wickert, P.; Leene, J.; Magnusson, M. H.; Deppert, K.; Samuelson, L. Nanowires with promise for photovoltaics. *IEEE Journal of Selected Topics in Quantum Electronics* **2010**, *17*, 1050–1061. DOI: 10.1109/jstqe.2010.2073681.

[3] LaPierre, R. R.; Chia, A. C. E.; Gibson, S. J.; Haapamaki, C. M.; Boulanger, J.; Yee, R.; Kuyanov, P.; Zhang, J.; Tajik, N.; Jewell, N.; Rahman, K. M. A. III–V nanowire photovoltaics: Review of design for high efficiency. *physica status solidi (RRL) - Rapid Research Letters* **2013**, *7*, 815–830. DOI: 10.1002/pssr.201307109.

Friday

Biomedical Applications of Carbon Nanomaterials

Silvia Giordani[1]

[1] *Dublin City University, School of Chemical Sciences*
silvia.giordani@dcu.ie

Abstract

Carbon nanomaterials have emerged as a highly versatile class of materials with transformative potential in biomedicine. This tutorial lecture provides an overview of the key carbon nanomaterial platforms, including carbon nanotubes, graphene derivatives, and fullerenes, and their biomedical applications, with a particular focus on carbon nano-onions (CNOs).

CNOs, also known as multi-layer fullerenes, are an exciting class of nanostructures that show great versatility and applicability across several fields of technology and biomedicine. Consisting of multiple concentric layers of sp^2 hybridized carbon, CNOs are emerging as platforms for biomedical applications owing to their ability to be internalised by cells and their low toxicity.

This lecture will cover the synthesis and chemical functionalisation strategies developed to tailor CNO surface properties, including modification with different functional groups and conjugation with molecules such as fluorophores, which enhances water solubility, biocompatibility, and cell penetration capability. Key biomedical applications will be discussed, including their use as multimodal imaging probes for bioimaging, exploiting their cell-penetration properties and minimal systemic toxicity, as well as their promise as nanocarriers for targeted drug delivery and cancer therapy. Recent advances in boron/nitrogen co-doped CNOs as next-generation nanocarriers, combining aqueous dispersibility and biocompatibility, will also be highlighted.

Attendees will gain a comprehensive understanding of the unique physicochemical properties that make CNOs a compelling platform for the development of novel theranostic and healthcare technologies.

Cyanobacteria–Nanoparticle Biohybrid Systems: Toward Enhanced Energy Production and Agricultural Applications

Yolanda Angulo[1] et al

[1] *Centro de Nanociencia y Nanotecnología; Universidad de las Fuezas Armadas ESPE; Sangolqui-Ecuador*
yrangulo@espe.edu.ec

Abstract

The development of biohybrid systems integrating nanomaterials with photosynthetic organisms represents an emerging research direction with high potential to address global challenges in sustainable energy production and next-generation agriculture. This work presents a nano–bio platform based on the green synthesis of metallic nanoparticles of gold, silver, palladium, and copper, and their functional integration into cyanobacteria with the aim of enhancing their energy-related performance.

The controlled incorporation of metallic nanoparticles into cyanobacteria led to the enhancement of photosynthetic processes and electron transfer pathways, resulting in a significant increase in the energy output of the biohybrid system. These findings demonstrate how Nano-to-Bio interface engineering can generate new energy-related functionalities in living systems, establishing a solid foundation for the development of advanced bioenergy platforms.To advance toward functional and scalable architectures, this project explores the fabrication of structured biohybrid systems through 3D printing of nanoparticle-doped cyanobacteria. This research line, currently supported by a nationally funded project in Ecuador, seeks to integrate principles from nanotechnology, synthetic biology, and materials engineering to develop reproducible and adaptable bioenergy systems suitable for diverse technological contexts.

In a complementary approach, the application of these biohybrid systems in agriculture is evaluated, where cyanobacteria–nanoparticle interactions showed positive effects on plant growth and performance, suggesting their potential use as advanced bioinputs for crop improvement. Overall, this work proposes a versatile and evolving biohybrid platform with clear opportunities for further optimization through modeling approaches, advanced characterization techniques, and technological scale-up. The interdisciplinary nature of the proposed system opens a strategic space for international collaborations focused on the joint development of sustainable solutions in energy and agriculture, particularly within the framework of global Nano-Bio research initiatives.

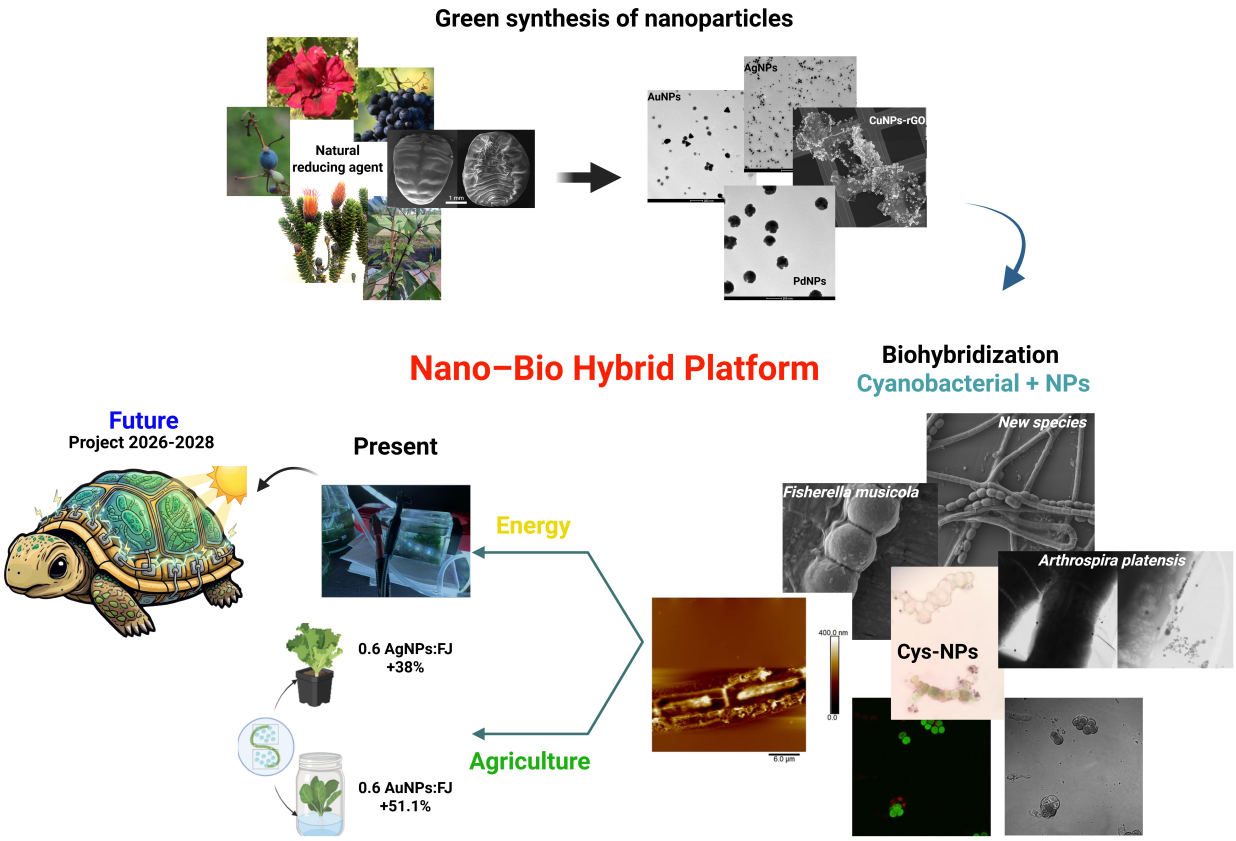

Figure 1: Nano–Bio Hybrid Platform: schematic representation of a biohybrid system based on green-synthesized metallic nanoparticles integrated into cyanobacteria, enabling enhanced energy production as the core functionality and complementary agricultural applications.

Mechanical Properties of Fuctionalized Chitosan Biofilms

Julio C. Chacón-Torres[1], Jennifer Andrango[2], Victor Hugo Guarochico Moreira[3], Julio Alberto Cáceres Zambrano[4], Carlos Andrés Cuenca Cabrera[5], Carlos Loyo[6]

[1]*School of Physical Sciences and Nanotechnology, Yachay Tech University, Urcuqui, 100119, Imbabura, Ecuador*
[2]*School of Biological Sciences and Engineering, Yachay Tech University, Urcuqui, 100119, Imbabura, Ecuador*
[3]*Facultad de Ciencias Naturales y Matemáticas, Escuela Superior Politécnica del Litoral, ESPOL, Campus Gustavo Galindo, Km. 30.5 Vía Perimetral, Guayaquil, 090902, Ecuador*
[4]*Facultad de Ingeniería en Mecánica y Ciencias de la Producción, Centro de Investigación y Desarrollo en Nanotecnología, Escuela Superior Politécnica del Litoral, ESPOL, Campus Gustavo Galindo, Km. 30.5 Vía Perimetral, Guayaquil, 090902, Ecuador*
[5]*Facultad de Ingeniería en Mecánica y Ciencias de la Producción, Escuela Superior Politécnica del Litoral, ESPOL, Campus Gustavo Galindo, Km. 30.5 Vía Perimetral, Guayaquil, 090902, Ecuador*
[6]*School of Chemical Sciences and Engineering, Yachay Tech University, Urcuquí, 100119, Imbabura, Ecuador*
jchacon@yachaytech.edu.ec

Abstract

Chitosan is one of the most used biopolymers due to its attractive properties, including availability, biodegradability, biocompatibility, low toxicity, and ease of chemical modification[1]. Its versatility allows it to be applied across both industrial and biomedical fields in various physical forms, such as hydrogels, nanofibers, and films[2]. However, chitosan's brittleness and moisture sensitivity hinder its feasibility to be used for film packing applications[3]. To address these limitations, our study explores the interfacial functionalization and cross-linking of chitosan with fillers such as graphite, graphene oxide, and silver nanoparticles.

In this work, chitosan based four nanostructured composite films (CNC) were synthesized via solvent casting method: (1) chitosan - Cs, (2) chitosan/graphite - Cs/G, (3) chitosan/graphene oxide Cs/GO, and (4) chitosan with silver nanoparticles - CS/AgNP. Homogeneous films were obtained on petri-dishes (15 cm diameter) allowed to dry in an extraction chamber at room temperature for 24 hours. Tensile stress studies were further conducted in rectangles cut from the film (see Fig. 1 a). SEM analysis shows structural variations on the fracture surfaces, showing rough and homogeneous areas oriented along the cross section of the film as see in Fig. 1 b for Cs/GO. We found the filler homogeneity to be a critical factor to maximize the load transfer, mechanical strength, and dimensional stability of the films.

The tensile stress results are presented in Figure 2 a-b, illustrating the differences in the Young's modulus, and the tensile strength respectively, as a function of the filler. This systematic approach not only improves understanding of mechanical behaviour in this biomaterial, but also provides novel information about how different fillers influence the lifetime and stability of chitosan films.

By studying these parameters, we have established a clear design criterion, minimizing variability between samples and ensuring reproducibility of mechanical and functional properties. Through a detailed analysis of the tensile behaviour and

polymer-nanofiller interactions, this study provides both quantitative and qualitative insights into the mechanical and physico-chemical performance of CNC materials. Our research addresses applications in both industrial and biomedical contexts, including food packaging, active coatings, wound dressings and bandages, and scaffolds for cell regeneration. These findings lead to the design of stronger, more functional, and more sustainable films, contributing to the creation of innovative biomaterials with high-performance suitable for industrial and biomedical applications.

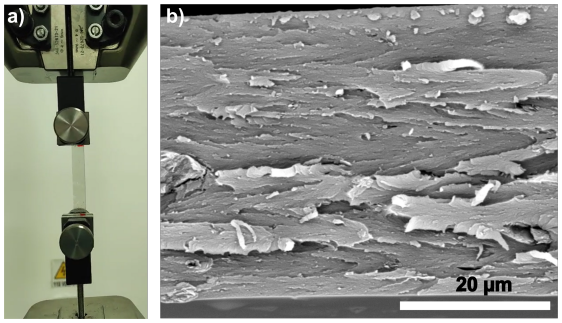

Figure 1: Mechanical testing and morphological analysis. a) Universal strain analysis of a chitosan/ graphene oxide (Cs/GO) sample during the initial tensile test. b) SEM micrograph of the cross-sectional area of the CNC Cs/GO sample after fracture.

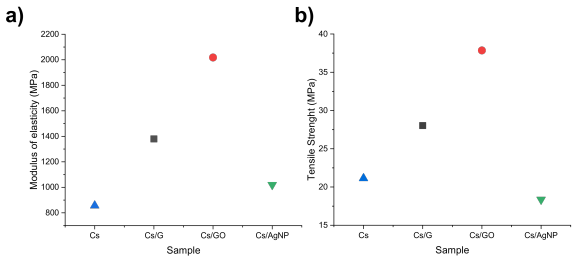

Figure 2: Young's modulus and tensile strain analysis. a) Young's modulus as a function of sample tested. b) Tensile strength as a function of sample tested. In both cases the strongest response is shown when GO is used as a filler on the CNC.

References

[1] Kluczka, J. Chitosan: Structural and chemical modification, properties, and application. *International Journal of Molecular Sciences* **2023**, *25*, 554.

[2] Wardhono, E. Y.; Pinem, M. P.; Susilo, S.; Siom, B. J.; Sudrajad, A.; Pramono, A.; Meliana, Y.; Guénin, E. Modification of physio-mechanical properties of chitosan-based films via physical treatment approach. *Polymers (Basel)* **2022**, *14*, 5216.

[3] Reddy, M. M.; Vivekanandhan, S.; Misra, M.; Bhatia, S. K.; Mohanty, A. K. Biobased plastics and bionanocomposites: Current status and future opportunities. *Progress in Polymer Science* **2013**, *38*, 1653.

Acta Microscopica Vol.35, Supp.1, 2026
Abstract Book NSSY 2026 - Galapagos 17th–23rd May 2026

Physicochemical Stability and Preliminary Biocompatibility of Geraniol-Loaded SNEDDS Nanoemulsions

Ochoa-Rodríguez Laura Raquel[1], Mauricio Sánchez Reina Araceli[1], Bravo-Alfaro Diego Alberto[2], Sumoza-Toledo Adriana[3], Luna-Bárcenas Gabriel[2], Mendoza-Galván Arturo[1]

[1] *Cinvestav Unidad Querétaro. Polymers and biomaterials Laboratory*
[2] *Tecnologico de Monterrey. Institute of Advanced Materials for Sustainable Manufacturing*
[3] *Universidad Veracruzana. Instituto de Investigaciones Médico Biológicas*
laura.ochoa@cinvestav.mx

Abstract

In this study, the stability of nanoemulsions prepared from two self-nanoemulsifying drug delivery system (SNEDDS) formulations with geraniol:surfactant ratios of 1:6 (T1) and 1:2.25 (T2) was evaluated over an eight-week period, using different water concentrations. The surfactants employed were Cremophor EL, Labrafil M1944CS, and Labrasol, which are commonly used in lipid-based delivery systems due to their emulsifying efficiency and biocompatibility. Physicochemical characterization was carried out by Fourier-transform infrared (FTIR) spectroscopy, analyzing both the pure components and the formulated nanoemulsions. For the stability study, samples of each nanoemulsion stored in glass vials were collected and analyzed at three different heights (top, middle zone, and bottom) in order to identify potential signs of system destabilization. Based on the chemical structures of the components used, the functional groups responsible for absorption in the infrared region were identified [1], which enabled the monitoring of specific spectral bands to evaluate nanoemulsion stability, even before the appearance of visible phase separation. The results indicated that nanoemulsions formulated with the T1 ratio remained stable throughout the entire study period when the water content was equal to or greater than 30%. In contrast, the T2 formulation exhibited lower stability, as nanoemulsions with a water content equal to or less than 43% showed significant differences in their FTIR spectra from the second week of storage onward, which coincided with the visual appearance of two phases. These results demonstrate that the geraniol:surfactant ratio plays a determining role in the physicochemical stability of nanoemulsions obtained from SNEDDS, highlighting the importance of formulation optimization during the early stages of system design. Spectroscopic analysis confirmed that the lower phase of the unstable nanoemulsions corresponded to a polyethylene glycol–water mixture [2], suggesting a preferential redistribution of the hydrophilic components of the system and a disruption of the original nanoemulsion structure. Likewise, in nanoemulsions that exhibited phase separation, the possible migration of the bioactive compound (geraniol) toward the surface of the nanoemulsion was monitored. This behavior was attributed to its lower density relative to water and was evidenced by tracking two characteristic absorption bands

of the compound. These results highlight the sensitivity of FTIR as a tool for the early detection of instability in nanoemulsions and its potential application as a complementary technique for stability assessment. To advance the biological evaluation, formulation T1, which exhibited the highest stability, was selected, and a qualitative cytotoxicity assessment was performed by fluorescence microscopy using the non-tumoral MCF-10A cell line. Nanoemulsions containing geraniol concentrations in the range of 1 to 100 μM were analyzed, along with the pure compound and the surfactant mixture. No signs of cell death were observed in any of the evaluated treatments, indicating a favorable preliminary biocompatibility profile and supporting the continuation of the biological evaluation of these systems as promising platforms for the delivery of bioactive compounds in pharmaceutical and biomedical applications.

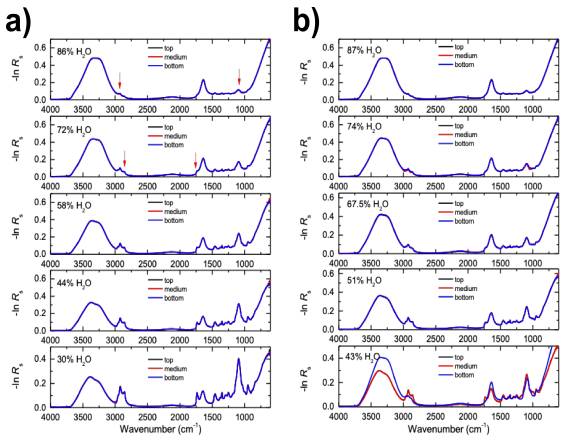

Figure 1: FTIR spectra of samples taken at different depths (height) of T1 and T2 NE with different water content: (a) T1 after storing for 8 weeks. (b) T2 after storing for 8 weeks.

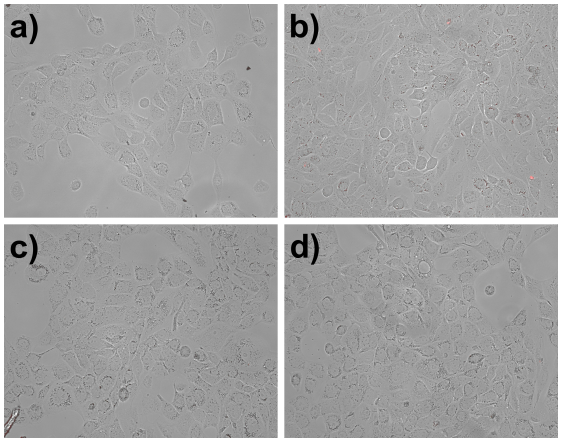

Figure 2: Fluorescence microscopy images of MCF-10A cells under different treatments: (a) untreated control; (b) pure geraniol (100 μM); (c) surfactant mixture; and (d) nanoemulsion (NE) containing 100 μM geraniol.

References

[1] Colthup, N.; Daly, L.; Wiberley, S., *Introduction to Infrared and Raman spectroscopy*, 3rd ed.; Academic Press, Inc.: San Diego, 1990.

[2] Rozenberg, M.; Loewenschuss, A.; Marcus, Y. IR spectra and hydration of short-chain polyethyleneglycols. *Spectrochimica Acta - Part A: Molecular and Biomolecular Spectroscopy* **1998**, *54*, 1819–1826. DOI: 10.1016/S1386-1425(98)00062-6.

2D Materials: Challenges and Opportunities in a Quantum World

Humberto Terrones[1]

[1] *Rensselaer Polytechnic Institute Physics, Applied Physics and Astronomy Department 110 Eighth Street, Troy, NY 12180*
terroh@rpi.edu

Abstract

In this talk I will describe the mean features which make 2D materials a great platform for future quantum devices emphasizing their role in quantum optical systems. I will discuss monolayer hexagonal boron nitride (hBN) as single photon emitter (SPE) and the challenges for defect control and coherence; hBN can exhibit spin defects which need to be structured and generated at will to have applications. I will talk about the possibilities of transition metal dichalcogenides (TMDs) and their Moiré arrangements as nonlinear optics platforms such as second harmonic generation (SHG), parametric down conversion, higher harmonics, entanglement, excitons and excitons coupled with light (exciton-polaritons), thus enriching the field of quantum nonlinearities for novel quantum applications.

Going beyond the classical view of cat-ions

Andrea Chimarro[1], Jean Villa[1], Romel Guañuna[1], Brayan Maisincho[1], María Belen Canchig[1], **Thibault Terencio**[1]

[1] *CaTS Research group, School of Chemical Sciences Engineering, Yachay Tech University, Urcuqui 100119, Ecuador*
tthibault@yachaytech.edu.ec

Abstract

Cations, beyond suggesting the name of a cute animal, is coming from the Greek origin kation meaning "going down". The term ion, introduced by the physicist and chemist Michael Faraday in 1834, involves the idea of moving. In chemistry, cations (alkali and alkaline-earth metals) are in general thought to have only little influence, apart from the charge that they bring, and their inherent size. In fact, almost the entirety of its ability to interact can be summarized as electrostatic interactions. This apparent simplicity of action has a consequence: chemists tend to forget their specific presence in various fields. In materials chemistry or nanoscience, they are also easily overlooked except for considering the possible interaction of negative guests within a structure. Even in high quality scientific articles, cations or anions present are not always precisely reported, quantified or characterized. But, in this research we bring light to a fundamental question: is it really true that cations do not matter so much? Interestingly, over recent years the focus has been more and more displaced on these "innocent" species. Since these do not normally fall into the range of covalent bonds where electrons are shared, they are the best representatives of Non Covalent Interactions (NCI). For example, the incorporation of cations within catalysts takes a growing importance recently in catalyst design or Lithium batteries. While more and more lithium and potassium ions are incorporated to increase efficiency and sometimes to lead to surprising properties, their effect is not entirely known and remains challenging to understand. Our strategy to tackle this problem has been simple: theoretical and computational chemistry calculations allow to acquire deeper insights on the effect of cations, directly looking at electronic distribution. Our approach is to use all methods in our quantum chemistry toolbox (DFT, TDDFT, post-HF, orbitals or ELF function) to observe precisely the effect of cations on electronic clouds, to provide precise clues to the experimental side. In this presentation, we intend to showcase different systems where cations can be designated as direct culprit for a big change of properties : 1) how cations can influence the luminescent properties of a natural polymer 2) how their presence can affect hydrogen bonding in general 3) how cations can affect the electronic distribution in the context of N_2 activation 4) if neighboring cations can affect even absorption/emission of light or even spin state. The conclusions are drawn mainly from the orbitals and the electron localization function (ELF) in the presence of cations. In every case, surprising phenomena appear upon detailed inspection. This information acquired is intended to be used to suggest specific cations for

specific applications, in the design of new catalysts, materials or nano-objects. We intend to respond to questions such as: How changes the structure of a polymer with lithium? [1] Which cation is the most capable of affecting hydrogen bonding? [2] Which cation would be most promising to facilitate N_2 activation? [3] Is it possible to modulate absorption and emission of light differentially? Our takeaway information for every scientist is that cations should not be completely overlooked as they are guilty of strange behaviors, thus, we strongly suggest to quantify them in all works. In the quantum realm, cations could be more interesting than just point charge and can induce a reorganization of neighboring electronic clouds, and why not, a change in the dynamic deformation of these clouds.

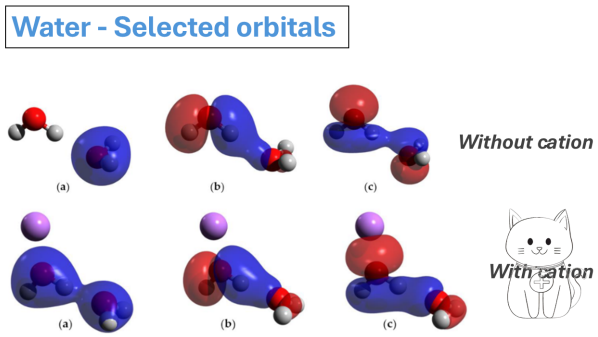

Figure 1: The effect of the cation presence on H-bond of water dimer through orbital view (3 selected orbitals).

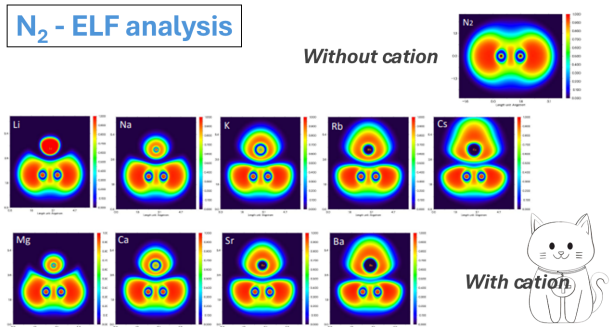

Figure 2: The effect of the cation presence (Li, Na, K, Rb, Cs, Mg, Ca, Sr, Ba) on nitrogen electronic cloud through Electronic Localization Function (ELF).

References

[1] Gurumendi, M.; López, F.; Borrero-González, L. J.; Terencio, T.; Caetano, M.; Reinoso, C.; González, G. Enhanced chitosan photoluminescence by incorporation of lithium perchlorate. *ACS Omega* **2023**, *8*, 13763–13774. DOI: 10.1021/acsomega.2c08072.

[2] Chimarro-Contreras, A.; Lopez-Revelo, Y.; Cardenas-Gamboa, J.; Terencio, T. Insights into the Effect of Charges on Hydrogen Bonds. *International Journal of Molecular Sciences* **2024**, *25*, 1613. DOI: 10.3390/ijms25031613.

[3] Villa-Arpi, J. C.; Guañuna, R.; Saucedo-Vazquez, J. P.; Terencio, T. Neighboring alkali cations as an efficient strategy for N2 activation: a DFT analysis. *International Journal of Molecular Sciences* **2026**, *27*, 1311. DOI: 10.3390/ijms27031311.

Acta Microscopica Vol.35, Supp.1, 2026
Abstract Book NSSY 2026 - Galapagos 17th–23rd May 2026

Monday

Poster Session

Acta Microscopica Vol.35, Supp.1, 2026
Abstract Book NSSY 2026 - Galapagos 17th–23rd May 2026

Electrochemically activated carbon nanostructures as nano-enhancers for phase change materials in sustainable thermal management systems: experimental and simulation analysis

Maria A. Sandoval-Riofrio, **Andres Chico-Proaño**, Juan Francisco Nicolalde, Javier Martinez-Gómez

[1] *School of Computing and Engineering, Talbot Campus, Bournemouth University, Fern Barrow, Poole BH12 5BB, UK*
[2] *Departamento de Ingeniería Química, Escuela Politécnica Nacional, Ladrón de Guevara E11-253, Quito EC170525, Ecuador*
[3] *Departamento de teoría de la señal y comunicación, (Área de Ingeniería Mecánica), Universidad de Alcalá, Escuela Politécnica, 28805 Alcalá de Henares, Madrid, España*
[4] *Facultad de Ingenierías Aplicadas y Desarrollo Industrial, Universidad Internacional Del Ecuador UIDE, Quito 170411, Ecuador*
[5] *Facultad de Arquitectura e Ingenierías, Universidad Internacional SEK, Albert Einstein s/n and 5th, Quito 170302, Ecuador*
andres.chico@epn.edu.ec

Abstract

The present research manuscript explores the synthesis and thermophysical optimization of composite materials based on Organic Phase Change Materials (OPCMs) integrated into Activated Carbon (AC) matrices. The core of this study falls within the Nanostructured Materials category as it investigates the confinement effects and interfacial interactions occurring within the high-surface-area nanoporous structure of the carbonaceous scaffold.

This work addresses the critical transition from bulk organic materials to high-performance composites, specifically targeting the enhancement of thermal conductivity and the prevention of liquid-phase leakage. According to the literature, the development of these composites relies on the "capillary forces and surface tension provided by the nanostructured pores of the carbon support to stabilize the PCM during phase transition" [1].

Furthermore, the manuscript evaluates the integration of these composites into Thermal Energy Storage (TES) and Cold Thermal Energy Storage (CTES) systems. By analyzing the synergistic effect between the OPCM and the AC, the research demonstrates that "the thermal performance of carbon-based PCM composites is dictated by the pore size distribution and the resulting interconnected thermal pathways at the nanoscale" [2]. This structural and morphological analysis at the nano-to-micro scale justifies its classification under the domain of advanced nanostructured materials for energy applications.

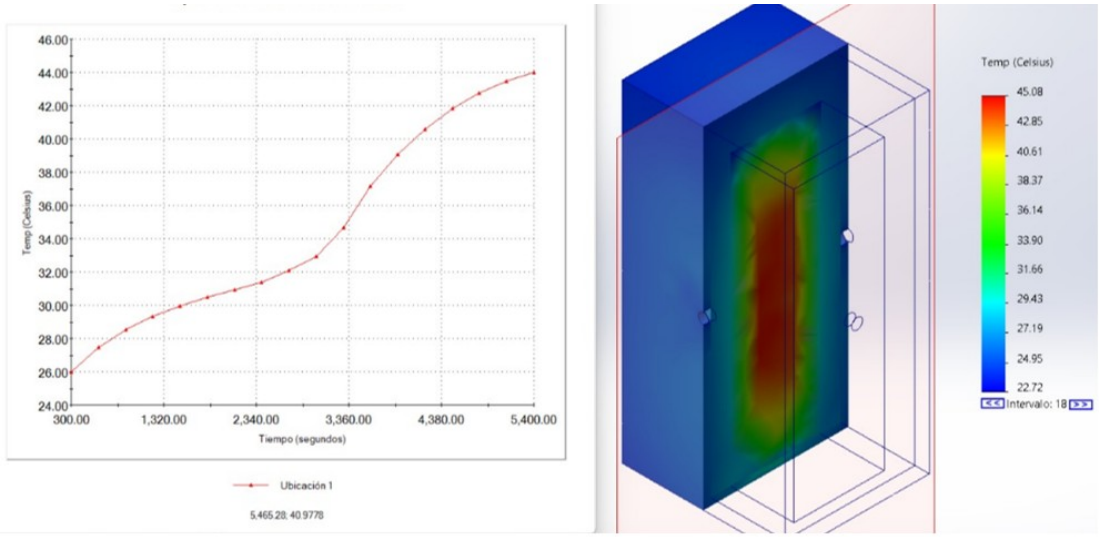

Figure 1: Simulation in a range of 24°C and 45°C during 1.5 hours with PS parameter as OPCM

References

[1] Yuan, Y.; Zhang, N.; Li, T.; Cao, X.; Long, W. Thermal performance enhancement of palmitic-stearic acid by adding graphene nanoplatelets and expanded graphite for thermal energy storage: A comparative study. *Energy* **2016**, *97*, 488–497. DOI: 10.1016/j.energy.2015.12.115.

[2] Sarier, N.; Onder, E. Organic phase change materials and their textile applications: An overview. *Thermochimica Acta* **2012**, *540*, 7–60. DOI: 10.1016/j.tca.2012.04.013.

Acta Microscopica Vol.35, Supp.1, 2026
Abstract Book NSSY 2026 - Galapagos 17th–23rd May 2026

Antibacterial Properties of Nanostructured Chitosan Biofilms

Jeniffer L. Andrango Quinga[1], Carlos Loyo[2], Maria Gabriela Ruiz Hinojosa[1], Julio C. Chacón-Torres[3]

[1]*School of Biological Sciences and Engineering, Yachay Tech University, Urcuquí, 100119, Imbabura, Ecuador*
[2]*School of Chemical Sciences and Engineering, Yachay Tech University, Urcuquí, 100119, Imbabura, Ecuador*
[3]*School of Physical Sciences and Nanotechnology, Yachay Tech University, Urcuquí, 100119, Imbabura, Ecuador*
jeniffer.andrango@yachaytech.edu.ec

Abstract

Chitosan is one of the most recently studied biopolymers due to its unique characteristics, such as biocompatibility, biodegradability, low toxicity, and antimicrobial activity [1]. These properties make chitosan effective for multiple biomedical applications and potential sustainable biomaterials development [2]. Its antibacterial response attracted special interest in the scientific community because the actual mechanism for the inhibition activity is not yet fully understood [3]. The main objective in this work is to disclose the fundamental principles behind the antibacterial response reported for chitosan through physical-chemical analysis of pristine and nanostructured chitosan biofilms (CNC).

Four nanostructured CNCs were developed using the solvent casting method as part of our research: (1) pristine chitosan - Cs, (2) chitosan/graphite - Cs/G, (3) chitosan/graphene oxide Cs/GO, and (4) chitosan with silver nanoparticles - CS/AgNP. The antibacterial activity was assessed by the inhibition halo test (antibiogram) for two bacterial strains: Staphylococcus aureus and Escherichia coli. After incubating at 37°C for 24 hours, the AgNP CNC showed the highest antibacterial response for both strains, with S. aureus having a larger zone of inhibition (ZOI) compared to E. coli (see Fig. 1a and 1b). SEM analysis reveals the morphological differences between the pristine matrix and the matrix filled with AgNP (Fig. 2a and 2b, respectively), suggesting that the microstructural changes could enhance AgNP-bacteria interactions and enhance inhibition activity.

The systematic analysis of the nanostructured biofilm molecular interactions of chitosan uncovered unknown conditions that are crucial for comprehending the impact of the chitosan's nanostructure and its antibacterial response. For instance, the antibacterial response of chitosan depends on preserving the intrinsic chitosan molecular structure on a film, the molecular filler used along the nanostructured composite formation, and the presence of antibacterial agents within the biofilm matrix. This study presents ground-breaking experimental evidence of the action mechanism responsible for the bacteriostatic/bactericidal properties of chitosan films and their derivatives. Our research addresses practical applications in medicine, food preservation, and environmental sanitation, including antibacterial coatings, wound dressings, and food packaging. These findings lead to optimiz-

ing the antimicrobial activity of chitosan-based materials to develop effective and sustainable alternatives to conventional antibacterial advanced materials.

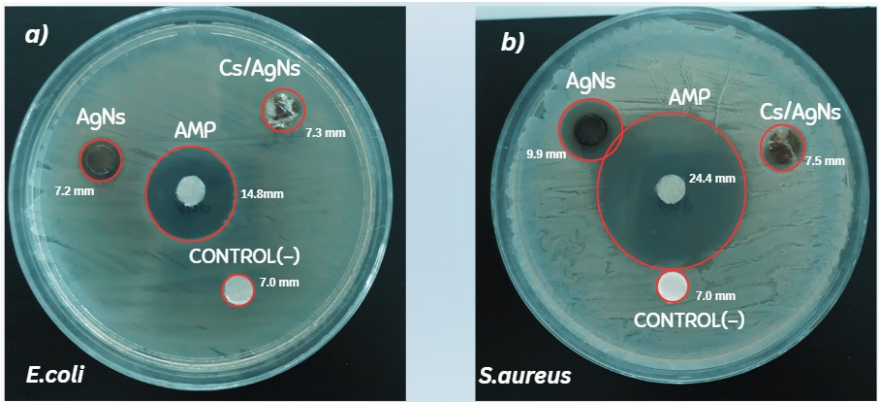

Figure 1: Antibacterial activity assessment. a) Inhibition halo test for chitosan with silver nanoparticles compared to pristine silver nanoparticles against E. coli b) Inhibition halo test for chitosan with silver nanoparticles compared to pristine silver nanoparticles against S. aureus.

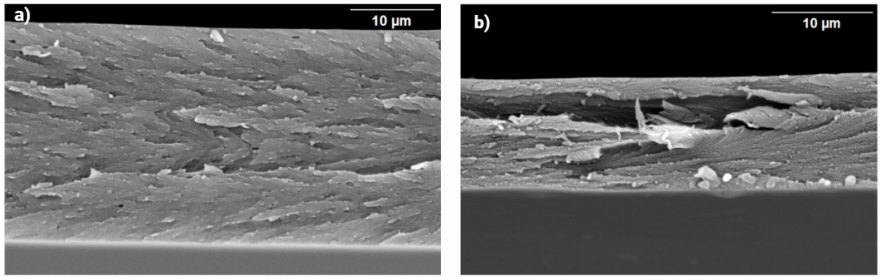

Figure 2: SEM micrograph from the cross-sectional area of chitosan-based biofilms (CNC). a) Pristine chitosan film (Cs) b) Chitosan with nanostructured with silver nanoparticles (Cs/AgNP).

References

[1] Wang, H. Biomaterials in medical applications. *Polymers (Basel)* **2023**, *15*.

[2] Dutta, P. K.; Dutta, J.; Tripathi, V. S. Chitin and chitosan: Chemistry, properties and applications. *Journal of Scientific Industrial Research* **2004**, *63*, 20–31.

[3] Yan, D.; Li, Y.; Liu, Y.; Li, N.; Zhang, X.; Yan, C. Antimicrobial Properties of Chitosan and Chitosan Derivatives in the Treatment of Enteric Infections. *Molecules* **2021**, *26*, 7136. DOI: 10.3390/molecules26237136.

Synthesis of Ag-impregnated hydrochars assisted by the concentrate derived from the spent liquor of hydrothermal carbonization

Daniela Armijos[1], Carlos Loyo[1], Alexis Debut[2], Sebastian Ponce[3,*], Herman A. Murillo[3,*]

[1] *School of Chemical Sciences and Engineering, Yachay Tech University, Hda. San José s/n y Proyecto Yachay, Urcuquí 100119, Ecuador*
[2] *Centro de Nanociencia y Nanotecnología, Universidad de las Fuerzas Armadas ESPE, Av. General Rumiñahui s/n y Ambato, Sangolquí 171103, Ecuador*
[3] *Department of Chemical Engineering, Universidad San Francisco de Quito USFQ, Diego de Robles s/n y Av. Interoceánica, Quito 170901, Ecuador*
danielaarmijos802@gmail.com

Abstract

Hydrothermal carbonization (HTC) is a promising process that converts biomass into valuable carbon-rich materials. This process has promise to support sustainable biorefinery designs. Although spent liquor (SL) is a significant portion of the HTC output stream, the solid carbonaceous product, hydrochar, has received significant attention for applications such as bioenergy, soil enhancement, and carbon sequestration [1, 2, 3]. The use of subcritical water conditions (180-250 °C and 2-6 MPa) increases the solubility and hydrolysis of biomass components [4, 5]. SL is composed of various organic molecules, such as volatile fatty acids, phenols, and furfurals, depending on the HTC working conditions and feedstock [6].

The recent research has initiated the exploration of strategies to enhance the overall efficiency and sustainability of HTC-based biorefineries by valorizing SL. For instance, Ding et al. (2022) demonstrated that the adsorption properties of hydrochar for dye removal can be improved by recycling SL from hydrothermally treated rice husk [7]. The bio-methane potential of SL obtained from oat fiber HTC through anaerobic digestion was also reported by Murillo et al. (2024) [8]. Additionally, the production of organic compounds from HTC spent liquor (OC-HTCSL) reactive concentrates that can facilitate the synthesis of additional materials has been suggested as a method of concentrating organic compounds from SL through water evaporation [1]. Notably, the successful production of stable silver nanoparticles (AgNPs) from HTC concentrates derived from Jatropha fruit fiber has been demonstrated [9]. This discovery has revealed a novel approach to the integration of nanomaterials into the HTC framework. Traditionally, the incorporation of nanoparticles into hydrochar matrices has been facilitated by "one-pot" green synthesis methods that employ plant extracts as stabilizing and reducing agents. These methodologies highlight the potential of natural antioxidants to make the synthesis of nanoparticles more environmentally harmless. SLs are an attractive alternative to plant extracts for the formation of nanoparticles and the modification of hydrochar, as they also demonstrate antioxidant activity [9].

Based on these findings, this study presents a sustainable ex-situ synthesis process for producing hydrochar-based catalysts impregnated with silver using various biomass feedstocks. The procedure deposits silver particles on hydrochar surfaces using concentrated organic compounds from spent liquors (SL) as natural reducing agents. The catalytic evaluation of the materials is evaluated using methyl orange reduction to determine their potential for wastewater treatment. A thorough characterization of silver-loaded hydrochars shows how metal particles interact with the carbon matrix. This technique enhances the value of HTC-derived products and follows with circular economy concepts by reusing process wastes to increase material functionality.

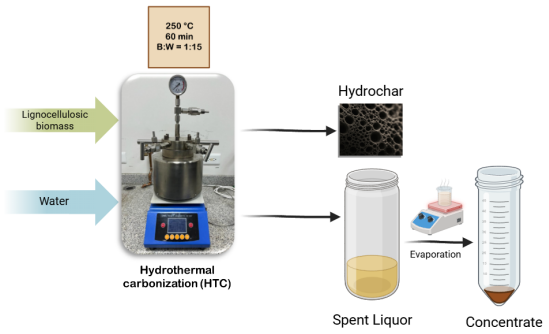

Figure 1: Obtaining the hydrochar and concentrate derived from spent liquor HTC process.

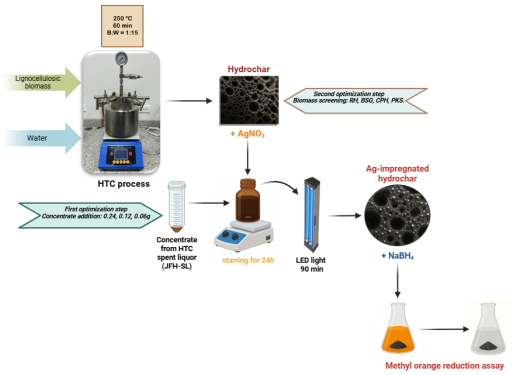

Figure 2: Impregnation and Optimization process for obtaining Ag-hydrochar catalyst.

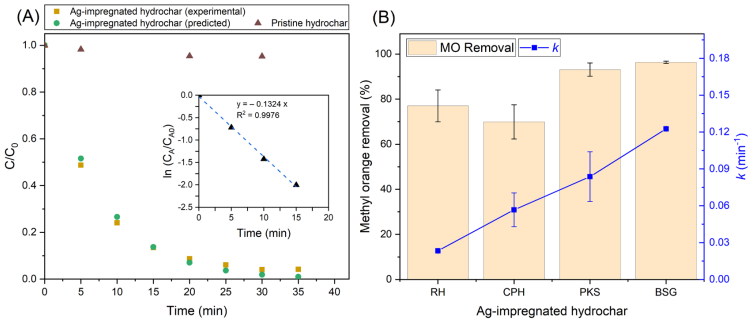

Figure 3: (A) Exemplary methyl orange removal and kinetic study for the Ag-impregnated hydrochar from BSG. (B) Methyl orange removal and reaction rate constants for all Ag-impregnated hydrochars.

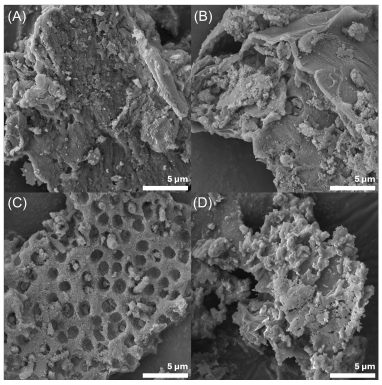

Figure 4: SEM images of Ag-impregnated hydrochars from (A) RH, (B) CPH, (C) PKS, (D) BSG.

References

[1] Murillo, H. A.; Juiña, E.; Vizuete, K.; Debut, A.; Echeverría, D.; Taco-Vasquez, S.; Ponce, S. Rapid Waste Motor Oil Conversion into Diesel-Range Hydrocarbons Using Hydrochar as Catalyst: Kinetic Study and Product Characterization. *Recycling* **2024**, *9*, 39. DOI: 10.3390/recycling9030039.

[2] Murillo, H. A.; Solís, M.; Vizuete, K.; Debut, A.; Morocho, V.; Cartuche, L.; Ponce, S. Innovative valorization of spent liquors from hydrothermal carbonization for light-induced nanoparticle synthesis. *Journal of environmental chemical engineering* **2024**, *12*, 113731. DOI: 10.1016/j.jece.2024.113731.

[3] Bona, D.; Bertoldi, D.; Borgonovo, G.; Mazzini, S.; Ravasi, S.; Silvestri, S.; Zaccone, C.; Giannetta, B.; Tambone, F. Evaluating the potential of hydrochar as a soil amendment. *Waste Management* **2023**, *159*, 75–83. DOI: 10.1016/j.wasman.2023.01.024.

Acta Microscopica Vol.35, Supp.1, 2026
Abstract Book NSSY 2026 - Galapagos 17th–23rd May 2026

Transition-Metal Complexes of Oxalate and Carbonate as EUV Photoresists

Norman Barreno[1], Stephen Smith[2], Robert Brainard[2]

[1] *School of Chemical Sciences and Engineering, Yachay Tech University*
[2] *Department of Nanoscale Science and Engineering, University at Albany, State University of New York (SUNY), Albany, NY 12203, USA*
norman.barreno@yachaytech.edu.ec

Abstract

Extreme ultraviolet (EUV) lithography at 13.5 nm demands photoresist materials with high absorption efficiency, chemical sensitivity, and robust film-forming behavior. Molecular organometallic resists (MORE) have emerged as promising alternatives to conventional polymeric systems due to their tunable ligand chemistry and enhanced EUV response [1]. In this work, transition-metal oxalate and carbonate complexes of palladium, platinum, and cobalt coordinated with phosphine ligands were synthesized and evaluated as candidate EUV photoresists.

Platinum carbonate and palladium oxalate complexes were prepared via ligand substitution reactions and characterized using ^{1}H NMR spectroscopy. While platinum complexes exhibited improved chemical stability, palladium oxalates displayed partial impurity formation, indicating the need for further purification optimization. Cobalt oxalate analogs were synthesized through precipitation-based routes, yielding crystalline solids suitable for formulation studies.

Thin-film resist formulations were developed using mixed solvent systems, with MeOH:PMA (2:1) producing the highest film uniformity during spin coating. Broadband UV and EUV exposure experiments were conducted to evaluate photochemical response and contrast behavior. Palladium oxalate formulations exhibited positive-tone contrast curves consistent with ligand-driven solubility switching, in agreement with previously reported oxalate-based EUV resists [2]. Comparative analysis further indicated enhanced sensitivity in platinum-based complexes, attributed to their higher EUV absorption cross sections.

These results highlight the critical role of oxalate ligands in promoting EUV-induced decomposition and demonstrate the influence of metal center selection on resist performance, supporting the continued development of next-generation molecular metal-based EUV photoresists.

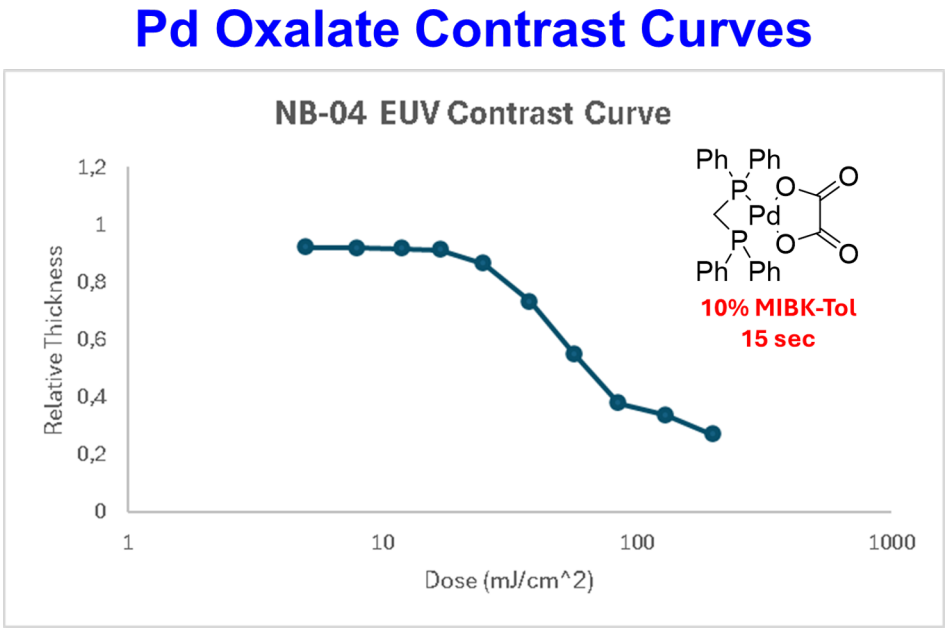

Figure 1: EUV contrast curve of palladium oxalate complex (NB-04) formulated at 10 wt% in MIBK:toluene and developed for 15 s.

References

[1] Brainard, R. L. et al. *J. Photopolym. Sci. Technol.* **2017**, *30*, 615.

[2] Sortland, M. et al. *J. Photopolym. Sci. Technol.* **2019**, *32*, 45.

From Waste to Medicine: Cocoa Bean Shell-AgNP Hydrothermal Synthesis for Enhanced Chitosan/Gentamicin Films for Potential Drug Delivery

Ian Boada[1], Sarah Briceño[1], Gema González[1]

[1] *School of Physical Sciences and Nanotechnology, Yachay Tech University, 100119-Urcuquí, Ecuador*
ian.boada@yachaytech.edu.ec

Abstract

Ecuador, the leading cocoa exporter in America and the fourth-largest worldwide, generates significant waste from cocoa production, including Cocoa Bean Shells (CBS) [1]. These shells are a generous source of bioactive compounds, such as phenolics, flavanols, pectin, and essential minerals [2]. Exploiting this underutilized source, a green and scalable hydrothermal approach to produce AgNP-functionalized carbon fibers from CBS was developed. The products of this reaction were characterized in terms of their chemical composition. From a biomedical perspective, chitosan-based films loaded with gentamicin and CBS-AgNPs for controlled drug delivery were fabricated. The films were characterized for chemical composition, morphology and drug release kinetics, demonstrating a excepted sustained antimicrobial efficacy against Gram-negative (Escherichia coli) bacteria.

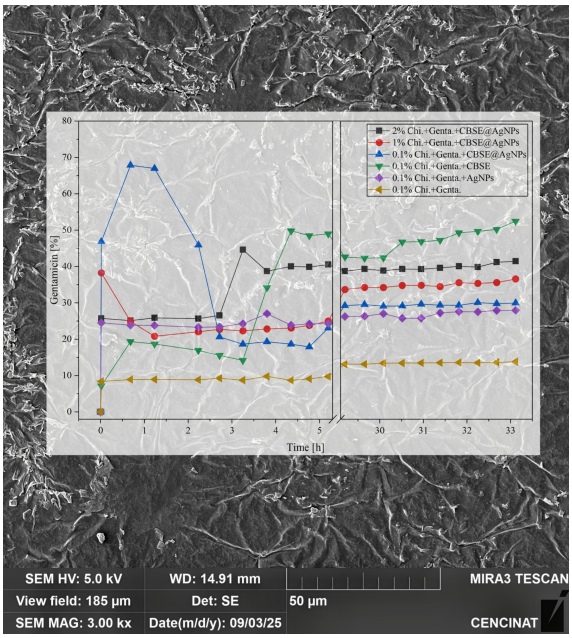

Figure 1: SEM Image of (AgNPs@CBSE + Gentamicin) Chitosan Films and its Pharmacokinetics Graph in acidic media.

References

[1] MAG Ecuador es el primer exportador de cacao en grano de América, 2022.

[2] Rojo-Poveda, O.; Barbosa-Pereira, L.; Zeppa, G.; Stévigny, C. Cocoa bean shell—a by-product with nutritional properties and biofunctional potential. *Nutrients* **2020**, *12*.

Acta Microscopica Vol.35, Supp.1, 2026
Abstract Book NSSY 2026 - Galapagos 17th–23rd May 2026

Laser Printing of Single-Walled Carbon Nanotube Conductive Tracks on Silicon

Daniela Briceño C.[1], Eduardo Castillo-Orozco[2]

[1] *Faculty of Mechanical Engineering and Production Sciences, Center for Research and Development in Nanotechnology*
[1] *Escuela Superior Politécnica del Litoral (ESPOL), Gustavo Galindo Campus, Km 30.5 Vía Perimetral, Guayaquil, Ecuador*
daalbric@espol.edu.ec

Abstract

Solar energy is crucial for an efficient transition from fossil fuels to a sustainable economy. Although conventional solar cells have achieved relatively high efficiencies, more efficient hybrid solar cells can be manufactured if suitable fabrication processes are developed. In this context, nanomaterials such as single-walled carbon nanotubes (SWCNTs) are a promising alternative for producing conductive tracks that capture free electrons in photovoltaic devices, where thermal stress and weight are critical factors.

This work focuses on the development of a process to deposit single-walled carbon nanotube conductive tracks for application in solar cells. The proposed method involves the deposition of a thixotropic nanosuspension by means of a doctor blade technique. The nanosuspension was formulated using SWCNTs dispersed in ethylene glycol and deposited onto a silicon wafer through an ethylene vinyl acetate mask. Localized heating using a CO_2 laser was applied for solvent evaporation and nanomaterial sintering, following a transient thermal model. The morphology of the deposited tracks was characterized by scanning electron microscopy.

Localized laser heating significantly improved the morphology, structure, and electrical behavior of the deposited tracks. The results indicate that selective sintering enhances inter-tubular connectivity without degrading the substrate. The optimum sintering condition was achieved at a surface temperature of approximately 120 °C, which enables the removal of the dispersing agent and promotes the formation of sintering necks, thereby reducing the electrical resistivity of the tracks. A sheet resistance on the order of 40 Ω was obtained.

These results demonstrate that laser sintering significantly reduces the electrical resistivity of SWCNT conductive tracks while operating at substantially lower temperatures than conventional processes, providing technical, energy, and environmental advantages for the fabrication of SWCNT-based conductive tracks.

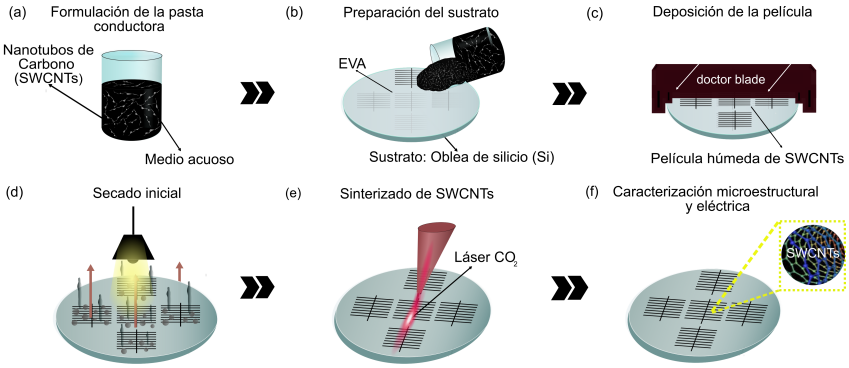

Figure 1: Experimental route for the fabrication of SWCNT electrodes

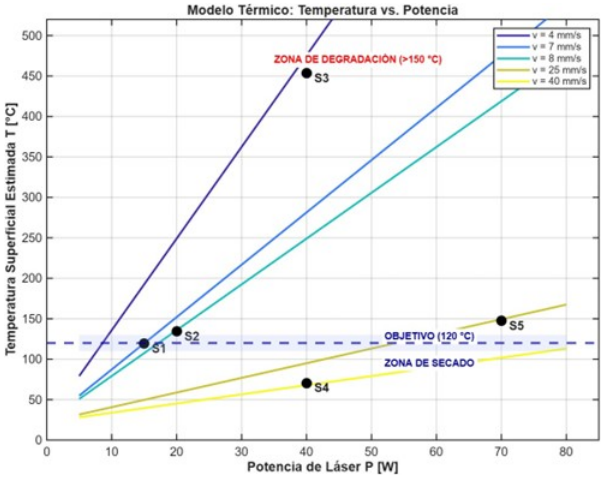

Figure 2: Isotherm map and experimental validation of the thermal sintering model for SWCNT films.

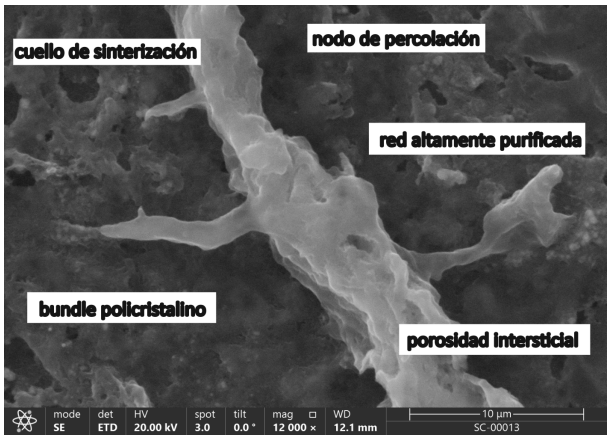

Figure 3: SEM micrographs of the microstructural network of SWCNTs sintered at 120 °C.

References

[1] Iijima, S. Helical microtubules of graphitic carbon. *Nature* **1991**.

[2] Hu, L.; Hecht, D. S.; Grüner, G. Percolation in Transparent and Conducting Carbon Nanotube Networks. *Nano Lett.* **2004**.

[3] Hecht, D. S.; Hu, L.; Irvin, G. Emerging Transparent Electrodes Based on Thin Films of Carbon Nanotubes, Graphene, and Metallic Nanostructures. *Advanced Materials* **2011**.

[4] Gómez, J.; Tigli, O.; Roca, M. Laser sintering of carbon nanotube networks for highly conductive and transparent electrodes. *Carbon* **2020**.

[5] Goldstein, J. I.; Newbury, D. E.; Michael, J. R.; Ritchie, N. W.; Scott, J. H. J.; Joy, D. C., *Scanning electron microscopy and X-Ray microanalysis*; Springer: 2017.

Acta Microscopica Vol.35, Supp.1, 2026
Abstract Book NSSY 2026 - Galapagos 17th–23rd May 2026

Hybrid Carbon Nanomaterials: Quantum Dot Encapsulation in Nanotube Cavities

Jose Campo[1], Johnny Chimborazo[1], Johanna Pilicita[1]

[1] *Yachay Tech University, School of Physical Science and Nanotechnology*
jose.campo@yachaytech.edu.ec

Abstract

This research focuses on the synthesis and characterization of carbon nanomaterials, emphasizing the confinement of carbon quantum dots (CQDs) within single walled carbon nanotubes (SWCNTs) as a novel strategy to engineer hybrid nanostructures with tunable electronic and optical properties. The confinement approach is motivated by the fact that the intrinsic properties of SWCNTs strongly dependent on chirality, diameter, and defect concentration can be significantly modulated by encapsulated nanostructures, creating new pathways for advanced nanoelectronics and optoelectronic applications.

The SWCNTs are synthesized by chemical vapor deposition (CVD), where silicon substrates are coated with optimized mixtures of iron (Fe) and cobalt (Co) catalysts in a polyvinyl alcohol stock solution using the electrospray method to stabilize and avoid degradation, this procedure focus to obtain the most homogenous deposition on substrate and avoid agglomerations, before thermal processing in an inert atmosphere within the CVD. Atomic Force Microscopy (AFM) equipment will be used to analyze the morphological structure of CNTs grown at nano scale and, Raman spectroscopy serves as the primary diagnostic tool, with the radial breathing modes (RBM) providing direct evidence of SWCNT formation, while the D, G, and 2D bands are used to assess defect density, in plane vibrations, and multilayer contributions. Experimental results confirm that only well-balanced Fe/Co catalyst mixtures yield distinct RBM signals characteristic of SWCNTs, whereas high catalyst concentrations or elevated methane flow rates lead to multi walled carbon nanotube (MWCNT) formation and defect structures [1].

In parallel, CQDs are synthesized from achiote seed biomass via a green route involving grinding, homogenization, sieving, ethanol treatment, drying, heat treatment (hydrothermal reactor), and purification using some methods in order to obtain the material with homogeneous particle size focused on the middle state to particle size, in addition to the freeze drying method to obtain powder material. The CQDs are characterized through UV–Vis, FTIR, SEM, and fluorescence spectroscopy to analyze material surfaces, morphology composition and topographical images. Their spectra exhibit absorption peaks associated with aromatic transitions, surface functional groups (O–H and C=C stretching vibrations), and stable photoluminescent features, particularly in purified middle-phase fractions.

The central stage of this study involves the encapsulation of CQDs within SWCNTs, using the nanotubes as nanoreactors and confinement vessels. This process is expected to stabilize the quantum dots, restrict their aggregation, and induce modified electronic coupling with the SWCNT walls. The hybrid carbon nanomaterials CQD&SWCNT are characterized through UV–Vis, FTIR, AFM, SEM, fluorescence and Raman spectroscopy to analyze and verify real state of confinement [2]. The confined system will be systematically analyzed to evaluate how encapsulation alters the optical response, defect states, and electron phonon interactions relative to free-standing CQDs and pristine SWCNTs. Through this hybrid approach, the work aims to demonstrate that CQD&SWCNT composites represent a promising platform for designing next-generation nanoscale devices.

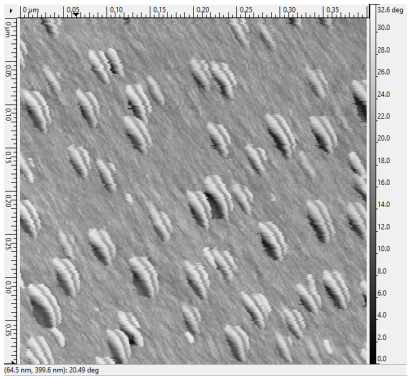

Figure 1: Morphological structure of CNTs with 5% Fe/Co catalyst.

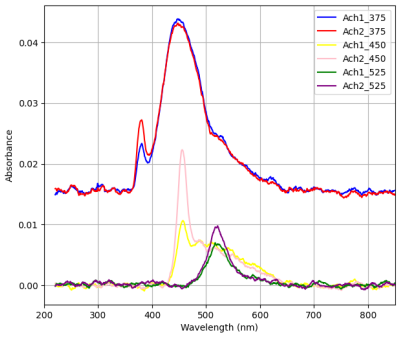

Figure 2: CQDs fluorescence of *Bixa orellana* using different lasers.

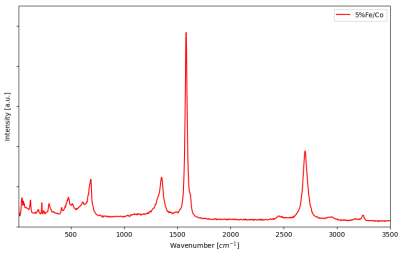

Figure 3: Raman Spectra of CNTs with 5%Fe/Co catalyst

References

[1] Liu, C.; Cheng, H.-M. Carbon nanotubes: controlled growth and application. *Mater. Today (Kidlington)* **2013**, *16*, 19.

[2] Voigt, D.; Primavera, G.; Uphoff, H.; Rethmeier, J. A.; Schepp, L.; Bredol, M. Ternary Chalcogenide-Based Quantum dots and Carbon Nanotubes: Establishing a toolbox for controlled formation of nanocomposites. *The Journal of Physical Chemistry C* **2022**, *126*, 9076–9090. DOI: 10.1021/acs.jpcc.2c01142.

Magnetic - Chitosan Microspheres for Microplastics Recovery

Anderson Cañamar[1], Gema González[1], Sarah Briceño[1]

[1]*School of Physical Sciences and Nanotechnology, Yachay Tech University, Urcuquí, Imbabura, Ecuador*
sergio.canamar@yachaytech.edu.ec

Abstract

Microplastic pollution has become a critical environmental issue due to the persistence, accumulation, and limited removal of synthetic polymers in aquatic systems. Among these contaminants, polyethylene terephthalate (PET) is one of the most prevalent microplastics detected in water bodies, originating mainly from the fragmentation of plastic packaging and textile fibers [1]. The present work addresses this problem by proposing the use of magnetic chitosan based microspheres as an eco-friendly and recoverable adsorbent material for removing PET microplastics from aqueous media. The relevance of this approach lies in the urgent need for sustainable remediation technologies that can combine high removal efficiency with low environmental impact and easy post-treatment separation. Biopolymer-based adsorbents such as chitosan offer a promising alternative to conventional synthetic materials due to their biodegradability, low toxicity, and chemical versatility [2]. In this study, the objective is to synthesize and characterize the material to evaluate the removal of microplastics. Therefore, the chitosan microspheres were synthesized via ionic gelation and subsequently modified through the incorporation of magnetite particles and EDTA functionalization to enhance adsorption capacity and facilitate magnetic recovery. The resulting materials were lyophilized to obtain porous structures suitable for microplastic adsorption. Morphological, structural, and compositional characterization was performed using scanning electron microscopy (SEM), energy dispersive X-ray spectroscopy (EDX), Fourier transform infrared spectroscopy (FTIR), Raman spectroscopy, and thermogravimetric analysis (TGA), confirming the successful formation and functionalization of the microspheres. The removal performance of PET microplastics was monitored by UV–Vis spectroscopy, exploiting the characteristic absorbance band in the 280–300 nm range associated with $\pi \rightarrow \pi^*$ electronic transitions of aromatic groups in PET [3]. Adsorption experiments showed a consistent decrease in absorbance intensity over time and with increasing quantity of material, indicating effective PET removal. This study, focused on the characterization of the material, contributes to addressing the challenge of microplastic contamination by providing a sustainable, alternative, and easily recoverable adsorption strategy, reinforcing the applicability of biopolymer magnetic composites in water treatment and environmental remediation.

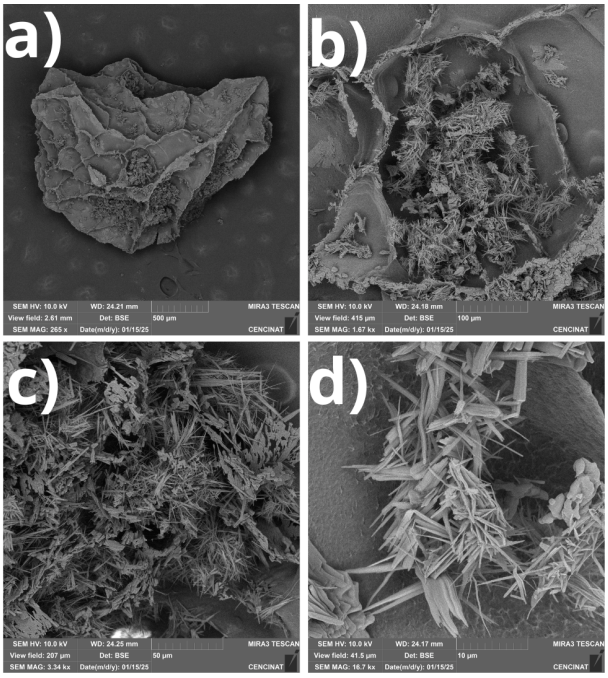

Figure 1: BSE–SEM micrographs of the chitosan-based microsphere (CH) acquired at different magnifications, illustrating its hierarchical morphology. (a) Low-magnification SEM image showing the overall morphology of an irregular particle aggregate. (b) Intermediate-magnification image revealing the internal structure of the particle, characterized by fractured regions and fibrous features. (c) Higher-magnification SEM image highlighting a dense network of elongated, needle-like structures distributed within the matrix. (d) High-magnification detail of the acicular structures, showing their morphology and local arrangement on the particle surface. All images were acquired in backscattered electron (BSE) mode at an accelerating voltage of 10.0 kV, with scale bars of 500 μm (a), 100 μm (b), 50 μm (c), and 10 μm (d), respectively.

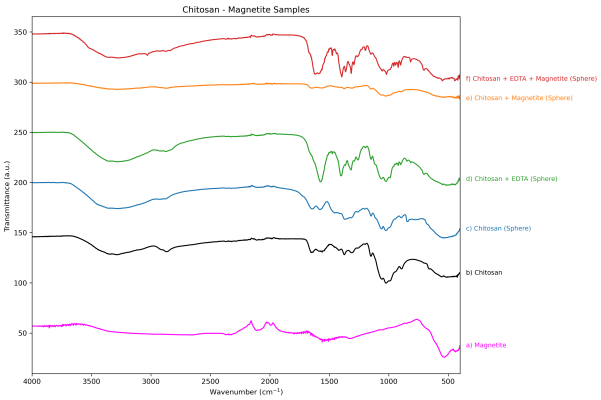

Figure 2: FTIR spectra of magnetite and chitosan-based materials recorded in the range 4000–400 cm^{-1}. (a) Magnetite (M). (b) Pristine chitosan. (c) Chitosan spheres (CH). (d) EDTA-functionalized chitosan spheres (CH+EDTA). (e) Magnetite-doped chitosan spheres (CHM). (f) Magnetite- and EDTA-functionalized chitosan spheres (CHM+EDTA). The spectra are vertically offset for clarity and illustrate the characteristic vibrational bands associated with the polymer matrix, EDTA functional groups, and iron oxide incorporation.

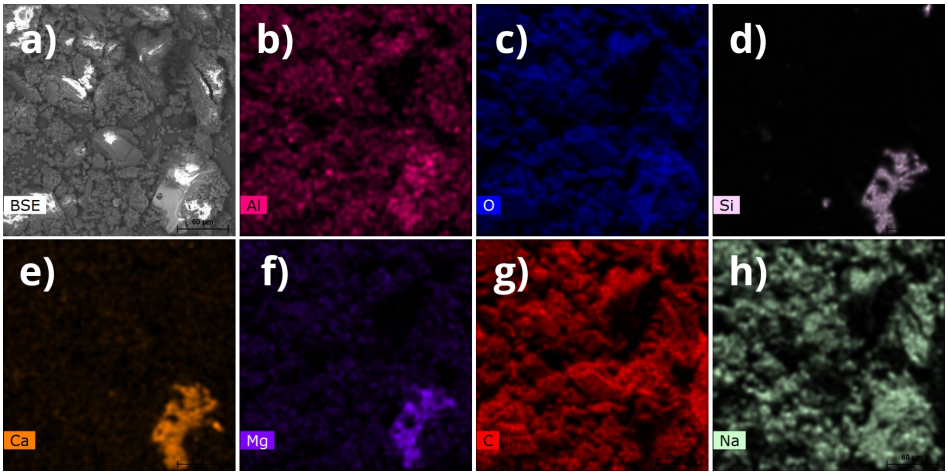

Figure 3: SEM–EDX analysis of glitter particles. (a) Backscattered electron (BSE) SEM micrograph showing the surface morphology and compositional contrast of the glitter sample. (b–h) EDX elemental maps of Al, O, Si, Ca, Mg, C, and Na. All maps correspond to the same analyzed area as the BSE image, with a scale bar of 60 μm.

Table 1: Removal efficiency (%) of PET and Glitter at different concentrations, calculated from UV–Vis peak absorbance measurements.

Sample (ppm)	Material	A_0	Best time	Removal (%)
Glitter 100	CH	0.2286	–	0.00
	CH + EDTA	0.2310	1 Day	21.86
	CHM	0.2311	1 Day	23.02
	CHM + EDTA	0.2432	–	0.00
Glitter 500	CH	0.7504	1 Day	19.23
	CH + EDTA	0.7749	1 Day	23.63
	CHM	0.7715	1 Day	25.34
	CHM + EDTA	0.7649	–	0.00
PET 100	CH	0.3470	1 Hour	2.97
	CH + EDTA	0.3128	1 Day	20.14
	CHM	0.3068	4 Days	12.13
	CHM + EDTA	0.2972	–	0.00
PET 500	CH	1.4744	1 Day	40.80
	CH + EDTA	1.4862	1 Day	46.84
	CHM	1.4738	1 Day	43.09
	CHM + EDTA	1.4881	1 Day	7.04

References

[1] Andrady, A. L. Microplastics in the marine environment. *Marine Pollution Bulletin* **2011**, *62*, 1596–1605.

[2] Crini, G.; Badot, P.-M. Application of chitosan, a natural aminopolysaccharide, for dye removal from aqueous solutions. *Progress in Polymer Science* **2008**, *33*, 399–447.

[3] George, N.; Kurian, T. Recent developments in the chemical recycling of postconsumer poly(ethylene terephthalate) waste. *Industrial & Engineering Chemistry Research* **2014**, *53*, 14185–14198.

Acta Microscopica Vol.35, Supp.1, 2026
Abstract Book NSSY 2026 - Galapagos 17th–23rd May 2026

Synthesis and characterization of hybrids based on VCL-PEGDA stimuli-responsive gels and carbon quantum dots with potential luminescent properties

Simón Choez[1], Antonio Díaz-Barrios[1], Jhonny Chimborazo[2], Lola de Lima[1]

[1]*School of Chemical Sciences and Engineering, YachayTech, Urcuqui, Ecuador*
[2]*School of Physical Sciences and Nanotechnology, YachayTech, Urcuqui, Ecuador*
choez.simon0908@gmail.com

Abstract

The development of functional hybrid materials that combine polymeric matrices with nanostructured components has attracted increasing attention in recent years due to their potential applications in sensing, bio-related technologies, and smart materials [1]. In particular, thermo-responsive polymeric systems integrated with fluorescent nanomaterials offer promising opportunities for the design of stimuli-responsive platforms capable of transducing environmental changes into optical signals. Within this context, polymer–nanoparticle hybrid systems based on biocompatible components are of particular interest for the development of advanced luminescent materials [2].

The aim of this work is to synthesize and characterize hybrid materials based on thermo-responsive hydrogels and carbon quantum dots (CQDs) and to evaluate their luminescent properties as a function of the polymer network structure. Specifically, hydrogels based on vinyl caprolactam (VCL) were combined with CQDs obtained from watermelon seed as a sustainable carbon source, with the objective of investigating how crosslinking degree and nanoparticles influence the photoluminescence behavior of the resulting hybrid systems.

Thermo-responsive hydrogels were synthesized via emulsion polymerization using VCL as the main monomer. Two types of polymeric systems were prepared: a VCL homopolymer hydrogel and copolymeric hydrogels obtained by incorporating polyethylene glycol diacrylate (PEGDA) as a crosslinking agent at different concentrations. Carbon quantum dots were synthesized through a hydrothermal method using watermelon seed as the precursor, followed by purification to obtain stable fluorescent nanoparticles. Hybrid materials were prepared by mixing the synthesized hydrogels with controlled amounts of CQDs to ensure homogeneous incorporation within the polymeric matrix.

To assess the polymerization conversion of the hydrogels and to estimate the effective incorporation of CQDs, total solids content was determined for each sample. Structural and chemical characterization of the hydrogels, CQDs, and hybrid materials was performed using Fourier Transform Infrared (FT-IR) and Raman spectroscopy, confirming polymer formation and nanoparticle integration. The thermal stability of both hydrogels and hybrid systems was evaluated by thermogravimetric

analysis (TGA), providing information on their degradation behavior and stability upon CQD incorporation. The optical and luminescent properties of the materials were investigated using photoluminescence spectroscopy, focusing on emission intensity and behavior as a function of hydrogel composition.

The results demonstrate a clear enhancement in photoluminescence intensity for the hybrid materials compared to the corresponding base hydrogels. Furthermore, an increase in the crosslinking degree of the polymeric network led to a systematic increase in photoluminescence intensity, indicating a strong relationship between polymer structure and optical response. This behavior is attributed to improved confinement and stabilization of the carbon quantum dots within more highly crosslinked hydrogel networks, which reduces non-radiative decay pathways and enhances fluorescence emission.

In conclusion, the hybrid materials developed in this study exhibit tunable luminescent properties governed by the structural characteristics of thermo-responsive polymeric gels. The combination of VCL-based hydrogels with carbon quantum dots derived from a sustainable source results in functional nanomaterials with enhanced fluorescence and favorable thermal stability. These findings highlight the potential of such hybrid systems as prospective thermo-responsive and luminescent platforms for sensing and bio-related applications, positioning them as promising candidates for future development in smart material technologies.

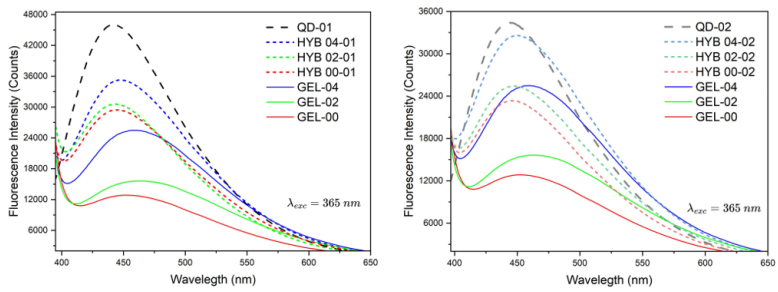

Figure 1: Fluorescence spectra of hydrogels, carbon dots, and hybrid materials.

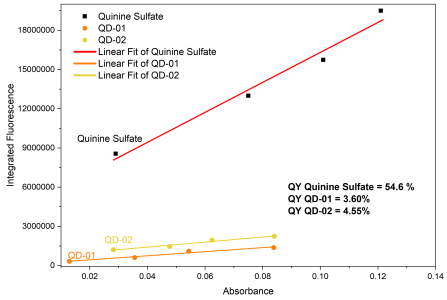

Figure 2: Relative quantum yield of carbon quantum dots (QD-01, QD-02).

References

[1] Park, W.; Shin, H.; Choi, B.; Rhim, W.-K.; Na, K.; Han, D. K. Advanced hybrid nanomaterials for biomedical applications. *Progress in Materials Science* **2020**, *114*, 100686. DOI: 10.1016/j.pmatsci.2020.100686.

[2] Sarwan, T.; Kumar, P.; Choonara, Y. E.; Pillay, V. Hybrid Thermo-Responsive Polymer Systems and their biomedical applications. *Frontiers in Materials* **2020**, *7*. DOI: 10.3389/fmats.2020.00073.

Acta Microscopica Vol.35, Supp.1, 2026
Abstract Book NSSY 2026 - Galapagos 17th–23rd May 2026

Nanoparticles for Intranasal Delivery of Temozolomide With Potential Application in the Treatment of Glioblastoma Multiforme

Marlus Chorilli[1], Alberto Gomes Tavares Junior[1]

[1] *Innovative Pharmaceutical Technology Group, School of Pharmaceutical Sciences, São Paulo State University (UNESP), Araraquara, São Paulo, Brazil*
marlus.chorilli@unesp.br

Abstract

Glioblastoma multiforme (GBM) is an aggressive and lethal type of brain tumor, known for its high resistance to conventional treatments. Originating from glial cells or their precursors, GBM is marked by its cellular heterogenicity, aggressiveness and invasiveness. Clinical manifestations range from headaches and neurological deficits to seizures, depending on the location and size of the tumor in the brain. The key determinant factor of GBM aggressiveness is the communication between GBM cells and their surrounding microenvironment [1]. Despite advances in treatment modalities such as surgery, radiation, and chemotherapy, the prognosis for GBM patients remains poor, with a median overall survival of approximately 12–15 months [2]. The blood-brain barrier (BBB) poses a significant challenge, restricting drug delivery to the tumor, which reduces the effectiveness of chemotherapy and increases side effects. Temozolomide (TMZ) is the most common chemotherapeutic agent used for GBM, but it has limitations, including low stability and short half-life. Additionally, TMZ's therapeutic effect is impacted by GBM's molecular heterogeneity and genetic alterations, such as mutations in the MGMT gene, that can confer resistance to TMZ, reducing its effectiveness [3]. To overcome these issues, this study aimed to develop and characterize nanoparticles made of zein, a biocompatible and biodegradable protein derived from corn, for the controlled delivery of TMZ. Zein is also a sustainable alternative to synthetic polymers. The nanoparticles were prepared using the nanoprecipitation method. The formulations were characterized both with (TMZ-ZNP) and without the drug (ZNP). The TMZ-ZNP formulation had a mean diameter of 557.0 nm, PDI of 0.27 and a zeta potential of 34.7 mV, and a high encapsulation efficiency of 66.8%. The encapsulation of TMZ significantly altered the physicochemical properties of the particles. The in vitro release profile showed that free TMZ has a rapid release, with over 80% of the drug released within the first 8 hours. In contrast, the TMZ-ZNP formulation provided a sustained release for up to 48 hours (Figure 1), suggesting a mechanism of drug diffusion through the nanoparticle matrix. Thermal (DSC) and spectroscopic (FTIR) analyses confirmed the presence of TMZ inside the polymeric matrix. In cytotoxicity assays, the zein nanoparticles were shown to be biocompatible, while the TMZ-ZNP formulation demonstrated a significant antiproliferative

effect on U87-MG glioblastoma cells, with cell viability decreasing as concentration and exposure time increased. The results indicate that zein nanoparticles are a promising platform for the controlled delivery of temozolomide, with the potential to improve treatment efficacy and reduce side effects of glioblastoma multiforme. The efficient encapsulation and sustained release profile make this system a relevant candidate for future investigations, particularly for intranasal administration.

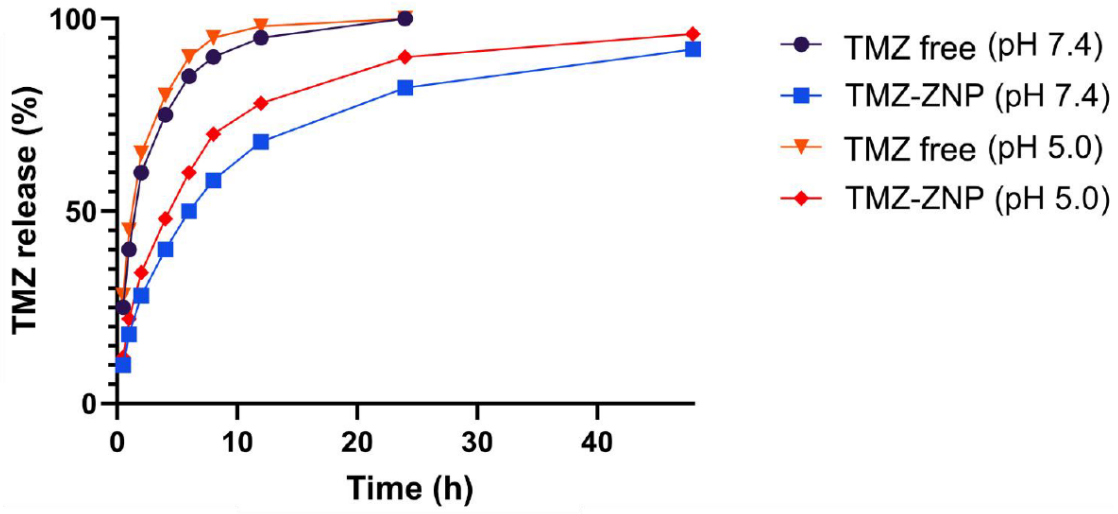

Figure 1: *In vitro* release profile of temozolomide (TMZ) from zein nanoparticles (TMZ-ZNP) in release media pH 6.8 and 5.0 at 37 °C

References

[1] Hameedat, F.; Mendes, B. B.; Conniot, J.; Di Filippo, L. D.; Chorilli, M.; Schroeder, A.; Conde, J.; Sousa, F. Engineering nanomaterials for glioblastoma nanovaccination. *Nature Reviews Materials* **2024**, *9*, 628–642. DOI: 10.1038/s41578-024-00684-z.

[2] Duarte, J. L.; Di Filippo, L. D.; Vilella, K. J. A.; Dutra, J. A. P.; Ribeiro, D. M.; Da Silva, M. F.; De Medeiros, A. I.; Chorilli, M. Chitosan-coated nanoemulsion for intranasal administration increases temozolomide mucosal permeation, cellular uptake, and In vitro cytotoxicity in glioblastoma multiforme cells. *Journal of Drug Delivery Science and Technology* **2024**, *102*, 106390. DOI: 10.1016/j.jddst.2024.106390.

[3] Liu, H.; Qiu, W.; Sun, T.; Wang, L.; Du, C.; Hu, Y.; Liu, W.; Feng, F.; Chen, Y.; Sun, H. Therapeutic strategies of glioblastoma (GBM): The current advances in the molecular targets and bioactive small molecule compounds. *Acta Pharmaceutica Sinica B* **2021**, *12*, 1781–1804. DOI: 10.1016/j.apsb.2021.12.019.

Effect of graphene oxide on the germination and early growth of agronomically important plants

Sarahi Josefina Estrada Loredo[1], Moisés Roberto Vallejo Pérez[2], Daniel Sánchez Campos[1], Daniela Edith Salado Leza[1,3]

[1] *Instituto de Física, Universidad Autónoma de San Luis Potosí, Av. Parque Chapultepec 1570, Privadas del Pedregal, 78295 San Luis Potosí, S.L.P., México*
[1] *Coordinación para la Innovación y Aplicación de la Ciencia y la Tecnología (CIACYT), Centro de Investigación Aplicada en Ambiente y Salud (CIAAS), Avenida Sierra Leona No. 550, Colonia Lomas Segunda Sección, CP 78210, San Luis Potosí, S.L.P., México*
[1] *Investigadoras e Investigadores por México, SECIHTI, Av. Insurgentes Sur 1582, Col. Crédito Constructor, 03940 Alcaldía Benito Juárez, Ciudad de México, México*
sarahijel@hotmail.com

Abstract

In Mexico, the use of carbon nanomaterials like graphene oxide (GO) and nanotubes has grown significantly due to their mechanical, thermal, and electrical properties, making them highly attractive for technological, medical, and industrial applications [1]. However, there is limited mandatory regulation and little awareness of voluntary guidelines governing their use, increasing the risk of environmental release during production, application, or disposal, which enable nanomaterials to enter the food chain and interact with various organisms. This study focuses on the impact of GO on plants, a relatively underexplored area that is crucial for assessing ecological risks and food safety. Based on the Mexican voluntary standards (NMX) and international methodologies such as; the International Rules for Seed Analysis (ISTA) and Organisation for Economic Cooperation and Development (OECD) Guideline 208, a reproducible methodology was developed to evaluate the effects of both commercial and lab-synthesized GO on young plants through germination and early growth assays. The work was conducted in three stages: material stability assessment, germination assays, and growth analysis (root and shoot length, leaf area, fresh and dry biomass, relative leaf water content, and biochemical parameters including chlorophyll, macronutrients, and antioxidant enzyme activity). The established methodology provides a standardized and robust framework to assess carbon nanomaterials environmental risks, and contribute to the responsible and sustainable use of them.

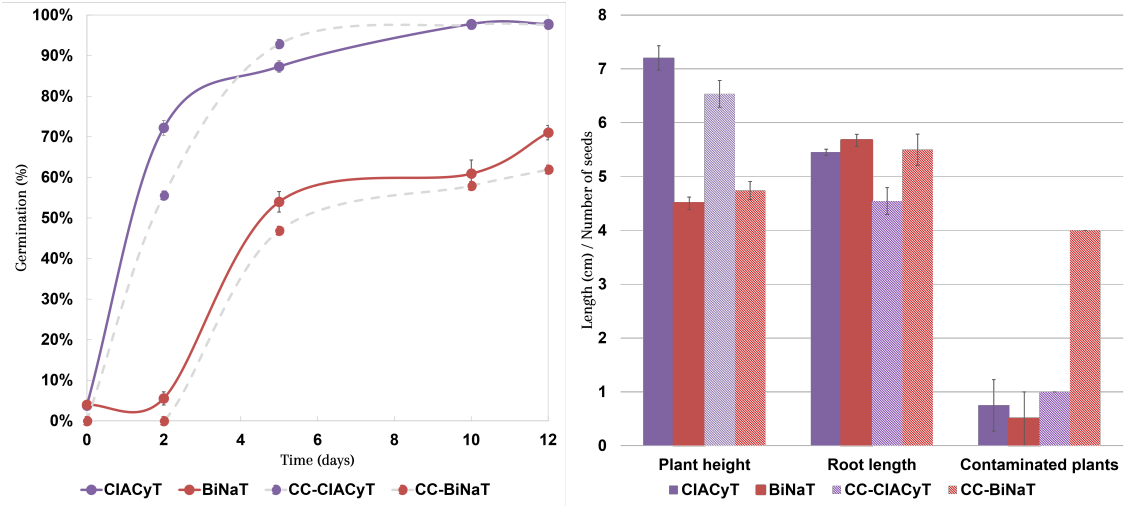

Figure 1: Methodology standardization: germination percentage and early growth of control plants.

References

[1] Khodakovskaya, M. V.; de Silva, K. In *Nanoscience and biotechnology for environmental applications*; Springer: 2018, pp 1–15. DOI: 10.1007/978-3-319-70614-6_73-2.

[2] Gottschalk, F.; Sun, T.; Nowack, B. Environmental concentrations of engineered nanomaterials: Review of modeling and analytical studies. *Journal of Environmental Management* **2018**, *222*, 487–499. DOI: 10.1016/j.jenvman.2018.07.087.

Acta Microscopica Vol.35, Supp.1, 2026
Abstract Book NSSY 2026 - Galapagos 17th–23rd May 2026

Conductive Bio-Based Polymer Composites with Percolated Graphite Networks

Daniela Fernández-Sánchez[1], Armando Encinas[1]

[1] *Instituto Potosino de Investigación Científica y Tecnológica. Advanced Materials Division*
dani.181097@hotmail.com

Abstract

The development of biopolymer composites represents a sustainable alternative to conventional polymers in various application areas [1], which has generated increasing interest across different sectors [2] aimed at improving their properties through the incorporation of compounds or filler materials. In particular, conductive polymer composites exhibit attractive properties such as low toxicity, biocompatibility, and low cost, thereby expanding their potential applications in sensors, batteries, diodes, and other electronic devices [3]. The objective of this work was to develop conductive composites based on biodegradable organic materials, such as corn zein, gelatin, and pectin, with potential application as functional inks. For this purpose, graphite was used as a conductive filler, and its concentration was varied within the different polymer matrices. The results showed that the incorporation of graphite at different concentrations allows modulation of both the mechanical properties and the electrical transport properties of the composites, enabling the identification of an optimal percolation threshold, as shown in Fig. 1. Additionally, gelatin-based inks exhibited a change in electrical resistance as the bending angle was modified, indicating their potential use as piezoresistive inks (see Fig. 2) and pressure sensors. In contrast, zein-based systems, due to their insolubility in water, present advantages for use in humid environments without material loss. When comparing the intermediate concentrations in the different polymer matrices, conductivity values of 0.282 S/cm for zein, 0.048 S/cm for pectin, and 0.018 S/cm for gelatin are obtained. Overall, the developed materials constitute viable candidates for application in flexible bioplastics and printed sensors on biopolymeric substrates, enabling the monitoring of different variables through electrical signals measurable by resistive, capacitive, and piezoelectric methods.

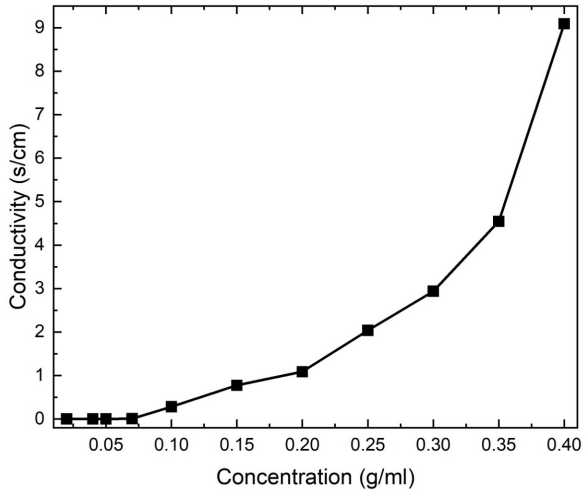

Figure 1: Percolative behaviour of the electrical conductivity in Zein–graphite composites as a function of the filler fraction.

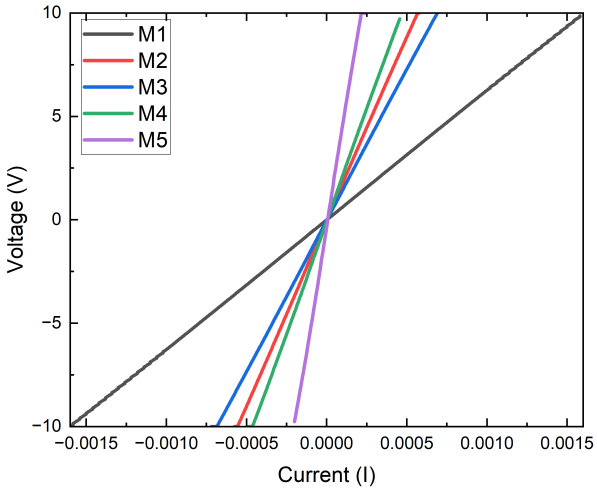

Figure 2: Resistance change as a function of the bending angle for the gelatin–graphite film.

References

[1] Bartoli, M. et al. **2022**, *15*, 2506.

[2] Gowthama et al. **2021**, *9*, 2213.

[3] Huang et al. **2019**, *11*, 187.

Acta Microscopica Vol.35, Supp.1, 2026
Abstract Book NSSY 2026 - Galapagos 17th–23rd May 2026

Growth temperature influence on graphitic ribbons synthesis: Characterization and systematic cyclic voltammetry study

Flores-López Zacek David[1], Macclesh-del-Pino-Pérez Luis Alejandro[1], Orea-Calderón Brenda Irais[1], Jiménez-Ramírez Luis Ernesto[1], Muñoz-Sandoval Emilio[1], López-Urías Florentino[1]

[1] *IPICYT, Advanced Materials Division*
zacek.flores@ipicyt.edu.mx

Abstract

Carbon nanotube sponges (CNTSs) are extremely lightweight, complex graphitic nanostructures. Owing to their mechanical properties, CNTSs can be elastically distorted into any shape and repeatedly compressed. This type of structure is lighter than water owing to its low density and hydrophobic nature. Their high electrical conductivity has shown promising applications, including flexible and compressible conductors, innovative materials, sensors, and nanocomposites. In 2010, Gui et al. [1] reported the synthesis of CNTSs by chemical vapor deposition (CVD) using a solution of ferrocene and 1,2-dichlorobenzene at 860 °C for 4 h under a carrier gas atmosphere of Ar and H_2. Their results showed that CNTSs exhibit thermal stability, electrical conductivity, robustness, and resistance, which can be exploited in multifunctional structures, sensors, electrodes, and membranes. Martinez-Iniesta et al. [2] synthesized nitrogen-doped carbon nanoribbon sponges (CNRS) via CVD using two sprayer approach. They used, for sprayer-1, a mixture of toluene, N,N-dimethylformamide, ferrocene, and thiophene, and, for sprayer-2, a mixture of acetone, isopropanol, ferrocene, and thiophene. The two independent solutions were nebulized and introduced into a tubular quartz reactor, which was tested at three different synthesis temperatures. Their results showed a rough surface, oxygen-containing functional groups, and defects, which could be attributed to nitrogen incorporation. This approach offers a counterpoint to the conventional method of preparing carbon nanotube-based sponges. These carbon structures have been described as one-dimensional confined graphene sheets, exhibiting high charge-carrier mobility, a considerable bandgap, and versatile electronic properties, which correlate with their structural defects, particularly those at the edges and ribbon orientation [3]. Based on this knowledge, we encourage the improvement of a methodology for synthesizing CNRS via aerosol-assisted chemical vapor deposition (AACVD). To optimize their structural and electrochemical properties for use as charge-carrier supports in electrode materials for electrochemical devices. We present the AACVD method starting with four main precursors: acetone, isopropanol, ferrocene, and thiophene. Each precursor plays a crucial role in the synthesis pathway, final morphology, and electrical properties. For instance, acetone and isopropanol serve as carbon sources and introduce an oxygen double bond

in addition to the hydroxyl group. These functionalities can then be translated into quinone, carbonyl, ether, or hydroxyl groups in graphene sheets. The precursor mixture solution was nebulized in a quartz tube reactor inside a tubular furnace at 980, 1020, and 1050 °C for 1 h each with a gas flow rate of 1 L/min. After the reaction, the resulting carbon material was scraped off using a stainless-steel rod. CNRSs were characterized by scanning electron microscopy (SEM), X-ray diffraction (XRD), Raman spectroscopy, diffuse reflectance infrared Fourier transform spectroscopy (DRIFTS), cyclic voltammetry (CV), and electrochemical impedance spectroscopy (EIS). SEM revealed an interconnected zigzag ribbon morphology in the graphitic materials (Fig. 1), which was interlinked with the fiber-like structures. The XRD patterns show prominent sp^2 carbon peaks at approximately 26° and 43°. Additionally, a peak corresponding to turbostratic graphite is observed at approximately 25°. The diffraction patterns revealed interplanar spacings of 0.166, 0.152, and 0.152 nm for the samples synthesized at 980, 1020, and 1050 °C, respectively. The Raman spectra showed peaks characteristic of a graphene-like sample, including the D and G bands, as well as the complementary D1, D2, and D4 bands. A 2D band appears at approximately 2700 cm^{-1}. CV and EIS analyses revealed capacitive behavior with resistivity effects. The oxidative and reductive peaks corresponding to metallic species were attributed to the addition of the ferrocene catalyst.

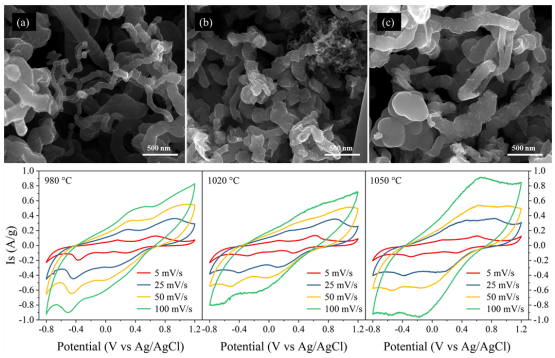

Figure 1: Morphological and electrochemical characterization of CNRSs synthesized by AACVD at different growth temperatures. Top panels: SEM micrographs of samples grown at (a) 980 °C, (b) 1020 °C, and (c) 1050 °C, revealing an interconnected zigzag ribbon network. Bottom panels: cyclic voltammetry (CV) curves recorded at scan rates of 5, 25, 50, and 100 mV s^{-1} (potential vs Ag/AgCl), highlighting the effect of growth temperature on the capacitive response.

References

[1] Gui, X. et al. *Adv. Mater.* **2010**, *22*, 617.

[2] Martínez-Iniesta, A. D. et al. *Diam. Rel.Mater.* **2023**, *138*, 110209.

[3] Wang, H. et al. *Nat. Rev. Phys.* **2021**, *3*, 791.

Arsenic removal from aqueous solutions using biochar derived from green banana peel

Giseth Freire[1], Katherine Vaca-Escobar[1,*], Santiago Guerrero[1], Milton Villacis-García[2,*], Santiago Quishpe[2], Indira Izquierdo[1], Nicolas Cevallos[2], Patricio Espinoza-Montero[1,*]

[1] *Pontificia Universidad Católica del Ecuador*
[1] *Universidad Central del Ecuador*
gmfreire@puce.edu.ec

Abstract

Arsenic contamination in water bodies poses a serious environmental and public health concern due to its high toxicity and chronic effects on exposed populations. In South America, the presence of this metalloid arises largely from natural leaching of sedimentary rocks, placing rural communities that depend on untreated groundwater at elevated risk.

In this study, biochar derived from green banana peels was investigated as a low-cost adsorbent for arsenic removal from aqueous media. Following the principles of the circular economy, agro-industrial waste was repurposed to develop a sustainable material with potential applicability in resource-limited settings, thereby contributing to both environmental protection and public health [1].

The biochar was produced via pyrolysis of green banana peels in a tubular furnace under an inert argon atmosphere, using a heating rate of 5 °C min^{-1} up to 750 °C, with a final yield of 37%. Arsenic concentrations were quantified using the molybdenum blue method, where As(V) was reduced to As(III) to form a blue complex subsequently analyzed by UV-Vis spectrophotometry [2]. A calibration curve (0.5–5 ppm) enabled reliable correlation between absorbance and arsenic concentration. The material demonstrated high adsorption performance, achieving a removal efficiency of 90%.

Adsorption kinetics were evaluated by sampling aliquots at defined intervals until equilibrium was attained. Isothermal adsorption experiments were also conducted under controlled temperature and time conditions, at varying arsenic concentrations, also the best model that describe adsorption is Freundlich isotherm, confirming the material's capacity to increase adsorption, and the adsorption capacity is 164.7 $(mg/g)(L/mg)^{(1/n)}$.

Overall, this work identifies green banana peel–derived biochar as a promising adsorbent for arsenic removal from aqueous solutions. Its simple preparation, economic accessibility, and environmental sustainability highlight its potential as a practical strategy to improve water quality and mitigate health risks in vulnerable populations.

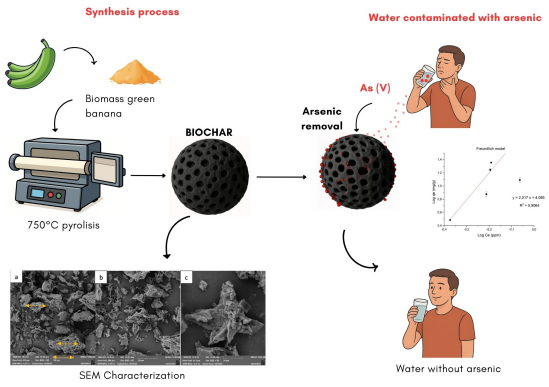

Figure 1: Graphical abstract.

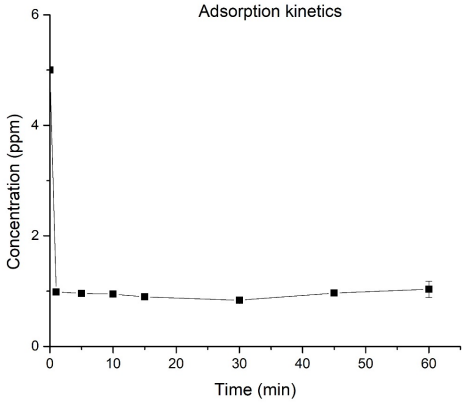

Figure 2: Adsorption kinetics.

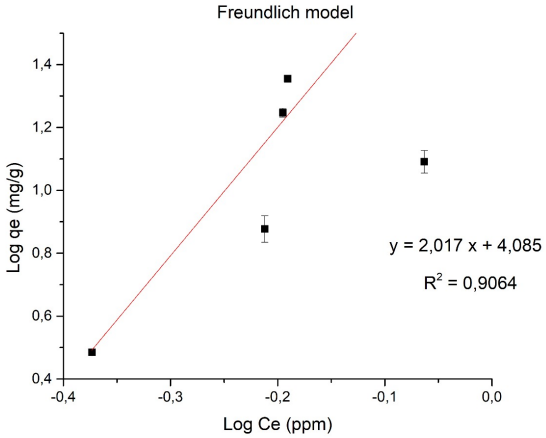

Figure 3: Isotermical Model

References

[1] Zimmerman, A. J.; Gutierrez, D. G.; Campos, V. M.; Weindorf, D. C.; Deb, S. K.; Chacón, S. U.; Landrot, G.; Flores, N. G. G.; Siebecker, M. G. Arsenic speciation in titanium dioxide (TiO_2) waste produced via drinking water filtration: Potential environmental implications for soils, sediments, and human health. *Environmental Advances* **2021**, *3*, 100036. DOI: 10.1016/j.envadv.2021.100036.

[2] Ramírez, S.; Jiménez, Y.; Esperanza, G.; Ribalta, J.; Rodríguez, R. Determinación de arsénico por el método del azul de Molibdeno en muestras de aguas provenientes de una planta de procesamiento de minerales auríferos. *Revista Cubana de Química* **2017**, *20*, Verificar coherencia entre volumen y URL, 3–12, http://scielo.sld.cu/pdf/ind/v29n1/ind01117.pdf.

Acta Microscopica Vol.35, Supp.1, 2026
Abstract Book NSSY 2026 - Galapagos 17th–23rd May 2026

Synthesis and characterization of composites based on vinyl polymers and nanoparticles with potential photocatalytic properties

David Garcés[1], Antonio Díaz-Barrios[1], Miguel Herrera[1], Pablo Cisneros[1]

[1] *School of Chemical Sciences and Engineering, Yachay Tech University, Urcuquí, Ecuador*
david.garces@yachaytech.edu.ec

Abstract

In recent decades, the development of functional nanostructured materials has become increasingly important in the development of advanced technologies that address environmental problems, increasing the need for more efficient, stable, and reusable systems. In particular, the treatment of wastewater contaminated with persistent organic pollutants (POPs), such as synthetic dyes, pesticides, and pharmaceuticals, presents a significant challenge due to their high chemical stability, toxicity, and resistance to conventional treatments. Photocatalytic processes based on inorganic semiconductors have yielded satisfactory results in the degradation of these pollutants; however, their implementation is limited by problems associated with nanoparticle agglomeration, the difficulty of catalyst recovery, loss of activity after several use cycles, and low efficiency under visible light. To overcome these challenges, the integration of nanophotocatalysts into polymer matrices emerges as an effective strategy for designing hybrid materials that combine structural stability, dispersion control, and functional synergy [1]. The aim of this work is to design, synthesize, and evaluate hybrid compounds based on a crosslinked vinyl polymer matrix and bismuth oxychloride ($Bi_4O_5I_2$) and zinc oxide (ZnO) semiconductor nanoparticles for the synergistic removal of organic pollutants through combined adsorption and photocatalysis mechanisms under ultraviolet and visible radiation. The materials were obtained from a vinyl acetate-butyl acrylate (VAc-BA) copolymer, synthesized by semicontinuous emulsion polymerization [2], in combination with a polyethylene glycol diacrylate crosslinked N-vinylcaprolactam hydrogel (VCL-PEGDA). This polymer system acted as a structural matrix for the immobilization and stabilization of the inorganic phases. $Bi_4O_5I_2$ nanoparticles were generated via hydrothermal synthesis [3], while commercial ZnO was incorporated as a co-photocatalyst, forming a hybrid system with an enhanced photoactive response. Methodologically, the hybrid compounds were prepared using a 2^3 factorial experimental design, considering variables such as nanoparticle loading (5–10% w/w), semiconductor type, and dispersion conditions. This allowed for homogeneous dispersion within the polymer matrix, resulting in a structurally stable and functionally active compound. The structural, optical, and thermal characterization of the materials was performed using X-ray diffraction (XRD), UV-Vis spectroscopy, thermogravimetric analysis (TGA), and contact angle measurements.

The results showed that $Bi_4O_5I_2$ and ZnO nanoparticles have band gap energies of 2.72 eV and 3.25 eV, respectively, allowing them to be activated in different regions of the electromagnetic spectrum. The compounds exhibited contact angles ranging from 40° to 62°, indicating a moderately hydrophilic surface, favorable for adsorption processes in aqueous media, as well as thermal stability up to approximately 327 °C. Photocatalytic activity was evaluated using methylene blue as a model contaminant. Under dark conditions (7 hours), an initial contaminant removal of approximately 9–17% was recorded, attributed to adsorption processes on the polymer matrix. Under ultraviolet irradiation (365 nm), the compounds achieved degradation efficiencies of 77 to 99% after 180 minutes of treatment, while under visible light irradiation (540 nm), values of 55 to 72% were obtained over the same period. Kinetic analysis suggests that the degradation process follows a pseudo-first-order model, indicating a mechanism dominated by the generation of reactive oxygen species induced by the photoelectronic excitation of semiconductors. The combination of pre-adsorption and photodegradation demonstrates a synergistic effect directly related to the hybrid design of the material. The results show that the developed nanostructured polymer compounds are efficient, reusable, and structurally stable photocatalytic materials capable of integrating synergistic adsorption and photocatalysis mechanisms. The immobilization of $Bi_4O_5I_2$ and ZnO nanoparticles within a flexible polymer matrix overcomes the limitations associated with traditional photocatalytic systems, demonstrating the potential of these hybrid materials for environmental remediation applications, offering reusable and low-energy solutions for the sustainable treatment of pollutants in vulnerable ecosystems.

Table 1: Physical and thermal properties of the synthesized polymer-semiconductor composites: dimensions, surface area, mass, contact angle, and maximum degradation temperature determined by TGA.

Material	Diameter (mm)	Thickness (mm)	Surface area (mm^2)	Mass (mg)	Contact angle (°)	Max. degradation temp. (°C)
I	90.6 ± 0.1	0.16 ± 0.04	6442.9 ± 17.1	746 ± 9	46.6 ± 1.2	328.2
$B_L/Z_L/\Phi_H$	89.4 ± 0.1	0.14 ± 0.05	6279.2 ± 10.0	1221 ± 7	47.0 ± 0.9	333.9
$B_L/Z_H/\Phi_L$	89.5 ± 0.1	0.14 ± 0.04	6291.0 ± 5.8	816 ± 8	55.4 ± 0.9	333.9
$B_L/Z_H/\Phi_H$	90.4 ± 0.1	0.14 ± 0.05	6421.1 ± 11.5	1429 ± 11	44.6 ± 0.5	323.6
$B_H/Z_L/\Phi_L$	88.6 ± 0.1	0.13 ± 0.04	6169.6 ± 14.0	870 ± 13	61.7 ± 0.5	426.4
$B_H/Z_L/\Phi_H$	89.6 ± 0.1	0.14 ± 0.05	6307.1 ± 10.5	1442 ± 9	51.8 ± 0.8	327.4
$B_H/Z_H/\Phi_L$	90.3 ± 0.1	0.13 ± 0.04	6409.9 ± 7.1	884 ± 16	48.4 ± 0.5	326.6
$B_H/Z_H/\Phi_H$	90.4 ± 0.1	0.13 ± 0.05	6423.9 ± 12.8	1458 ± 11	40.1 ± 1.6	319.6

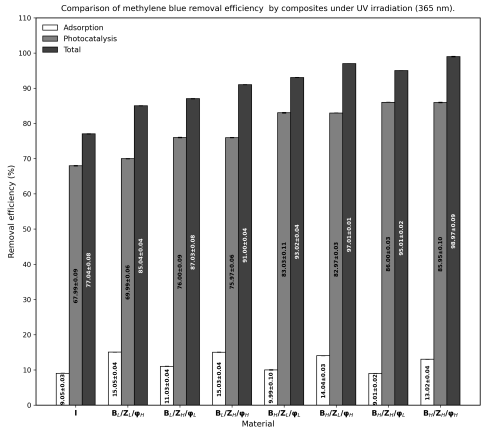

Figure 1: Comparison of methylene blue removal efficiency (%) by the synthesized polymer-semiconductor composites under UV irradiation (365 nm). The white, gray, and dark bars represent the contributions of adsorption, photocatalysis, and total removal efficiency, respectively. Error bars indicate standard deviation ($n = 3$).

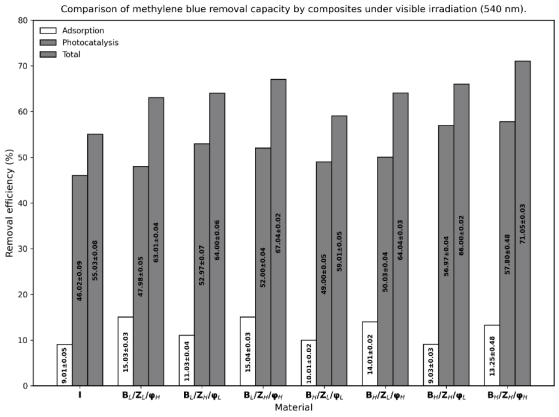

Figure 2: Comparison of methylene blue removal efficiency (%) by the synthesized polymer-semiconductor composites under visible light irradiation (540 nm). The white, gray, and dark bars represent the contributions of adsorption, photocatalysis, and total removal efficiency, respectively. Error bars indicate standard deviation ($n = 3$).

References

[1] Nagaraja, K.; Arunpandian, M.; Hwan Oh, T. *J. Ind. Eng. Chem.* **2024**.

[2] Díaz-Barrios, A. et al. *Mater. Chem. Phys.* **2020**, *255*, 123476.

[3] Huidobro, L.; Domingo, A.; Gómez, E.; Serra, A. *Chemosphere* **2024**, *366*, 143532.

Acta Microscopica Vol.35, Supp.1, 2026
Abstract Book NSSY 2026 - Galapagos 17th–23rd May 2026

Sustainable development of carbon nanostructures on recycled steel: annealing-induced surface optimization for CNT growth and enhanced surface conductivity

Domenica Garcia[1], Fausto Chicaiza[1], Pedro Zamora[1], Rosa Almache-Hernandez[1]

[1] *Grupo de Investigación en Aplicaciones Avanzadas de Nanotecnología*
domenica.garcia@yachaytech.edu.ec

Abstract

Carbon nanotubes ($CNTs$) are promising nanomaterials due to their exceptional electrical and thermal properties, enabling applications in energy storage, smart grids, and energy-efficient infrastructure [1]. The production of carbon nanotubes ($CNTs$) faces significant economic challenges due to the high cost of commercial precursors and environmental impact. This study investigates a sustainable and alternative route by utilizing recycled steel from industrial workshops as a low-cost catalytic substrate. The methodology was structured into four consecutive stages: first, the conditioning and ultrasonic cleaning of the steel substrates to eliminate industrial contaminants; second, the synthesis of a cobalt and nickel thin films via DC sputtering, aimed at obtaining a precursor layer with controlled nanometric thickness to ensure uniform catalyst distribution [2]; third, a thermal annealing process was applied to induce morphological restructuring of the metallic layer within the temperature range of 400 °C to 1000 °C, promoting the formation of active nucleation sites at the nanometric scale for both $Ni/Steel$ and $Co/Steel$ systems; and fourth, the growth of $CNTs$ via Chemical Vapor Deposition (CVD) at 750 °C, using acetylene (C_2H_2) as the carbon source in an inert argon (Ar) atmosphere. Raman spectroscopy analysis reveals the successful formation of carbon nanotubes ($CNTs$) on the annealed and no annealed surfaces. The Raman spectra in Figure 1 confirm the formation of carbon nanotubes on the no annealed surface, as evidenced by the presence of the characteristic D ($\sim$ 1350 cm^{-1}), G ($\sim$ 1580 cm^{-1}), and $2D$ ($\sim$ 2700 cm^{-1}) bands [1]. The appearance of the $2D$ band further supports the formation of multi-walled carbon nanotubes. The Raman spectra presented in Figure 2 show a clear evolution of carbon nanotubes with increasing annealing temperature [1]. This approach establishes a solid foundation for the development of low-cost nanotechnology, allowing the final phase of structural and electronic characterization to precisely determine which catalytic configuration optimizes electron transport [3].

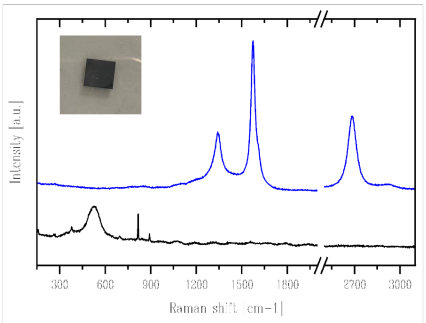

Figure 1: Raman spectroscopic analysis of the synthesis process. (a) Catalyst precursor state (black line): Raman spectrum of the industrial steel substrate after conditioning and pre-annealing, showing a baseline free of carbonaceous signals. (b) Post-synthesis growth (blue line): Spectrum following chemical vapor deposition (CVD), where the emergence of the D, G, and well-defined 2D bands confirms the successful nucleation of carbon nanotubes. The presence of these features on the non-annealed surface demonstrates the catalytic activity of the recycled steel.

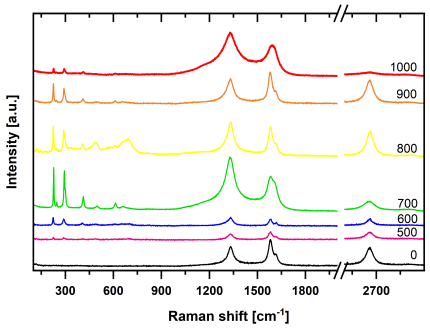

Figure 2: Structural evolution of CNTs as a function of annealing temperature under 633 nm laser excitation. The black line (a) represents the control sample without annealing, establishing the baseline for catalytic activity on the raw substrate. The colored spectra (b–h) illustrate the evolution of CNT growth as the annealing temperature increases from 400 °C to 1000 °C. This progression demonstrates that, while growth is feasible without prior thermal treatment, higher temperatures significantly optimize the crystallinity of the carbon nanotubes, as evidenced by the intensification of the 2D band and the clearer definition of radial breathing modes (RBM), characteristic of high-quality, small-diameter structures.

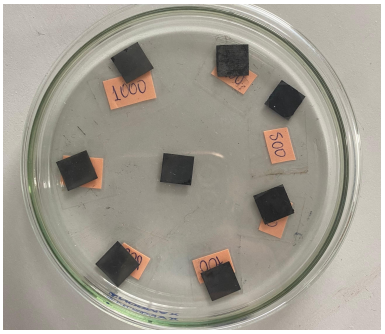

Figure 3: Visual macrograph of the synthesized samples. Digital photograph of the recycled steel substrates after the Chemical Vapor Deposition (CVD) process at different annealing temperatures (400 °C – 1000 °C).

References

[1] Chicaiza, F. et al. Synthesis and Characterization of Carbon Nanotubes on Industrial Recycled Steel Substrates. *RevTeX Phys. Rep.* **2024**.

[2] Thissen, N. F. W. et al. Controlled growth of carbon nanotubes on metallic substrates via DC sputtering and CVD. *Carbon* **2017**, *121*, 389–400.

[3] Sampaio, D. V. et al. Structural and electronic characterization of carbon nanotubes for energy applications. *J. Nanomater.* **2016**, *2016*, art. 1.

Xerogel-based hybrid system loaded with quantum dots and nanotubes for controlled release of vitamins B6 and B12: Physicochemical characterization and release kinetics

Cárdenas María Isabel[1], **Gómez Angel**[2], Gonzáles Gema[2]

[1] *Yachay Tech University. School of Chemical Sciences and Engineering*
[1] *Yachay Tech University. School of Physical Sciences and Nanotechnology*
angel.gomez@yachaytech.edu.ec

Abstract

Vitamins B_6 and B_{12} are essential for physiological processes; however, their oral administration presents challenges due to their high aqueous solubility and rapid renal clearance [1].In another hand Xerogels, porous solid materials offer effective platforms for catalysis, adsorption, and drug delivery systems [2]. Sol-gel science: the physics and chemistry of sol-gel processing, London, Academic Press, pp. 510-515). In this work, a hybrid alginate xerogel doped with carbon quantum dots (CQDs) and carbon nanotubes (CNTs) was designed, synthesized, and characterized for the controlled release of these vitamins. CQDs were synthesized by thermal treatment of rose stems (200 °C, 10 h), while CNTs were obtained by synthesis with nitrate precursors and functionalization with nitric acid. The xerogel was prepared by ionic crosslinking with Ca^{2+}, incorporating 0.01 % w/v of each nanomaterial in a 2 % sodium alginate matrix. The hybrid xerogel exhibited greater structural stability than the pure control, forming thin sheets and well-defined spheres, with lower swelling capacity (80 % vs 100 %). Fluorescence spectroscopy confirmed the optical emission of the integrated CQDs. Electrical analysis revealed a conductivity of 10^{-5} S cm^{-1} for the hybrid xerogel, superior to the control (10^{-6} S cm^{-1}) and comparable to materials for electronic applications. FTIR characterization showed similar spectra between the hybrid xerogel without vitamins B6 and B12 and the one containing them, attributable to the low concentration of vitamins (0.01 % w/v) and confirming the absence of new chemical bonds, which evidences the physical integration of the vitamins into the alginate matrix. In vitro release assays demonstrated that the hybrid xerogel released vitamins B_6 and B_{12} in a prolonged manner over 24 h, in contrast to the pure xerogel which showed complete reabsorption within 60 min. The hybrid system released 47 % less vitamin B_6 and 52 % less vitamin B_{12} than the control, evidencing controlled release kinetics. These results confirm the potential of the nanocomposite as a dual-functional material for controlled drug delivery systems and bioelectronic applications.

Sample	Thickness (cm)	R_b (Ω)	σ (S/cm)
Alg–CQDs/CNTs-1	0.01105	293.767	3.76×10^{-5}
Alg–CQDs/CNTs-2	0.01028	205.415	5.00×10^{-5}
Alg–CQDs/CNTs-3	0.00623	244.679	2.54×10^{-5}
Alg–CQDs/CNTs-4	0.00730	173.041	4.22×10^{-5}
Alg (control)	0.02700	432.464	6.24×10^{-6}

Figure 1: DC conductivity of xerogel films, reported as the mean of three sweeps.

	Vitamin B6			Vitamin B12		
Capsule	QD+CNT	Pure	Diff. (%)	QD+CNT	Pure	Diff. (%)
1	0.0083	0.0156	46	0.00009	0.00018	50
2	0.0155	0.0165	6	0.00016	0.00030	47
3	0.0175	0.0191	8	0.00021	0.00044	52
4	0.0274	0.0417	34	0.00033	n.d.[a]	––

Figure 2: Maximum release and percentage difference between QD+CNT xerogel and pure xerogel.

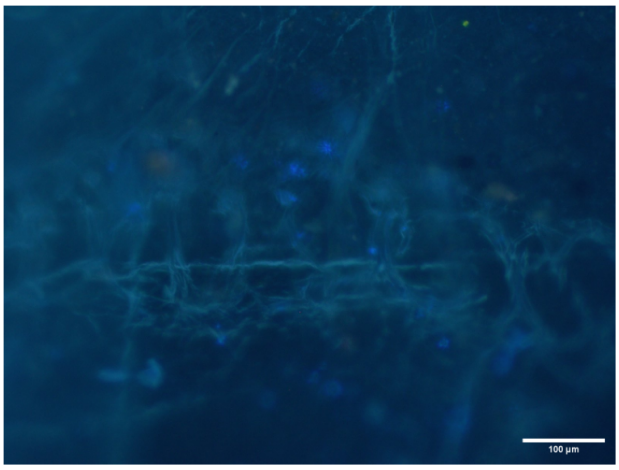

Figure 3: Xerogel with CQDs and CNTs.

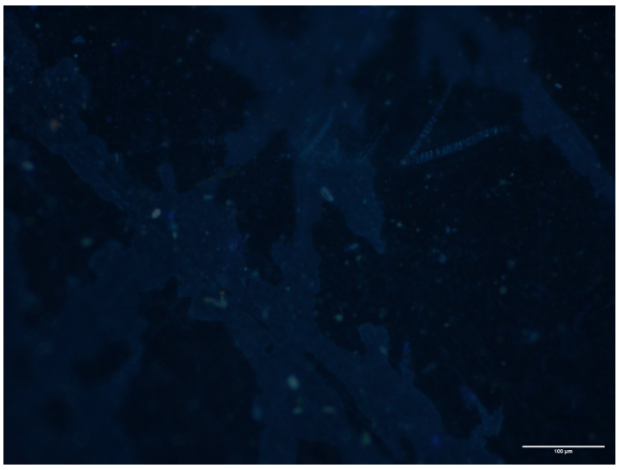

Figure 4: Xerogel without CQDs and CNTs.

References

[1] Sugandhi, V. V. et al. *Food Sci. Nutr.* **2024**, *12*, 48–83.

[2] Brinker, C. J., *Sol-gel science: the physics and chemistry of sol-gel processing*; Academic Press: London, 1990, pp 510–515.

Computational Study of External Quantum Efficiencies: A quantum photoinduced treatment of OPV

Duncan J. Mowbray[1], **Daniel E. Gonzalez-Tamayo**[1], Vito Despoja[1]

[1] *School of Physical Sciences and Nanotechnology*
daniel.gonzalez@yachaytech.edu.ec

Abstract

Photovoltaics are a renewable, clean, and cost-effective energy source that does not produce greenhouse gases or other pollutants. For these reasons, they make a valuable contribution to sustainable development. Organic photovoltaic (OPV) solar cells aim to create a solution that is environmentally friendly, has a lower energy cost for production, and avoids the restriction of the theoretical limit on the maximum efficiency of silicon-based photovoltaics. In order to develop optimized OPV materials, modeling the quantum efficiency of a solar cell using ab initio methods to accurately describe their performance, i.e., photoinduced quantum transport, is necessary. To address this problem, we require an accurate an efficient description of the optical absorption (OA) process, charge carrier generation, and the resulting charge transport through an OPV. Herein we perform calculations at the independent-particle approximation (IPA) level to describe the coupling to leads, interaction with an external electromagnetic field, and resulting transmission probability through a conducting circuit within the non-equilibrium Green's function (NEGF) formalism. In this study, we employ a linear combination of atomic orbitals (LCAO) representation of the Kohn–Sham (KS) wave functions to obtain the system's density of states (DOS) and hamiltonian at the density functional theory (DFT) level. With these quantities, we can obtain the system's external quantum efficiency (EQE), i.e., the fraction of incoming photons of a specific energy that generate charge carriers. Specifically, we apply this approach to three candidate low-dimensional OPV systems, i.e., (6,4), (8,4), and (10,2) single-walled carbon nanotubes (SWCNTs), attached in the following plots. This work aims to contribute to the computational design of novel low- dimensional OPV systems that can significantly improve research and development in this field and enhance the efficiency and performance of such devices.

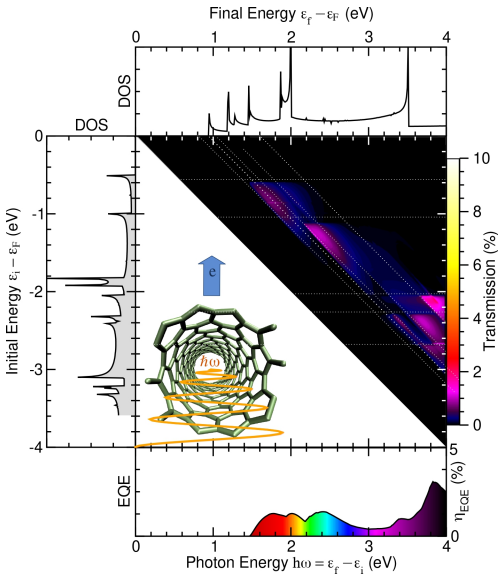

Figure 1: We illustrate the full External Quantum Efficiencie calculation procedure for this particular chirality, revealing three principal energy regions where absorption can take place, each one corresponding to distinct excitation processes. From the color bar in the transmission map, we can interpret the degree to which incoming photons are efficiently converted into charge carriers, based on the intensity and spread of the overlapping regions observed.

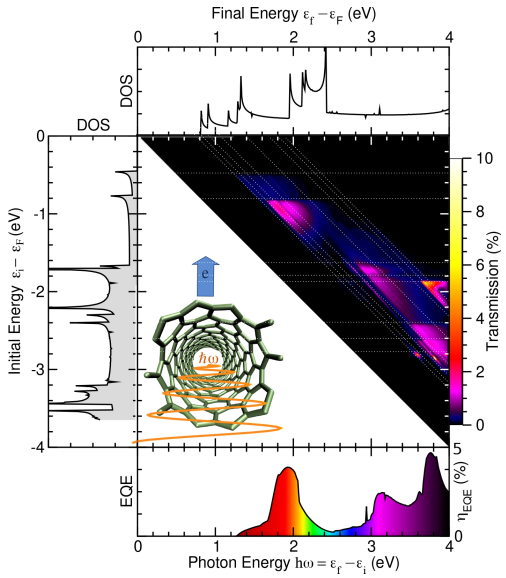

Figure 2: For the (10,2) SWCNT, offers a detailed depiction of the EQE calculation pathway, where the main features of light-matter interaction emerge clearly through three distinct regions of allowed optical transitions. These are reflected in the variations of the transmission probability, and the color-coded intensity map shows how much of the incoming photon energy is effectively transformed into moving charge carriers.

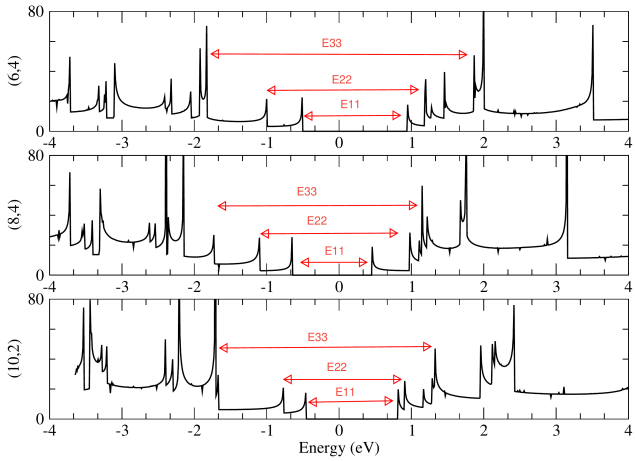

Figure 3: DOS of (6,4), (8,4), and (10,2) SWCNT. The x-axis represents the range of the energy in eV, and the y-axis shows DOS in arbitrary units. The red arrows represent optical transitions between electronic states, labeled here as $E11$, $E22$, and $E33$, for each SWCNT, representing the first, second, and third allowed optical transitions.

Acta Microscopica Vol.35, Supp.1, 2026
Abstract Book NSSY 2026 - Galapagos 17th–23rd May 2026

Hard Carbon Derived from Banana Pseudostem (Musa paradisiaca): A Sustainable Approach for Energy Storage Materials

Luis Corredor-González[1], Juan Pablo Saucedo-Vázquez[1], Zaillmar Morales-Navarro[1], M. Fernanda Bósquez Cáceres[2], Y. Balladores[3], Sabrina Acevedo[4], Julio C. Chacón-Torres[2], Carlos Reinoso[2], **Joseph Granja-Vélez**[1]

[1] *Yachay Tech University, School of Chemical Sciences and Engineering, Urcuquí 100119, Ecuador*
[1] *Yachay Tech University, School of Physical Sciences and Nanotechnology, Urcuquí 100119, Ecuador*
[1] *Condensed Matter Physics Laboratory, Physics Center, Venezuelan Institute for Scientific Research*
[1] *Zulian Institute of Technological Research (INZIT), La Cañada de Urdaneta, Venezuela*
joseph.granja@yachaytech.edu.ec

Abstract

Hard Carbon (HC) is a material of significant current interest due to its potential applications in energy storage and electronic devices. In parallel, there is a growing accumulation of organic residues from the agroindustrial sector; in Ecuador, it is estimated that more than forty million metric tons are produced every nine months [1], originating from the banana industry, making it an abundant and low-cost biomass. In this work, HC was synthesized from banana organic residues (Musa paradisiaca) through thermal carbonization at different temperatures: 1100 ∘C, 1000 ∘C, 900 ∘C, 800 ∘C, and 700 ∘C, in order to evaluate the effect of this synthesis parameter on the resulting microstructure and its influence on the desired properties of the new material, which is crucial for understanding and optimizing its performance in energy storage applications. The synthesized products were characterized using a set of complementary techniques. Raman spectroscopy was used to evaluate the structural quality of the material. The peak around 1580-1569 cm-^{1} (Figure 1) corresponds to the G vibration, associated with the vibrations of C bonds with sp2 hybridization (table 1.), characteristic of graphitic carbon. XPS spectroscopy showed a decrease in sp3 hybridization C as the carbonization temperature increased (Figure 2). Oxygen analysis in HC confirms its preference for bonding to sp3 C located at the edges or in defects. FTIR was also used to determine the functional groups on the HC surface. The structural analysis was complemented by the XRD technique on polycrystalline samples, which provided information on the crystalline arrangement of the product obtained. Finally, thermogravimetric analysis provided data on the thermal stability of the material and identified its thermal oxidation point, which is essential for understanding its behavior in response to temperature changes. Unlike graphite, HC exhibits a structure with structural defects and closed micropores that facilitate ionic storage, including adsorption at defective sites and nanopore filling. These structural features make HC compatible with larger-radius ions, such as sodium [2], positioning it as

a key candidate for the development of more sustainable next-generation batteries, particularly in view of the geopolitical, environmental, and economic limitations associated with lithium-ion batteries. Additionally, preliminary studies on cation adsorption were carried out using the synthesized HC, employing methylene blue as a model molecule to evaluate the interaction of the material with positively charged species in solution. The use of Hard Carbon as an anode material opens the possibility for the development of more advanced energy storage systems, such as solid-state batteries and sodium-based batteries, where structural stability of HC and compatibility with the larger ionic radius of Na+ constitute relevant advantages.

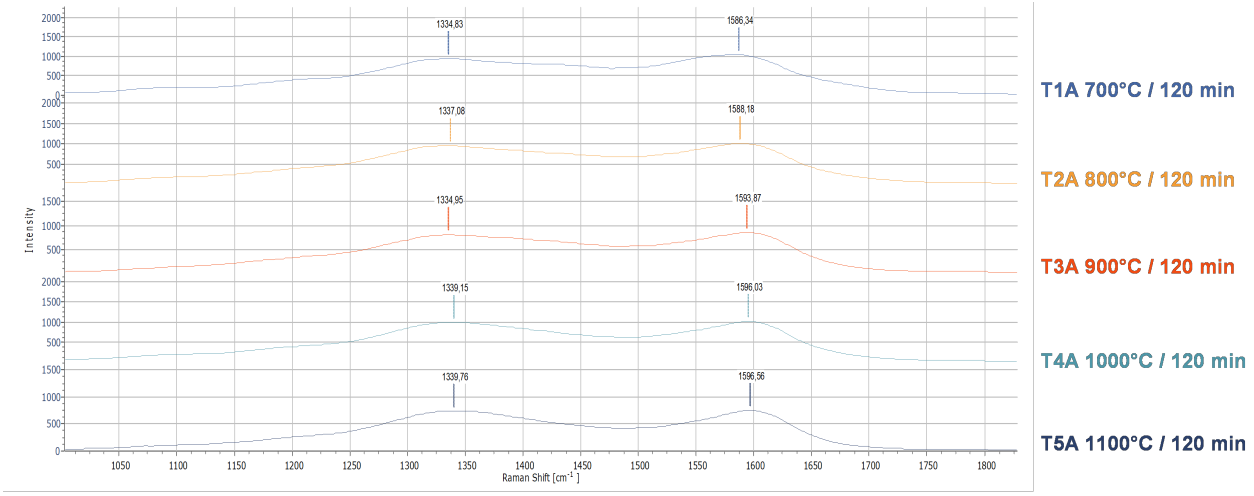

Figure 1: Raman spectra of HC prepared at different temperatures.

Table 1: Intensity ratio between G and D bands (IG/ID).

Sample	G band intensity	D band intensity	I_G/I_D ratio
T1A	1043	938.5	0.8994
T2B	1010	961.6	0.9524
T3A	853.4	806.2	0.9447
T4A	1015	990.8	0.9757
T5A	747.9	738.9	0.9879

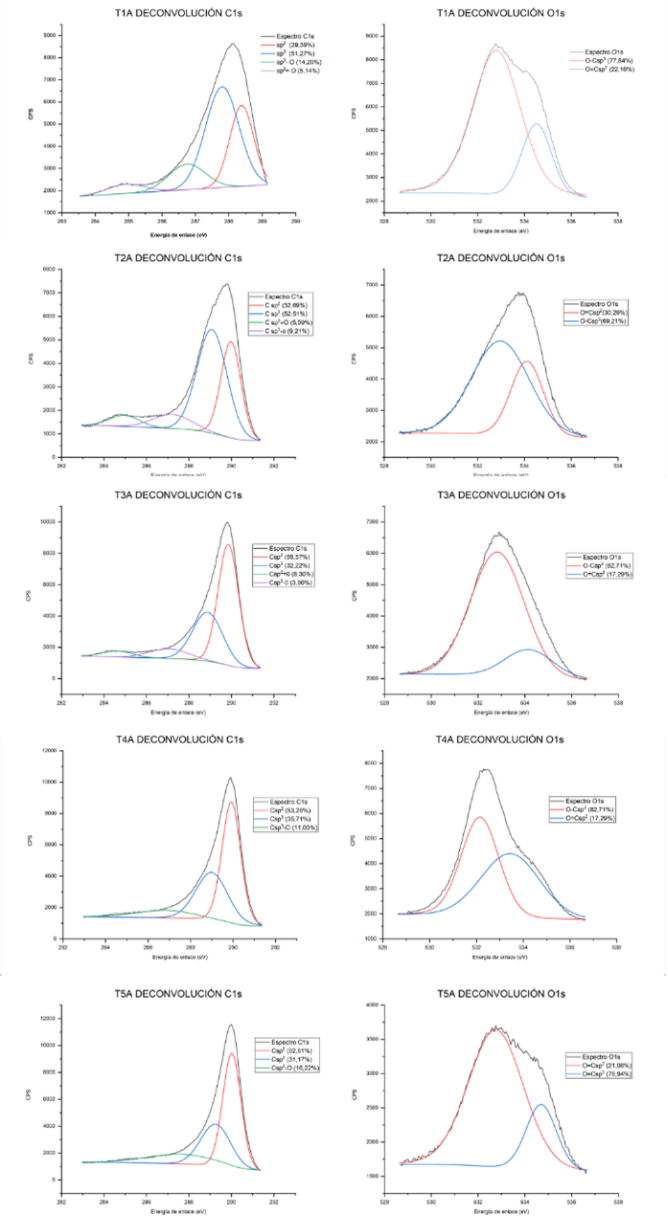

Figure 2: XPS spectra of HC prepared at different temperatures.

References

[1] Pérez, R. et al. Upcycling the Banana Industry in Ecuador: A Methodology to Estimate Organic Waste Availability and a Catalogue of Potential Biodegradable Products. 2023.

[2] Hasa, I.; Dou, X.; Buchholz, D.; Shao-Horn, Y.; Passerini, S. Hard carbons for sodium-ion batteries: Structure, analysis, sustainability, and electrochemistry. *Materials Today* **2019**, *23*, 87–104.

Acta Microscopica Vol.35, Supp.1, 2026
Abstract Book NSSY 2026 - Galapagos 17th–23rd May 2026

Efficient N_2 activation in transition metal complexes: Computational approach

R. Guañuna[1,2], A Escobar[1,2], E. Villegas[1], J. Saucedo[1,2], T. Terencio[1,2]

[1] *School of Chemistry Science and Engineering, Yachay Tech University, Urcuquí, Ecuador*
[1] *CATS Research Group (CAtalysis Theory & Spectroscopy), Yachay Tech University, Urcuquí, Ecuador*
romel.guanuna@gmail.com

Abstract

Nitrogen is one of the most abundant elements in nature, accounting for approximately 78% of the Earth's atmosphere. Nevertheless, due to its high stability, molecular nitrogen (N_2) is unreactive, limited by its strong bond energy (945 kJ/mol) resulting from its triple bond (N≡N) [1]. In nature, various organisms employ metalloenzymes to activate nitrogen; in particular, the enzyme nitrogenase, which contains Mo, V, and Fe centers, enables the bioactivation of N_2 and its subsequent transformation [2, 3]. Additionally, metallic cations (alkali and alkaline earth metals) play a significant role in the electronic polarization of N_2, stabilizing its $\pi*$ orbitals an essential step for its activation [3].

This study developed a computational approach to investigate M–N_2 systems, including cooperative and multimetallic configurations. Structural, electronic, and orbital parameters were evaluated with the goal of designing a prototype molecule capable of efficiently activating N_2. Calculations were performed using the ORCA v5.0.4 quantum chemistry package, employing the B3LYP functional and the def2-TZVP basis set. In order to compute key properties such as N–N bond length, bond order, vibrational frequency, electronic polarization, and orbital distribution assessing how these factors influence nitrogen activation. Various systems were explored, considering both the nature of the metal and its coordination mode (end-on and side-on). Transition metals from groups 3 to 12 were studied, with notable results for Y, Os, Hf, Fe, Pt, and Cu, which demonstrated moderate activation. Additionally, cations such as Li^+, Na^+, K^+, Mg^{2+}, and Ca^{2+} were found to induce significant polarization effects. It was also observed that some metals with filled d orbitals can attain energy levels comparable to those of N_2, thereby contributing to its activation. Recent studies have explored various strategies for N_2 activation, each with its own advantages and challenges. Based on the analysis of the results, this research aims to propose an efficient and sustainable strategy for nitrogen activation. Identifying optimal conditions while integrating factors such as energy efficiency, selectivity, scalability, and environmental sustainability as a foundation for future experimental designs.

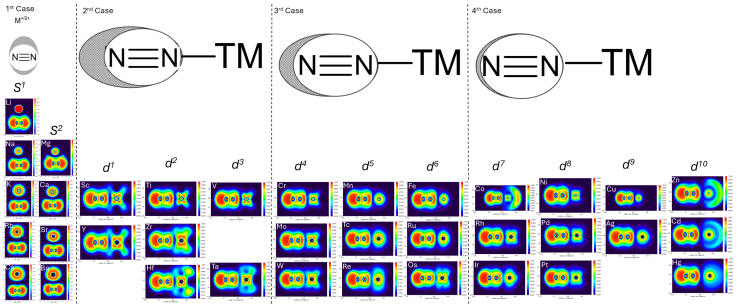

Figure 1: N2 electron cloud modification to Side on and end on systems

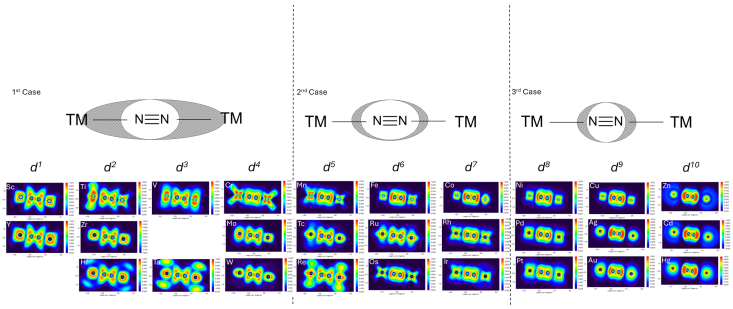

Figure 2: N2 electron cloud modification to bridging end-on system

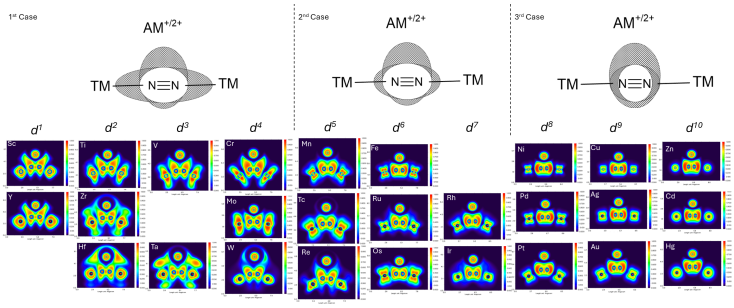

Figure 3: N2 electron cloud modification to Multimetallic cooperative system (TM bridging end-on and AM/AEM side-on system).

References

[1] Allen, A. D.; Loescher, R.; Stevens, J. R.; Whiteley, R. N. Dinitrogen Complexes of the Transition Metals.

[2] Ruiz Herrera, B. L.; Campos González Angulo, J. A.; Barba Behrens, N. Cofactor FeMco (M = Mo, V, Fe) En La Nitrogenasa. *Educación química* **2008**, *19*, 34–41.

[3] Park, H.; Meloni, G. Activation of Dinitrogen with a Superalkali Species, Li3F2. *ChemPhysChem* **2018**, *19*, 256–260. DOI: 10.1002/CPHC.201701232.

Acta Microscopica Vol.35, Supp.1, 2026
Abstract Book NSSY 2026 - Galapagos 17th–23rd May 2026

Development of hydroxyapatite-functionalized polyacrylonitrile polymeric membranes (PAN/HAp) and their application for fluoride removal in aqueous medium

Santiago Guerrero-Jaramillo[1], Giseth Freire[1], Katherine Vaca Escobar[1], Alexis Debut[2], Pablo Bonilla[3], Patricio J. Espinoza-Montero[1,*]

[1] *Pontificia Universidad Católica del Ecuador, Escuela de Ciencias Químicas, Avenida 12 de octubre y Roca, Apartado postal: 17 01 21 84, Quito, Ecuador*
[2] *Centro de Nanociencia y Nanotecnología CENCINAT, Universidad de la Fuerzas Armadas ESPE,171103, Sangolquí, Ecuador*
[3] *Universidad Central del Ecuador. Apartado postal: 17 01 21 84, Quito, Ecuador*
[*] *Corresponding author*
sfguerreroj@puce.edu.ec

Abstract

The health of many Andean communities in South America is compromised by the consumption of volcanic waters with high fluoride concentrations, leading to widespread cases of dental and skeletal fluorosis. This situation underscores the urgent need for affordable and efficient defluoridation technologies suitable for rural and resource-limited setting. In this study, we evaluated polyacrylonitrile (PAN) membranes functionalized with synthetic hydroxyapatite (HAp) as adsorptive materials for fluoride removal from aqueous solutions [1]. The membranes were fabricated by electrospinning and subsequently functionalized with Hap. Their performance was examined through batch adsorption experiments and incorporated into a low-cost filtration device manufactured using 3D-printed polylactic acid (PLA). The filter operated under gravity-driven conditions, ensuring energy-free water treatment. Experimental results showed that membranes containing 1.0% (w/v) HAp achieved fluoride removal efficiencies exceeding 80%. Adsorption data were well described by the Langmuir isotherm, indicating monolayer adsorption, while kinetic analyses revealed a pseudo-second-order model, suggesting physisorption as the dominant mechanism. Importantly, the gravity-fed filter reduced fluoride concentrations from 20 ppm to 4 ppm when processing 1500 mL of contaminated water per cycle, reaching values close to international drinking water guidelines [2]. These findings demonstrate the combined advantages of PAN-HAp membranes, including high-performance adsorption, material stability, and straightforward integration into low-cost filtration systems. The proposed technology offers a promising and scalable strategy to mitigate fluoride-related health risks in vulnerable communities, contributing to safer water access and improved public health outcomes.

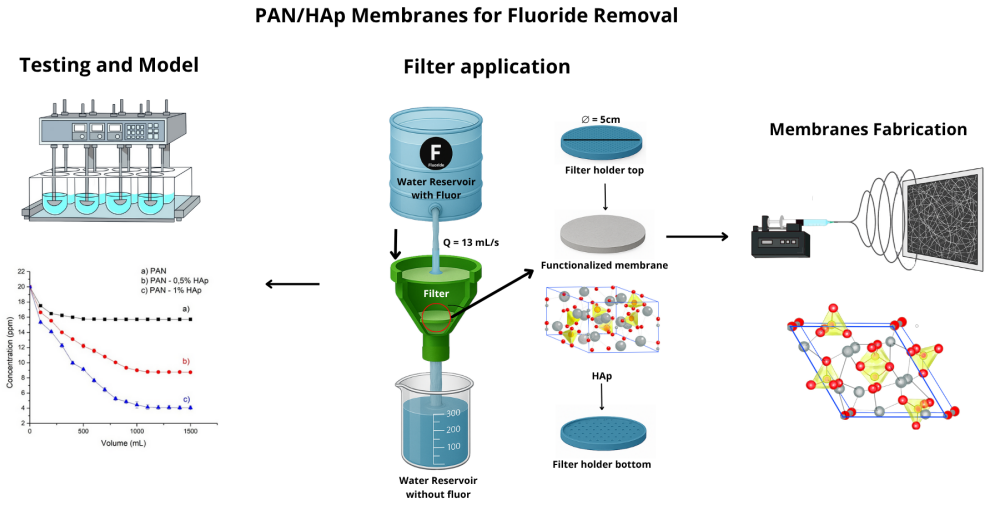

Figure 1: Graphical abstract

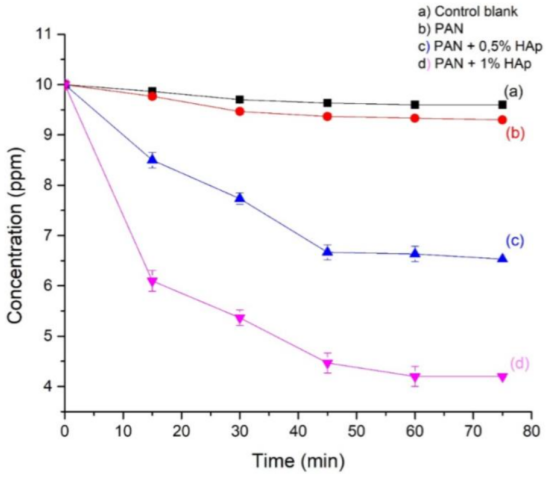

Figure 2: TAdsorption kinetics of a) blank, b) PAN, c) PAN-0.5% HAp, and d) PAN-1% HAp

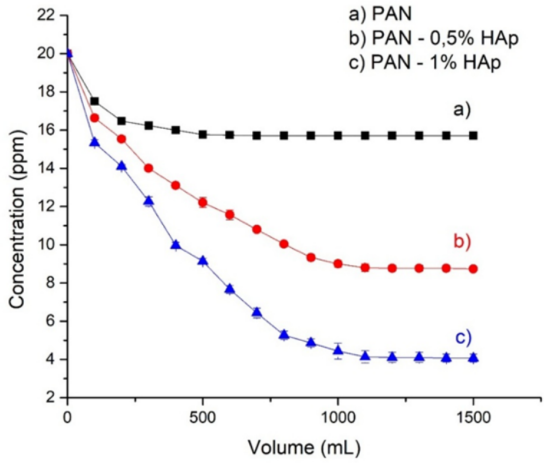

Figure 3: Performance of the PAN/HAp membrane in fluoride removal as a function of the volume treated

References

[1] DenBesten, P.; Li, W. Chronic fluoride toxicity: dental fluorosis. *Monographs in oral science* **2011**, *22*, 81–96. DOI: 10.1159/000327028.

[2] Ahmad, S.; Singh, R.; Arfin, T.; Neeti, K. Fluoride contamination, consequences and removal techniques in water: a review. *Environmental Science Advances* **2022**, *1*, 620–661. DOI: 10.1039/d1va00039j.

Density Functional Theory Calculations to model the Adsorption of Microplastics on $CoFe_2O_4$

Daheny Lopez[1], Duncan Mowbray[1], Sarah Briceño[1]

[1]*School of Physical Sciences and Nanotechnology, Yachay Tech University, Imbabura, Ecuador*
daheny.lopez@yachaytech.edu.ec

Abstract

Microplastic pollution is a significant and growing environmental concern. Polyethylene terephthalate (PET) is one of the most prevalent microplastics, posing substantial risks to aquatic ecosystems [1]. A promising removal technique is magnetic extraction, utilizing hydrophobic magnetic nanoparticles (MNPs) to adsorb microplastics for subsequent separation from water [2]. In this work we investigate the adsorption of PET microplastics onto cobalt ferrite nanoparticles ($CoFe_2O_4$ NPs) using a combined computational and experimental approach. Density functional theory (DFT) calculations will be employed to model the adsorption process and determine optimal interaction parameters, with time-dependent density functional theory (TDDFT), quasiparticle GW, and Bethe-Salpeter equation (BSE) methods employed to obtain the optical absorption spectra. Experimentally, $CoFe_2O_4$ NPs will be synthesized, functionalized to enhance hydrophobicity, and applied in PET adsorption studies, with the material's adsorption efficiency thoroughly characterized using advanced analytical techniques. These findings aim to provide both a fundamental understanding and an effective strategy for mitigating microplastic contamination in water.

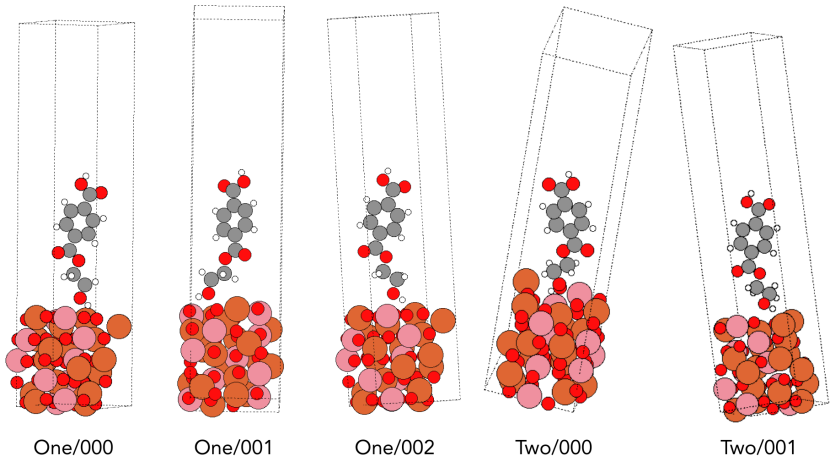

Figure 1: Modeling different adsorption configurations computationally

Sample	Energy					PET: Adsorption Energy	PET :Binding Energy	Adsorption Energy/ KbT	KPET/ (1+KPET)	WATER: Binding Energy	Delta_E	Kwaterpet	Kwaterpet / (1+ Kwaterpet)
	Water Adsorbed	Clean_one_ Water	Clean_CoFe 2O4	Pet	Pet Adsorbed								
/PET/one/001	-533.508721	-13.792319	-518.508564	-162.052448	-681.233281	-0.672269	0.672269	26.890760	1.000000	1.207838	0.535569	2012734335	0.99999999950316
/PET/one/000	-532.81287	-13.792319	-518.508564	-162.052448	-681.215064	-0.654052	0.654052	26.162080	1.000000	0.511987	-0.142065	0.003405	0.00339314210627
/PET/one/002	-533.265389	-13.792319	-518.508564	-162.052448	-681.256109	-0.695097	0.695097	27.803880	1.000000	0.964506	0.269409	47875.5397	0.99997911294330
/PET/two/000	-532.886617	-13.792319	-518.508564	-162.052448	-680.924358	-0.363346	0.363346	14.533840	1.000000	0.585734	0.222388	7299.1998	0.99986301744718
/PET/two/001	-533.236464	-13.792319	-518.508564	-162.052448	-681.303684	-0.742672	0.742672	29.706880	1.000000	0.935581	0.192909	2244.7737	0.99955471916279

Figure 2: Energy Values for the Adsorption Configurations

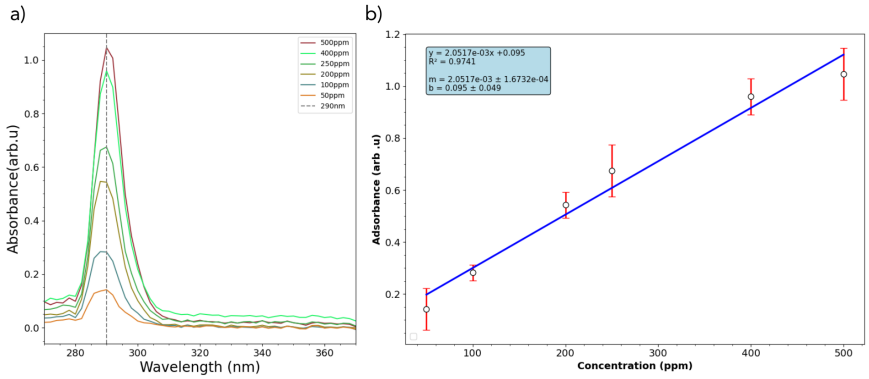

Figure 3: (a) UV-vis spectra of PET at different concentrations, and (b) PET calibration curve.

Number of Species		LCAP PBE -D3 ENERGY (eV)					
Number of PET	Water Molecule		Energy(eV)	Energy per unit of PET	Diff per Molecule		fmax
	# H2O	Energy					
1	0	-13.0422	-140.3209	-140.3209	-140.3209	0.0000	
1	1	-13.0422	-154.0055	-140.9634	-140.9634	-0.6424	0.0221
2	1	-13.0422	-294.9471	-140.9525	-140.9416	-0.6207	0.0289
3	1	-13.0422	-435.8810	-140.9463	-140.9339	-0.6129	0.0290
4	1	-13.0422	-576.8725	-140.9576	-140.9915	-0.6706	0.0292
5	1	-13.0422	-717.8495	-140.9615	-140.9771	-0.6561	0.0298
6	1	-13.0422	-858.7645	-140.9537	-140.9149	-0.5940	0.0299
7	1	-13.0422	-999.7558	-140.9591	-140.9913	-0.6704	0.0288
8	1	-13.0422	-1140.6945	-140.9565	-140.9387	-0.6177	0.0220
9	1	-13.0422	-1281.6886	-140.9607	-140.9941	-0.6732	0.0228
10	1	-13.0422	-1422.7445	-140.9702	-141.0559	-0.7350	0.0295
11	1	-13.0422	-1563.5415	-140.9545	-140.7970	-0.4760	0.0279
12	1	-13.0422	-1704.5972	-140.9629	-141.0557	-0.7348	0.0291

Figure 4: PET Energies

References

[1] Costa, T. B.; Santana, G. B.; Silva, E. M.; Conceição, K. G.; Diaz, G. Z.; Melo, D. Q.; ...; Vidal, C. B. Impact of UV-B Photoaging on Chlorpyrifos Adsorption by PET Microplastics: Insights from Experimental and DFT Analysis. *ACS omega* **2024**, *9*, 46439–46446.

[2] Vohl, S.; Kristl, M.; Stergar, J. Harnessing magnetic nanoparticles for the effective removal of micro-and nanoplastics: a critical review. *Nanomaterials* **2024**, *14*, 1179.

Acta Microscopica Vol.35, Supp.1, 2026
Abstract Book NSSY 2026 - Galapagos 17th–23rd May 2026

Wednesday

Poster Session

Acta Microscopica Vol.35, Supp.1, 2026
Abstract Book NSSY 2026 - Galapagos 17th–23rd May 2026

From excited states to a precise description of van der Waals interactions

Maisincho Brayan[1], Terencio Thibault[1], Jimenez Carlos[2], Cardenas Jorge[3]

[1] *Yachay Tech University. School of Chemical Sciences and Engineering*
[2] *TU Darmstadt*
[3] *Leibniz Institute for Solid State and Materials Research*
brayan.maisincho@yachaytech.edu.ec

Abstract

In the landscape of theoretical chemistry, while covalent and ionic bonds construct the skeletal framework of molecules, it is the intermolecular van der Waals (vdW) interactions that govern supramolecular assembly and dynamics. These non-covalent forces are the architects of soft-matter materials, the drivers of biochemical recognition in pharmaceutical design, and the determinants of polymer folding. Despite their ubiquity and fundamental importance, vdW interactions—specifically the dispersion component—remain challenging to describe fully using standard Density Functional Theory (DFT) [1]. Typically, this component is introduced ad-hoc through semi-classical corrections (e.g., Grimme's D3) [2]. However, dispersion arises fundamentally from quantum mechanical electronic fluctuations, where photon exchange mediates attractive forces across both the London ($1/R^6$) and Casimir–Polder ($1/R^7$) regimes [3]. Theoretically, high-level quantum chemical methods should naturally recover this effect by capturing the full correlation energy. This research aims to provide a first-principles description of dispersion interactions by explicitly analyzing the excited-state symmetrized contributions to the polarizability. By moving beyond ground-state approximations, we isolate the specific electronic transitions that drive long-range molecular attraction. To investigate this, we established a computational protocol centered on the methane dimer system using the ORCA 6.1 suite and the accurate ANO-RCC-QZP basis set. We employed Complete Active Space Self-Consistent Field (CASSCF) calculations, initialized with MP2 natural orbitals, and progressively expanded the active space (from 2 to 12 orbitals) and the number of solved roots (up to 100 states). Perturbative corrections (CASPT2) were applied to recover dynamic correlation. Group theory was rigorously applied to enforce the correct topological description of the molecular orbitals, ensuring consistency with theoretical literature. This approach prevented the spurious orbital mixing observed in symmetry-broken calculations. The monomer was treated under D_2 symmetry (descent from T_d) and the staggered dimer under C_{2h} (descent from D_{3d}). A critical innovation in this workflow was the development of a custom Python module to automate the post-processing of quantum data. This tool extracts transition electric dipole moments and excitation energies from the output to reconstruct the dynamic polarizability tensor $\alpha(i\omega)$ via

the Sum-Over-States (SOS) formalism. To avoid resonance singularities present on the real frequency axis, the integration was performed over the imaginary frequency axis. The isotropic C_6 dispersion coefficients were then determined by numerical integration using the Casimir-Polder identity, and the resulting dispersion energies were calculated in the London limit ($E_{disp} \approx -C_6/R^6$). Results (Figure 1) indicate a stark contrast in efficacy. The linear response TD-DFT method successfully recovers 95% of the reference dispersion energy (compared to the Hartree-Fock plus London Dispersion, HFLD, benchmark). Conversely, wavefunction-based methods face significant convergence challenges. Even with chemically robust active spaces (e.g., CASPT2(8,12) with 20 states), the method recovers only 30% of the total dispersion. Analysis of the electronic response to the field (Figure 2) reveals that while Multireference methods correctly describe the topological shape of the $\alpha(i\omega)$ curve, the magnitude is significantly underestimated. This suggests that the majority of the dispersion energy stems from excitations into high-energy diffuse or virtual orbitals that lie outside the feasible valence active space. In conclusion, while expanding the CAS active space helps identify the symmetry-adapted excitations contributing to dispersion, the slow convergence of the correlation energy renders this approach computationally demanding. To surpass the efficiency of TD-DFT, future wavefunction-based strategies must explicitly integrate triple excitations or include diffuse orbitals in the active space to capture the dynamic long-range correlation required for precise vdW descriptions.

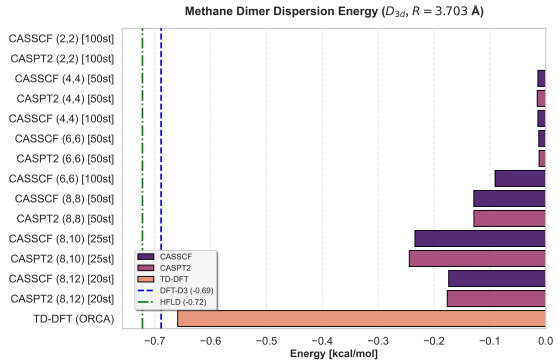

Figure 1: Methane dimer dispersion energy (D_{3d}, R = 3.703 Å).

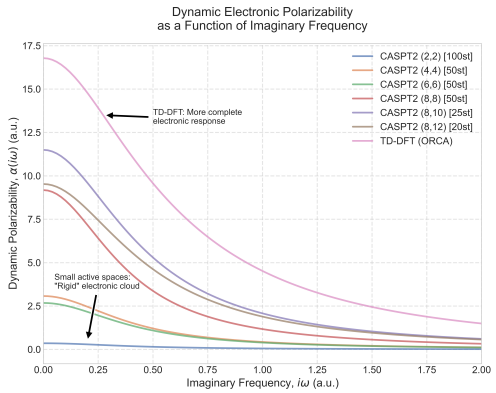

Figure 2: Dynamic electronic polarizability as a function of imaginary frequency.

References

[1] Passerone, D. et al. *Phys. Chem. Chem. Phys.* **2010**, *12*, 992.

[2] Grimme, S. et al. *J. Chem. Phys.* **2010**, *132*, 154104.

[3] Holstein, B. R. *Am. J. Phys.* **2001**, *69*, 441.

Acta Microscopica Vol.35, Supp.1, 2026
Abstract Book NSSY 2026 - Galapagos 17th–23rd May 2026

Phytochemical profiling, antioxidant properties, and anticancer activity of Pourouma cecropiifolia Mart.. from the Ecuadorian Amazon

Carlos Méndez-Durazno[1], Pablo A. Cisneros-Perez[2,3], Noroska G. S. Mogollón[3], Jose R. Mora[4], Sebastián A. Cuesta[4,5], Natalia Bailón-Moscoso[6], Juan Carlos Romero-Benavides[7], Raúl Monge-Sevilla[1], Lenys Fernández[1], David Romero-Estévez[8], Patricio J. Espinoza-Montero[1,*]

[1] *Escuela de Ciencias Químicas, Pontificia Universidad Católica del Ecuador, Quito, Ecuador*
[2] *Grupo de Investigación Aplicada en Materiales y Procesos (GIAMP), School of Chemical Sciences and Engineering, Yachay Tech University, Urcuqui, Ecuador*
[3] *Biomolecules Discovery Group, Universidad Regional Amazónica Ikiam, Tena, Ecuador*
[4] *Departamento de Ingeniería Química, Universidad San Francisco de Quito, Diego de Robles y Vía Interoceánica, Quito, Ecuador*
[5] *Department of Chemistry, Manchester Institute of Biotechnology, The University of Manchester, Manchester, UK*
[6] *Departamento de Ciencias de la Salud, Universidad Técnica Particular de Loja, San Cayetano Alto, Loja, Ecuador*
[7] *Departamento de Química, Facultad de Ciencias Exactas y Naturales, Universidad Técnica Particular de Loja, Loja, Ecuador*
[8] *Centro de Estudios Aplicados en Química (CESAQ), Pontificia Universidad Católica del Ecuador, Quito, Ecuador*
camendezd@puce.edu.ec

Abstract

Despite recent advancements in cancer therapies, a subset of patients develops subsequent drug resistance and various adverse effects. Natural products and their structural derivatives are increasingly recognized as promising anticancer agents, given their antioxidant and anti-mutagenic properties [1–3]. Some fruits are used as promising anticancer agents due to their antioxidant and antimutagenic properties. This work explores the potential of the fruit of Pourouma cecropiifolia Mart.. as a source of compounds with anticancer activity. The research covers: (i) phytochemical profiling of hydroethanolic extracts from the peel, pulp, and seeds of P. cecropiifolia Mart. using liquid ultra-performance chromatography quadrupole time-of-flight mass spectrometry (UPLC-QTOF-MS); (ii) evaluation of antioxidant and anticancer potential of the extracts against carcinoma cell lines (HeLa, RKO, MCF-7, and T47D); and (iii) in silico docking analyses with human cytochrome P450 1A1 (CYP 1A1) and CYP 1B1. A total of 18 compounds were tentatively identified by UPLC-QTOF-MS, including flavonoids, phenolic glycosides, lignans, phenolic acids, terpenes, iridoid glycosides, proanthocyanidins, curcuminoids, and naphthodianthrone. Molecular docking simulations identified nortracheloside and epicatechin as potential inhibitors of CYP 1A1 and CYP 1B1, suggesting cytotoxic activity. The antiproliferation assay showed that pulp extracts had moderate activity against human breast ductal cancer cells.

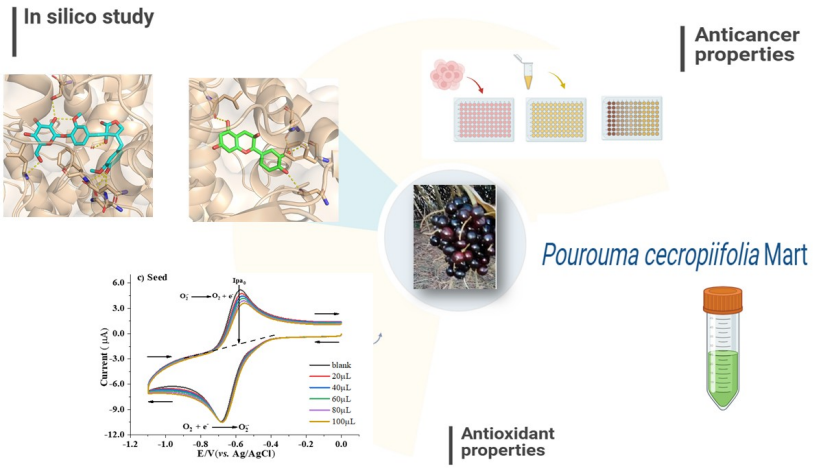

Figure 1: Graphical abstract

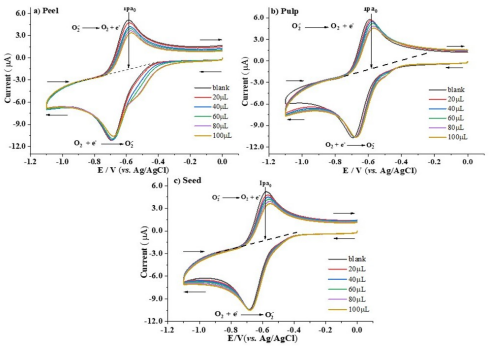

Figure 2: Voltammograms of the oxidation current peak of the superoxide anion at the glassy carbon electrode surface in the presence of varying concentrations of ethanolic extracts from a) peel, b) pulp, and c) seed of P. cecropiifolia Mart. Measurements were performed in DMS + Bu4NPF6 0.05 M at a scan rate of 0.1 V s-1.

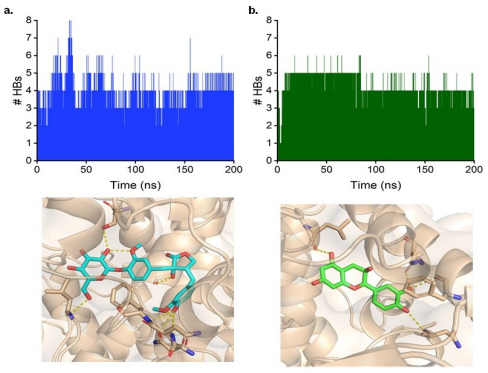

Figure 3: Hydrogen bond analysis of human cytochrome P450 1A1 in complex with a) nortracheloside and b) epicatechin

References

[1] Karges, J. Encapsulation of Ru(II) Polypyridine Complexes for Tumor-Targeted Anticancer Therapy. *BME Frontiers* **2023**, *4* 0024.

[2] Mazurakova, A. Anti-breast cancer effects of phytochemicals: primary, secondary, and tertiary care. *EPMA Journal* **2022**.

[3] Liang, X. et al. Metal-organic framework-based photodynamic combined immunotherapy against the distant development of triple-negative breast cancer. *Biomaterials Research* **2023**, *27* 120.

Acta Microscopica Vol.35, Supp.1, 2026
Abstract Book NSSY 2026 - Galapagos 17th–23rd May 2026

Optical Coherence Tomography Enhancement via Tartrazine Optical Clearing in Biological Tissues

Genesis M. Mendoza-Celorio[1], Pieter Livens[2], Manuel J. Marques[2], Joris J.J. Dirckx[2], Sam Van der Jeught[1]

[1] *Department of Applied Engineering-InViLab Groeneborgerlaan 171, Antwerp 2020, Campus Groenenborger, Belgium*
[2] *Department of Physics-BIMEF Groenenborgerlaan 171, Antwerp 2020, Campus Groenenborger, Belgium*
genegmmc@gmail.com

Abstract

In this work, we investigate the use of tartrazine as an optical clearing agent [1, 2] to enhance imaging performance in optical coherence tomography (OCT). Light scattering limits OCT penetration depth and contrast in biological tissues, particularly in heterogeneous media such as skin. Tartrazine, a water-soluble dye, is explored as a simple approach to reduce these effects. Experiments are performed using ex-vivo chicken breast tissue and ex-vivo rabbit eardrum as representative models. Chicken tissue is used to evaluate optical clearing in a highly scattering environment, while the rabbit tympanic membrane provides a thin biological structure with potential clinical relevance. Samples are treated with tartrazine solutions and OCT imaging is conducted before and after application. Preliminary observations indicate an increase in tissue transparency and improved OCT signal penetration after treatment.



Figure 1: Photograph of ex-vivo chicken tissue. The sample on the left was immersed in water as a control, while the sample on the right was immersed in tartrazine solution. Both samples are placed over a paper with the word "HELLO" to illustrate differences in transparency.



Figure 2: The control sample (left) treated with water remains opaque while the tartrazine-treated sample (right) shows increased transparency, allowing improved visibility of the underlying features.

References

[1] Miller, D. A.; Xu, Y.; Highland, R.; Nguyen, V. T.; Brown, W. J.; Hong, G.; Yao, J.; Wax, A. Enhanced penetration depth in optical coherence tomography and photoacoustic microscopy in vivo enabled by absorbing dye molecules. *Optica* **2024**, *12*, 24. DOI: 10.1364/optica.546779.

[2] Ou, Z. et al. Achieving optical transparency in live animals with absorbing molecules. *Science* **2024**, *385*, eadm6869. DOI: 10.1126/science.adm6869.

Acta Microscopica Vol.35, Supp.1, 2026
Abstract Book NSSY 2026 - Galapagos 17th–23rd May 2026

Development and characterization of hydrogels containing solid lipid nanoparticles as carriers of α-bisabolol for sensitive skin inflammation

Meneses-Arguelles Rossie Inelle[1], Rodríguez-Fuentes César Uriel[1], Cano-Sarmiento Cynthia[1]

[1] *Tecnológico Nacional de México/Instituto Tecnológico de Veracruz, Unidad de Investigación y Desarrollo en Alimentos, Veracruz, México*
inellemeneses@hotmail.com

Abstract

Sensitive skin is associated with impaired barrier function of the stratum corneum, leading to recurrent inflammatory responses and increased vulnerability to external aggressors such as environmental pollutants and ultraviolet radiation; this condition is highly prevalent, with approximately 71% of adults reporting some degree of cutaneous sensitivity [1]. Moreover, conventional topical treatments for sensitive skin, commonly focused on barrier repair or inflammation control, may present challenges related to tolerability due to the presence of potentially irritating components, which has prompted interest in safer alternatives based on natural bioactive compounds. α-Bisabolol, a sesquiterpene derived from chamomile (Matricaria chamomilla), exhibits anti-inflammatory, analgesic, and antioxidant properties; however, its topical application is limited by its low solubility, high volatility, and rapid oxidative degradation [2]. To overcome these limitations, its encapsulation in solid lipid nanoparticles (<500 nm) may improve its protection against degradation and promote deeper skin penetration. Furthermore, incorporation of these nanoparticles into a hydrogel matrix improves their retention and homogeneous distribution on the skin surface, optimizing topical delivery [3]. In this context, this study aimed to develop and characterize a hydrogel containing α-bisabolol-loaded solid lipid nanoparticles for applications in sensitive skin. The SLN was evaluated in terms of physicochemical properties, stability, antioxidant and anti-inflammatory activity, while the rheological behavior of hydrogels was also obtained. SLNs were prepared by hot emulsification followed by high-energy application (homogenization/sonication), using glyceryl monostearate as the solid lipid and combinations of Tween® 80 and phosphatidylcholine (PC) as surfactants. A 3^2 factorial design was applied by varying the α-bisabolol concentration (1,2 and 4 μL/mL) and the Tween® 80: PC ratio (1:0, 2:1 and 4:1). The formulations were characterized in terms of average particle size (APS), polydispersity index (PDI), and zeta potential (ZP) on day 0 and after 28 days of storage, and the formulation with the best performance was selected. This formulation was subsequently evaluated for suspension stability behavior over 5 days to define the appropriate

period for hydrogel formation. Hydrogels were prepared using Carbopol® 940 (0.1%, 0.2%, 0.3%,0.4% and 0.5% p/v), determining the critical gelation concentration and performing rheological evaluation through oscillatory and rotational tests. The formulations exhibited an initial APS ranging from 100 to 300 nm, with PDI values between 0.2-0.3 and negative ZP (-15.7 to -20.0 mV). After 28 days of storage, variations in these parameters were observed, including an increase in APS and PDI, reflecting physical instabilities such as particle aggregation, particularly in formulations without PC (Figure 1). The formulation containing 4 μL/mL of α-bisabolol and a Tween®:PC ratio of 2:1 showed the most favorable storage stability and was therefore selected for subsequent evaluations. This system shows good stability throughout the 5-day evaluation period ideal for gel development. Regarding the hydrogels, the critical gelation concentration was determined at 0.3% p/v (Figure 2), and rheological analysis revealed good structural stability, pseudoplastic behavior, and adequate resistance to shear stress associated with skin spreading, indicating suitable performance during topical application (Figure 3). Overall, these results demonstrate that the incorporation of 4 μL/mL of α-bisabolol into SLNs with a Tween80®: PC ratio of 2:1 provides favorable physicochemical characteristics. Furthermore, its incorporation into a hydrogel matrix results in a formulation with desirable application properties for topical delivery, suggesting its potential as a promising treatment for inflammation in sensitive skin.

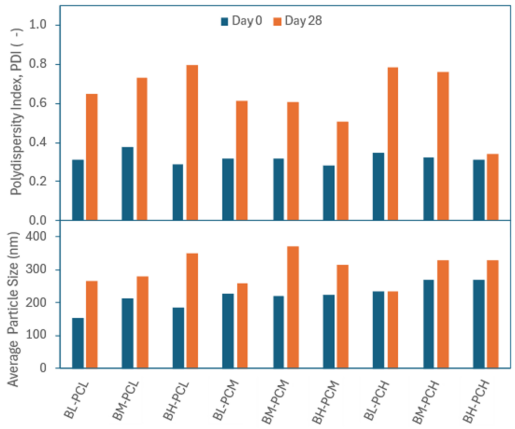

Figure 1: Evolution of average particle size (APS) and polydispersity index (PDI) of solid lipid nanoparticles at day 0 and after 28 days of storage. BL, BM and BH indicate different concentrations of α-bisabolol, while PCL, PCM and PCH indicate different ratios of Tween ® 80:PC.

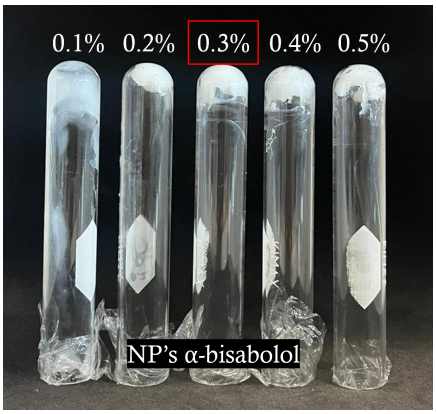

Figure 2: Critical gelation concentration of Carbopol® 940 in hydrogels carrying α-bisabolol solid lipid nanoparticles.

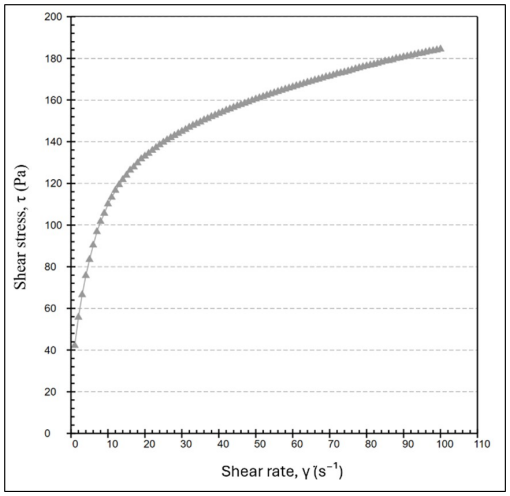

Figure 3: Rheological behavior via flow curve analysis of 0.3% Carbopol® 940 hydrogel carrying α-bisabolol solid lipid nanoparticles.

References

[1] Chen, W.; Dai, R.; Li, L. The prevalence of self-declared sensitive skin: a systematic review and meta-analysis. *Journal of the European Academy of Dermatology and Venereology* **2019**, *34*, 1779–1788. DOI: 10.1111/jdv.16166.

[2] Ramazani, E.; Akaberi, M.; Emami, S. A.; Tayarani-Najaran, Z. Pharmacological and biological effects of alpha-bisabolol: An updated review of the molecular mechanisms. *Life Sciences* **2022**, *304*, 120728. DOI: 10.1016/j.lfs.2022.120728.

[3] Karami, H.; Niavand, M. R.; Haddadi, R.; Noriyan, A.; Vafaei, S. Y. Development of a hydrogel containing bisabolol-loaded nanocapsules for the treatment of atopic dermatitis in a Balb/c mice model. *International Journal of Pharmaceutics* **2024**, *656*, 124029. DOI: 10.1016/j.ijpharm.2024.124029.

Exploring the Use of Chitosan-Based Gels and LED Light in Sustainable Crop Development

Tahis Montalvo[1], Gema González[2], Byron Jorque[2], Sarah Briceño[2], Armando Reyna-Bello[1]

[1] *Universidad de las Fuerzas Armadas, Sede de Santo Domingo*
[2] *School of Physical Sciences and Nanotechnology, Yachay Tech University*
tayis060723@gmail.com

Abstract

The effect of chitosan-based microgels, with and without encapsulated nutrients, on early growth of Solanum lycopersicum (tomato) was assessed under LED wavelengths commonly used in controlled-environment agriculture: blue (λ = 450 nm), green (λ = 525 nm), and red (λ = 730 nm). The experiment was performed in a closed, floating-root hydroponic system to isolate the combined influence of spectral light quality and localized nutrient delivery. Red light produced the strongest enhancement of seedling development, yielding the highest fresh weight (248.28 ± 31.51 mg) and stem height (3.65 ± 0.25 cm) when nutrient-enriched chitosan gel (CS–NPK) was applied. These findings are consistent with the role of red light in activating phytochrome-mediated responses that promote stem elongation and biomass accumulation, while also underscoring how precisely tuned environmental controls can boost hydroponic tomato performance in controlled systems [1]. In contrast, blue light intensified leaf coloration, suggesting stronger photomorphogenic responses, whereas green light showed an intermediate effect on stem biomass and height. Importantly, nutrient-loaded chitosan gels consistently outperformed nutrient-free gels, highlighting microgel-mediated nutrient delivery as a promising strategy to increase input efficiency and plant vigor. Given the growing relevance of hydroponics as a sustainable alternative to conventional soil-based cultivation—particularly when paired with optimized nutrient delivery and environmental control—this approach offers a scalable pathway toward more resource-efficient tomato production [2].

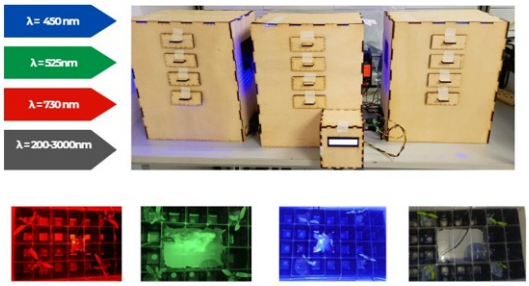

Figure 1: Modular LED-Controlled Growth Chambers for Early Seedling Development Under Defined Light Spectra (450, 525, 730 nm and Broad-Spectrum 200–3000 nm)

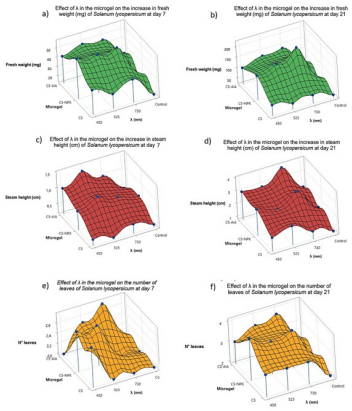

Figure 2: Response surface plots: combined effect of microgel type and light wavelength (λ) on key growth parameters: a. and b. fresh weight (mg), c. and d. stem height (cm), e. and f. number of leaves. (Left side figures correspond to day 7 (a, c, e); right side figures correspond to day 21 (b, d, f)).

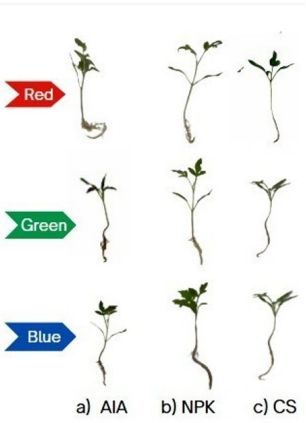

Figure 3: Seedling leaves under different wavelengths, a) AIA, b) NPK and c) CS.

References

[1] Yamamoto, A.; Seki, M.; Koseki, K.; Yabuta, Y.; Shimizu, K.; Arima, J.; Watanabe, F.; Bito, T. Production and characterization of cyanocobalamin-enriched tomato (Solanum lycopersicum) fruits grown using hydroponics. *Journal of the Science of Food and Agriculture* **2022**, *103*, 3685–3690. DOI: 10.1002/jsfa.12297.

[2] Goh, Y. S.; Hum, Y. C.; Lee, Y. L.; Lai, K. W.; Yap, W.-S.; Tee, Y. K. A meta-analysis: Food production and vegetable crop yields of hydroponics. *Scientia Horticulturae* **2023**, *321*, 112339. DOI: 10.1016/j.scienta.2023.112339.

[3] Renganathan, P.; Puente, E. O. R.; Sukhanova, N. V.; Gaysina, L. A. Hydroponics with Microalgae and Cyanobacteria: Emerging Trends and Opportunities in Modern Agriculture. *BioTech* **2024**, *13*, 27. DOI: 10.3390/biotech13030027.

Acta Microscopica Vol.35, Supp.1, 2026
Abstract Book NSSY 2026 - Galapagos 17th–23rd May 2026

Advances in Thermal Conductivity Enhancement of Bio-Based Phase Change Materials through Nano-Additives: A Comprehensive Review

Juan Francisco Nicolalde[1], Javier Martínez-Gómez[1], Víctor H. Guerrero[1], Andrés Chico[1], Gabriela Yanez[1]

[1] *Universidad de Alcalá, Departamento de teoría de la señal y comunicación, (Área de Ingeniería Mecánica) Escuela Politécnica, 28805 Alcalá de Henares, Madrid, España*
[2] *Facultad de Ingenierías Aplicadas y Desarrollo Industrial, Universidad Internacional Del Ecuador UIDE, Quito 170411, Ecuador*
[3] *Facultad de Arquitectura e Ingenierías, Universidad Internacional SEK, Albert Einstein s/n and 5th, Quito 170302, Ecuador*
[4] *Departamento de Ingeniería Química, Escuela Politécnica Nacional (EPN), Quito 170525, Ecuador*
[5] *Department of Materials, Escuela Politécnica Nacional (EPN), Quito 170525, Ecuador*
[6] *Centro de Estudios Aplicados en Química, Pontificia Universidad Católica del Ecuador (PUCE), Quito 170525, Ecuador*
junicolaldego@uide.edu.ec

Abstract

The present review manuscript provides a systematic transition from conventional Phase Change Materials (PCMs) to sustainable Bio-based Phase Change Materials (BPCMs), ultimately focusing on the cutting-edge development of Nano-enhanced Bio-based Phase Change Materials (NeBPCMs). The core of this work aligns with the Nanostructured Materials category as it explores how the controlled dispersion of nano-additives (such as carbon nanotubes, graphene, and metal-oxide nanoparticles) creates a complex, high-surface-area internal architecture within the bio-matrix.

As noted in the literature, the transition from bulk BPCMs to NeBPCMs is fundamentally a challenge of nanostructural design, where the "inclusion of nanoparticles serves to overcome the low thermal conductivity inherent in organic matrices through the formation of percolation networks". Furthermore, this review critically assesses the role of nanostructuring in enhancing the structural stability and preventing leakage in Thermal Energy Storage (TES) and Cold Thermal Energy Storage (CTES) applications [1].

The manuscript evaluates how the morphology and spatial distribution of these nano-additives dictate the thermophysical performance of the composite, stating that "the efficiency of TES systems is directly proportional to the interfacial thermal resistance managed at the nanoscale". By integrating these multi-scale perspectives—from molecular interactions to macro-scale applications in renewable energy systems [2]—this review establishes a comprehensive framework for the development of next-generation nanostructured thermal materials.

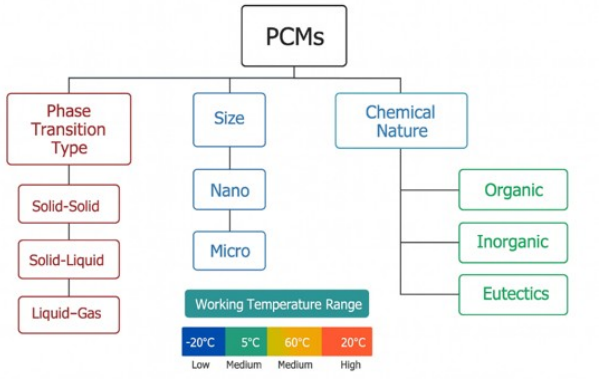

Figure 1: PCMs classification

Metallic nanoparticles				
Nanomaterial	**Base PCM**	**Enhanced Properties**	**Mass fraction**	**Reference**
Copper - Graphene	Beeswax-Coconut oil	TC +604%	2 wt%	(Abdolahimoghadam & Rahimi, 2024b)
Silver	Myristic acid	TC +109.2%	0.3 wt%	(Sivasamy et al., 2019)
Gold (Au)	Coconut oil	Energy storage capacity on a Ag shell +4.87%	25 ppm	(Kazaz et al., 2024b)

Figure 2: Nanoenhaced BPCM by metallic nanoparticles

Metallic oxide nanoparticles				
Aluminum oxide (Al_2O_3)	Myristic acid	TC +149%	2 wt%	(Quikhalfan et al., 2019)
	Coconut oil	Heat transfer rate +8.83%	1 wt%	(Aurangzeb et al., 2022)
Cupric oxide (CuO)	Myristic acid	TC +145%	2 wt%	(Quikhalfan et al., 2019)
	Palmitic-stearic acid eutectic mixture	TC +118.87%	3 wt%	(Agrawal et al., 2022)
Hybrid Silver-Graphene	Lauric Acid	TC +57%; Laten heat +8%	3.5 wt%	(Bhutto et al., 2024)
Manganese dioxide (α-MnO_2)	Capric acid	Laten heat of fusion Up to 9.94%	3 wt%	(Anand et al., 2022)
Iron Oxide – Magnetite (Fe_3O_4)	Coconut oil	Heat transfer rate +8.83%	1 wt%	(Aurangzeb et al., 2022)

Figure 3: Nanoenhaced BPCM by metallic oxide nanoparticles

Carbon based nanoparticles				
Carbon black	Lauric Acid	TC +195%	3.5 wt%	(Mishra et al., 2020)
Carbon Nanotubes (CNT)	Coconut oil	TC +24.1%; Heat transfer rate 33.38%	1 wt%	(Aurangzeb et al., 2022)
	Capric – Stearic acid eutectic mixture	TC +258.3%	5 wt%	(Sarı et al., 2019)
Graphene	Palm wax	TC +13.6%	2 wt%	(Hasbi et al., 2023)
	Beeswax	TC +31.1%	2 wt%	(Hasbi et al., 2023)
	Coconut oil	TC +4.9%	2 wt%	(Hasbi et al., 2023)
Graphite	Lauric acid	Heat energy storage efficiency +72.5%	7 wt%	(Mansor et al., 2023)

Figure 4: Nanoenhaced BPCM by carbon based nanoparticles

References

[1] Zhang, X.; Shi, Q.; Luo, L.; Fan, Y.; Wang, Q.; Jia, G. Research progress on the phase change materials for cold thermal energy storage. *Energies* **2021**, *14*, 8233. DOI: 10.3390/en14248233.

[2] Abdolahimoghadam, M.; Rahimi, M. New hybrid nano- and bio-based phase change material containing graphene-copper particles hosting beeswax-coconut oil for solar thermal energy storage: Predictive modeling and evaluation using machine learning. *Energy* **2024**, *307*, 132604. DOI: 10.1016/j.energy.2024.132604.

Acta Microscopica Vol.35, Supp.1, 2026
Abstract Book NSSY 2026 - Galapagos 17th–23rd May 2026

Synthesis and layer-by-layer assembly of a silicon–organic hybrid diode

Sebastian Ojeda Maza[1], Araceli Granja[1], Werner Bramer[2], Johnny Chimborazo[2], Miguel Herrera-Robledo[1], Floralba López[1]

[1] *Yachay Tech University, School of Chemical Sciences and Engineering*
[1] *Yachay Tech University, School of Physical Sciences and Nanotechnology*
wilmer.ojeda@yachaytech.edu.ec

Abstract

In the quest for sustainable solutions to global energy challenges, hybrid silicon-organic diodes stand out as a transformative technology with the potential to improve optoelectronic devices. By integrating light-trapping nanostructures and conductive π-polymers, these diodes enable scalable and cost-effective approaches for energy harvesting and sensing. However, interfacial heterogeneity and non-ideal charge extraction at hybrid junctions often constrain performance. Here, we design and characterize a layer-by-layer heterostructure diode with an n-Phos/p-SiNW@Ag/TEOS/PANI architecture that combines optimized silicon nanowire (SiNW) texturing for optical trapping with a robust hybrid top contact enabled by Ag nanoparticle (AgNP) decoration and TEOS-assisted polyaniline integration.

To maximize optical confinement while minimizing series resistance, p-type single-side-polished Si wafers were textured by metal-assisted chemical etching (MACE). The front surface was etched at room temperature in 4.8 M HF and 0.005 M $AgNO_3$ for 10 to 120 s, followed by oxidation in 4.8 M HF and 0.1 M H_2O_2 for 30 min and removal of residual Ag in 30% w/w HNO_3. Optical response was evaluated by UV-Vis diffuse reflectance to obtain the weighted-average reflectance (WAR%) and the theoretical current-density limit Jsc,max. AgNPs were photoreduced onto SiNWs from a bath containing 10 mM $AgNO_3$, 0.19 mmol citric acid, and 0.5 mL of 40% HF diluted to 250 mL, under xenon irradiation at 325 nm for 5 min, yielding the SiNW@Ag interface. Organic layers were incorporated by spin coating. Polyaniline (PANI, emeraldine salt) was dissolved in 0.5% w/v formic acid for 48 h in the dark, and a TEOS:IPA adhesion-promoter solution (3:7 v/v) was inserted between SiNW@Ag and PANI. Finally, the wafer backside was phosphorus-doped by controlled diffusion in a CVD furnace to form the n-p junction.

Characterization included UV-Vis diffuse reflectance (WAR% and Jsc,max), AFM, SEM/EDX, Raman/SERS, XRD, four-point probe measurements (sheet resistance), I-V measurements, and EIS with equivalent-circuit fitting. Diffuse reflectance showed a systematic decrease in WAR% with increased MACE time, consistent with enhanced optical trapping in the nanowire network [1]. The SiNW-120 substrate exhibited WAR% = 22.24% and Jsc,max = 35.19 mA/cm^2, indicating

about 80% absorption. MACE increased sheet resistance from 108.7 ohm/sq (c-Si) to 157.20 ohm/sq (SiNW), while Ag decoration reduced it to 28.76 ohm/sq (SiNW@Ag). Direct PANI coating increased resistance (SiNW@Ag/PANI: 207.47 ohm/sq), whereas inserting TEOS reduced sheet resistance to 0.82 ohm/sq and increased conductivity to 2300.97 S/m, highlighting the impact of interface engineering on charge extraction.

After backside phosphorus diffusion, the final n-Phos/p-SiNW@Ag/TEOS/PANI diode showed improved rectification relative to n-Phos/p-SiNW@Ag, including a lower knee voltage (Vk: 1.6 V to 0.16 V), reduced leakage current (Ileak: 1.54×10^{-4} A to 9.05×10^{-5} A), a decreased ideality factor (n: 8.8 to 5.0), and an enhanced current-based rectification ratio (Rrect-I: 26.75 to 36.39). EIS supported accelerated interfacial transport after TEOS/PANI incorporation, with Rs decreasing to 19.75 ohm and Rp dropping from 8.13×10^4 ohm to 2.13×10^4 ohm, while the capacitive response approached ideal behavior. Overall, optimizing SiNWs and controlling the SiNW@Ag/TEOS/PANI interface provides a practical pathway to improve light capture and electrical performance in hybrid diodes, reinforcing the central role of interfaces in high-performance hybrid optoelectronics.

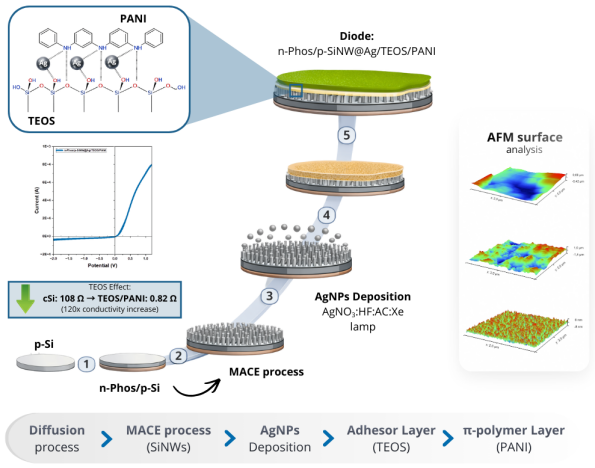

Figure 1: Graphical abstract of the stepwise fabrication of the n-Phos/p-SiNW@Ag/TEOS/PANI hybrid diode, highlighting TEOS-assisted PANI integration for improved interfacial charge extraction.

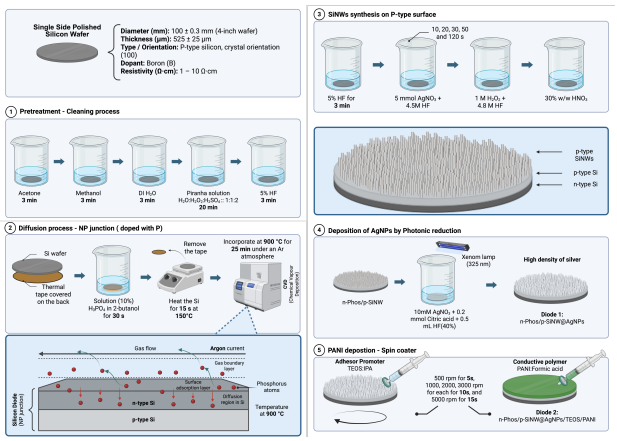

Figure 2: Methodology schematic for the step-by-step fabrication of the n-Phos/p-SiNW@AgNPs/TEOS/PANI hybrid diode: wafer cleaning, backside P diffusion (n–p junction), SiNW formation by MACE, AgNP photoreduction, and TEOS/PANI spin-coating.

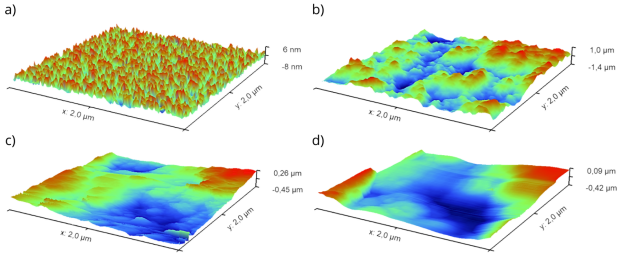

Figure 3: Three-dimensional AFM surface topographies of (a) c-Si, (b) SiNW, (c) SiNWs@Ag, and (d) SiNW@Ag/TEOS/PANI.

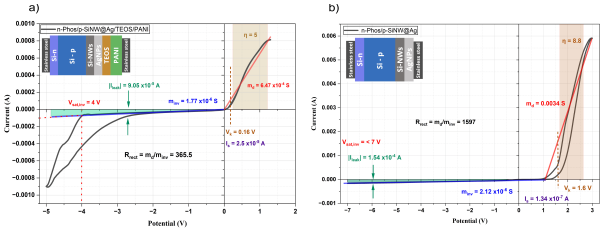

Figure 4: I–V characteristics of (a) n-Phos/p-SiNW@Ag/TEOS/PANI and (b) n-Phos/p-SiNW@Ag diodes

References

[1] Bai, S.; Du, Y.; Wang, C.; Wu, J.; Sugioka, K. Reusable Surface-Enhanced Raman Spectroscopy Substrates Made of Silicon Nanowire Array Coated with Silver Nanoparticles Fabricated by Metal-Assisted Chemical Etching and Photonic Reduction. *Nanomaterials* **2019**, *9*, 1531. DOI: 10.3390/nano9111531.

Acta Microscopica Vol.35, Supp.1, 2026
Abstract Book NSSY 2026 - Galapagos 17th–23rd May 2026

Ab initio study of the electronic properties and magnetic phases of thermoelectric oxide material $Ca_3Co_4O_9$

Alan I. Palma[1], Henry P. Pinto[1]

[1] *CompNano Group– Yachay Tech University, School of Physical Sciences and Nanotechnology*
alan.palma@yachaytech.edu.ec

Abstract

Thermoelectric materials can be used as an alternative sustainable energy source, as they can convert waste heat into power. We performed density-functional theory (DFT) calculations to study the layered calcium cobaltite ($Ca_3Co_4O_9$). We model this system using the generalized gradient approximation (PBE) functional and meta-generalized gradient approximation (meta-GGA) R2SCAN functional. A rational approximation for the supercell was considered to determine the structural and electronic properties and the magnetic phases. The initial magnetic phases are expected to relax to ferromagnetic, antiferromagnetic, and ferrimagnetic phases. Considering the energy, we select the most likely phases, compute the band structure, and discuss it in light of the available experimental data. These results are important for future work, as further calculations are expected to determine the thermoelectric properties of calcium cobaltite [1].

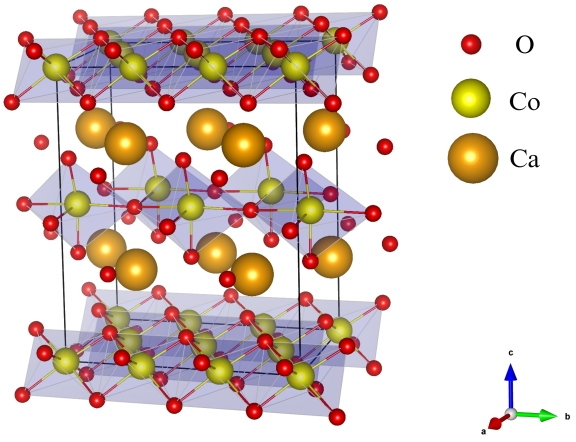

Figure 1: Layered calcium cobaltite $Ca_3Co_4O_9$ supercell (3/2) with CoO 2 octahedra highlighted.

References

[1] Lemal, S.; Varignon, J.; Bilc, D. I.; Ghosez, P. Thermoelectric properties of layered calcium cobaltite Ca 3 Co 4 O 9 from hybrid functional first-principles calculations. *Physical Review B* **2017**, *95*, 075205.

Acta Microscopica Vol.35, Supp.1, 2026
Abstract Book NSSY 2026 - Galapagos 17th–23rd May 2026

Design of pathogen-responsive nanoencapsulated fungicides for soil-borne disease control

Michael A. Pantoja[1]

[1] *Yachay Tech University, School of Physical Sciences and Nanotechnology, Ecuador*
andrespm64@gmail.com

Abstract

Soil-borne fungal diseases represent a persistent challenge in sustainable agriculture due to their long-term survival structures and the limited effectiveness of conventional chemical treatments. Nanotechnology-based delivery systems offer new opportunities for targeted and stimuli-responsive release of agrochemicals, improving efficacy while reducing environmental impact [1].

In this work, we propose a fungicidal nanoencapsulation strategy designed for soil disinfection, where the nanocarrier responds selectively to biochemical signals secreted by the pathogen. These fungal-derived metabolites, associated with growth and nutrient acquisition, are expected to trigger the release of the active agent directly at the infection site, thereby reducing off-target effects and unnecessary chemical dispersion.

The proposed system is based on hybrid polymeric nanocapsules composed of a calcium-crosslinked alginate matrix coated with a bioadhesive chitosan outer layer. This architecture is designed to remain stable under neutral soil conditions while potentially responding to mildly acidic microenvironments generated by pathogen metabolic activity. As a model antifungal compound, timol, a naturally derived phenolic agent with documented antifungal properties, was selected and encapsulated within the polymeric core [2].

The proposed system is particularly relevant for the control of *Spongospora subterranea*, the causative agent of powdery scab in potato crops, a pathogen characterized by persistent resting spores and limited effective management options [3]. While the nanoencapsulated formulation has been successfully synthesized, experimental validation under simulated soil conditions and field-scale characterization are still ongoing.

This approach demonstrates the potential of bioresponsive nanomaterials as a versatile platform for precision agriculture and could be extended to other soil-borne fungal pathogens and crop systems.

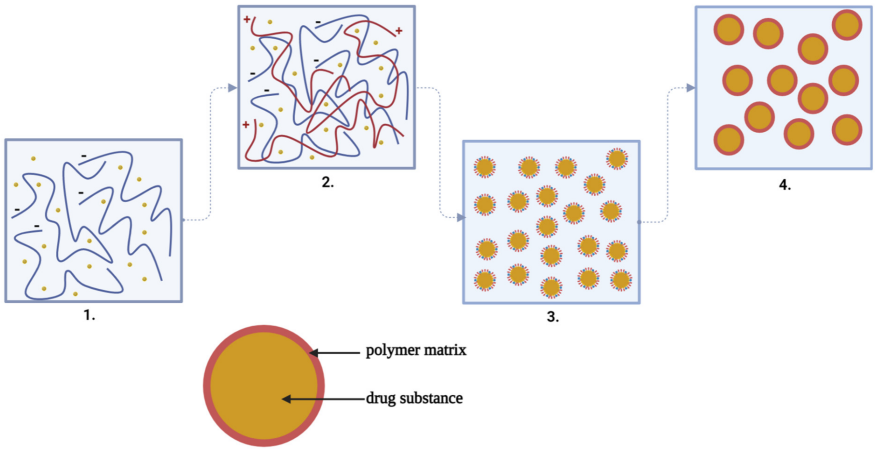

Figure 1: Schematic representation of the nanoencapsulated fungicidal system based on an alginate matrix.

References

[1] Vega-Vásquez, P.; Mosquera-Sánchez, L. P.; López-Galindo, A. Nanostructured delivery systems for controlled release of agrochemicals in sustainable agriculture. *Revista Colombiana de Química* **2020**, *49*, 35–45.

[2] Álvarez-Hernández, M. H.; Martínez-Hernández, G. B.; Castillejo, N.; Martínez, J. A.; Artés-Hernández, F. Development of an antifungal active packaging containing thymol and an ethylene scavenger. Validation during storage of cherry tomatoes. *Food Packaging and Shelf Life* **2021**, *29*, 100734. DOI: 10.1016/j.fpsl.2021.100734.

[3] Strydom, M. J.; van der Merwe, J. J.; Visser, M. Powdery scab of potato: biology, epidemiology and management of Spongospora subterranea. *Frontiers in Bioengineering and Biotechnology* **2024**, *12*, 1297018.

Acta Microscopica Vol.35, Supp.1, 2026
Abstract Book NSSY 2026 - Galapagos 17th–23rd May 2026

KUST-1 as a platform for the controlled release of drugs: Synthesis, Characterization, and kinetic study

Cinthia Perugachi[1], Thibault Terencio[1], Floralba Lopez[1]

[1]*School of Chemical Sciences and Engineering, Yachay Tech University, 100119 Urcuquí, Ecuador*
cinthia.perugachi@yachay.edu.ec

Abstract

In this research, a porous material was synthesized and evaluated as a promising system for controlled drug delivery, specifically addressing its structural stability challenges. The copper-based metal-organic framework (MOF) $Cu_3(BTC)_2$ (BTC = 1, 3, 5-benzenetricarboxylate), known as HKUST-1, is one of the most widely studied systems due to its high surface area, pore volume, and the presence of unsaturated Cu(II) sites with an affinity for coordinating molecules [1]. The study focused on demonstrating the adsorption and encapsulation applications of this material. Initially, solvothermal and hydrothermal synthesis mechanisms were compared against modified variants to develop economically viable methods and improve chemical stability against environmental factors [2]. In this context, a mild synthesis method was implemented, which proved ideal for the purposes of this research. The material was characterized using Powder X-Ray Diffraction (PXRD), Thermogravimetric Analysis (TGA), and Infrared Spectroscopy (FTIR), confirming the integrity of the crystalline structure and the presence of characteristic functional groups. Furthermore, a systematic chemical stability study was conducted using solvents of varying polarities (water, ethanol, hexane, and acetone) via UV-Visible spectroscopy, identifying the optimal conditions to preserve the porous network. The experimental phase continued with the design and execution of two drug-loading methods: in situ (pre-synthesis) and post-synthesis, using paracetamol as a model molecule. In the in situ strategy, the drug was integrated during the MOF nucleation process, while in the post-synthesis approach, encapsulation was performed by activating the vehicle and subsequently immersing it in a drug solution [3]. Encapsulation efficiency was validated through a dual approach: experimentally via PXRD, UV-Vis, TGA, and FT-IR. Results show an 80 percent of yield for the material synthesized by the mild method and 75 percent for the in situ synthesis. Diffraction patterns confirmed the structure by indexing the Miller indices correspond-ing to the HKUST-1 phase reported in the literature. Through UV-Vis stability kinetics, it was determined that ethanol is the most suitable dispersion solvent, with an estimated material lifetime of 24 hours before significant structural changes occur. TGA analysis quantified a loading efficiency of 20 percent for the in situ method, which was superior to the post-synthesis method performed at a known concentration of 4 ppm. Release tests, conducted

in phosphate-buffered saline (PBS), provide the foundation for defining the material's potential in biomedical applications. As a preliminary conclusion, HKUST-1 demonstrates a remarkable capacity for drug encapsulation, positioning itself as a versatile platform in nanomedicine. This work represents the beginning of a research line that seeks to combine the porosity and mechanical stability of inorganic networks with the biodegradability and solubility control required for advanced therapeutics [4]. Finally, future theoretical calculations within this study will allow for the correlation between pore size and the drug's molecular volume, further validating encapsulation efficacy.

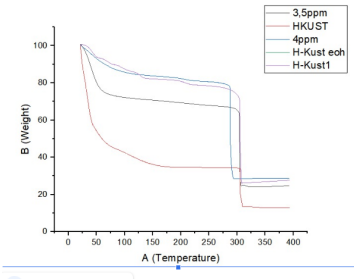

Figure 1: TGA MIX TEST

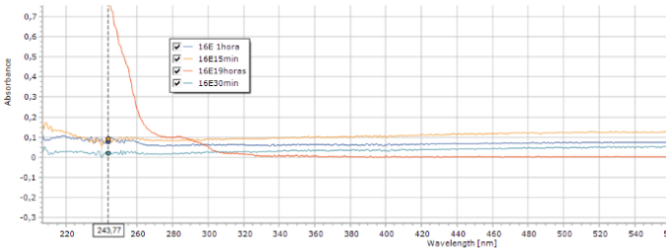

Figure 2: Stability test

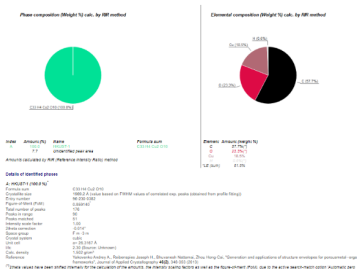

Figure 3: Analisys of composition

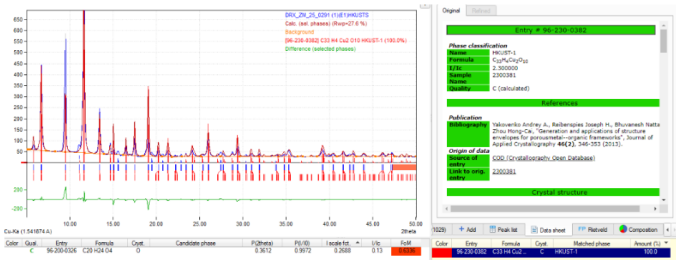

Figure 4: Hkust-1 structure

References

[1] Gautam, S.; Singhal, J.; Lee, H.; Chae, K. Drug delivery of paracetamol by metal-organic frameworks (hkust-1): improvised synthesis and investigations. *Materials Today Chemistry* **2022**, *23*, 100647.

[2] Álvarez, J. R.; Sánchez-González, E.; Pérez, E.; Schneider-Revueltas, E.; Martínez, A.; Tejeda-Cruz, A.; Islas-Jácome, A.; González-Zamora, E.; Ibarra, I. A. Structure stability of hkust-1 towards water and ethanol and their effect on its co 2 capture properties. *Dalton Transactions* **2017**, *46*, 9192.

[3] Singh, C.; Jha, C. B.; Anand, A. S.; Kohli, E.; Manav, N.; Varshney, R.; Upadhyayula, S.; Mathur, R. Copper-based metal–organic framework as a potential therapeutic gas carrier: Optimization, synthesis, characterization, and computational studies. *ACS Applied Bio Materials* **2025**, *8*, 2440.

[4] Loera-Serna, S.; Zarate-Rubio, J.; Medina-Velazquez, D. Y.; Zhang, L.; Ortiz, E. Encapsulation of urea and caffeine in cu3 (btc) 2 metal–organic framework. *Surface Innovations* **2016**, *4*, 76.

Acta Microscopica Vol.35, Supp.1, 2026
Abstract Book NSSY 2026 - Galapagos 17th–23rd May 2026

Visible light driven degradation of bisphenol A using BiOI/BiOBr heterojunctions immobilized in poly(vinyl alcohol

Pillajo Anahi[1], Ojeda Sebastián[1], Criollo Jhon[1], Cuaspa Vanessa[1], Debut Alexis[2], Bautista Jefferson[1], Morales Zhaillmar[1], Herrera Robledo Miguel[1]

[1] *Yachay University. Chemical Sciences and Engineering*
[2] *ESPE University. Chemistry Department*
anahi.pillajo@yachaytech.edu.ec

Abstract

The increasing presence of endocrine disrupting compounds in aquatic environments represents a critical challenge for environmental sustainability and public health. Among these contaminants, bisphenol A (BPA) is widely detected in industrial wastewater and natural water bodies due to its extensive use in polymer manufacturing and its resistance to conventional treatment methods [1]. Advanced oxidation processes based on semiconductor photocatalysis have emerged as promising alternatives for water remediation, particularly when driven by visible light to reduce energy consumption and improve environmental compatibility [2]. In this context, bismuth oxyhalides have attracted considerable attention due to their layered crystal structures, suitable band gaps, and chemical stability under irradiation conditions [3].

The aim of this work is to develop and evaluate sustainable photocatalytic systems based on BiOI/BiOBr heterojunctions immobilized in a poly(vinyl alcohol) (PVA) matrix for the visible light driven degradation of BPA in water. The study seeks to elucidate the role of heterojunction formation on photocatalytic performance by systematically comparing different halide ratios with single component control materials, namely PVA@BiOI and PVA@BiOBr. This approach enables isolation of the contribution of interfacial charge separation to pollutant removal efficiency, thereby strengthening the causal interpretation of the results.

The photocatalytic materials were synthesized using a hydrothermal method, enabling the simultaneous formation of BiOI, BiOBr, and BiOI/BiOBr heterojunctions directly in the poly(vinyl alcohol) (PVA) matrix, with controlled halide ratios (3:1, 2:1, and 1:3). This incorporation ensures effective immobilization, enhanced mechanical stability, and improved applicability for sustainable water treatment. Structural and interfacial features were examined using X-ray diffraction (XRD), Raman spectroscopy, scanning electron microscopy (SEM), and Fourier transform infrared spectroscopy (FTIR). Optical properties were evaluated by diffuse reflectance spectroscopy (DRS) to determine the optical band gap (E_g), Urbach energy (E_U), and weighted average reflectance (WAR). Photocatalytic activity was assessed through BPA degradation under visible light irradiation following a dark adsorption stage.

The photocatalytic performance is dominated by the optimized heterojunction system, BiOI/BiOBr@PVA (3:1), which achieved approximately 39% BPA removal under visible light irradiation, clearly outperforming all other compositions as shown in Figure 2. This enhanced activity is supported by complementary structural, optical, and kinetic analyses. FTIR spectra confirm strong interfacial interactions between PVA and the bismuth oxyhalides, evidenced by shifts and intensity changes in the O–H and C–O vibrational bands, indicating effective immobilization and chemical coupling within the composite matrix. XRD analysis reveals the coexistence of well defined tetragonal BiOI and BiOBr phases without secondary phases, with an estimated crystallite size favoring efficient charge transport across the heterointerface.

Optical characterization further explains the superior performance of the 3:1 heterojunction. As shown in Figure 1, diffuse reflectance spectroscopy yields an optical band gap of approximately $E_g \approx 2.73$ eV, enabling effective visible light absorption, while a reduced weighted average reflectance for BiOI/BiOBr@PVA (3:1) (WAR $\approx 61.41\%$) indicates minimized photon losses compared to the other compositions. In addition, the Urbach energy for the optimized composite ($E_U \approx 0.131$ eV) suggests a relatively low density of sub-band-gap defect states, limiting non-radiative recombination. The photocatalytic reaction follows pseudo first order kinetics, with an apparent rate constant of $k = 4.47 \times 10^{-3}$ s^{-1}, corroborating the efficient utilization of photogenerated charge carriers . Collectively, these quantitative results summarized in Table 1, demonstrate that the synergistic combination of optimized heterojunction architecture and PVA immobilization is responsible for the enhanced BPA degradation efficiency observed for the PVA@BiOI/BiOBr (3:1) system.

In conclusion, this work demonstrates that BiOI/BiOBr heterojunctions immobilized in a PVA matrix constitute an effective and sustainable strategy for the visible light driven degradation of BPA in water. The inclusion of single component control materials confirms that the enhanced performance arises primarily from interfacial charge separation rather than from individual photocatalyst properties alone. By combining efficient pollutant removal with low energy operation and environmentally compatible materials, the proposed system contributes to the development of advanced water treatment technologies aligned with sustainability goals. The findings highlight the potential of heterostructured photocatalysts for addressing emerging water contamination challenges in a resource efficient manner.

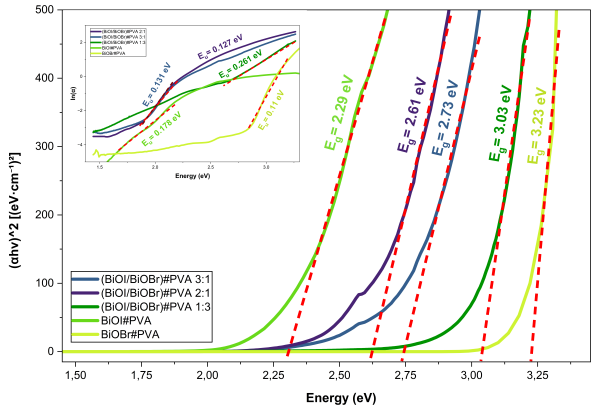

Figure 1: Tauc plots derived from DRS spectra for estimating the optical bandgap (Eg) and Urbach energy (EU) of BiOI/BiOBr@PVA.

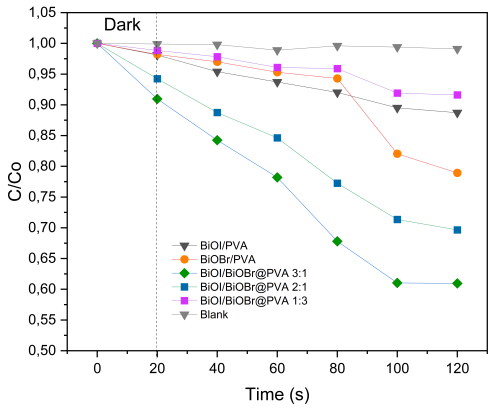

Figure 2: Photocatalytic degradation profiles (C/C_0 vs. time) of BiOI/BiOBr@PVA compounds with different molar ratios and pure compounds

Material	*Eg (eV)*	*EU (eV)*	*WAR (%)*	*k (s⁻¹)*
PVA@BiOI	2.29	0.178	59.53	1.03×10^3
PVA@BiOBr	3.23	0.110	79.93	1.96×10^3
BiOI/BiOBr@PVA (1:3)	3.03	0.261	69.91	7.65×10
BiOI/BiOBr@PVA (2:1)	2.61	0.127	60.53	3.18×10^3
BiOI/BiOBr@PVA (3:1)	2.73	0.131	61.41	4.47×10^3

Table 1: Summary of optical and kinetic parameters of BiOI/BiOBr heterojunction photocatalysts immobilized in PVA.

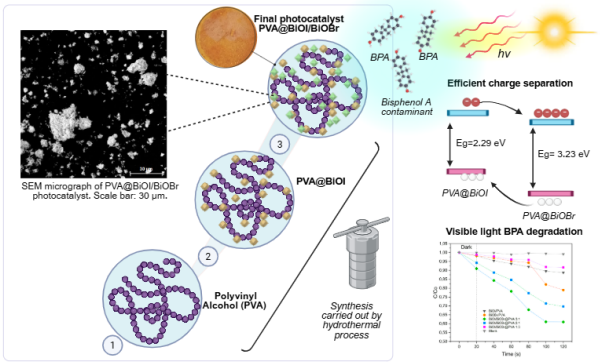

Figure 3: Graphical abstract of BiOI/BiOBr heterojunctions for bisphenol A degradation.

References

[1] Vandenberg, L. N.; Hauser, R.; Marcus, M.; Olea, N.; Welshons, W. V. Human exposure to bisphenol A (BPA). *Reproductive toxicology* **2007**, *24*, 139–177.

[2] Yuan, Z.; Jiang, Z. Applications of BiOX in the photocatalytic reactions. *Molecules* **2023**, *28*, 4400. DOI: 10.3390/molecules28114400.

[3] Jamil, T. S.; Mansor, E. S. Enhancing photocatalytic performance of BiOX for bisphenol-A degradation. *Research Article* **2018**, *2018*, 155–160.

Acta Microscopica Vol.35, Supp.1, 2026
Abstract Book NSSY 2026 - Galapagos 17th–23rd May 2026

Comparative Study of Electrodeposition Techniques Applied to Gas Diffusion Layers (GDLs) for Electrical Conductivity Enhancement

D. Rodriguez[1], A. Sanchez[1], M. Silva[1], J. Armijos[1], B. Tipan[1], J. Escorza[1]

[1] *Yachay Tech University, School of Physical Sciences and Nanotechnology, Urcuqui, 100119, Ecuador*
dylan.rodriguez@yachaytech.edu.ec

Abstract

Gas diffusion layers (GDLs) are essential components in a wide range of electrochemical systems, where they play a critical role in charge transport, gas management, and mechanical support at the electrode interface. Typically composed of porous and electrically conductive materials, GDLs are positioned between the catalyst layer and the current collector, enabling efficient reactant distribution, electron transport, and removal of gaseous species generated during electrochemical reactions. One of the main limitations affecting the performance of electrochemical devices is the presence of ohmic losses, which originate from the intrinsic electrical resistance of cell components and hinder efficient electron transport through the electrode assembly. In particular, a high electrical conductivity of the GDL is required to minimize ohmic losses and contact resistance with adjacent layers, as widely reported in the literature [1]. Consequently, the development of strategies to enhance the conductive properties of GDL membranes has become an important research focus in electrochemical materials science, aiming to improve overall device efficiency and durability.

The aim of this work is to improve the electrical conductivity of GDL membranes through the deposition of conductive salts. To achieve this objective, two electrodeposition techniques are investigated: pulsed potentiostatic electrodeposition and continuous (direct) current electrodeposition. Electrodeposition represents a versatile surface modification strategy, enabling the controlled incorporation of conductive species onto porous substrates while maintaining their functional architecture. The comparative evaluation of pulsed and continuous deposition modes allows assessment of the influence of deposition conditions on the electrical and structural properties of the modified GDL membranes.

The electrodeposition process is carried out using a three-electrode electrochemical cell operated under either pulsed potential or continuous current conditions. This configuration allows precise control of key parameters, including applied potential, pulse duration, and relaxation time. Prior to deposition, GDL membranes undergo surface cleaning and activation to ensure reproducibility and promote adhesion between the deposited material and the carbon substrate. Pulsed electrodeposition is particularly advantageous for porous materials, as it enables improved

control over deposition kinetics and mass transport, reducing the risk of excessive growth and pore blockage [2].

Electrochemical characterization is performed using cyclic voltammetry to evaluate the charge transport behavior of the pristine and modified GDL membranes. The voltammograms presented in Fig. 1 show a linear and symmetric current–potential response, indicating a dominant ohmic behavior with negligible faradaic contributions. Cu-modified GDLs display higher current responses compared to the pristine membrane, evidencing an improvement in electrical conductivity. Among the modified samples, the GDL prepared via pulsed electrodeposition shows the highest slope in the voltammograms, confirming enhanced electron transport properties compared to both the untreated GDL and the continuously deposited counterpart.

Morphological characterization is carried out using atomic force microscopy (AFM) to analyze surface coverage and microstructural features of the pristine and Cu-modified GDL membranes. The AFM images shown in Fig. 2 reveal that the untreated GDL consists of a fibrous carbon network with a highly porous structure and smooth fiber surfaces, confirming the absence of surface deposits. Continuous-current electrodeposition results in partial and non-uniform coverage, characterized by localized deposits along the carbon fibers. In contrast, pulsed electrodeposition leads to a more homogeneous distribution of the deposited material across the GDL surface. Complementary chemical analyses further confirm the presence and stability of the electrodeposited layer on the modified membranes.

In conclusion, both pulsed and continuous electrodeposition techniques enable successful incorporation of conductive material onto GDL membranes, as confirmed by electrochemical and morphological analyses. However, pulsed potentiostatic electrodeposition results in a more uniform surface coverage and a greater improvement in electrical conductivity. These findings prove that electrodeposition, particularly under pulsed conditions, is an effective approach for enhancing the conductive properties of GDL membranes and mitigating ohmic losses in electrochemical systems.

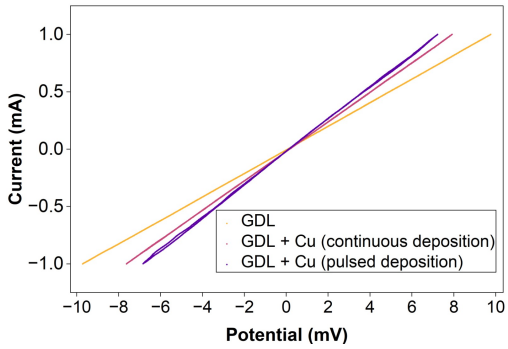

Figure 1: Cyclic voltammograms comparing the electrochemical response of pristine GDL and Cu-modified GDL membranes prepared by continuous and pulsed electrodeposition.

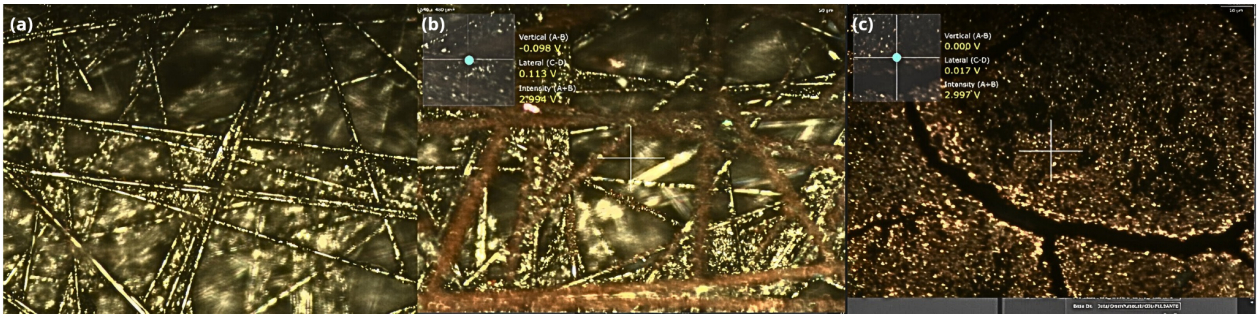

Figure 2: AFM images of (a) GDL membrane, (b) Cu-modified GDL obtained by continuous current electrodeposition, and (c) Cu-modified GDL prepared by pulsed electrodeposition. The images reveal differences in surface coverage and material distribution induced by the deposition technique.

References

[1] Guo, H. et al. *Materials* **2022**, *15*.

[2] Chakrabartty, S. et al. *ChemCatChem* **2024**.

From biological carbon capture to nanostructured biosorbents: processing and characterization of bio-derived carbons

Grzegorz S. Jodłowski[1], **María J. Salazar Macías**[1], Oskar Kaniuczak[1]

[1] *AGH University of Krakow. Faculty of Energy and Fuels, Poland*
[1] *Universidad San Francisco de Quito. College of Biological and Environmental Sciences, Ecuador*
jsalazar@estud.usfq.edu.ec

Abstract

Biological systems provide an attractive platform for producing functional carbon materials while simultaneously addressing challenges related to carbon dioxide mitigation and waste valorization. Microalgae-based systems and biomass-derived carbons enable the conversion of renewable feedstocks into carbonaceous materials, bridging biological CO_2 capture with the engineering of porous solids for environmental and materials science applications [1, 2]. The aim of this work was to integrate two complementary research streams: microalgae-based CO_2 capture and waste-biomass-derived biosorbent production, in order to demonstrate a unified bio-to-nano pathway for generating nanostructured carbon materials with distinct functional roles, ranging from carbon sequestration to liquid-phase adsorption. In the first research stream, *Chlorella* spp. microalgae were cultivated in a coupled gas–liquid photobioreactor system operated for nine weeks under elevated CO_2 concentrations. Two laboratory-scale reactors, each consisting of a 1 L liquid phase and a 1.7 L gas phase, were supplied with a gas mixture containing approximately 10% CO_2. Under these conditions, photosynthetic carbon fixation yielded 7.47 g of dry algal biomass, corresponding to a cumulative CO_2 uptake of 13.52 g. The harvested biomass was dried and pyrolyzed at 450 °C for 60 minutes under a nitrogen atmosphere, producing a stable algal biochar and illustrating the conversion of biologically captured carbon into a solid carbonaceous product [1]. The second research stream focused on the production of nanostructured biosorbents from non-algal waste biomass, including clove rods, walnut shells, orange peels, and spruce cone husks. Following drying and size reduction, approximately 50 pyrolysis experiments and 20 activation experiments were conducted in a quartz tube furnace to ensure reproducibility. Pyrolysis was carried out at 850 °C under nitrogen flow, followed by CO_2 physical activation at the same temperature to induce controlled pore development through carbon gasification, a well-established route for tailoring porosity in biomass-derived carbons [2]. The resulting materials were characterized in terms of mass yield, textural properties, and adsorption performance. Adsorption capacity was evaluated using the Methylene Blue test, while nitrogen adsorption measurements were used to determine BET surface area. Activated biosorbents exhibited a strong enhancement in both surface area and dye uptake compared to their corresponding chars, with adsorption capacities reaching up to

782 mg g^{-1}. However, materials showing extreme increases in BET surface area did not necessarily exhibit proportional improvements in dye adsorption, reflecting limitations associated with pore size distribution and accessibility for larger adsorbate molecules, as described for methylene blue-based assessments [3]. Beyond adsorption capacity and surface area metrics, the comparative analysis of different biomass precursors highlights the role of nanoscale pore architecture in determining material functionality. Despite undergoing identical thermochemical treatments, the resulting carbons exhibited markedly different responses to activation, underscoring the influence of precursor composition on pore formation mechanisms. In particular, the contrast between materials displaying balanced micro–mesoporosity and those dominated by microporosity reveals critical limitations for the adsorption of larger organic molecules. These observations emphasize that surface area alone is insufficient to predict performance, and that pore accessibility, connectivity, and surface chemistry must be considered when designing bio-derived nanostructured carbons for targeted applications. Such insights are especially relevant for the rational engineering of biosorbents intended for liquid-phase remediation and highlight the importance of precursor selection and process control in nanomaterials design. In contrast, algal biochar was not optimized for adsorption applications but demonstrated effective stabilization of biologically assimilated CO_2 into a solid carbon matrix. Overall, this work presents a coherent framework linking biological CO_2 capture, thermochemical conversion, and the engineering of nanostructured carbon materials. The results emphasize that effective material performance emerges from the interplay between pore structure, accessibility, and processing strategy, highlighting sustainable pathways for the development of functional carbon materials from bio-derived feedstocks.

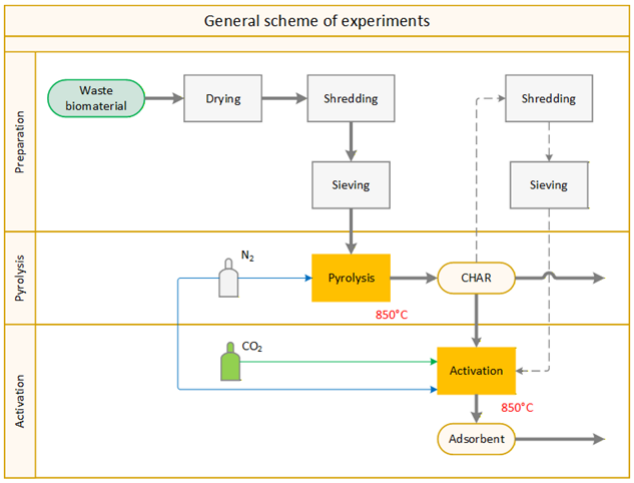

Figure 1: General scheme of experiments illustrating the preparation of waste biomaterials, pyrolysis under nitrogen atmosphere, and subsequent CO_2 activation leading to the production of nanostructured biosorbents.

Biomass precursor	BET surface area (char) (m^2/g)	BET surface area (activated) (m^2/g)	Methylene Blue number (char) (mg/g)	Methylene Blue number (activated) (mg/g)
Clove rod	12.739	188.170	207	647
Walnut shells	138.930	423.514	127	237
Orange peel	0.567	325.556	527	782
Spruce cone husks	34.402	495.514	223	658

Figure 2: BET surface area and methylene blue adsorption capacity of chars and CO2-activated biosorbents derived from different waste biomass precursors. The data demonstrate strong precursor-dependent responses to physical activation. While activation leads to substantial increases in BET surface area for all materials, particularly for orange peel-derived carbons, adsorption performance does not scale proportionally with surface area. This behavior highlights the influence of pore size distribution, pore accessibility, and surface chemistry on dye uptake.

References

[1] Wu, W.; Tan, L.; Chang, H.; Zhang, C.; Tan, X.; Liao, Q.; Zhong, N.; Zhang, X.; Zhang, Y.; Ho, S.-H. Advancements on process regulation for microalgae-based carbon neutrality and biodiesel production. *Renewable and Sustainable Energy Reviews* **2022**, *171*, 112969. DOI: 10.1016/j.rser.2022.112969.

[2] Bedia, J.; Peñas-Garzón, M.; Gómez-Avilés, A.; Rodriguez, J. J.; Belver, C. A Review on the Synthesis and Characterization of Biomass-Derived Carbons for Adsorption of Emerging Contaminants from Water. *C – Journal of Carbon Research* **2018**, *4*, 63. DOI: 10.3390/c4040063.

[3] Nunes, C. A.; Guerreiro, M. C. Estimation of surface area and pore volume of activated carbons by methylene blue and iodine numbers. *Química Nova* **2011**, *34*, 472–476. DOI: 10.1590/s0100-40422011000300020.

Acta Microscopica Vol.35, Supp.1, 2026
Abstract Book NSSY 2026 - Galapagos 17th–23rd May 2026

Laser beam induced current based assessment of a recycled p-type silicon Solar Cell

K. Sulca[1], V. Hinojosa[1], O. Martinez[1]

[1] *Gds-Optronlab, Dpto. Física de la Materia Condensada, Universidad de Valladolid, Paseo de Belén 19, 47011, Valladolid, Spain*
kabirpaul.sulca@uva.es

Abstract

Laser Beam Induced Current (LBIC) mapping has been used as an advanced, spatially resolved electrical characterization technique capable of revealing local photoelectrical phenomena that remain inaccessible to conventional macroscopic measurements. By scanning a tightly focused laser beam across the device surface and recording the corresponding induced current, LBIC enables a direct correlation between local charge collection efficiency and material or process induced inhomogeneities [1]. This high sensitivity to localized recombination, electrically active defects, and transport limitations makes LBIC particularly valuable for the characterization of non-standard or reprocessed photovoltaic materials [2]. In the case of recycled silicon solar cells, where complex recycling steps may introduce subtle yet electrically significant degradation, LBIC provides a powerful diagnostic approach to evaluate the true impact of material reuse. Moreover, beyond qualitative imaging, LBIC data can be analyzed quantitatively to extract minority carrier transport parameters, reinforcing the technique's role as a comprehensive tool for advanced materials characterization. In this work, LBIC is applied to evaluate the electrical impact of recycling processes on a p-type crystalline silicon solar cell through spatial mapping of the induced photocurrent and quantitative transport analysis. The experimental LBIC setup and the operating principle of the technique are presented in Figure 1, including (a) the LBIC setup and (b) a schematic representation of the system functionality. The system employs a tightly focused laser beam with controlled wavelength and power, which is raster-scanned across the solar cell surface with micrometric spatial resolution. At each position, the locally induced photocurrent is recorded under short-circuit conditions, allowing the construction of high-resolution current maps directly linked to carrier collection efficiency. This configuration enables a sensitive, contact-based yet non-destructive electrical probing of the photoactive area, positioning LBIC as a powerful tool for the spatially resolved characterization of electronic and optoelectronic semiconductor materials. Figure 2 presents the main LBIC results, including (a) the induced current map and (b) the corresponding reflected light map of the recycled p-type silicon solar cell. The induced current map reveals a pronounced spatial non-uniformity in photocurrent generation, with localized low-current regions distributed across the device area. These regions are not correlated with variations in optical reflectance,

indicating that the observed losses are primarily of electrical origin rather than optical shading effects. The local photocurrent exhibits a non-uniform response, highlighting the presence of electrically active defects and recombination-enhanced zones likely introduced during the recycling process. Such low-current regions can be attributed to fabrication-related defects, including bulk recombination centers, surface damage, or metallization-related inhomogeneities. Beyond qualitative defect identification, the LBIC data are further exploited to estimate the minority carrier diffusion length of the recycled cell. Following a previously established methodology, the busbar is used as an effective groove to analyze the lateral decay of the induced current [3]. Figure 3 shows (a) a selected line scan extracted from the LBIC map and (b) its exponential fitting, from which the diffusion length is determined. This approach provides a direct, contact-free evaluation of carrier transport properties in recycled silicon devices. Overall, this study demonstrates that LBIC is an effective diagnostic tool for both defect visualization and quantitative transport analysis in recycled silicon solar cells, offering valuable insights into the electrical consequences of recycling processes and their impact on device performance.

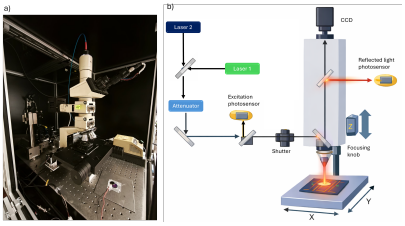

Figure 1: a) LBIC setup and b) setup schematic representation

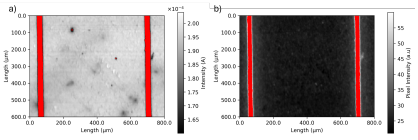

Figure 2: LBIC images: a) Induced Current and b) reflected Light

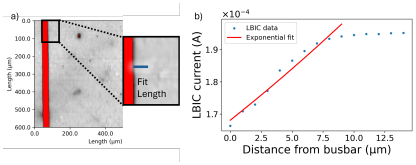

Figure 3: a) Linea profile and b) LBIC line plot and exponential fit

References

[1] Moralejo, B.; González, M. A.; Jiménez, J.; Parra, V.; Martínez, O.; Gutiérrez, J.; Charro, O. LBIC and Reflectance Mapping of Multicrystalline Si Solar Cells. *Journal of Electronic Materials* **2010**, *39*, 2010 39:6 (2010), 39, 663., 663.

[2] Takeshita, T.; Murakami, E. Analysis of Multicrystalline Si Solar Cell Improvement Using Laser-Beam-Induced Current Technique. *IEEE Transactions on Device and Materials Reliability* **2024**, *24*, 219.

[3] Navas, J.; Guillén, E.; Alcaíntara, R.; Fernaíndez-Lorenzo, C.; Martín-Calleja, J.; Oskam, G.; Idígoras, J.; Berger, T.; Anta, J. A. Direct estimation of the electron diffusion length in dye-sensitized solar cells. *Journal of Physical Chemistry Letters* **2011**, *2*, 1045.

Acta Microscopica Vol.35, Supp.1, 2026
Abstract Book NSSY 2026 - Galapagos 17th–23rd May 2026

Nickel Sulfide Nanostructures and Nitrogen-Doped Multiwalled Carbon Nanotubes: Synthesis, Characterization, and Electrochemical Properties

Torres-Xolocotzin A. Paulina[1], Saldaña-Colorado Jessica[2], Flores-López Zacek D.[3], Padilla-Teniente Brenda V.[2], Sánchez-Blanco Francisco J.[3], Orea-Calderón Brenda I.[3], Jiménez-Ramírez Luis E.[3], Macclesh del Pino-Pérez Luis A.[3], López-Urías Florentino[3]

[1] *UASLP, Facultad de Ciencias*
[2] *UASLP, Facultad de Ciencias Químicas*
[3] *IPICYT División de Materiales Avanzados*
anapaulinax@gmail.com

Abstract

Nitrogen-doped multi-walled carbon nanotubes (N-MWCNTs) were produced by aerosol-assisted chemical vapor deposition (AACVD). N-MWCNTs were grown at high temperatures (900 °C and 1020 °C) using nickelocene, benzylamine, and thiophene as precursors. The morphology, structure, composition, and surface chemistry of the N-MWCNTs were characterized using Scanning Electron Microscopy (SEM), X-Ray Diffraction (XRD), Fourier Transform Infrared (FT-IR) spectroscopy, Raman spectroscopy, and electrochemical measurements, including Cyclic Voltammetry (CV) and Electrochemical Impedance Spectroscopy (EIS). The N-MWCNTs exhibited a rough surface with Ni-based nanoparticles. The SEM images revealed morphological differences induced by the growth temperature. At 900 °C, the nanotube diameter was approximately 40 nm, with an entangled structure and exhibited a rough surface with bamboo-like features, suggesting periodic modulation along the tube length. This morphology is due to the incorporation of nitrogen and the catalytic effects that favor the formation of compartmentalized structures [1]. The observed roughness can also be attributed to the anchored nanoparticles. In contrast, at 1020 °C, the N-MWCNTs appeared thicker and more robust, with a smoother surface texture and larger diameter (100 nm). The apparent reduction in the external roughness at higher temperatures could be related to the enhanced graphitization and metal nanoparticle sintering. The XRD patterns revealed that both the samples exhibited a broad reflection centered at approximately 26°, corresponding to the (002) graphitic plane of carbon, confirming the presence of turbostratic carbon domains with varying degrees of structural order [2], and NiS2. In addition, the Ni3C crystallographic phase was identified at 900°C [3]. The Ni3C nanoparticles catalyzed the growth of carbon nanotubes, whereas the NiS2 nanoparticles were anchored to the surface. Raman spectroscopy revealed a significant contribution from sp3 carbon materials.

CV curves of the N-MWCNTs synthesized at 900 °C and 1020 °C were measured at different scan rates ranging from 5 to 100 mV/s. CV profiles at 900 °C

exhibit a nearly rectangular shape without defined redox peaks, indicating a typical electrical double-layer capacitive behavior. This suggests that charge storage occurs primarily through the surface adsorption/desorption of ions, with minimal Faradaic contributions. The proportional increase in the current response with the scan rate confirms good electrochemical stability and capacitive efficiency. In contrast, the CV curves at 1020 °C exhibited prominent redox peaks, reflecting faradaic charge storage associated with reversible redox reactions. The redox activity increases with higher scan rates, suggesting fast, reversible electron transfer. This Faradaic behavior is consistent with the enhanced crystallinity and surface chemistry of the high-temperature sample, as previously confirmed by Raman and XRD analyses. These results highlight the critical influence of growth temperature on the electrochemical mechanisms of hybrid materials. These findings reveal exciting possibilities for the use of N-MWCNTs in energy storage. By demonstrating that the electrochemical functionality (from capacitive to Faradaic) can be tailored through the synthesis temperature, this work provides both fundamental insight and a practical blueprint for designing advanced application-specific electrodes.

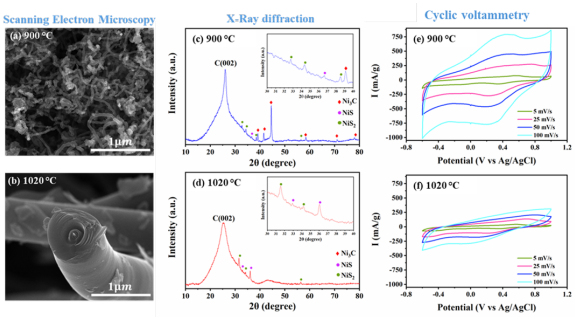

Figure 1: (a-b) SEM micrographs showed that the N-MWCNTs exhibit random growth with a rough surface. (c-d) X-Ray diffraction refers to the typical crystallographic planes of graphitic materials, and the crystallographic cards used for Ni3C and NiS2 are JCPDS 06-0697 and JCPDS 11-0099, respectively. (e-f) Cyclic voltammetry at different scan rates of N-MWCNTs synthesized at (e) 900 °C and (f) 1020 °C. At 900°C, a significant increase in the electrochemical surface area is observed compared to a higher temperature.

References

[1] Tsierkezos, N. G.; Karagianni, A.; Reddmann, E. F.; Ritter, U.; Sanchez, D. E.; Terrones, M.; Kordatos, K. V. Multi-walled carbon nanotubes co-doped with sulfur and nitrogen as sensors for the simultaneous electrochemical determination of biomolecules. *Journal of Solid State Electrochemistry* **2024**, *29*, 1945–1961. DOI: 10.1007/s10008-024-06157-1.

[2] Li, Z.; Lu, C.; Xia, Z.; Zhou, Y.; Luo, Z. X-ray diffraction patterns of graphite and turbostratic carbon. *Carbon* **2007**, *45*, 1686–1695. DOI: 10.1016/j.carbon.2007.03.038.

[3] Fujieda, S.; Shinoda, K.; Suzuki, S.; Jeyadevan, B. Synthesis of Ni Carbide Nanoparticles with Ni_3C-Type Structure in Polyol Solution Containing Dispersant. *MATERIALS TRANSACTIONS* **2012**, *53*, 1716–1720. DOI: 10.2320/matertrans.m2012160.

Acta Microscopica Vol.35, Supp.1, 2026
Abstract Book NSSY 2026 - Galapagos 17th–23rd May 2026

Structure and Optical Properties of Heterometallic Luminescent Antenna Complexes EuxLa1-xTTA3Phen for Latent Fingerprint Detection (LFPs)

Bryan Vargas[1], Andrey Mereshchenko[1]

[1] *Yachay Tech University*
bryan.vargas@yachaytech.edu.ec

Abstract

Rare earth elements (REEs) exhibit very similar chemical properties while displaying markedly different physical behaviors, which makes them attractive for applications in optics, sensing, and advanced functional materials. In particular, europium (III) complexes are widely studied due to their sharp emission lines and long excited state lifetimes. However, the intrinsic f–f transitions of lanthanide ions are parity forbidden, resulting in weak direct absorption. This limitation can be overcome by coordinating lanthanide ions with organic ligands that act as sensitizing antennas, efficiently absorbing excitation energy and transferring it to the metal center [1].

In this work, we investigate the effect of partially substituting optically active Eu^{3+} ions with optically inactive La^{3+} ions on the structural and optical properties of heterometallic luminescent antenna complexes $Eu_xLa_{(1-x)}TTA_3Phen$, with potential application in latent fingerprint detection (LFPs). Previous studies have shown that partial substitution of Eu^{3+} with optically inactive rare-earth ions such as La^{3+} can significantly modify the structural and photophysical properties of heterometallic antenna systems [2].

A straightforward and reproducible synthesis route was developed to obtain a series of complexes with varying Eu/La ratios while preserving the same coordination framework. Structural and chemical characterization was performed using X-ray diffraction (XRD) and Fourier-transform infrared spectroscopy (FTIR). XRD patterns revealed well-defined diffraction peaks for all compositions, indicating high crystallinity and the preservation of the crystal structure upon La^{3+} incorporation. Minor peak shifts were observed as the Eu/La ratio varied, suggesting an isostructural substitution of Eu^{3+} by La^{3+} ions within the lattice without the formation of secondary phases (Figure 1). FTIR spectra confirmed successful coordination between the metal centers and the TTA and phenanthroline ligands, with subtle variations in vibrational bands reflecting changes in the local chemical environment induced by rare-earth doping (Figure 2).

The optical properties of the $Eu_xLa_{(1-x)}TTA_3Phen$ complexes were studied using photoluminescence spectroscopy under UV excitation at 365 nm. All samples exhibited the characteristic emission bands of Eu^{3+} corresponding to the $^5D_0 \rightarrow {}^7F_J$

transitions, with the hypersensitive $^5D_0 \rightarrow {}^7F_2$ transition dominating the emission spectra (Figure 3). A systematic variation in emission intensity and spectral fine structure was observed as a function of La^{3+} content, indicating that partial substitution effectively modifies the local symmetry and energy-transfer efficiency within the antenna system. In addition, the measurements revealed changes in excited-state lifetimes, suggesting a reduction of non-radiative deactivation pathways for specific Eu/La ratios.

These results demonstrate that controlled La^{3+} doping provides an effective strategy to tune both the structural and luminescent properties of Eu-based antenna complexes. The optimized compositions exhibit enhanced emission performance, making them promising candidates for high-contrast luminescent visualization of latent fingerprints [3]. This study highlights the potential of heterometallic rare-earth antenna systems as advanced functional materials for forensic and optical sensing applications.

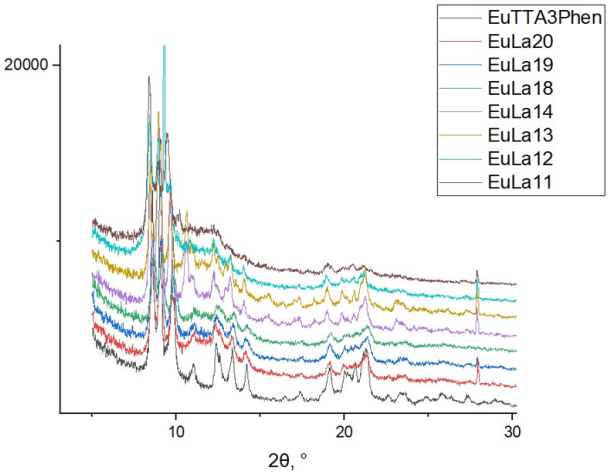

Figure 1: X-ray diffraction (XRD) patterns of $Eu_xLa_{(1-x)}TTA_3Phen$ complexes with varying Eu/La ratios. All samples display well-defined diffraction peaks, confirming their crystalline nature. The absence of additional peaks indicates no secondary phases are formed. Slight shifts in peak positions suggest an isostructural substitution of Eu^{3+} by La^{3+} within the lattice.

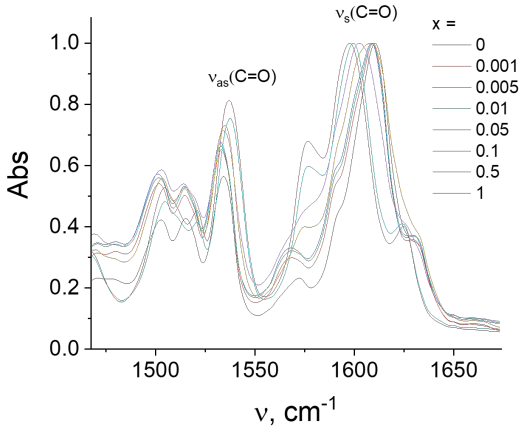

Figure 2: Fourier-transform infrared (FTIR) spectra of $Eu_xLa_{(1-x)}TTA_3Phen$ complexes with different Eu/La ratios. The spectra show characteristic vibrational bands associated with the TTA and phenanthroline ligands, confirming successful coordination. Subtle changes in band position and intensity reflect modifications in the local chemical environment induced by La^{3+} substitution.

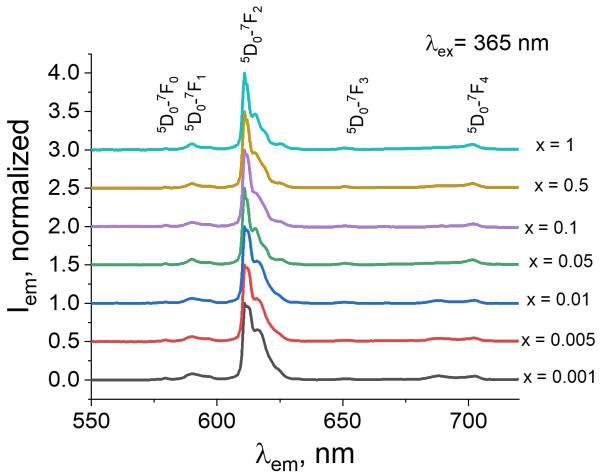

Figure 3: Photoluminescence emission spectra of $Eu_xLa_{(1-x)}TTA_3Phen$ complexes recorded under UV excitation at 365 nm for different Eu/La ratios. All samples exhibit the characteristic Eu^{3+} emission bands corresponding to the $^5D_0 \rightarrow {}^7F_J$ transitions, with the hypersensitive $^5D_0 \rightarrow {}^7F_2$ transition dominating the spectra. Variations in emission intensity and spectral profile are observed as a function of La^{3+} content, indicating modifications in the local coordination environment and energy-transfer efficiency.

References

[1] Wang, Z.; Hu, X.; Yang, Y.; Wang, W.; Wang, Y.; Gong, X.; Geng, C.; Tang, J. Synthesis of Mesoporous and Hollow SiO2@ Eu(TTA)3phen with Enhanced Fluorescence Properties. *Materials* **2023**, *16*, 4501. DOI: 10.3390/ma16134501.

[2] Butorlin, O. S.; Petrova, A. S.; Toikka, Y. N.; Kolesnikov, I. E.; Orlov, S. N.; Ryazantsev, M. N.; Bogachev, N. A.; Skripkin, M. Y.; Mereshchenko, A. S. The Structure and Optical Properties of Luminescent Europium Terephthalate Antenna Metal–Organic Frameworks Doped by Yttrium, Gadolinium, and Lanthanum Ions. *Molecules* **2024**, *29*. DOI: 10.3390/molecules29153558.

[3] Wiwasuku, T.; Chuaephon, A.; Puangmali, T.; Boonmak, J.; Ittisanronnachai, S.; Promarak, V.; Youngme, S. Multifunctional fluorescent Eu-MOF probe for tetracycline antibiotics and dihydrogen phosphate sensing and visualizing latent fingerprints. *RSC Advances* **2023**, *13*, 10384–10396. DOI: 10.1039/d3ra00100h.

Acta Microscopica Vol.35, Supp.1, 2026
Abstract Book NSSY 2026 - Galapagos 17th–23rd May 2026

Magnetic sands: A sustainable nanotech approach to microplastic removal

Josue Vargas[1], Alexandra Vera[1], Werner Bramer-Escamilla[1], Gema Gonzalez[1], Sarah Briceño[1]

[1] *Yachay Tech University School of Physics and Nanotechnology*
ivan.vargas@yachaytech.edu.ec

Abstract

Microplastics, defined as plastic particles smaller than 5 mm, including nanoplastics below 1 μm, have become one of the main environmental threats due to their extensive production and improper disposal of plastic materials. Their presence, now detected in water sources, food, and biological systems, has raised increasing concerns about their impact on ecosystems and human health (Vethaak & Legler, 2021). Despite this growing awareness and potential risks, reliable solutions and strategies remain insufficiently developed. Solving these problems requires the investigation of sustainable and local resources capable of efficient microplastic removal from water.

In this study, we investigate a low-cost remediation approach to microplastic removal using magnetic nanoparticles derived from the naturally titaniferous sands of Anconcito, Ecuador. After different analyses of these sands, it was found that they contain promising magnetic properties due to their composition, including high concentrations of magnetite (Fe_3O_4) and ilmenite ($FeTiO_3$), known for their magnetic responsiveness and adsorption potential, which are enhanced during nanoparticle synthesis. The process of magnetic nanoparticle synthesis was carried out through a top-down ball-milling process selected for its simplicity and scalability. Seven nanoparticle samples of different sizes were prepared depending on the milling time; these samples corresponded to 4, 8, 12, 16, 32, and 52 hours, all at the same frequency. After this, all samples were functionalized with polyethylene glycol (PEG) to improve surface affinity in water while preserving the magnetic properties required for efficient preparation.

The characterization provided Scanning Electron Microscope images (SEM) of the sand, also using X-Ray Diffraction (XRD) the crystal structure of the samples and its evolution during the ball-milling process were analyzed, revealing a gradual loss of its structural order associated with the mechanical synthesis process used. Fourier Transform Infrared (FTIR) was performed to confirm mineral composition and to ensure that the functionalization was successful, its characteristic peaks showed that the functionalization was correctly carried out by revealing the characteristic PEG peak. The study established calibration curves using UV–Vis spectroscopy for polyethylene terephthalate (PET) and polystyrene (PS) microplastics dispersed in water. Furthermore, several experiments were carried out

using controlled concentrations of microplastics dissolved in water and both functionalized and non-functionalized nanoparticles. Among all tested samples, PEG-functionalized nanoparticles milled for 12 hours presented the highest microplastic removal efficiency, achieving 97.08% adsorption for PET, significantly outperforming the untreated samples, showing the critical role of nanoparticle synthesis and surface modification. Overall, this study demonstrates that Ecuadorian titaniferous sands are a promising sustainable resource for magnetic separation technologies aimed at microplastic remediation. Moreover this study shows how controlled nanoparticles synthesis and surface functionalization improve adsorption efficiency. In addition this works contribute to magnetic nanomaterials focused on pollution research and their application in remediation systems particularly in countries with abundant and unexplored natural resources.

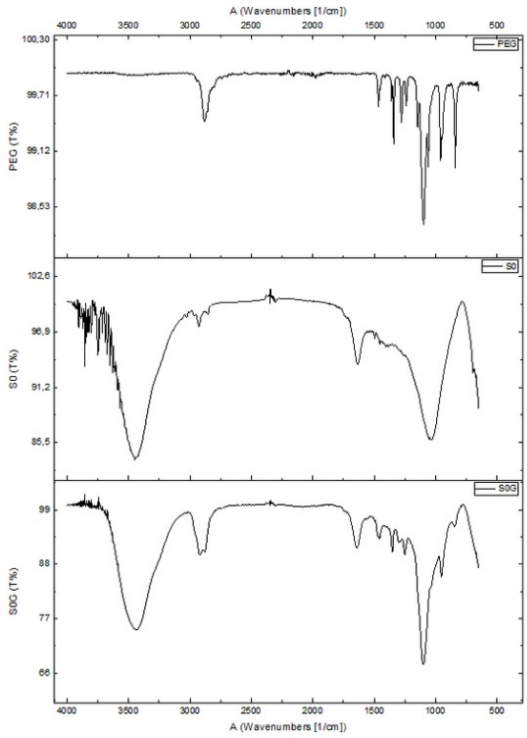

Figure 1: FTIR spectra of PEG, untreated sand, and PEG-functionalized nanoparticles, confirming successful surface functionalization through the appearance of characteristic PEG bands.

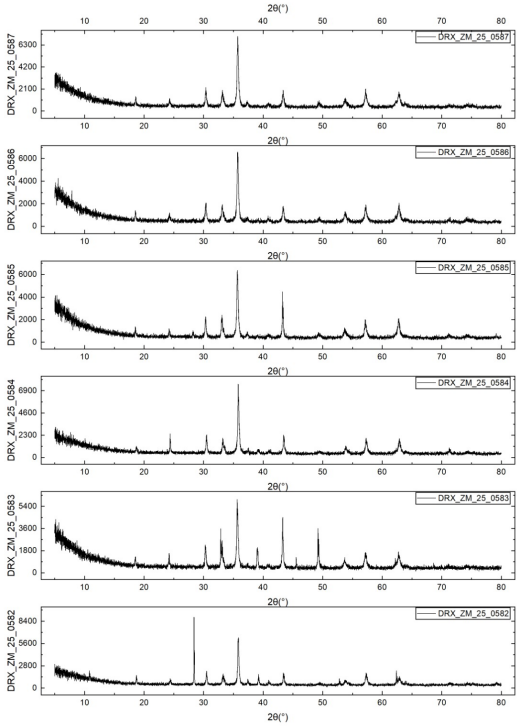

Figure 2: X-ray diffraction (XRD) patterns of raw titaniferous sand and magnetic nanoparticles obtained after different ball-milling times. The evolution of diffraction peaks reveals a progressive reduction in crystallinity and structural order with increasing milling duration, associated with the mechanical top-down synthesis process.

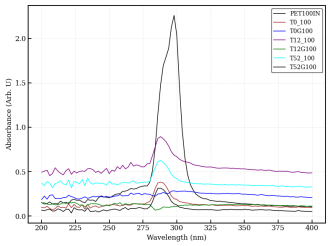

Figure 3: UV–Vis absorbance spectra of PET microplastics (100 ppm) before and after treatment with magnetic nanoparticles synthesized at different milling times, including PEG-functionalized samples. The 12 h PEG-functionalized nanoparticles show the highest removal efficiency.

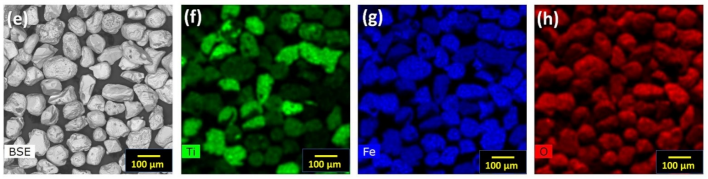

Figure 4: SEM–BSE image and EDS elemental maps of Ti, Fe, and O in titaniferous sand, confirming the mineral composition responsible for its magnetic properties.

References

[1] Zhang, Y. et al. *J. Environ. Sci.* **2025**, *147*, 677–687.

[2] Lopez, D. et al. *Nanotechnol. Environ. Eng.* **2025**, *10*, 83.

[3] Vethaak, A. D. et al. *Science* **2021**, *371*, 672–674.

Magneto-responsive electrospun PVA/chitosan nanofibers functionalized with magnetite nanoparticles for on-demand ciprofloxacin release

Velasco Henry[1], Landázuri Kevin[1], Quijia Christian[1]

[1]*School of Biological Sciences and Engineering, Yachay Tech University, Urcuquí, Ecuador*
henryvelascorojano@gmail.com

Abstract

Antimicrobial resistance is a growing concern worldwide, highlighting the need for drug delivery systems that allow controlled release of therapeutic agents. Magnetic nanoparticles incorporated into polymeric nanofibers have been investigated in various studies as a means to modulate release profiles through the application of external magnetic fields.

This work describes the synthesis and characterization of electrospun nanofibers composed of polyvinyl alcohol (PVA) and chitosan (CS), functionalized with magnetite (Fe_3O_4) nanoparticles and loaded with ciprofloxacin (CIP) as a model antimicrobial drug. The main objective was to assess the magnetic properties of the nanoparticles, the morphology of the resulting nanofibers, the release behavior of the system under passive conditions, and the effects observed in the presence of a low-frequency alternating magnetic field (AMF). Magnetite nanoparticles were synthesized using the chemical co-precipitation method, which involved the reaction of Fe^{2+} and Fe^{3+} salts in alkaline medium under controlled temperature, followed by repeated washing and drying steps to obtain the final powder. The nanoparticles were characterized by X-ray diffraction (XRD), transmission electron microscopy (TEM), and vibrating sample magnetometry (VSM) at body temperature (310 K). The polymeric precursor solution was prepared by blending PVA and CS in a 70:30 ratio, with dispersed magnetite nanoparticles and CIP incorporated prior to electrospinning. Process parameters, including applied voltage, flow rate, and tip-to-collector distance, were systematically adjusted to obtain consistent nanofiber mats, which exhibited a characteristic bead-on-string morphology. In vitro drug release studies were performed in phosphate-buffered saline (pH 7.4) at 37 °C, comparing passive diffusion with exposure to AMF (60 Hz, 246 mT). Antimicrobial activity was evaluated against Escherichia coli ATCC 2522 using turbidimetric growth assays conducted over 20 hours. XRD analysis confirmed the presence of magnetite with a calculated crystallite size of approximately 9.1 nm. VSM results indicated superparamagnetic behavior, with saturation magnetization of 45.4 emu/g and negligible coercivity. Scanning electron microscopy showed thin continuous fibers with average diameters of 24.73 ± 7.79 nm, interconnected by globular beads of approximately 413 nm in diameter. Bead-on-string morphology, which

can result from electrospinning conditions such as solution viscosity and jet instability [1], has been linked to biphasic release in related works [2]. Passive release profiles displayed a rapid initial burst, with about 97.5% of the loaded CIP released within the first 10 minutes. When the AMF was applied, variations in the release rate were observed, consistent with non-thermal mechanisms reported in similar magnetic nanoparticle systems [3]. The CIP-loaded nanofibers demonstrated antimicrobial effects, resulting in substantial reduction of E. coli growth during the observation period. The PVA/CS/Fe_3O_4/CIP nanofibers exhibited magnetic responsiveness and in vitro antimicrobial activity. The bead-on-string structure appeared to influence the observed release characteristics. These results indicate that the system could be suitable for additional studies on magnetically assisted drug delivery approaches.

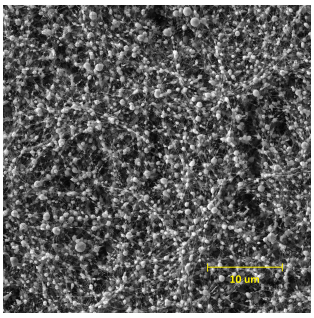

Figure 1: Scanning electron microscopy (SEM) imagen of electrospun PVA/chitosan/Fe_3O_4 nanofibers showing bead-on-string morphology. Scale bar: 10 µm.

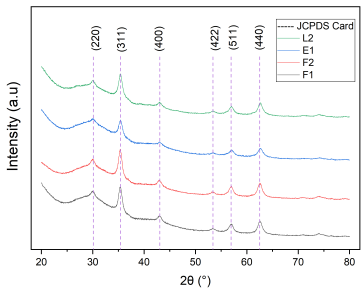

Figure 2: X-ray diffraction (XRD) pattern of synthesized magnetite nanoparticles confirming the inverse spinel structure.

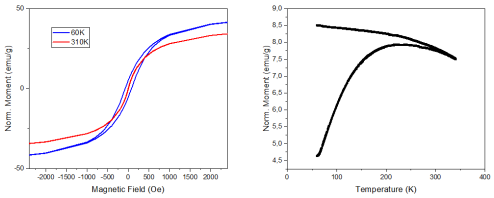

Figure 3: Vibrating sample magnetometry (VSM) hysteresis loop of magnetite nanoparticles at 310 K, showing superparamagnetic behavior with saturation magnetization of 45.4 emu/g.

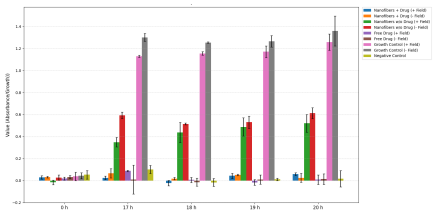

Figure 4: Turbidimetric growth inhibition assay results of ciprofloxacin-loaded nanofibers against Escherichia coli ATCC 2522 over 20 hours.

References

[1] Reneker, D. H.; Yarin, A. L. *Polymer* **2008**, *49*, 2387.

[2] Al-Dhahebi, A. M. et al. *Pharmaceutics* **2020**, *12*, 1073.

[3] Golovin, Y. I. et al. *J. Nanopart. Res.* **2017**, *19*, 64.

Acta Microscopica Vol.35, Supp.1, 2026
Abstract Book NSSY 2026 - Galapagos 17th–23rd May 2026

Phytochemical Characterization and Evaluation of the Pharmacological Properties of Ecuadorian Sugarcane (Saccharum officinarum L.) Extracts

Ariana Véliz[1], Paola Ordoñez[1], Génesis Recalde[2], Lola De Lima[1]

[1] *School of Chemical Sciences and Engineering, Yachay Technological University, Urcuquí, Ecuador*
[1] *School of Biological Sciences and Engineering, Yachay Technological University, Urcuquí, Ecuador*
ariana.veliz@yachaytech.edu.ec

Abstract

This study reports the processing, characterization, and biofunctional evaluation of Ecuadorian sugarcane (*Saccharum officinarum* L.) extracts as natural bioactive materials obtained from an agro-industrial resource. Different plant organs (leaves, stems, roots, and flowers) were processed by exhaustive Soxhlet extraction using solvents of increasing polarity (hexane, ethyl acetate, methanol, ethanol 70%, and water) to generate chemically representative fractions suitable for comparative materials characterization.

Extraction yields showed a strong dependence on both plant organ and solvent polarity, with the highest yield obtained for the aqueous flower extract (78%), followed by the methanolic stem extract (51%). Qualitative phytochemical screening revealed the presence of multiple classes of secondary metabolites, including polyphenols, flavonoids, tannins, alkaloids, saponins, and triterpenoids, indicating a complex chemical composition across the processed materials. Quantitative analysis demonstrated that polar extracts contained the highest concentrations of bioactive components, with the aqueous flower extract exhibiting the highest total phenolic content (863.5 µg/mg) and elevated flavonoid levels observed in aqueous flower and methanolic root extracts (179.3 µg/mg).

The functional performance of the processed extracts was assessed through antioxidant activity assays. DPPH and ABTS radical scavenging tests showed a strong correlation between phenolic content and antioxidant response, with the aqueous flower extract presenting the highest antioxidant capacity in the ABTS assay (TEAC: 0.267 µg/mg). Structural and chemical characterization by Fourier Transform Infrared Spectroscopy (FTIR) confirmed the presence of hydroxyl, carbonyl, and aromatic functional groups associated with bioactive compounds, while High-Performance Liquid Chromatography (HPLC) revealed distinct chromatographic fingerprints as a function of plant organ and extraction solvent, supporting the role of solvent-driven processing on material composition.

Antimicrobial performance evaluation showed selective growth inhibition predominantly associated with aqueous extracts. The aqueous root extract exhibited inhibitory effects against *Escherichia coli*, *Staphylococcus aureus*, *Bacillus cereus*, and *Pseudomonas aeruginosa*, while the aqueous stem extract inhibited the growth

of *Escherichia coli*. These results demonstrate that controlled extraction processing directly influences the chemical architecture and biofunctional properties of sugarcane-derived materials, supporting their potential application in value-added bioactive and functional material systems.

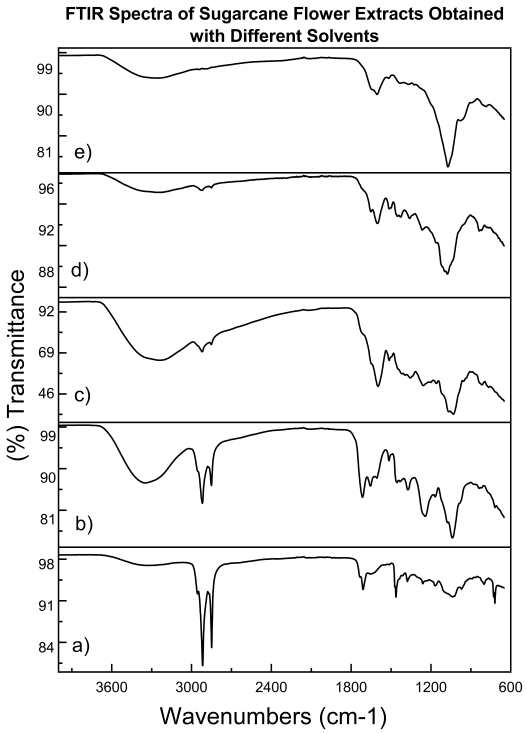

Figure 1: FTIR spectra of sugar cane flower extracts obtained with different solvents: a) hexane extract (FHEX), b) ethyl acetate extract (FAC), c) methanol extract (FME), d) ethanol 70% extract (FE70), and e) water extract (FWA). The spectra show characteristic absorption bands in the region of 4000-600 cm^{-1}, which indicate the presence of functional groups from secondary metabolites.

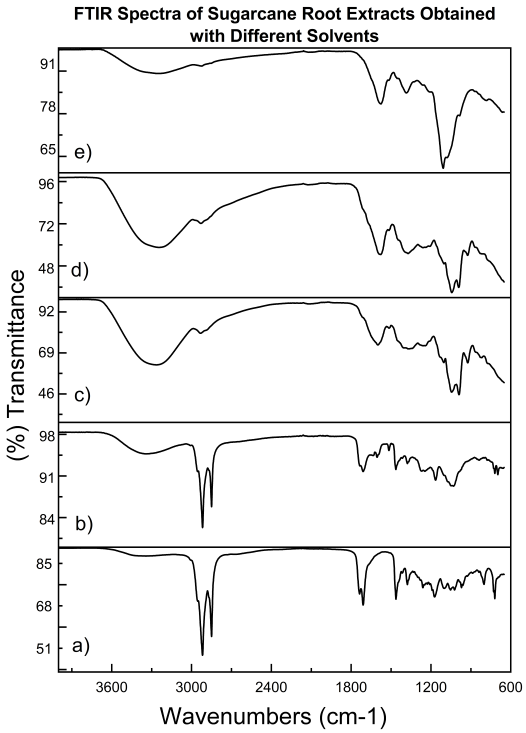

Figure 2: FTIR spectra of sugar cane root extracts obtained with different solvents: a) hexane extract (FHEX), b) ethyl acetate extract (FAC), c) methanol extract (FME), d) ethanol 70% extract (FE70), and e) water extract (FWA). The spectra show characteristic absorption bands in the region of 4000-600 cm^{-1}, which indicate the presence of functional groups from secondary metabolites.

References

[1] Molina-Cortés, A.; Quimbaya, M.; Toro-Gomez, A.; Tobar-Tosse, F. Bioactive compounds as an alternative for the sugarcane industry: Towards an integrative approach. *Heliyon* **2023**, *9*, e13276. DOI: 10.1016/j.heliyon.2023.e13276.

Acta Microscopica Vol.35, Supp.1, 2026
Abstract Book NSSY 2026 - Galapagos 17th–23rd May 2026

$BiFeO_3$/BiOBr Hybrid Photo-Piezocatalysts: Synthesis, Structural–Optical Characterization, and ROS-Mediated Rhodamine B Degradation

Andrés G. Vera-Ochoa[1], Pablo A. Cisneros-Pérez[1], Zaillmar Morales-Navarro[1], Juan Pablo Saucedo-Vázquez[1]

[1]*School of Chemical Sciences and Engineering, Yachay Tech University, 100119 Urcuquí, Ecuador*
marcus98@outlook.com

Abstract

Rhodamine B (RhB) is a synthetic cationic xanthene dye extensively used in textile, food, printing, dyeing, cosmetic, leather, and related commercial sectors. Its high chemical stability, photostability, and poor biodegradability favor persistence in aquatic environments, while recent *in vivo* evidence links RhB exposure with bioaccumulation, oxidative stress, reproductive toxicity, and teratogenic effects in the F1 generation [1]. In this work, $BiFeO_3$/BiOBr hybrid photo-piezocatalysts were synthesized through a hydrothermal route using Bismuth(III) Nitrate Pentahydrate ($Bi(NO_3)_3{\cdot}5H_2O$), Iron(III) Nitrate Nonahydrate ($Fe(NO_3)_3{\cdot}9H_2O$), KBr, and KOH as precursors, followed by magnetic stirring, hydrothermal treatment, centrifugation, washing, and powder recovery, as schematized in Fig. 1. The synthetic design was guided by the strong dependence of $BiFeO_3$ phase purity on hydrothermal parameters, since uncontrolled conditions can promote secondary $Bi_2Fe_4O_9$ formation [2], and by the visible-light photocatalytic response of BiOBr, whose layered oxyhalide structure, moderate band gap, and morphology-dependent activity are favorable for dye degradation [3, 4]. SEM analysis of the hybrid powder revealed an agglomerated plate-/flake-like morphology, while XRD confirmed the coexistence of $BiFeO_3$ and BiOBr crystalline contributions and evidenced improved phase control relative to $BiFeO_3$ samples prone to $Bi_2Fe_4O_9$ formation, as shown in Fig. 2. Diffuse reflectance spectroscopy processed by the Kubelka–Munk method resolved two apparent optical thresholds at approximately 1.62 and 2.67 eV, consistent with the dual semiconductor character of the hybrid system. Photo-piezo degradation assays were carried out using an initial RhB concentration of 5 ppm and a catalyst-to-RhB mass ratio of 50:1 under simultaneous light irradiation and ultrasonic stimulation. At a light power of 40 W, the $BiFeO_3$/BiOBr hybrid catalyst decreased the RhB concentration to $C_t/C_0 = 0.1048$ after 195 min (Fig. 3). The degradation followed pseudo-first-order kinetics, with a rate constant of $k_{app} = 0.01037$ min^{-1} and $R^2 = 0.99693$. A dependence of k_{app} on irradiation power, 60W increased the degradation rate by a factor of 1.62, giving an $k_{app} = 0.0168$ min^{-1}. These results indicate that coupling piezoactive $BiFeO_3$ with photoactive BiOBr promotes structural-optical complementarity and enhances ROS-mediated RhB degradation under dual photo-piezo activation.



Figure 1: Representative hydrothermal workflow for $BiFeO_3$/BiOBr hybrid powder synthesis.

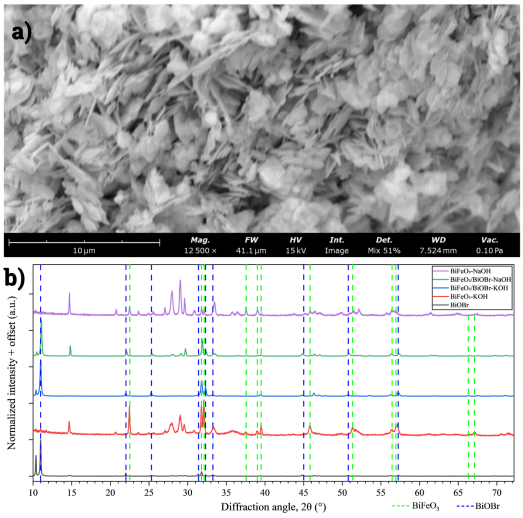

Figure 2: Morphological and structural characterization of the $BiFeO_3$/BiOBr hybrid catalyst. a) SEM micrograph shows an agglomerated plate-/flake-like morphology. b) XRD patterns of $BiFeO_3$ and BiOBr crystalline reflections.

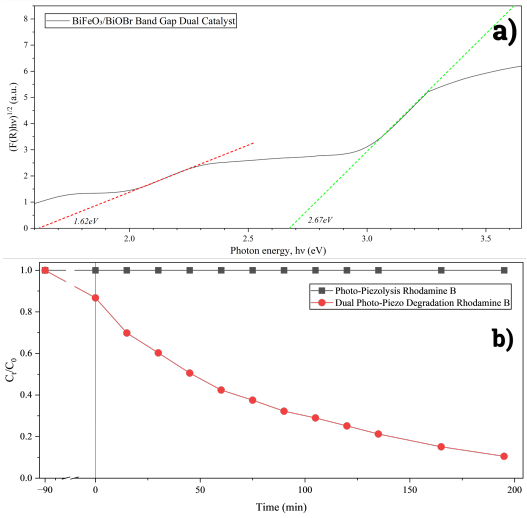

Figure 3: a) Optical behavior of the $BiFeO_3$/BiOBr hybrid catalyst by Kubelka-Munk analysis from DRS. b) Catalytic RhB degradation.

References

[1] Priya, P. S.; Nandhini, P. P.; Vaishnavi, S.; Pavithra, V.; Almutairi, M. H.; Almutairi, B. O.; Arokiyaraj, S.; Pachaiappan, R.; Arockiaraj, J. Rhodamine B, an organic environmental pollutant induces reproductive toxicity in parental and teratogenicity in F1 generation in vivo. *Comparative Biochemistry and Physiology Part C Toxicology & Pharmacology* **2024**, *280*, 109898. DOI: 10.1016/j.cbpc.2024.109898.

[2] Taazayet, W. B.; Zouari, I. M.; Hosni, N.; Dkhil, B.; Mliki, N. T. Facile synthesis of pure BiFeO3 and Bi2Fe4O9 nanostructures with enhanced photocatalytic activity. *Journal of Materials Science Materials in Electronics* **2021**, *33*, 2518–2533. DOI: 10.1007/s10854-021-07459-0.

[3] Wang, X.; Zhang, F.; Yang, Y.; Zhang, Y.; Liu, L.; Lei, W. Controllable synthesis and photocatalytic activity of Nano-BiOBR photocatalyst. *Journal of Nanomaterials* **2020**, *2020*, 1–7. DOI: 10.1155/2020/1013075.

[4] Fan, Z.; Zhao, Y.; Zhai, W.; Qiu, L.; Li, H.; Hoffmann, M. R. Facet-dependent performance of BiOBr for photocatalytic reduction of Cr(vi). *RSC Advances* **2015**, *6*, 2028–2031. DOI: 10.1039/c5ra18768k.

Optimization of Electrochemical Sensors by Using Conducting Polymers and Carbon Quantum Dots (CQDs)

Shamison Villarreal[1], Alex Palma Cando[1], Ibeth Rendón Enríquez[1], María Belen Canchig[1]

[1] *Yachay Tech University*
ptriciovi@gmail.com

Abstract

Emerging contaminants (ECs) in aquatic environments have become a major concern due to their persistence, bioaccumulation, and potential health risks (Smith et al., 2022). This study focuses on developing electrochemical sensors based on conducting polymers—3,4-ethylenedioxythiophene (PEDOT), polypyrrole (PPy), and poly(1,3,5-tris(N-carbazolyl)benzene) (PTCB)—modified with carbon quantum dots (CQDs) for detecting metronidazole (MNZ) as a model EC. CQDs were synthesized via a bottom-up hydrothermal route using citric acid and diethylenetriamine (DETA), and each polymer was individually electropolymerized onto glassy carbon electrodes (GCE) in the presence of CQDs, forming sandwich-type configurations to enhance nanoparticle retention and film stability (Garcia et al., 2021). The modified electrodes were characterized by FTIR and UV–Vis–NIR spectroscopy, confirming the preservation of the polymeric structures, while cyclic voltammetry (CV) was employed to evaluate their electrochemical behavior toward MNZ detection. The incorporation of CQDs significantly improved the electrochemical response in PEDOT- and PPy-based nanocomposites, enhancing current intensity and peak resolution compared to the pristine polymers. In contrast, the effect was minimal or negative in the PTCB-based system, likely due to the lower intrinsic conductivity of this polymer (Lee and Kim, 2020). All modified electrodes exhibited good adhesion and CQD retention after washing tests, demonstrating the robustness of the electropolymerized matrices. These findings show that the interaction between CQDs and conducting polymers depends strongly on the polymer's electronic nature, highlighting the potential of PEDOT/CQDs and PPy/CQDs electrodes as promising materials for developing sensitive and stable electrochemical sensors for detecting ECs in aqueous environments.

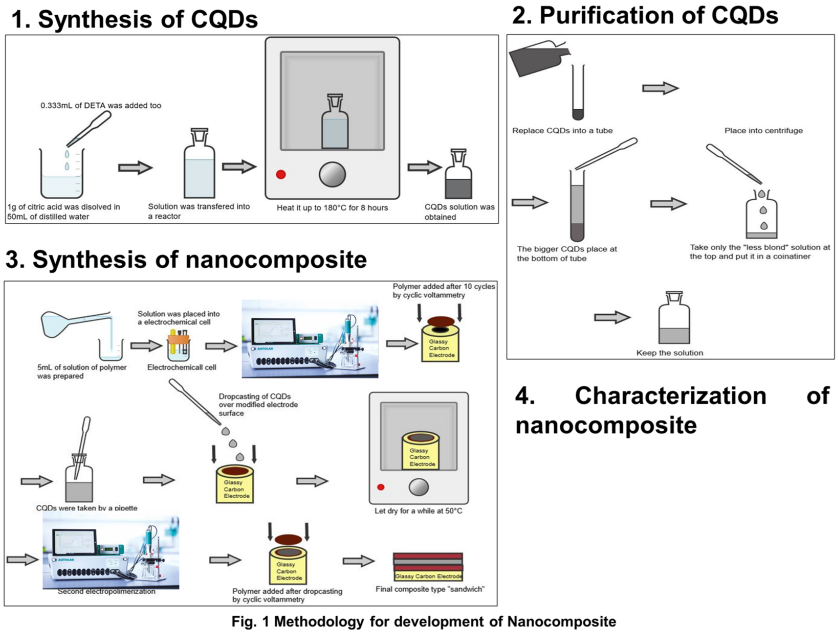

Figure 1: Methodology for development of Nanocomposite

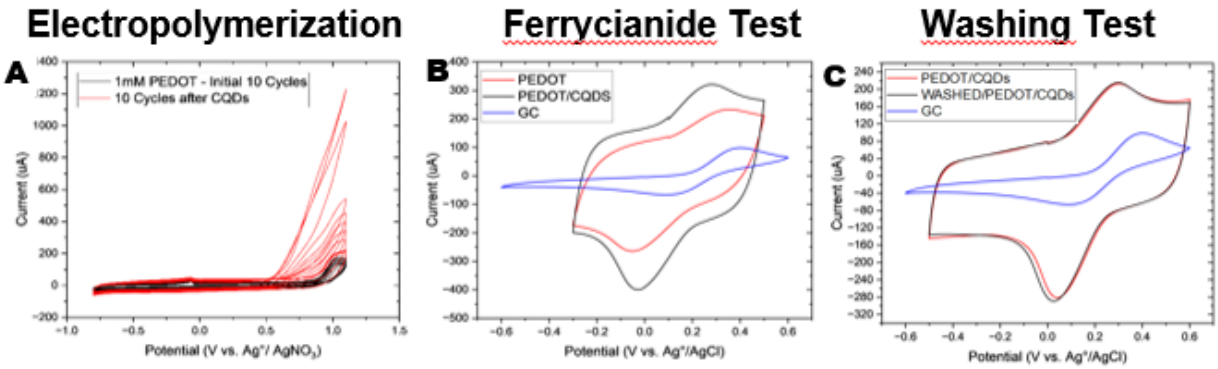

Figure 2: PEDOT Characterization

References

[1] Zhu, J.; Wang, J.; Hou, J.; Zhang, Y.; Liu, J.; Van der Bruggen, B. Graphene-Based Antimicrobial Polymeric Membranes: A Review. *J Mater Chem A Mater* **2017**, *5*, 6776–6793. DOI: 10.1039/C7TA00009J.

[2] Hena, S.; Gutierrez, L.; Croué, J. P. Removal of Metronidazole from Aqueous Media by C. Vulgaris. *J Hazard Mater* **2020**, *384*. DOI: 10.1016/J.JHAZMAT.2019.121400.

[3] Zambrano Mero, J. D.; Delgado Párraga, A. G.; Zambrano Mero, E. T.; Peñaherrera Villafuerte, S. L. Contaminantes Biológicos Presentes En Fuentes de Agua Del Centro-Sur de La Provincia de Manabí, Ecuador. *Siembra* **2022**, *9*, e4011. DOI: 10.29166/SIEMBRA.V9I2.4011.

Acta Microscopica Vol.35, Supp.1, 2026
Abstract Book NSSY 2026 - Galapagos 17th–23rd May 2026

Diatomites grounded Carbon Nanotubes and potential applications in Li-ion systems

Pedro Zamora[1], Sarah Briceño[1], María Fernanda Bósquez-Cáceres[1], Carlos Reinoso[1], Alexis Debut[2], Gema González[1]

[1]*School of Physical Sciences and Nanotechnology, Yachay Tech University, Urcuquí, EC*
[1]*Department of Life Sciences and Agriculture, ESPE - A.F. University, Sangolqui, EC*
pedro.zamora@yachaytech.edu.ec

Abstract

Diatomites are formed of a silica framework, characterized by an ordered porous system of algae microfossils and sediments, generated in aquatic environments and under long-lasting geological activity. Therefore they are locally accessible, in places like the Guayllabamba basin in Ecuador, relatively easy to handle and used for several applications [1]. In particular, after ultrasonic cleaning, suspension and piranha treatment; 3 different samples went through LiCl salt wet impregnation, thermal treatment (TT), and posterior characterization. Moreover, the diatomites' surfaces, and in-situ synthesis of catalyst nanoparticles (NPs) on them; served as substrates and precursors for this novel nanocomposite biomaterial. In fact, co-precipitation of Cobalt Ferrite ($CoFe_2O_4/Fe:Co$) metallic alloy NPs, was achieved for this synthesis; with a molar proportion of 5:3 for Iron and Cobalt Nitrate salts used. As followed by Chemical Vapor Deposition (CVD) [2], in an Ar and Acetylene (C_2H_2) atmosphere at 750°C; it allowed the successful integration of dense Multi Walled Carbon Nanotubes (MWCNTs) coatings. Indeed, they were studied through spectroscopic techniques, X-Ray Diffraction (XRD), X-Ray Photoelectron Spectroscopy (XPS), Scanning and Transmission Electron Microscopy (SEM and TEM); that were performed to corroborate the elemental composition, structure and their changes. Consequently, it was possible to identify the weight gained for each sample, size and disposition of these CNTs: which diameters were around 90nm and covered the substrates almost completely. Furthermore, as the samples were dried and powdered through the different methodology steps, they were pressed in solid pellets using Polyvinylpyrrolidone (PVP) as binder; for the ones that were not consistent enough without it. All this, to be tested through electrochemical impedance spectroscopy (EIS) and Cyclic Voltammetry (CV) to identify their overall electrochemical behavior [3] in Solid-State Electrolyte (SSE) like systems with Cu and Pt electrodes. As a result, they showed stable capacitive responses for the raw samples and the ones containing the Fe:Co NPs, and the well-known conductive behavior; expected for the CNTs coated samples. In addition, they went through CV and Galvanostatic Charge-Discharge tests in an electrochemical cell: first with the pellets connected and hold between Cu tape as working electrodes. However, some of the crude samples and the ones containing the CNTS dissolved in

the LiCl [Deionized Water and Dimethyl Carbonate (DW/DMC) mix] electrolyte. Therefore, attaching the samples to graphite rods, with a conductive adhesive, is another strategy to be carried out. And finally, to complete the cell, Pt was used as counter electrode and Ag/AgCl as the reference electrode. In fact, the results obtained from these systems were used to evaluate the nanocomposites' potential for Li-ion batteries or supercapacitors, and their equivalent circuits. Altogether, this research studies new bio-based, micro- and nanostructured materials, as the next generation of alternative energy technologies.

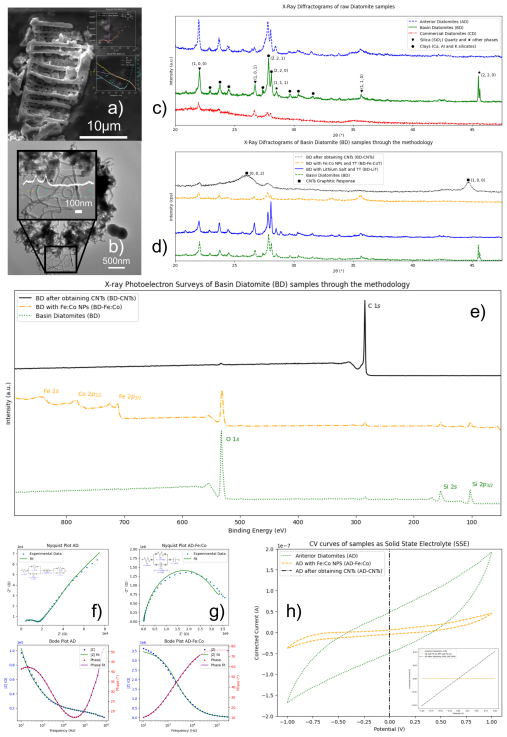

Figure 1: a) BD-Fe:Co SEM and EIS, b) BD-CNTs TEM and Raman Spectra, c) AD, BD and CD XRD, d) XRD of BD samples through the methodology, e) XPS of BD samples, f) AD EIS in SSE system, g) AD-Fe:Co EIS in SSE system, h) AD, AD-Fe:Co and AD-CNTs CVs.

References

[1] Maldonado Pinos, P. N. Natural and doped diatoms for photodegradation under visible light, B.S. thesis, Universidad de Investigación de Tecnología Experimetal Yachay, 2020.

[2] Mina-Villarreal, M. C.; Briceño, S.; Vizuete, K.; Debut, A.; González, G. Growth of carbon nanotubes and carbon spheres on diatoms. *Journal of Porous Materials* **2023**, *30*, 343–349.

[3] Silva, M.; Briceño, S.; Vizuete, K.; Debut, A.; González, G. Structural and electrochemical characterization of diatomite with lignin, glucose, activated carbon and magnetic nanoparticles. *Carbon Trends* **2025**, *19*, 100492.

Acta Microscopica Vol.35, Supp.1, 2026
Abstract Book NSSY 2026 - Galapagos 17th–23rd May 2026

Influence of Carbonization Temperature on the Structure and Surface Chemistry of Hard Carbon Derived from Banana Pseudostem

Luis G. Corredor[1], Juan Pablo Saucedo-Vázquez[1], Jean Jiménez-Castro[1], Jefferson R. Bautista-Jiménez[1], Zaillmar Morales-Navarro[1], Daniela G. Navas-León[1], **Jenny E. Zamora Cepeda**[1]

[1]*School of Chemical Sciences and Engineering, Yachay Tech University, 100119 Urcuquí, Ecuador.*
jennyzamora1200@gmail.com

Abstract

The continuous discharge of synthetic dyes into aquatic environments represents a significant environmental concern due to their high stability, toxicity, and resistance to conventional thewastewater treatment processes. Among these dyes, methylene blue is widely used in textile, pharmaceutical, and chemical industries, and is frequently detected in industrial effluents [1]. In this context, adsorption has emerged as an efficient and versatile technique for dye removal from water, particularly when low-cost and sustainable adsorbent materials are employed. Carbon based materials derived from biomass have gained increasing attention due to their availability, tunable surface properties, and reduced environmental impact.

The aim of this work was to evaluate the adsorption capacity and kinetic behavior of biomass derived Hard Carbon (HC) for the removal of methylene blue from aqueous solutions.

Hard carbon (HC) was synthesized from the pseudostem of Musa paradisiaca (Cavendish) through controlled carbonization. The biomass precursor was separated into cortical and internal stem fractions, yielding compact and fibrous morphologies, with an additional milled form obtained by particle size reduction. Carbonization was performed in a chemical vapor deposition furnace under inert atmosphere at temperatures between 700 and 1100 °C (100 °C increments) and residence times of 120 minutes to evaluate the influence of thermal parameters on HC formation. Post-carbonization modification was carried out via solvent free mechanochemical sodium intercalation, using agate mortar and ball milling. Sodium salts were incorporated at HC:Na mass ratios of 1:0.05, 1:0.1, and 1:0.2, and treated at 180 °C for 24 h to promote ion insertion into the hard carbon structure.

XRD analysis confirmed the formation of non-graphitizable hard carbon across all carbonization temperatures, shown in Figure 1, as evidenced by the presence of broad diffraction features associated with the (002) and (100) planes. At lower carbonization temperatures (700-800°C), the (002) reflection appeared as a diffuse and low-intensity band, indicative of a highly disordered carbon structure with significant interlayer spacing heterogeneity. As the carbonization temperature increased to 900 °C and above, a progressive sharpening and increased intensity of the

(002) band were observed, accompanied by a slight shift toward higher diffraction angles. This behavior suggests a gradual reduction in interlayer spacing and an increase in short-range structural ordering within turbostratic carbon domains [2]. FTIR spectroscopy provided complementary evidence of these temperature driven transformations, which are shown in Figure 2. Samples carbonized at lower temperatures exhibited distinct absorption bands associated with hydroxyl at 3410 $cm^{-}1$, aliphatic C-H at 1629 $cm^{-}1$, the band found at 1037 $cm^{-}1$ was associated to the sp^2 carbon stretchment. As carbonization temperature increased, these bands gradually diminished in intensity, reflecting the thermal elimination of functional groups and the advancement of aromatization. At temperatures above 900 °C, FTIR spectra were dominated by weak features characteristic of condensed aromatic carbon structures, in agreement with XRD and XPS observations. A calibration curve for methylene blue was established to enable accurate concentration determination, shown in Figure 3. Standard methylene blue solutions with concentrations of 0.5, 1, 2, 4, 6, 8, 10, and 12 ppm were prepared from a stock solution and analyzed by UV-Vis spectrophotometry. The maximum absorption intensity of methylene blue was identified at a wavelength of 665 nm, which was selected for all subsequent measurements Fig. 4. The calibration curve exhibited a strong linear relationship between absorbance and concentration within the studied range. Adsorption experiments were conducted by contacting a known mass of hard carbon with methylene blue solutions of different initial concentrations under controlled conditions. Samples were collected at predetermined time intervals to study the adsorption kinetics. After solid-liquid separation, the residual methylene blue concentration in the solution was determined using UV-Vis spectrophotometry based on the previously obtained calibration curve.

The results indicated a progressive decrease in methylene blue concentration in solution with increasing contact time, demonstrating the effective uptake of the dye by the hard carbon material. The adsorption process exhibited a rapid initial stage followed by a slower approach to equilibrium, which is characteristic of adsorption controlled by surface interactions and intraparticle diffusion. The kinetic analysis provided valuable insight into the interaction between methylene blue molecules and the surface of the biomass-derived hard carbon.These outcomes underscore the potential of hard carbon synthesized from biomass as a cost-effective and sustainable carbonaceous material for the removal of organic dyes in wastewater treatment processes.

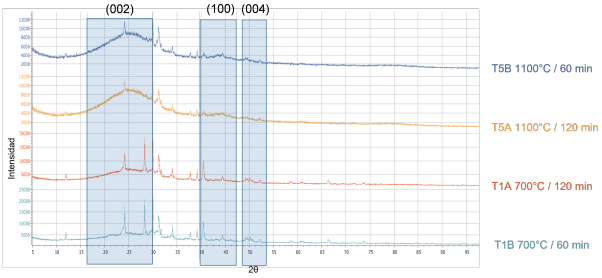

Figure 1: Diffractogram of the biomass analyzed at different temperatures

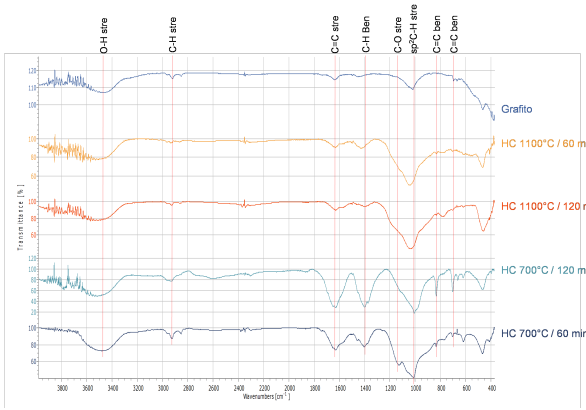

Figure 2: FTIR Spectra of Hard Carbon at different temperatures

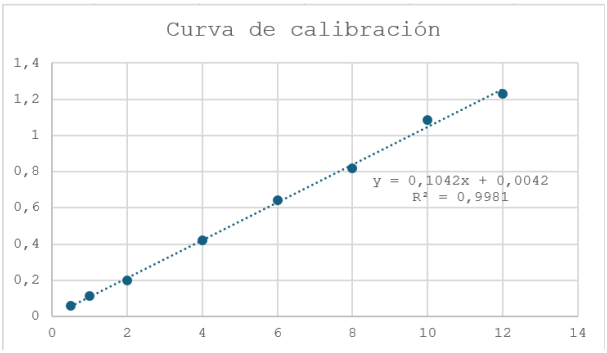

Figure 3: UV-Vis calibration curve for methylene blue solutions at 655 nm

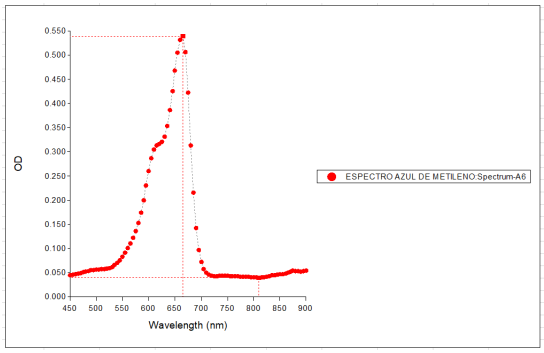

Figure 4: UV-Vis absorption spectrum of methylene blue showing the maximum absorption peak.

References

[1] Rafatullah, M.; Sulaiman, O.; Hashim, R.; Ahmad, A. Adsorption of methylene blue on low-cost adsorbents: a review. *Journal of hazardous materials* **2010**, *177*, 70–80.

[2] Dou, X.; Hasa, I.; Saurel, D.; Vaalma, C.; Wu, L.; Buchholz, D.; Bresser, D.; Komaba, S.; Passerini, S. Hard carbons for sodium-ion batteries: Structure, analysis, sustainability, and electrochemistry. *Materials Today* **2019**, *23*, 87–104. DOI: 10.1016/j.mattod.2018.12.040.